Biological interactions between cell populations in heterogeneous tumour spheroids

Marcin Dawid Paczkowski

Linacre College

University of Oxford

A thesis submitted for the degree of

Doctor of Philosophy

Trinity 2017

“The whole is more than the sum of its parts”

Acknowledgements

I would like to express my deepest gratitude to Prof Helen Byrne for her incredible support and encouragement. I would like to thank Dr Pavitra Kannan for helping me find my way around the lab and Dr Mike Partridge for all his help and expertise. I would also like to thank the Doctoral Training Centre for the training and funding provided and all my colleagues at the DTC, Mathematical Institute, Department of Oncology, Department of Computer Science and Linacre College for all the useful discussions. Last but definitely not least, I would like thank my best friend Mags, to whom I dedicate this thesis.

Abstract

When radiotherapy is prescribed in the clinic, the tumour is assumed to be homogeneous. However, tumours are composed of many distinct cell populations that interact with each other and their environment. It is unclear how this heterogeneity affects tumour growth and response to treatment. Additionally, much of cancer research considers tumour cells in isolation, neglecting the context in which the disease develops. Experimental approaches alone are not sufficient to understand the complexity of the interactions occurring in the cancer ecosystem. In this thesis we use a multidisciplinary approach combining *in vitro* experiments, mathematical modelling and parameter inference methods to explore the impact of cellular heterogeneity on tumour growth and radiation response. Our objectives are: i) to determine if intratumour heterogeneity affects bulk radiation response; ii) to characterise the interactions between co-cultured cell populations; iii) to determine how interactions between different cell populations are affected by radiation.

In the first part of the thesis we design a 3D experimental model in which we co-culture pairs of prostate cancer cell lines with distinct phenotypes and derived from the same tumours. We use the experimental model to study the growth and radiation response of heterogeneous tumours (Chapter 2). We then use nonlinear regression and approximate Bayesian computation algorithm to fit the Verhulst logistic and Lotka-Volterra mathematical models to our data to characterise how the cell populations interact when co-cultured in tumour spheroids before and after exposure to ionising radiation (Chapters 3 and 4). Our third piece of work involves the development of a cellular automaton model of avascular tumour growth to allow for spatial variation within the tumour. The cellular automaton model is simulated for a range of parameter values and fitted to the logistic model to determine the relationship between microscale and macroscale parameters describing tumour growth and to study the dynamics between co-cultured cell populations.

The work presented in this thesis highlights the benefits of multidisciplinary research for understanding cancer heterogeneity. We show that intratumour heterogeneity affects bulk tumour growth and radiation response. We demonstrate how complex biological interactions can be identified and quantified via mathematical modelling and inference. We also show how experimental design studies can streamline biological experiments. Taken together, this work presents a framework for uncovering the effect of cellular heterogeneity on tumour growth with a particular emphasis on interclonal interactions.

Contents

1 Introduction **1**

1.1 Cancer and its treatment 1

1.1.1 What is cancer? 1

1.1.2 Cancer treatment 2

1.1.3 Factors affecting radiotherapy 6

1.1.3.1 Cell cycle 6

1.1.3.2 Hypoxia 7

1.1.3.3 Intratumour heterogeneity 7

1.2 Mathematical modelling of cancer 12

1.2.1 Continuum models of tumour growth 13

1.2.2 Discrete and hybrid models of tumour growth 17

1.2.3 Models of anti-cancer treatment 19

1.3 Summary and thesis aims 22

1.4 Statement of authorship 24

2 The impact of intratumour heterogeneity on tumour growth and radiation response **25**

2.1 Introduction 25

2.2 Materials and Methods 27

2.2.1 Cell lines 27

2.2.2 Cell lines transduction 28

2.2.3 Radiation clonogenic assay 28

2.2.3.1 Normoxia 28

2.2.3.2 Hypoxia 29

2.2.4 Proliferation assay 29

2.2.5 Formation of tumour spheroids 30

2.2.6 Radiation treatment of spheroids 30

2.2.7 Brightfield microscopy 30

2.2.8 Image analysis . . . 31
2.2.9 Measurements of cell populations . . . 31
2.3 Results . . . 32
2.3.1 Characterisation of intrinsic radiosensitivity of cell lines under normoxia and hypoxia . . . 32
2.3.2 Radiation response in heterogeneous monolayers of tumour cells 33
2.3.3 Optimal conditions for tumour spheroids formation . . . 33
2.3.4 Growth and radiation response of tumour spheroids . . . 35
2.3.4.1 Homogeneous spheroids . . . 35
2.3.4.2 Heterogeneous spheroids . . . 36
2.3.5 Measurements of control and resistant cell populations in tumour spheroids . . . 38
2.4 Discussion . . . 43

3 Parameter inference and uncertainty quantification in a simple model of avascular tumour growth 46
3.1 Introduction . . . 46
3.2 Methods . . . 49
3.2.1 Mathematical and statistical models . . . 49
3.2.2 Synthetic data . . . 50
3.2.3 Parameter estimation . . . 50
3.2.3.1 Weighted least squares (WLS) . . . 51
3.2.3.2 Proportional error model (PEM) . . . 51
3.2.4 Confidence intervals . . . 53
3.2.4.1 Asymptotic confidence intervals . . . 53
3.2.4.2 Monte Carlo confidence intervals . . . 53
3.2.4.3 Bootstrap confidence intervals . . . 53
3.2.4.4 Outliers . . . 55
3.2.5 Approximate Bayesian computation . . . 55
3.2.6 Predictive power analysis . . . 56
3.3 Results: synthetic data . . . 56
3.3.1 Parameter estimation . . . 56
3.3.2 Confidence intervals . . . 58
3.3.3 Posterior distributions of model parameters . . . 60
3.3.4 Model predictions for synthetic data . . . 62
3.4 Results: application to experimental data . . . 64

3.4.1 DU145 homogeneous spheroids . . . 66
3.4.2 PC3 homogeneous spheroids . . . 69
3.5 Discussion . . . 71

4 Mathematical modelling of biological interactions in heterogeneous tumour spheroids 75
4.1 Introduction . . . 75
4.2 Mathematical model for heterogeneous avascular tumour growth . . . 76
4.3 Case study: experimental design I . . . 78
4.3.1 Introduction . . . 78
4.3.2 Methods . . . 78
4.3.2.1 Synthetic data . . . 78
4.3.2.2 Statistical noise model . . . 80
4.3.2.3 Parameter estimation . . . 80
4.3.3 Results . . . 80
4.4 Case study: experimental design II . . . 82
4.4.1 Introduction . . . 82
4.4.2 Methods . . . 83
4.4.3 Results . . . 83
4.5 Case study: fitting protocols . . . 86
4.5.1 Introduction . . . 86
4.5.2 Methods . . . 86
4.5.2.1 Synthetic data . . . 86
4.5.2.2 Two-step fitting protocol . . . 86
4.5.2.3 Two-step fitting protocol with data on proportions pooled . . . 87
4.5.2.4 Pooled data fitting protocol . . . 87
4.5.3 Results . . . 87
4.5.3.1 Intrinsic parameters . . . 87
4.5.3.2 Interaction parameters . . . 90
4.5.3.3 Goodness of fit comparison . . . 90
4.5.3.4 Estimating noise levels . . . 92
4.6 Application: parameter inference for heterogeneous PC3 and DU145 tumour spheroids . . . 93
4.6.1 Introduction . . . 93
4.6.2 Results . . . 94

4.6.2.1 PC3 untreated heterogeneous tumour spheroids . . . 94
4.6.2.2 DU145 untreated heterogeneous tumour spheroids . . 96
4.6.2.3 PC3 irradiated heterogeneous tumour spheroids . . . 97
4.6.2.4 DU145 irradiated heterogeneous tumour spheroids . 98
4.7 Discussion . . . 99

5 Cellular automaton model of avascular tumour growth 103
5.1 Introduction . . . 103
5.2 Model description . . . 105
5.2.1 Cellular automaton model . . . 108
5.2.1.1 Rules for specifying cell state . . . 109
5.2.1.2 Cell division . . . 109
5.2.1.3 Cell death and lysis . . . 111
5.2.2 Oxygen dynamics . . . 111
5.2.2.1 Nondimensionalisation . . . 112
5.2.2.2 Numerical scheme . . . 113
5.2.3 Model parameters . . . 114
5.2.3.1 Computational grid . . . 114
5.2.3.2 Cell cycle duration . . . 114
5.2.3.3 Oxygen concentration . . . 115
5.3 Relationship between model parameters at micro- and macro-scale levels 116
5.3.1 Variability in the CA model of homogeneous spheroid growth . 116
5.3.2 Fitting logistic model to CA spheroid growth curves . . . 118
5.3.3 Relationships between CA and logistic model parameters . . . 123
5.3.3.1 Oxygen consumption and lysis . . . 123
5.3.3.2 Oxygen-dependent transition thresholds . . . 126
5.4 Summary . . . 129

6 Cellular automaton model of avascular heterogeneous tumour growth 132
6.1 Introduction . . . 132
6.2 Experimental data from PC3 spheroids . . . 134
6.3 Parameter estimation in CA model of homogeneous spheroid growth . 137
6.3.1 ABC inference in the CA model using synthetic growth curves 137
6.3.2 Parameter sensitivity analysis . . . 140
6.4 Simulations of the growth of heterogeneous spheroids . . . 146
6.4.1 C_1R_2 spheroids . . . 147
6.4.2 Growth curves of heterogeneous spheroids . . . 150

6.4.3 Compositions of heterogeneous spheroids 150
6.5 Lotka-Volterra model for *in silico* data from heterogeneous CA spheroids 152
6.6 Discussion 156

7 Conclusions and future work **159**

A **165**
A.1 Parameter estimates and 95% CIs for synthetic data 165
A.2 The effect of the number of data points on the parameter estimates . 167
A.3 Parameter estimates and 95% CIs for homogeneous spheroids data . . 168

B **169**
B.1 Analysis of the Lotka-Volterra interactions model 169
B.2 Fitting protocols: kinetic parameters 171
B.3 Fitting protocols: interaction parameters 175

C **178**
C.1 Analysis of the reaction-diffusion equation numerical solver: spatial grid size 178

D **185**
D.1 CA simulations of the growth of heterogeneous spheroids 185
D.2 Lotka-Volterra fits to *in silico* heterogeneous CA spheroids 189

Bibliography **193**

List of Figures

1.1 Energy deposition profiles of photons, protons, and carbon ions. . . . 4
1.2 Types of biological interactions among tumour cell populations. . . . 9
1.3 Qualitative behaviour of simple tumour growth laws. 14
1.4 A cross section through a DU145 tumour spheroid. 15

2.1 Radiation response of PC3 and DU145 cell lines under normoxia. . . 32
2.2 Radiation response of PC3 and DU145 cell lines under hypoxia. . . . 33
2.3 The growth of untreated and irradiated heterogeneous populations of PC3 and DU145 cells. 34
2.4 A typical set of experimental results showing that the PC3 cells do not form spheroids in the absence of Matrigel. 35
2.5 PC3 tumour spheroids obtained in different conditions. 36
2.6 Representative images of PC3 spheroids. 37
2.7 Representative images of DU145 spheroids. 37
2.8 Growth curves of homogeneous spheroids. 38
2.9 Growth curves of heterogeneous spheroids. 39
2.10 The proportions of different cell populations measured using the GFP and DsRed channels on a FACS machine. 40
2.11 Proportions of different cell populations within heterogeneous PC3 spheroids. 41
2.12 Proportions of different cell populations within heterogeneous DU145 spheroids. 42

3.1 A diagram showing the differences between the WLS and PEM methods. 52
3.2 Diagram depicting the process of MC simulations. 54
3.3 Noisy synthetic data and corresponding best fits to the logistic model. 57
3.4 The normalised 95% asymptotic, bootstrap and Monte Carlo confidence intervals of the parameter estimates in the logistic model fitted to the fast growing spheroids data. 60

3.5 The normalised 95% asymptotic, bootstrap and Monte Carlo confidence intervals of the parameter estimates in the logistic model fitted to the slow growing spheroids data. 61
3.6 A representative example of the histograms describing distributions of parameters generated with the bootstrap and MC simulations. 61
3.7 Posterior distributions of the logistic model parameters inferred for the fast growing spheroids data. 62
3.8 Posterior distributions of the logistic model parameters inferred for the slow growing spheroids data. 63
3.9 The effect of the tolerance value δ on the posterior distributions of estimated parameters. 63
3.10 The predictive power of the logistic model for the slow growing spheroids. 65
3.11 The predictive power of the logistic model for the fast growing spheroids. 66
3.12 Matrices summarising the predictive power of the logistic model for the slow and fast growing synthetic spheroids. 67
3.13 A typical example of the predictive power of the logistic model within the ABC framework. 67
3.14 Best fits of the logistic model to the DU145 control and resistant spheroids data. 68
3.15 95% confidence intervals for the parameter values estimated from the DU145 control and resistant data. 69
3.16 The approximate marginal posterior distributions for the DU145 control and resistant homogeneous spheroids. 70
3.17 Best fits of the logistic and exponential models to the PC3 control data and the logistic model to the PC3 resistant data. 70
3.18 95% confidence intervals for the parameter values estimated from the PC3 control and resistant data fitted to the exponential and logistic models respectively. 72
3.19 The approximate marginal posterior distributions for the PC3 control and resistant data fitted to the exponential and logistic models respectively. 72

4.1 Synthetic growth curves resulting from solving the Lotka-Volterra model (4.1) with the parameter values as in Tables 4.2 and 4.3. 79
4.2 Estimated values of the interaction parameters for the synthetic PC3 spheroids data. 81

4.3 Estimated values of the interaction parameters for the synthetic DU145 spheroids data. 82
4.4 Point estimates of the interaction parameters. 84
4.5 Estimates and 95% CIs of λ_C and λ_R. 85
4.6 Estimated values of the parameters r_C, K_C, $V_C(0)$, r_R, K_R and $V_R(0)$ for the synthetic PC3 and DU145 spheroids data with 10% noise. . . 88
4.7 Comparison of estimated parameter values in the Lotka-Volterra model fitted to the synthetic PC3 and DU145 spheroids data with 10% noise. 89
4.8 Estimated values with 95% CIs of λ_C and λ_R for the synthetic PC3 and DU145 spheroids data with 10% noise. 91
4.9 Comparison of the weighted sums of squared residuals for the three fitting protocols. 92
4.10 Best fits to the untreated PC3 heterogeneous spheroids data obtained with the two-step (A), two-step pooled (B) and pooled (C) fitting protocols. 95
4.11 Best fits to the untreated PC3 heterogeneous spheroids data obtained with the two-step (A), two-step pooled (B) and pooled (C) fitting protocols shown on a longer timescale. 96
4.12 Best fits to the non-irradiated DU145 heterogeneous spheroids data obtained with the pooled fitting protocol. 97
4.13 Best fits to the PC3 irradiated heterogeneous spheroids data obtained with the pooled fitting protocol. 98
4.14 Best fits to the DU145 irradiated heterogeneous spheroids data obtained with the pooled fitting protocol. 99

5.1 Flowchart corresponding to the algorithm used to implement the CA model. 107
5.2 Two most commonly used types of neighbourhoods in CA models. . . 108
5.3 The amount by which τ_{cycle} for a given cell is reduced after each computational step of length τ as a function of the number of the cell's neighbours. 110
5.4 Chain shifting following a cell division event. 111
5.5 Chain shifting following lysis. 112
5.6 Typical results from simulations of the 2D CA model. 117
5.7 Distributions of and pairwise correlations between estimates of r, K and $V(0)$ in the logistic model. 119

5.8 Best fits to the CA spheroid growth curves obtained with the four fitting methods. 120
5.9 Errors (sums of squared residuals) associated with the four models. . 121
5.10 Estimated parameter values in the logistic model obtained with weighted-data regression for r and K. 122
5.11 Estimated parameter values in the logistic model using CA growth curves generated for a range of (κ, p_{lys})-pairs. 124
5.12 Synthetic growth curves showing initial stages of spheroid growth with $p_{lys} = 0.005$, $\kappa = 100$ (a) and $\kappa = 250$ (b). 125
5.13 Spatial distributions of CA spheroids measured along spheroid radius for $\kappa = 100$ at saturation size. 126
5.14 Parameter values in the logistic model estimated from a range of CA growth curves for different $(c_{\mathcal{Q}}, c_{\mathcal{N}})$-pairs. 127
5.15 Time of hypoxia and necrosis onset (a) and relative spheroid compositions at growth saturation (b) for different values of $c_{\mathcal{Q}}$ and $c_{\mathcal{N}} = 0.1$. 127
5.16 Time of necrosis onset (a) and relative spheroid compositions at growth saturation (b) for different values of $c_{\mathcal{N}}$ and $c_{\mathcal{Q}} = 0.9$. 128
5.17 Correlations between volumes at necrosis onset and at saturation size of spheroids generated for different values of $c_{\mathcal{N}}$ (a) and κ (b). 129

6.1 A diagram depicting our strategy to test the null hypothesis that the co-cultured PC3 cell populations do not interact directly. 133
6.2 Experimental volume measurements and best fits to the growth curves data describing PC3 spheroids grown in low glucose conditions. . . . 135
6.3 Images showing spatial distribution of stained PC3 spheroids. 136
6.4 Posterior probability distributions and pairwise correlations between CA model parameters. 138
6.5 Posterior probability distributions of $c_{\mathcal{Q}}$ for different values of tolerance δ. 139
6.6 Posterior probability distributions of κ for different values of tolerance δ. 139
6.7 Posterior probability distributions and correlations between $c_{\mathcal{Q}}$ and κ for different values of tolerance δ. 140
6.8 The mean squared errors (MSEs) between the volume measurements of the PC3 Ctrl spheroids and synthetic spheroids generated with the CA model for a range of κ, p_{lys}, $c_{\mathcal{Q}}$ and $c_{\mathcal{N}} = c_{\mathcal{Q}} - 0.05$. 142

6.9 The lowest MSEs between volume measurements of the synthetic and experimental PC3 Ctrl spheroids for each value of κ and corresponding spatial distributions of the spheroids on day 7. 143
6.10 Zoomed-in version of plots from Fig. 6.8. Red dots show the points with minimum MSE for each value of κ. 144
6.11 Spatial distribution of C_1 and C_2 spheroids. 145
6.12 Spatial distribution of R_1 and R_2 spheroids. 146
6.13 Growth curves of heterogeneous C_1R_2 spheroids. 147
6.14 Cross-sections through the heterogeneous C_1R_2 spheroids. 148
6.15 Series of plots showing how the spatial distribution of heterogeneous C_1R_2 spheroids changes over time. 149
6.16 Proportions of the control and resistant cells in the heterogeneous PC3 and C_2R_2 spheroids. 151
6.17 Growth curves of heterogeneous *in silico* spheroids in which the co-cultured cell populations differ only by the oxygen consumption rates. 155
6.18 Spatial distributions of heterogeneous *in silico* spheroids in which the co-cultured populations differ only by the oxygen consumption rates. 155

B.1 Existence of non-trivial equilibrium point 170
B.2 Estimated values of the kinetic parameters for the synthetic PC3 spheroids data with 5% and 20% noise. 171
B.3 Estimated values of the kinetic parameters for the synthetic DU145 spheroids data with 5% and 20% noise. 172
B.4 Comparison of estimated parameter values in the Lotka-Volterra model fitted to the synthetic PC3 spheroids data with 5% and 10% noise. . 173
B.5 Comparison of estimated parameter values in the Lotka-Volterra model fitted to the synthetic DU145 spheroids data with 5% and 10% noise. 174
B.6 Estimated values with 95% CIs of λ_C and λ_R for the synthetic PC3 spheroids data with 5% and 10% noise. 176
B.7 Estimated values with 95% CIs of λ_C and λ_R for the synthetic DU145 spheroids data with 5% and 10% noise. 177

C.1 Representative spheroids and oxygen profiles along their radii. 179
C.2 Spatial distributions of CA homogeneous spheroids generated for a range of κ and p_{lys}. 181
C.3 Estimates of r, K and $V(0)$ obtained with four different regression models for a range of values of κ and p_{lys}. 182

C.4 Errors (sums of squared residuals) obtained for four regression models for a range of values of κ and p_{lys}. 183
C.5 Spatial distributions of CA homogeneous spheroids generated for a range of $c_{\mathcal{Q}}$ and $c_{\mathcal{N}}$ values and the best fits obtained with weighted-data regression for r and K. 184

D.1 Growth curves of heterogeneous C_1R_1 spheroids. 186
D.2 Series of plots showing how the spatial distribution of heterogeneous C_1R_1 spheroids changes over time. 186
D.3 Growth curves of heterogeneous C_2R_1 spheroids. 187
D.4 Series of plots showing how the spatial distribution of heterogeneous C_2R_1 spheroids changes over time. 187
D.5 Growth curves of heterogeneous C_2R_2 spheroids. 188
D.6 Series of plots showing how the spatial distribution of heterogeneous C_2R_2 spheroids changes over time. 188
D.7 Best fits of the Lotka-Volterra interactions model to the C_1R_2 spheroids data. 189
D.8 Best fits of the Lotka-Volterra interactions model to the C_2R_2 spheroids data. 190
D.9 Best fits of the Lotka-Volterra interactions model to the C_2R_1 spheroids data. 191
D.10 Best fits of the Lotka-Volterra interactions model to the C_1R_1 spheroids data. 192

Chapter 1

Introduction

1.1 Cancer and its treatment

1.1.1 What is cancer?

The World Health Organisation predicts that a third of the people in developed countries will suffer from cancer at some time during their lives. Despite great progress in treatments for some types of cancer, it is unlikely that successful treatments for all types will be found in the near future. Although cancer can be traced back to a single cell with DNA damage, further changes in its progeny must occur before it becomes malignant [4]. Hanahan and Weinberg proposed six traits that most cancers acquire during tumorigenesis [83]. Healthy cells require growth signals to proliferate and anti-growth signals to maintain homoeostasis. Cancer cells have the capability to disrupt the signalling pathways responsible for the maintenance of homoeostasis, and therefore liberate themselves from growth and anti-growth signals. Homoeostasis in healthy tissues is also sustained via control of apoptosis or programmed cell death. The ability to evade apoptosis is another hallmark of cancer.

The three traits described so far are not sufficient for tumorigenesis. Cancer cells must also escape limited potential for replication programmed into most normal cells. The final two hallmarks identified by Hanahan and Weinberg include the ability to induce and sustain angiogenesis[1] and to invade other tissues. Proliferating cells must be located within 100 µm of a blood vessel to receive oxygen and nutrients. Once tissues are formed angiogenesis is suspended and highly regulated. In order to grow cancer cells must develop the ability to trigger the formation of new blood vessels. Without angiogenic capacity cancer cells are dormant and cannot metastasise[2]. As a

[1] formation of new blood vessels

[2] spread to new areas of the body and establish secondary cancers

result, disrupting angiogenesis has become an important anti-cancer target [5].

The six hallmarks of cancer were updated by Hanahan and Weinberg a decade later by the addition of two further traits [84]. They speculated that cancer cells can reprogram energy metabolism to rely on anaerobic glycolysis as the means for energy production. Additionally, the authors argued that cancer cells must be able to escape the immune system constantly monitoring tissues and organs.

1.1.2 Cancer treatment

As explained in the previous section cancer development is a multistep process. A large body of evidence suggest that most cancers are, at least in principle, preventable [4]. Environmental effects have been shown to be one of the major factors contributing to cancer incidence. These include exposure to UV and ionising radiation, smoking tobacco, viral infections and unhealthy diet. Although changing lifestyle habits could reduce the risk of developing the disease, not all cancers can be avoided. In such cases treatment is necessary.

The main types of treatment for cancer include surgery, chemotherapy and radiotherapy. Their main goal is to eradicate all cancer cells. In some cases, it may be more appropriate to control the progression of the disease via biotherapy whereby living organisms are used to support the immune system. Advances in screening methods can lead to early detection of primary tumours, before they spread to neighbouring tissues [4]. In such cases surgery may be the most appropriate treatment option. Surgery is often used to remove breast, colon, rectum, thyroid and prostate tumours [175] and is typically followed by either chemotherapy or radiotherapy (adjuvant therapy). Chemo- or radio-therapy can be applied before surgery to shrink the tumour (neoadjuvant therapy). Surgery may be less effective if the tumour has already metastasised. Moreover, all types of cancer treatment are associated with mild to severe side effects [175].

Although primitive forms of chemotherapy have been practised since the ancient times, the modern era of using chemotherapeutic agents to cure cancer began in the 1940s [145]. Autopsy findings from soldiers exposed to mustard gas during the First World War, led to its use to treat lymphoid tumours [76]. Around the same time antifolates were shown to suppress cancer cell proliferation in children with leukaemia [64]. These discoveries stimulated a period of government- and academia-led research into cancer drug development [42]. Initially, there was little interest from industry as cancer drugs were considered a high risk investment. In the late 1980s multiple advances in genetic and molecular cell biology led to the era of targeted

therapy. Drugs, such as imatinib[3], targeting particular pathways were shown to lead to tumour remission with relatively few side effects [101].

Drug discovery is now a multi-billion pound industry, with hundreds of chemotherapeutic agents in clinical trials [42]. Nanoparticle therapeutics are a particularly promising type of chemotherapy. These small particles comprising therapeutic drugs with polymers and lipids can carry the drug to specific locations while protecting it from degradation [49]. Due to improved pharmacokinetics and pharmacodynamics, nanoparticle therapeutics can have better anticancer effects than the drugs alone. At the same time, they can significantly reduce side effects. Currently, the major problem with nanoparticle therapeutics is their large-scale production.

Wilhelm Röntgen's discovery of X-rays in 1895 and the pioneering work of Marie Skłodowska-Curie on radioactivity marked the beginning of the field of radiation therapy. A century later radiotherapy (RT) is used by more than half cancer patients, despite accounting for only 5% of the total cost of cancer care [51]. RT involves exposing tumours to either external or internal radiation sources. External radiotherapy, which is used more commonly, consists of directing a beam of ionising radiation at the tumour using linear accelerators [95]. Alternatively, to minimise the exposure of healthy tissue, a radiation source can be placed directly at the tumour site—a form of RT known as brachytherapy.

Ionising radiation works by ejecting electrons from molecules in the affected cells. These electrons cause further damage, such as breaking of chemical bonds in DNA [95]. Indeed DNA is the key target of radiation. The main types of DNA damage include single- and double-strand breaks. For example, 1 Gy of radiation can cause about 1000 single- and 20–40 double-strand breaks. Cells have developed an elaborate system of DNA damage response mechanisms. Depending on the type of DNA damage, cells can initiate various pathways, such as apoptotic pathway, DNA repair pathway or temporary cell cycle arrest [95].

Ionising radiation can be divided into photon radiation and particle radiation. The former is used more commonly and includes X-rays and gamma rays. Photon beams have high energy levels and usually travel through a patient's body causing damage to *all* cells on their path. On the other hand, particle radiation involves energy release from carbon ions or proton beams after they have been transmitted by a certain distance (Fig. 1.1). Such beams deposit the energy at the end of their path, forming so called Bragg peaks [172]. A clear advantage of photon beam RT is

[3]inhibitor of the BCR-ABL tyrosine kinase

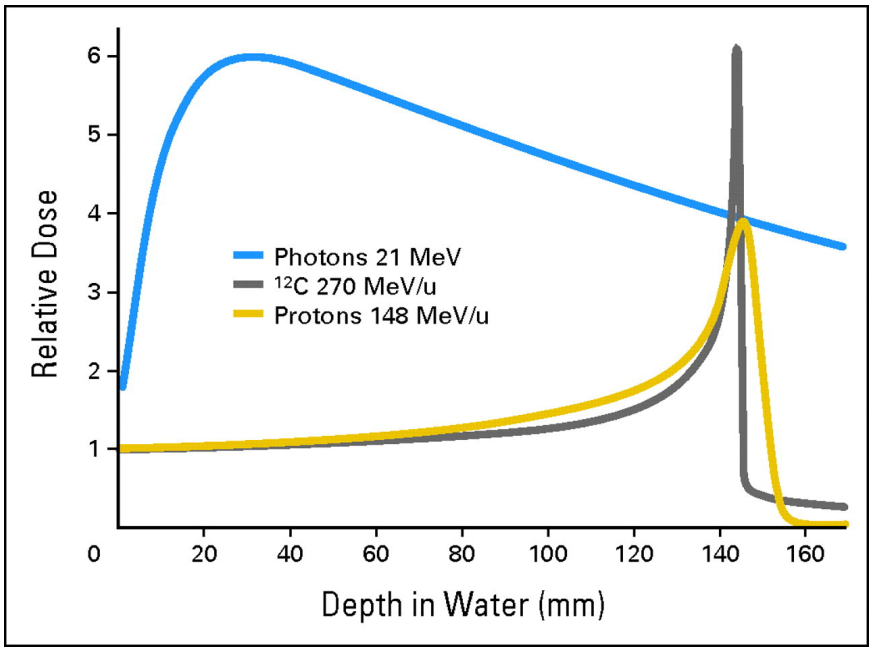

Figure 1.1: Energy deposition profiles of photons, protons, and carbon ions [172].

that more radiation can be delivered to the tumour site while normal tissue exposure is minimised.

The DNA damage response mechanism activated following radiation injury can trigger many pathways simultaneously [95]. Additionally, there are many possible ways in which a cell can die. Consequently, cell death in the context of RT has been defined as the loss of clonogenic capacity by the cell. The mechanisms of cellular death include apoptosis. However, since most cancer cells can evade activation of this pathway, its contribution to cellular death following radiation is believed to be insignificant in most cancers. Autophagy is a poorly understood form of cell death that might play an important role in response to RT but it is a subject of active research [168]. Whereas apoptosis is seen as a controlled programmed cell death, necrosis is a chaotic process resulting in the breakdown of a cell and the release of its components into the stroma. Another form of cell death in the context of RT is senescence. Although senescent cells remain metabolically intact, they have permanently lost their reproductive capacity. As with apoptosis, activation of the senescence pathway depends on the type of cancer [95].

Although the DNA damage response mechanism is effective in repairing initial radiation injury, it cannot prevent some cells with DNA breaks from attempting division [95]. Such cells may divide once or more but eventually lose their reproductive potential and various cell death pathways are activated. This process, referred to as

mitotic catastrophe, is believed to be the main contributor to cellular death following radiation damage, and occurs at a relatively long time after the initial injury. It is therefore important to realise that quantifying one type of cell death is not a reliable indicator of the total amount of damage caused by radiation treatment.

An interesting development in investigating the effects of radiation on cellular fate was the discovery of the so called radiation-induced bystander effects (RIBE). First reported in the 1950s, studies involving RIBE gained momentum in the last decade as an important contributor to radiation damage [132]. This still poorly understood phenomenon has been defined as any biological effect following irradiation experienced by cells that have not been directly exposed to radiation [133]. RIBE can be manifested as DNA damage, genomic instability, mutations and gene expression in cells that have not been traversed by radiation beams. While the mechanisms responsible for RIBE have not yet been elucidated, the existing evidence suggests that signalling between cells can occur via gap junctions or soluble factors released into the medium [157]. RIBE are typically observed following low-dose treatments and could be exploited to improve the efficacy of radiation treatment. However, RIBE may contribute to secondary cancer formation when the signals released by irradiated cancer cells cause damage to the surrounding healthy cells, leading to mutations and potentially triggering carcinogenesis.

The overarching goal of RT is to maximise the damage to cancer cells while minimising normal cells exposure. Technological advances in imaging and treatment planning techniques in the last four decades have led to a more targeted therapy [21]. Introduction of computed tomography and magnetic resonance imaging allowed clinicians to accurately determine the location and size of tumours and to avoid hitting healthy tissue with radiation beams. The shift from 2D to 3D conformal RT led to further advances, such as intensity-modulated RT [18]. This method enables clinicians to deliver radiation to irregularly-shaped targets, increasing the dose to tumours while sparing vital organs. To improve the precision of the delivered dose even further, imaging technologies have been incorporated into treatment equipment [92]. Such image-guided RT, can correct for minor imprecisions in the beam path arising due to patient breathing or other movement.

The *anatomical* imaging techniques described in the previous paragraph can inform a clinician about the tumour's size and location relative to other organs. In contrast, *functional* imaging can provide information about tumour physiology and biochemistry [21]. Positron-emission tomography (PET) can detect isotopes attached to molecules that are upregulated in cancer cells. For example, PET imaging can

detect areas within a tumour that are characterised by increased proliferation or hypoxia. Metabolic changes in tumours can be also studied using magnetic resonance spectroscopy.

Due to radiation effects on normal tissue surrounding the tumour, RT is typically applied in fractions over a period of time. Fractionated therapy exploits the fact that cancer cells proliferate faster than normal cells and the latter are generally better at repairing damage [18]. Thus the dose and time between fractions are selected to allow normal cells to recover to minimise side effects. However, both early and late normal tissue responses must be taken into consideration, as depending on the fractionation schedule differential early and late radiation responses can be observed [190]. This realisation has led to the development of various RT schedules, such as hyperfractionation where a dose per fraction is reduced but the number of fractions is increased, or hypofractionation where few higher doses are given [95].

1.1.3 Factors affecting radiotherapy

RT frequently fails to eradicate all cancer cells in the treatment region and this can lead to disease recurrence. To explain fractionated RT failures, Withers [199] proposed four factors determining the treatment outcome. The four Rs of RT were identified as: repair, repopulation, redistribution and reoxygenation. Later, the list was supplemented by radiosensitivity [179]. These five factors are briefly discussed below.

1.1.3.1 Cell cycle

As mentioned earlier, the DNA damage response mechanism is an effective way to repair radiation injury in normal cells. Activation of cell cycle checkpoints is common pathway caused by ionising radiation [149]. Progression through the cell cycle is halted to allow DNA damage repair. Several cell cycle checkpoints have been identified including a checkpoint at the transition from the G_1 to the S phase, a checkpoint in the S phase and two checkpoints in the G_2 phase—one early on and one just before mitosis [95]. However, the defective DNA damage response mechanism in most cancer types prevents tumour cells from being stopped from cell cycle progression, which can be exploited to improve RT outcome [91]. Sinclair and Morton [176, 177] observed as early as 1960s that cells are most resistant to radiation when in the S phase of cell cycle. Sensitivity increases in the G_1 phase and even further just before and during mitosis. Differential sensitivity to radiation in normal and cancer cells leads

to cell cycle redistribution between fractions. Since actively proliferating cells are more radiation-sensitive, by applying successive fractions before normal cells resume division, a window of opportunity is created to hit the more sensitive cancer cells [149]. Consequently, modulating DNA repair mechanism and cell cycle checkpoints have been suggested as targets for strategies to improve RT outcome [19].

1.1.3.2 Hypoxia

Radiation response is also critically dependent on cellular oxygenation status [77]. Ionising radiation can create free radicals—highly reactive molecules with unpaired electrons such as reactive oxygen species which can break chemical bonds in molecules like DNA [95]. Well oxygenated cells are three times more sensitive to radiation than anoxic cells [166]. Normal tissues have generally adequate oxygen supply from the vascular system. However, due to uncontrolled proliferation, cancer cells eventually outgrow their oxygen supply. Thomlinson and Gray [191] observed that solid tumours with radius above 200 µm were characterised by central necrotic regions which were not present in tumours with radius less than 160 µm. Their findings led to the realisation that most tumours have regions of necrosis surrounded by a layer of hypoxic but viable cells, and an outer rim of proliferating cells located close to vascular stroma. Such histological feature is the result of the oxygen diffusing from the source on the outside of the neoplasm. The thickness of the observed layers depend on the oxygen consumption rate of the individual cells comprising the tumour [191].

Following the discovery by Thomlison and Gray, hypoxia became a major target of cancer treatment. In particular, the concept of reoxygenation has been exploited in fractionated RT. When tumours are irradiated, the majority of damage is experienced by cells in well oxygenated regions. The surviving hypoxic cells subsequently become oxygenated due to tumour shrinkage or release of the pressure on occluded blood vessels [95]. Following oxygenation of the previously hypoxic cells, another round of RT can be applied. The disadvantage is that freshly oxygenated cells resume proliferation which can lead to repopulation. The development of chemotherapeutic agents sensitising cancer cells to radiation has been an active area of research [19, 131, 148].

1.1.3.3 Intratumour heterogeneity

Although tumours often originate from a single cell, at the time of detection most tumours present extensive genotypic and phenotypic heterogeneity. The concept of intratumour heterogeneity (IH) is not new; cancer has long been considered a clonal

disease [138], though the idea was initially met with scepticism [85]. Today, the presence of multiple cancer cell subpopulations within a single neoplasm could supplement the list of hallmarks of cancer. Two hypotheses have been developed to explain IH: the cancer stem cells hypothesis and the clonal evolution hypothesis [40].

The cancer stem cell (CSC) hypothesis emerged following an observation that some phenotypically distinct subclones of cells derived from human leukaemia could establish the disease in mice, whereas other subclones could not [105]. The CSC hypothesis is based on the idea that a particular group of cells is responsible for initiation, progression and recurrence of tumours [40]. These cells—just like stem cells—can self-renew and differentiate into other non-stem cancer cell types. According to the cancer stem cell hypothesis all cancers are initiated by a set of mutations acquired by a normal stem cell which gives rise to a cancerous lesion. A small pool of genetically unstable cancer stem cells is maintained in a growing tumour and further mutations in such cells lead to establishing of new subclones, thus generating intratumour heterogeneity. The consequence of this still controversial hypothesis is that targeting cancer stem cells can effectively treat the disease. For if the pool of cells with limitless proliferating potential can be eliminated then the remaining cancer non-stem cells are irrelevant for the disease progression.

According to the clonal evolution hypothesis any normal cell has the potential to initiate a tumour, so long as it acquires the mutations giving it growth advantage over other normal cells [40]. Thus Darwinian forces of natural selection select for the cells with higher fitness promoting cancer progression. Proliferating cancer cells can mutate further due to genetic instability characteristic to neoplastic cells. Any mutation that leads to the cell's growth advantage over its neighbours can lead to the establishment of a new phenotype. Subpopulations with higher fitness are more likely to expand within developing tumours than those with lower fitness. This dynamic system is believed to be responsible for the observed IH and led researchers to consider cancer as an evolutionary process [119] or even an ecosystem drawing parallels with population dynamics [17].

Traditionally, tumour progression was described as a linear process, with successive fitness-promoting mutations leading to selective clonal sweeps [115]. However, tumour composition is often highly heterogeneous, with distinct clones coexisting within a neoplasm. The likely mechanisms of coexistence include: fitness-neutral mutations, different niches occupied by cancer subclones, spatial distribution of subclones and fluctuating microenvironmental conditions leading to coexistence in non-equilibrium [119].

Viewing cancers from the ecological perspective implies the existence of biological interactions of the phenotypically distinct tumour cell subpopulations among themselves and with the microenvironment [115]. The ecological interactions can have positive, negative or neutral effect on the fitness of interacting species (Fig. 1.2). *Competition* is believed to be the most important type of interactions between cancer

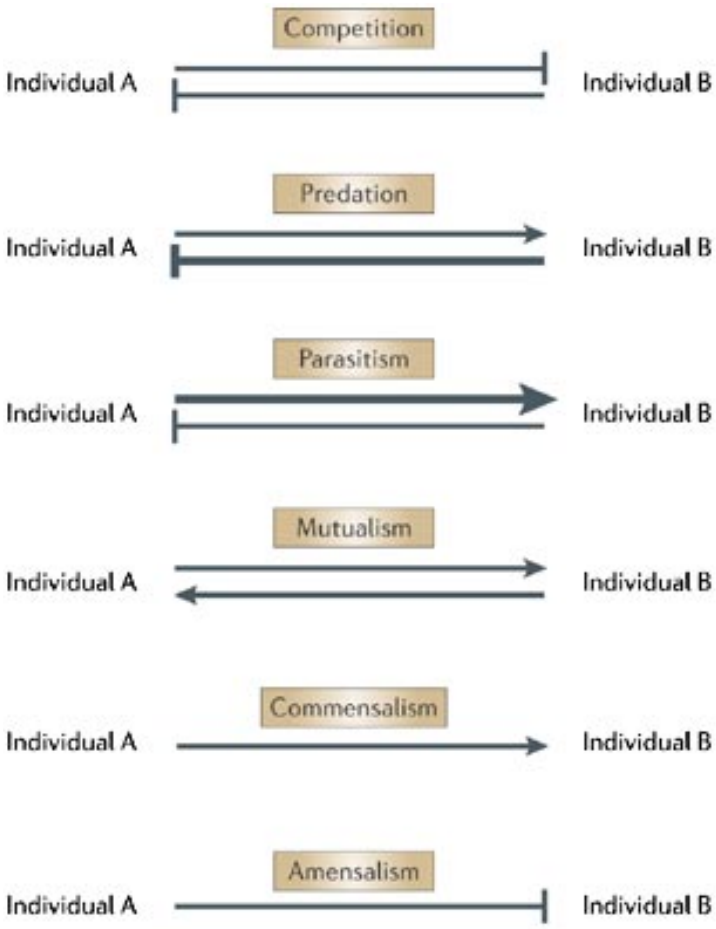

Figure 1.2: Types of biological interactions among tumour cell populations [119].

cell subpopulations [115]. Clones can interact indirectly in the form of competition for space, oxygen and other nutrients, or directly via cell-to-cell communication and release of soluble factors [119]. *Amensalism* is a form of competition in which one population inhibits the growth of another but is itself unaffected. Positive interactions include: *commensalism*, when one species benefits the other without any cost or benefit to itself; and *mutualism*, when both populations cooperate to achieve mutual benefit [188]. For example, Cleary et al. [45] showed that heterogeneous breast cancer cells injected in mice cooperated to maintain the production of Wnt1 signalling

molecule, essential for tumour progression.

Other biological interactions may be beneficial to one subpopulation but detrimental to the other. Such antagonistic interactions, although abundant in natural ecosystems, are rarely observed in tumour growth [115]. Depending on the relative strength of the positive and negative effects between two species, we distinguish *predation* and *parasitism*. The former is believed to occur between cancer cells and immune system. An example of parasites include the so called free-riders which benefit from the metabolic activity of their neighbours [119].

The emergence and maintenance of IH is not only influenced by genetic instability and clonal interactions but also by the tumour microenvironment. Cancer cells can reshape their microenvironment by recruiting fibroblasts, activating the immune system and initiating angiogenesis [97]. Fitness-driven clonal evolution is context-dependent in that survival and expansion of cancer subpopulations depends on the mutations that provide growth advantages *in a given microenvironment*.

The cancer stem cell and clonal evolution hypotheses described above need not be mutually exclusive. Both models assume that cancers are initiated if a single cell acquires mutations giving it growth advantage over other cells. However, some critical differences exist between the two concepts. Most notably, according to the stem cell hypothesis, IH is generated from a small pool of cells which due to genetic instability differentiate into multitude of cancer subclones [40]. In contrast, the clonal evolution hypothesis assumes that any cell has the potential to drive tumour progression and IH emerges as a result of various interactions among the subclones and with the microenvironment. However, stemness could be a continuous property describing cellular capacity for proliferation and Darwinian forces could also work on cancer stem cells. The two hypotheses suggest different treatment approaches. Targeting cancer stem cells could lead to tumour collapse, whereas all subclones with distinct phenotypes would have to be eliminated according to the clonal evolution hypothesis [40].

Regardless of which hypothesis is correct, IH poses a significant challenge for disease progression and treatment. Although advanced non-invasive techniques for imaging IH are currently being developed [139], local invasive biopsies remain the major diagnostic method. One of the crucial challenges in curing cancers is the existence of therapy-resistant subpopulations of cells that can be selected for by treatment. As mentioned above, the BCR-ABL tyrosine kinase inhibitor imatinib led to unprecedented initial response in chronic myeloid leukaemia patients [50]. However, many patients relapsed due to the presence of subpopulations of cells resistant to imatinib.

In some cases, samples taken prior to treatment were shown to include the resistant subpopulations [164] which confirms that imatinib treatment creates selective pressure favouring the outgrowth of the treatment-resistant cells. A number of suggestions have been put forward to exploit IH. For example, the selective advantage of benign or drug-sensitive subclones could be increased leading to the outgrowth of malignant or drug-resistant cells before treatment is administered [115]. Adaptive therapies have also been suggested as a way to maintain the population of drug-sensitive cells in order to prevent the drug-resistant cells from expanding [71].

Although intratumour heterogeneity and interclonal interactions have been studied in the context of response to chemotherapy, it is unclear what impact they have on tumour response to radiation. A telling example demonstrating the importance of cell-cell communication are the radiation-induced bystander effects. In this thesis, we aim to investigate how the information on the extent of IH can be exploited to improve RT outcome. In particular, our objective is to develop methodology allowing to study the impact of IH on radiation response and vice-versa. We build upon early work by Bonnie Miller, Gloria Heppner, John Leith and colleagues who conducted a series of experiments with co-cultured cell populations. The observation that clones derived from a single tumour differed in many characteristics including growth rate, morphology, drug and radiation sensitivity (e.g., [107]) prompted these researchers to investigate potential interactions between the clones. Miller, Heppner and others focused on cell lines isolated from a mammary tumour [129, 125, 130, 128, 124] whereas Leith and co-workers studied human cells [107, 109, 108, 110].

Miller et al. [129] injected cell lines derived from the same tumour into both flanks of mice. They found that the presence of clone 410 on one flank inhibited the growth of clones 168 and 410 on the other flank. Clone 168 did not have the same effect. When cyclophosphamide (CY) was given to the mice, the sensitivity of the CY-resistant 410 tumours was increased by the presence of the CY-sensitive 168 tumours on the other flank [125]. The sensitivity of the 168 tumour was not affected by the presence of either cell line. When mixtures of cell lines 168 and 4T07 derived from the same tumour where injected in mice, 4T07 cells suppressed the growth of 168 cells even when seeded at the 100:1 ratio in favour of line 168 [130]. Miller et al. also investigated the response of co-cultured tumours injected into mice to the drugs methotrexate [128] and melphalan [124]. They found that tumours composed of 66 and 4T07 cells were as responsive to methotrexate as were the tumours composed of the 4T07 cells alone [128]. However, the mixture of 168 and 4T07 cells was less sensitive than that of cells 4T07 alone. The sensitivity to melphalan of line 66 was

increased when the cells were mixed with 4T07 cells [124]. However, no effect was observed when 4T07 tumours were grown on the other flank of mice. Collectively, the results reported by Miller and colleagues, including the observation that cellular composition of tumours did not reflect their response to treatment and the lack of system-wide mechanism responsible for the drug-sensitivity transfer between cell lines, point to immense complexity of the growth properties of heterogeneous tumours.

Leith and co-workers arrived at similar conclusions following experiments in which mixtures of colon cancer clones (denoted A and D) were injected in mice. In one study, they estimated parameter values in the Gompertz model of tumour growth for each subpopulation separately and based on the estimates attempted to predict the growth of heterogeneous tumours [109]. It was not possible. In another study, Leith et al. [110] mixed clones A and D at the ratios 9:1 and 1:9, and injected the mixtures in mice. The composition of the tumours did not change over time. However, when the tumours were irradiated with a single dose of 15 Gy, the composition post-irradiation changed in that the fraction of the majority population increased in both types of tumours. Further experiments, in which only the normal tissue was irradiated prior to mixtures seeding, yielded similar results. The authors concluded that the changes in composition of heterogeneous tumours were the result of the radiation damage experienced by tumour stroma rather than direct injury to tumour cells.

1.2 Mathematical modelling of cancer

Mathematical models can represent biological systems by the means of abstraction using mathematical language. They provide a framework for studying how different biological processes interact, for elucidating the mechanisms involved in cancer, for testing biological hypotheses, suggesting new experiments and generating testable hypotheses. Mathematical models have been long used in cancer research to describe, explain and predict tumour initiation, progression, metastasis and response to treatment [12, 34, 167, 112, 33, 60, 58, 7]. Mathematical models of tumour growth can be categorised into two broad classes: continuum and cell-based discrete models, but other classifications are also possible. We describe below some models of tumour growth with particular emphasis on avascular tumour growth models and response to RT.

1.2.1 Continuum models of tumour growth

Continuum models are usually applicable at the tissue level, where individual cellular behaviour is less important than macro-scale behaviour. In such models the variables are treated as continuous fields and ordinary (ODE) or partial (PDE) differential equations, accompanied by appropriate initial and boundary conditions, are used to describe them. Model variables can represent densities or volume fractions of tumour and normal cells, extracellular matrix, vascular network, growth factors or cell substrates such as oxygen or glucose. Depending on the complexity of the model, the resulting equations can be solved analytically (e.g. [78]), or numerically (e.g. [48, 89]).

The simplest continuum models of tumour growth describe temporal changes in tumour size [72]. They are based on ODEs and neglect spatial effects, instead describing the evolution of tumour radius or volume over time. In the most basic case, the change in tumour size is a result of the difference between proliferating and dying cells. Such models can be written as

$$\frac{dV}{dt} = V \cdot f(V) \tag{1.1}$$

where V is the tumour size and $f(V)$ is the per capita rate of tumour growth. If $f(V)$ is constant then the tumour grows exponentially. Although exponential growth is often observed during early stages, as the tumour gets bigger its growth rate decreases [72]. Avascular tumours or tumour spheroids[4] do not tend to grow beyond a certain size due to diffusion-limited supply of metabolites [185]. Thus the per capita growth rate $f(V)$ is a size-dependent function.

A number of ODE-based models have been used to describe tumour growth—the Verhulst logistic, Gompertz and von Bertalanffy models standing out as the most widely used [72]. These, together with other classical models, have been fit to xenograft [120], *in vitro* tumour spheroids [114] and *in vivo* tumour [20, 171] data to assess their descriptive and predictive powers. The Gompertz model emerged as the best description of the considered growth curves in most cases [120, 114, 20, 171] but none of the models provided sufficient predictive power [20]. Qualitative behaviour of some of the classical ODE models of tumour growth is shown in Fig. 1.3.

The classical models have been extended in several ways to provide more realistic descriptions of tumour growth and to test various hypotheses [82, 169]. As explained above, the growth of avascular tumours and tumour spheroids is halted when the balance between cell proliferation and death is attained. However, *in vivo* tumours

[4] experimental *in vitro* models of avascular tumours

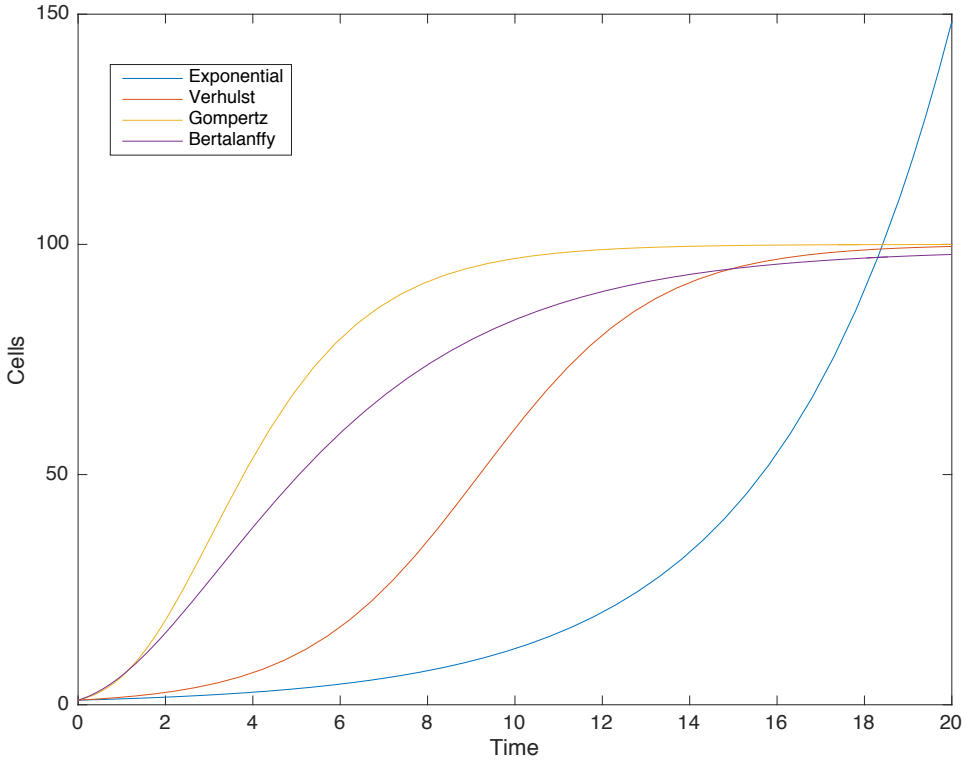

Figure 1.3: Qualitative behaviour of simple tumour growth laws.

can produce angiogenic factors to stimulate the development of vasculature [66]. This prompted Hahnfeldt et al. [82] to derive a dynamic expression for the carrying capacity[5] of the tumour by coupling its growth and vasculature. The difference between vasculature stimulation and inhibition due to anti-angiogenic treatment led to a growth plateau. In addition to angiogenesis, vasculogenesis[6] can also contribute to formation of blood vessels [28]. The combined effect of angiogenesis and vasculogenesis was shown to be similar to the effect of each of these processes considered separately with a vascular tumour growth model consisting of coupled ODEs [178]. Model analyses revealed that the tumour could either reach avascular or vascular equilibria, or grow unboundedly.

Although ODE-based models have proven useful, they neglect spatial effects. The pioneering work on tumours and tumour spheroids conducted by Thomlinson and Gray [191] and Sutherland and colleagues [184, 185] revealed their structure and

[5] maximum sustainable size

[6] *de novo* formation of blood vessels

growth dependence on diffusing metabolites and then stimulated the development of early spatio-temporal models of avascular tumour growth [32, 78]. Tumour spheroids are spherical structures that receive oxygen and nutrients via diffusion from their surroundings. The tumour may contain up to three distinct zones: a central necrotic core containing dead cells, an intermediate quiescent zone containing viable hypoxic cells, and an outer rim of proliferating cells (Fig. 1.4). Greenspan [78] viewed the tumour

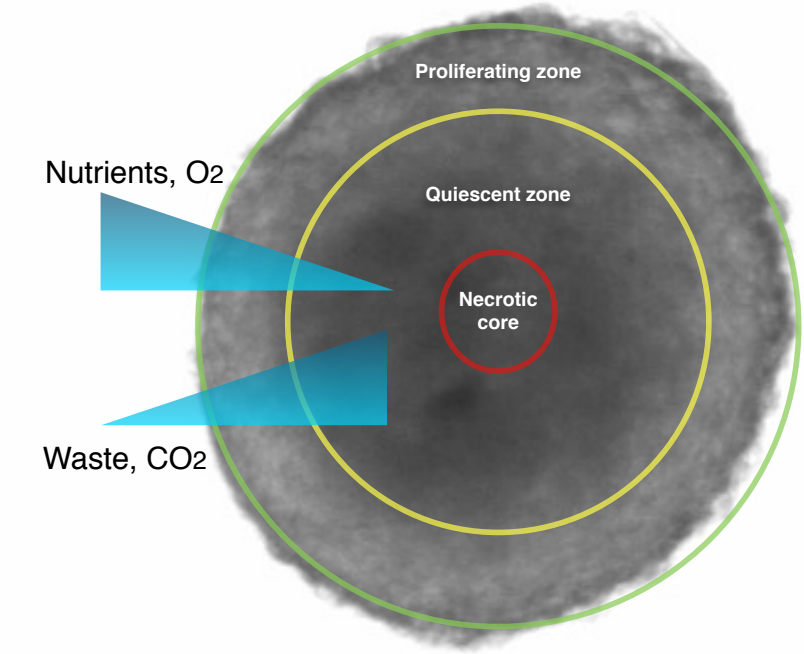

Figure 1.4: A cross section through a DU145 tumour spheroid.

as a radially symmetrical sphere whose radius evolves over time. He assumed that the size of the tumour was controlled by the diffusion of externally supplied oxygen or internally produced necrosis factor (modelled with a reaction-diffusion equation). Local rates of cell proliferation and death were regulated by the distribution of diffusible factors leading to the formation of necrotic, quiescent and proliferating zones. By allowing necrotic debris to be removed from the tumour interior, proliferating cells from the outer region could move inwardly striking a balance between cell growth and death, and leading to an equilibrium size.

This early work provided a good qualitative agreement with data on spheroid growth. However, its simplicity prompted others to extend Greenspan's model [12, 167]. For example, Greenspan [79] and Byrne and Chaplain [36] studied the stability

of radially symmetric structure of avascular carcinomas where the balance between surface tension or cell-cell adhesion forces and forces generated by expanding tumour mass was disturbed. Model analysis revealed that the stability of the radially symmetric steady state solution can be broken when cell-cell adhesion is weak [36]. Other modifications included considering two populations of cells within a tumour: live and dead cells [197]. The concentrations of live and dead cells depended on the local concentration of a nutrient (all modelled with nonlinear PDEs) and the changes between the two states generated a velocity field within the spheroid. Based on the models by Greenspan, Byrne and Chaplain and others, Cristini et al. [48] performed computer simulations demonstrating that tumour growth and its progression could be controlled by two parameters relating cellular birth, death, mobility and adhesion.

In the last two decades a number of multiphase models of tumour growth have been developed [151, 104, 8, 29, 38, 39, 30, 89]. Please et al. [151] described tumour cells and extracellular fluid as incompressible phases exchanging water. Cell birth and death were the only mechanisms for cell movement. Although cell proliferation was regulated by the concentration of oxygen diffusing from tumour surroundings, the formation of the necrotic core was a result of stresses within the tumour. In particular, necrosis occurred when the pressure of extracellular water exceeded the pressure of cellular phase causing the cells to rupture. This model was later extended to include initially neglected drag forces between cells and extracellular water [104]. Byrne et al. [38] showed that models such as that of Greenspan [79] could be recovered as limiting cases from a two-phase model. A similar two-phase model considering tumour cells and extracellular matrix [29] was later extended to explicitly consider blood vessels phase [30] and healthy cells [89].

Continuum spatio-temporal models have been also used to describe processes such as angiogenesis [14, 35] and cancer invasion and metastasis [70]. For example, Balding and McElwain [14] developed a one-dimensional model in which they explicitly tracked the densities of a tumour angiogenesis factor (TAF), capillary tips and blood vessels. TAF was assumed to be produced by tumour cells at a constant rate and diffuse towards the blood vessels. In response to TAF concentration, the capillary tips emerge from the blood vessels and move by chemotaxis[7] towards the TAF source producing new vessels. The model was later extended to include TAF consumption rate and additional capillary tip proliferation rate triggered at a certain TAF concentration [35]. Numerical simulations of these models reproduced many qualitative features of angiogenesis. Gatenby and Gawlinski [70] in a seminal paper developed

[7]cell movement in response to a chemical signal

a model of cancer invasion by considering the densities of tumour cells, hydrogen ions and extracellular matrix. Cancer cells were assumed to proliferate following the logistic growth and undergo nonlinear diffusion, secreting hydrogen ions. Diffusing hydrogen ions were assumed to degrade the extracellular matrix, thus creating the space for invading tumour. The model predicted the existence of a gap between the tumour front and regressing extracellular matrix which was later verified experimentally. One of the many extensions to this model includes the work of Anderson et al. [10] who studied the role of haptotaxis[8] on cancer invasion in two-dimensions.

1.2.2 Discrete and hybrid models of tumour growth

Deterministic continuum models of the type described in the previous section treat tumours as continuous masses. Such models neglect stochastic effects and subcellular phenomena and are therefore more suitable for tissue scale modelling. Moreover, continuum models tend to lump physical properties into few parameters which, although simplifies mathematical analysis, can make them difficult to interpret. Discrete models provide an alternative approach as they view each cell individually, assigning specific rules or properties to model their function and behaviour. Such models can be formulated on a regular lattice (e.g., cellular automata) or off-lattice. Lattice-based models confine cells to a computational grid which makes them easier to implement. However, such uniform spacing can introduce artificial constraints on the system. Lattice-free models are more flexible but their complexity can make them computationally demanding.

One of the most basic lattice-based models of tumour growth was developed by Qi et al. [159]. By employing a number of cellular automata (CA) rules implementing cell division and the cytotoxic effects of the immune system, the authors were able to reproduce Gompertzian growth of cancer. A more complicated, three-dimensional CA model, that also reproduces Gompertzian growth, was developed by Kansal et al. [100]. This model was based on a fixed but non-uniform lattice. To generate such lattice of the Voronoi tessellation, a random set of points representing sites was first assigned to a space. Each cell was then defined as the region nearer to a given site than any other site. Although Kansal and colleagues did not model the effects of O_2 or other nutrients explicitly, they were able to recreate the necrotic, quiescent and proliferative regions observed in avascular tumours by considering the distance between a given cell and the tumour's boundary. Thus cells farther away from the boundary were

[8] cell movement up a gradient of a cellular adhesion site

assumed to have insufficient nutrition supply and underwent quiescence or death. The model was used to study the emergence of a second tumour clone by introducing in a random cell a set of mutations changing its growth dynamics [100, 99].

In addition to studying cancer invasion in 2D using a PDE-based approach, Anderson et al. [10] also developed an equivalent 2D CA model that they derived from the continuum description of the same process [10]. As before, cancer cells were assumed to secrete enzymes degrading the extracellular matrix. Individual tumour cells were then able to migrate into the space created by diffusion and haptotaxis. By discretising the invasion model (which also included cell proliferation in contrast to the PDE model), Anderson and co-workers showed how stochastic effects enabled individual tumour cells to migrate much further than predicted with the continuum model. This model was later extended by including the effects of cell adhesion and oxygen concentration to study the effect of the microenvironment on the tumour phenotypic diversity [9].

The invasion models described above [10, 9] are in fact hybrid, rather than discrete models. They combine descriptions of tumour growth at the level on individual cells with continuum field descriptions of diffusible chemicals such as O_2. Hybrid models combining the advantages of the continuum and discrete approaches are increasing in popularity. Gerlee and Anderson [73, 74] modified the hybrid CA model of invasion further to study clonal evolution in cancer. The behaviour of each cell was assumed to depend on local environmental conditions. They found that tumours characterised by high O_2 consumption or growing in low O_2 settings were more aggressive with fingered morphology [73, 74]. They also found that glycolytic phenotype is more likely to emerge in poorly oxygenated but dense tissues [74]. More modifications and extension of similar models of tumour invasion can be found in [160].

Hybrid models enable modelling of biological phenomena occurring on multiple scales. Alarcón, Byrne and Maini [2, 3] extended their previous CA model [1] for vascular tumour growth to develop an integrative framework for studying cancer across the intracellular, cellular and vascular scales. At the vascular layer, a network of adaptable blood vessels was assumed to provide the source of oxygen of which concentration was modelled with a reaction-diffusion equation. Blood vessel networks were initially mapped onto hexagonal lattices together with normal and cancer cells at the cellular layer. Each element of the grid was assigned a state vector containing a number of components such as the type or cell cycle phase of the cell occupying the element, local concentrations of O_2, vascular endothelial growth factor (VEGF) and the substances controlling the cell cycle. Cell cycle dynamics, apoptosis and VEGF

production were controlled at the intracellular level. These processes, controlled by the local O_2 concentration, were modelled with ODEs. Thus the authors integrated multiple biological phenomena across three tissue scales allowing them to study the effect of changes of model components on the population.

1.2.3 Models of anti-cancer treatment

Mathematical modelling can aid our understanding of key mechanisms that underlie tumour development and growth. Arguably, the major objective of cancer research is to determine how to eradicate neoplastic cells whilst sparing normal tissue. Mathematical models can be useful for designing optimal treatment strategies and predicting tumour response to anticancer interventions [33, 60]. Some models attempting to do so are described below, with particular emphasis on models of RT.

The linear-quadratic (LQ) model in its various forms is one of the few mathematical models used in the clinic to describe tissue radiation response. Although the model is empirical, it has mechanistic interpretations [142]. In its basic form, the LQ can be written as

$$\sigma = \exp[-\alpha n d - \beta n d^2] = \exp[-(\alpha + \beta d)D], \tag{1.2}$$

where σ represents the surviving fraction of clonogenic cells[9], α and β are the lethal lesions made by one- and two-track actions of radiation dose d, respectively, $D = nd$ is the total dose and n is the number of fractions.

Wheldon et al. [198] used the LQ model to find the optimal (in terms of number and duration of fractions and dose applied) fractionated RT schedule with exponential regrowth of tumour cells between treatments. Their work was later extended to include the effects of hypoxia [200]. Many researchers studied the impact of different growth laws on RT response within the LQ formalism [141, 117, 41, 189]. O'Donoghue [141] considered radiation response of tumours following the exponential and Gompertzian growth kinetics. Instead of assuming instantaneous cell death following radiation exposure (intrinsic feature of the LQ model), irradiated cells were removed from the tumour mass following exponential dynamics in his model. McAneney and O'Rourke [117], building on the work of Wheldon and colleagues [198], studied the effect of the exponential, logistic and Gompertz growth laws on various RT treatment schedules, such as standard fractionated daily protocols, weekday treatments, accelerated fractionation and other. They found that the fraction of eradicated tumour cells was similar in the exponential and logistic models. This fraction was

[9] cells that have the potential to proliferate and form colonies

much higher than the fraction of eradicated tumour cells predicted with the Gompertz model. Further extensions included considering heterogeneous cell populations. For example, after fitting imaging data of 11 lung cancer patients, Tariq et al. [189] found that explicitly modelling live and dead tumour cells was more appropriate than treating the tumours as a single population, whereas Bertuzzi et al. [23] considered the damage response of both cancer and normal tissue.

Spatially averaged, ODE-based models of anticancer treatment have been also used to study the effect of chemotherapy [144] and combined chemotherapy and radiotherapy [169, 63]. For example, Panetta and Adam [144] investigated the effect of pulsed and piecewise-continuous chemotherapy on tumour and normal cells where the former were either actively moving through the cell cycle or were in the resting stage. Ergun et al. [63] applied control theory to a model of a vascularised tumour to study the application of angiogenic inhibitors, radiotherapy and the combination of the two on the tumour. Their analysis revealed that the optimal protocol involves administration of dose-intensified anti-angiogenic treatment during the latter part of the RT fractionation protocol.

The anti-cancer treatment models described so far suffer from a common shortcoming—they do not consider spatial effects. In a series of papers, Bertuzzi and other [24, 26, 27] investigated the response to treatment of tumour cords[10]. A model of tumour cords in which cells are in the state of equilibrium [25] was extended to study their response to a single dose of treatment (RT and chemotherapy) [24]. The authors assumed a continuum description of the volume fractions of live and dead tumour cells and extracellular fluid. Cellular proliferation and sensitivity to treatment depended on the local concentration of O_2 which followed a reaction-diffusion equation. Numerical simulations of the model revealed its sensitivity to the type of treatment applied. The model was later extended to study resensitisation following chemotherapy [26] and reoxygenation after RT treatment [27], and modified to model the response of tumour spheroids to RT [22].

Enderling et al. [57, 59] extended their earlier model of tumour invasion and metastasis [10] to simulate the combined effects of surgery and RT on the recurrence of breast cancer. In particular, two treatment approaches were compared: targeted intraoperative radiotherapy (TARGIT) and external beam radiotherapy (EBRT) [57]. The former is a relatively new approach in which a high dose of RT is applied to the tumour bed immediately after tumour removal surgery. EBRT is the standard fractionated RT where multiple fractions of 2 Gy are applied over several weeks.

[10]cancer cells arranged in cylindrical structures around blood vessels

The authors first simulated tumour growth and invasion using a modification of the model by Anderson et al. [10]. When the tumour reached a clinically detectable size of 2 cm., the areas of high cancer cell density (where concentration of tumour cells was larger than concentration of normal tissue) were removed from the simulations and various RT treatments were simulated. In the last step, the tumour growth and invasion model was reapplied to simulate potential recurrence. The simulations revealed that both TARGIT and EBRT successfully eliminated tumour cells that could have invaded the surrounding tissue. However, TARGIT, in contrast to EBRT, could also eliminate the cells with potentially malignant mutations. The role of stepwise mutations from normal to tumour cells on breast cancer recurrence was further studied in [59].

An example of a clinically relevant spatio-temporal model is a model of glioblastoma developed by Swanson and colleagues [186, 187] which was subsequently extended to account for RT [165]. The original reaction-diffusion model including only two parameters: the diffusion coefficient and the net proliferation rate, was applied to data from magnetic resonance imaging (MRI) to predict potential regrowth of the glioma following surgery [187]. Rockne et al. [165] extended the model to include the effects of RT by incorporating the LQ model. With a fixed α/β ratio their model depended on only three parameters (α and the two original parameters), all meaningful to clinicians. The model was used to simulate a number of treatment protocols, suggesting that fewer radiation fractions (one per day) with higher doses is a more effective strategy than treating patients with lower doses more frequently.

Anti-cancer treatment response has been also studied using discrete and hybrid models. Typically, cells have been modelled as individual agents, chemotherapeutic agents concentrations with PDEs (with equations similar to those describing O_2 dynamics), and RT with the LQ model in various forms (e.g. [152]). Such hybrid models are multiscale, considering phenomena at multiple spatial and temporal scales. An example of such approach is a model developed by Ribba et al. [163] which integrated processes at the tissue, cellular and gene levels. At the gene level, a Boolean model controls the activation of genes assumed to be relevant in the development of colorectal cancer, in response to various signals from the other layers such as hypoxia or overpopulation levels. Various pathways activated at the gene level in turn control cell proliferation at the cell level, where a discrete model of cell cycle is used to describe different phases of the cycle. Radiation response is assumed to depend on current phase of the cell cycle which is consistent with previous observations [176, 177]. At the

tissue level, an advection equation governs the dynamics of the cell density and a diffusion equation models the O_2 concentration. Computer simulations emphasised the importance of O_2 availability, cell cycle stage and tumour geometry as determinants of radiation response.

Other multiscale models have considered the effects of cell cycle synchronisation [102, 103] and tumour oxygenation status [192] on radiation response. Additionally, Partridge [146] developed a cellular Monte-Carlo model of radiation damage repair in normal tissue. The effects of cell cycle and O_2 levels on the response of tumours to chemotherapy and RT were also investigated by Powathil et al. [152, 155] with a multiscale hybrid mathematical model, which was later extended to study the effect of RIBE on cancer and normal cells [154]. The model showed that at low radiation doses, RIBE caused more damage than direct irradiation.

Discrete models of tumour growth incorporating the LQ model to describe radiation damage have been also used to study heterogeneous tumours and their response to RT. For example, Enderling et al. [61] demonstrated that the spatial distribution of cancer stem cells plays a critical role in determining RT response. Alfonso et al. [6] used their model to simulate various heterogeneous dose distributions for tumour composed of two populations of cells: cancer stem cells (CSCs) with the potential to divide indefinitely, and much faster proliferating ordinary cancer cells (CCs) assumed to divide a finite number of times. Although the authors did not consider the effects of O_2 previously shown to have critical impact on radiation response [191], their model suggested boosting radiation doses in the regions occupied by the more resistant CCs.

Due to enormous body of literature on mathematical models of tumour growth it is not possible to discuss them all here but some comprehensive reviews can be found in [12, 34, 167, 112, 33, 60, 58, 7].

1.3 Summary and thesis aims

Traditionally, cancer has been studied by biologist in isolation and their attention has been focussed on genetic mutations. However, cancer cells exist within tissues and are surrounded by other cells. Together, cancer cells, normal cells and the microenvironment form an ecosystem [17]. Additionally, tumours are composed of many geno- and pheno-typically distinct populations of cells that interact with each other and their microenvironment. These interactions within the cancer ecosystem can have a significant impact on prognosis and treatment outcome. Experimental approaches alone may not be sufficient to address the complexity involved in viewing cancer from the

ecological perspective. Fortunately, a plethora of mathematical and computational models have been developed over the last 50 years enabling researchers to model and simulate various biological mechanisms and processes pertaining to tumour growth. With a few exceptions, these models have had little impact on cancer research. Lack of collaboration between modellers and biomedical researchers due to barriers in communication and other factors has been suggested as a potential justification for the relatively small contribution of mathematical modelling to cancer research [33]. This multidisciplinary thesis aims to bring together biological experiments, mathematical modelling and statistical inference methods to develop a methodology for studying the impact of intratumour heterogeneity on tumour growth and radiation response. Our objectives are to establish if intratumour heterogeneity affects bulk growth and radiation response of co-cultured human prostate cancer cell lines. We also aim to determine if the co-cultured cell lines interact and what types of interactions occur between them.

This thesis is structured as follows. In Chapter 2 we describe the methods and results of *in vitro* experiments designed to assess the impact of IH on tumour growth and radiation response, and to aid parameter inference process in mathematical modelling presented in later chapters. Chapter 3 begins with a synthetic data study conducted to compare a number of parameter inference methods and methods for uncertainty quantification in the estimated parameters. The methodology is then applied to data describing the growth of homogeneous tumour spheroids. In Chapter 4 we conduct an experimental design study to determine what data are required to estimate parameters in a Lotka-Volterra model of heterogeneous tumour growth. We consider the effect of three distinct protocols designed to fit the model to data and apply them to determine the types of interactions between co-cultured cell populations. In Chapter 5, a cellular automaton (CA) model of tumour growth is described and analysed. In particular, we study the relationship between the CA model parameters and parameters in a simple logistic model of tumour growth. The CA model is used in Chapter 6 to further study the interactions between clones in heterogeneous tumour spheroids. We also fit the CA model data to the Lotka-Volterra model to assess its ability to capture the dynamics between cell populations. Our conclusions and recommendations for future work are presented in Chapter 7.

1.4 Statement of authorship

Models development, simulations and parameter inference presented in this thesis were performed by Marcin Paczkowski. The experiments presented in Chapter 2 were conducted by Marcin Paczkowski except for:

- radiation clonogenic assay, proliferation assay and measurements of cell populations which were conducted jointly by Marcin Paczkowski and Dr Pavitra Kannan;
- cell lines transduction which was performed by the lab technician.

All data pertaining to PC3 spheroids presented in Chapter 6 were provided by Dr Pavitra Kannan.

Chapter 2

The impact of intratumour heterogeneity on tumour growth and radiation response

2.1 Introduction

As stated in Chapter 1, the concept of intratumour heterogeneity first appeared in the 70s and was met with disbelief [85]. A group of researchers at Roger Williams General Hospital isolated four distinct tumour subpopulations from a single mouse mammary cancer [52]. Their manuscript was initially rejected by reviewers since the prevailing hypothesis had been that tumours were monoclonal. Fortunately, this incident did not discourage the researchers from pursuing studies in this area and intratumour heterogeneity was quickly recognised as an important feature of many tumours.

Early laboratory studies involved either injecting mice with heterogeneous populations of cancer cells or observing the growth of heterogeneous populations *in vitro* in monolayers. The four cell lines isoloated from a single mammary tumour by Dexter et al. [52] differed in morphology, *in vitro* growth properties and other features, yet all four led to tumours of similar histology when injected in mice. Miller et al. [130] found that, when two cell lines (168 and 4T07) derived from the same mammary tumour were injected in mice, the latter suppressed the growth of the former, even if the initial composition was 100:1. Similar observations were made in monolayers.

Some studies have focused on the impact of intratumour heterogeneity on the response to chemotherapeutic agents. In one such study [125], the authors injected mice with a cyclophosphamide-sensitive cell line (168) on one flank and a cyclophosphamide-insensitive cell line (410) on the opposite flank. Other mice were injected with either 168 or 410 cells. After drug treatment, the drug sensitivity of the 410 tumours was af-

fected by the presence of the 168 tumours, but not vice-versa. In another study [124], mixed melphalan-sensitive (line 66) and insensitive (line 4TO7) cell lines (derived from the same mammary tumour) were injected into mice and, after tumours formed, the mice were treated with melphalan. The line 66 appeared to be more sensitive to the drug when co-cultured in 3D with the 4TO7 cells than when grown alone. Interestingly, the sensitivity of the cells from cell line 66 did not change when they were co-cultured with the 4TO7 cells in monolayers, suggesting that the increased sensitivity *in vivo* was mediated by signalling factors, cell-cell contact or microenvironment not found in monolayer models.

Heterogeneous responses to RT have also been investigated. Leith and coworkers [107] observed that clones derived from human colon and human lung carcinomas were heterogeneous in their intrinsic sensitivity to radiation, and suggested that such heterogeneity could explain for failure of some human carcinomas to respond to treatment. The dynamics of heterogeneous tumours were also shown to depend on the environment in which the tumours grew [108]. Mixtures of two populations derived from the same cell line (DLD-1) were injected in mice which had been previously treated with radiation. Although the authors observed no difference in volumetric growth, as compared to the non-irradiated mice, the composition of the tumours changed significantly between the two groups. Whereas tumours growing in non-irradiated stroma were stable in composition, the tumours in irradiated mice were dominated by the clone that was initially predominant.

Following this period of intensive research into intratumour heterogeneity in the late 70s and 80s, the interest shifted towards studying oncogenes and tumour suppressors [188]. Recently, the importance of intratumour heterogeneity has regained interest as researchers begin to view tumours as ecosystems [119]. A particular emphasis is being placed on the interactions between different subpopulations of cells within tumours [188].

To study interclonal interactions we require an appropriate experimental model, just as we need a model to test a hypothesis in mathematics. We seek a model that is as simple as possible to minimise variability but complex enough to allow us to study potential intercellular communication. As described above, monolayer cultures and xenograft tumours have been the models of choice. Monolayers are a popular model in cancer research but their 2D geometry makes them overly simplistic and means that some behaviours observed in 3D tissues do not manifest in monolayers. Xenografts, on the other hand, allow researchers to study tumours in *in vivo* settings but this introduces additional parameters that may be out of their control. Tumour

spheroids represent an experimental model that bridges *in vitro* and *in vivo* studies [183]. Tumour spheroids have been widely used in radiation biology research [170] and have become even more popular in the recent years [87] (see Chapter 1 for more details).

In this chapter we develop 2D and 3D *in vitro* models that allow us to study potential interactions between two cancer cell populations, derived from the same cell line, that exhibit different responses to radiation. Our approach differs from the work described above in that we use tumour spheroids, which are a more realistic representation of avascular tumours found *in vivo*, yet do not introduce additional complexity associated with xenograft models. Tumour spheroids have been previously used to study interactions between co-cultures of tumour and normal cells [118, 113]. Collagen-based 3D models have been also used to investigate the impact of interclonal heterogeneity on response to chemotherapeutic agents [126, 127]. However, to our knowledge, there have been no studies to assess the impact of intratumour heterogeneity on radiation response involving mixtures of tumour clones derived from the same cell line in tumour spheroids.

The remainder of this chapter is organised as follows. We begin by identifying two pairs of prostate cancer cell lines that differ in their sensitivity to radiation under low and high oxygen conditions. We then co-culture the control (radiation sensitive) and resistant (less radiation sensitive) subpopulations and observe their growth dynamics and radiation response in monolayer cultures. To assess the growth and radiation response of mixed cell populations in 3D, we design and develop a tumour spheroid model. We measure the volumetric growth and composition of spheroids seeded at different ratios of control and resistant cells following mock-irradiation and irradiation with a single dose of 6 Gy.

2.2 Materials and Methods

2.2.1 Cell lines

Four cell lines were used: PC3 Control (Ctrl), PC3 Resistant (Res), DU145 Control (Ctrl) and DU145 Resistant (Res). The PC3 Ctrl [98] cell line derives from a bone metastasis of human prostate adenocarcinoma and the DU145 Ctrl [180] cell line derives from a brain metastasis of a human prostate carcinoma. The PC3 Res and the DU145 Res cell lines (a gift from Dr. Stanley Liu, University of Toronto, Canada) were obtained by repeatedly irradiating the PC3 Ctrl and DU145 Ctrl cells at low doses (45×2 Gy), respectively. This treatment rendered the control cell lines resistant

to radiation. In the PC3 Res cells radiation resistance is promoted by miRNA-95 [88]. In the DU145 Res cells the mechanisms of resistance are unknown.

Cells were maintained as monolayers in Dulbecco's Modified Eagle Medium (DMEM, Invitrogen) with GlutaMAX supplemented with 10% fetal bovine serum and penicilin/streptomycin, in a humidified atmosphere containing 5% of CO_2 at 37°C. Cell lines were regularly checked for mycoplasma contamination using the MycoAlert Mycoplasma Detection Kit (Lonza) and were discarded after 8–10 passages in culture.

2.2.2 Cell lines transduction

Prostate cell lines were transduced[1] using lentiviral particles to produce stable fluorescent cell lines. Lentiviral particles were generated by transfection of 293T cells with the vectors pCDH1-CMV-GFP-EF1-Hygro or pCDH1-CMV-DsRed-EF1-Hygro (Systems Biosciences). Particles were collected and added to prostate cells. Control cells from PC3 and DU145 cell lines were transduced with GFP, whereas resistant cells from the cell lines were transduced with DsRed. 24 hours after transduction, particles were removed and medium containing hygromycin (Invitrogen) was added for selection. PC3 cells were selected using 120 µg/mL hygromycin, and DU145 cells were selected using 250 µg/mL hygromycin. GFP- and DsRed-positive cells (top 10%) were sorted by flow cytometry 7 days after transduction, expanded for 14 days under selection, and then re-sorted (top 30%) by flow cytometry to obtain the brightest cells for subsequent experiments.

2.2.3 Radiation clonogenic assay

2.2.3.1 Normoxia

Cells in exponential growth phase were seeded at 250, 500, 1000 and 2000 cells per well into six-well plates in DMEM in triplicate. Cells were incubated for 6 hours to allow attachment and then mock irradiated (0 Gy) or irradiated with 2, 4 or 6 Gy of ionizing radiation, respectively. The cells were then incubated for two weeks in a humidified atmosphere containing 5% CO_2 at 37°C. The resulting colonies were stained with crystal violet solution (0.5% crystal violet , 25% methanol, Sigma-Aldrich). Colonies were imaged (at 300 dpi resolution) and counted using GelCount software (Oxford Optronic). Colonies were defined as groups of cells numbering over 50 and a size

[1] transduction was performed by the lab technician

exclusion criterion was used to track colonies. Surviving fractions were calculated according to the formula

$$\frac{\text{number of colonies counted}}{\text{number of cells seeded} \times \text{plating efficiency}}$$

where plating efficiency is the ratio of the number of counted colonies to the number of seeded cells for the untreated case. The data were fitted to the linear quadratic model using GraphPad Prism 5.0 (GraphPad Software Inc.). The area under the radiation dose-response curve was used to calculate the radiation protection factor (RPF) by dividing the area under the curve (AUC) for the resistant cell lines by the area under the curve for the control cell lines [88].

2.2.3.2 Hypoxia

For radiation clonogenic assays in low oxygen conditions, cells were seeded at 250, 250, 250 and 500 cells per well for 0, 2, 4 and 6 Gy conditions. The cells were then incubated for 3 hours to allow attachment, and placed in a hypoxic chamber (Invivo Chamber 300; 0.1% O_2, 5% CO_2) for 6 hours. To maintain hypoxic conditions during irradiation, the six-well plates containing cells were placed in custom made airtight acrylic boxes prior to radiation treatment. After mock irradiation or irradiation at 2, 4 or 6 Gy the cells were incubated in normal conditions and analysed as described above.

2.2.4 Proliferation assay

Control and resistant cells were mixed at different ratios (Ctrl:Res; 1:0, 3:1, 1:1, 1:3 and 0:1), seeded at a density of 2.0×10^3 cells per well in 96-well black clear-bottom plates (Corning Costar) and incubated overnight to allow cells to attach. The medium was then replaced with 90 µL of fresh medium. The cells were mock irradiated (0 Gy) or irradiated with a single dose of 6 Gy and incubated. At designated times 10 µL of Presto Blue[2] (10X, Invitrogen) was added to each well and the cells were incubated for 2 hours. Fluorescence was measured at 560/590 ex/em using a plate reader (Tecan 200).

[2]Presto Blue is a reagent containing a blue cell-permeant compound that is nonfluorescent in solution. When added to cell solution it is rapidly absorbed by the cells, and then converted by viable cells to a red-fluorescent dye which can be detected by measuring fluorescence.

2.2.5 Formation of tumour spheroids

Cells grown as monolayers were detached with 1×Trypsin (Sigma) to generate single cell suspensions and were counted with NucleoCounter NC-100 (Chemometec), to minimise user-to-user bias and maximise reproducibility. This cell counting method, which is an alternative to the more traditional haemocytometer, relies on staining cells with propidium iodide (PI). Cells are first treated with Lysis buffer (Chemometec) which, by permeating the plasma membranes, allows the PI to be absorbed by the cells. Subsequent treatment with the stabilising buffer (Chemometec) ensures a more efficient uptake of the PI by the cell nuclei. A sample of the obtained lysate is loaded into a NucleoCassette and then placed into the NucleoCounter.

Cell suspensions were diluted and mixed at different ratios to form final solutions with a total concentration of 2.0×10^4 cells per mL. The PC3 Ctrl and Res, and the DU145 Ctrl and Res cells were mixed in pairs at the following ratios (Ctrl:Res): i) 1:0; ii) 3:1; iii) 1:1; iv) 1:3; v) 0:1. Cells were then seeded, with six wells per condition, in 96-well ultra-low attachment plates (Corning 7007) with round bottoms. To promote spheroid formation, basement membrane extract (Matrigel, BD Biosciences) was added to the cell suspension at a final concentration of 5% [90] in 100 µL per well. Seeding was performed on ice with cold pipette tips to prevent gelling of Matrigel. Finally, the plates were centrifuged at 800×g for 5 minutes at 4°C and then placed in an incubator for three days under standard cell culture conditions. After 72 hours, 100 µL of fresh medium was added to each well to bring total volume to 200 µL per well. The spheroids were re-fed every alternate day (after imaging) by carefully removing 100 µL of medium and adding 100 µL of fresh medium.

2.2.6 Radiation treatment of spheroids

Tumour spheroids formed three days after seeding. The 96-well plate containing spheroids was irradiated at 6 Gy using Caesium-137 gamma irradiator at a dose rate of 0.89 Gy / min. After irradiation, the spheroids were transferred back to the incubator. Non-irradiated spheroids were also removed from the incubator and then transferred back to maintain similar conditions.

2.2.7 Brightfield microscopy

Images of spheroids were taken from day 3 after seeding. The duration of the imaging period was determined by the phenotype of individual cell lines. The images were acquired with Simple PCI Imaging software (Hamamatsu) connected to an inverted

Leica DM IRBE microscope, at a resolution of 512×512 pixels, in 8-bit tif format, using a $4\times$ magnification lens. The final image resolution was 2.32 microns/pixel.

2.2.8 Image analysis

Image analysis was performed using a MATLAB-based software tool SpheroidSizer [43]. The software utilises the active contour algorithm which iteratively adjusts the initial contour based on the local image gradient to robustly compute the size of a spheroid. SpheroidSizer provides useful features such as quality control, allowing the user to examine and refine boundary contours in analysed images. Estimates of the spheroid volume V are based on the formula $V = 0.5 \times L \times W^2$, where L and W are measurements in semi-major and semi-minor axial lengths. This formula has been widely used and, in the absence of measurements in the third dimension, provides a good estimate of spheroid size [193]. The accuracy of SpheroidSizer in computing spheroid volume was successfully validated with our own image analysis software based on MATLAB's Image Processing Toolbox.

2.2.9 Measurements of cell populations

Heterogeneous spheroids were formed and irradiated as described in Sections 2.2.5 and 2.2.6. On predefined days, the spheroids were collected into FACS tubes, 3 spheroids per tube, and washed twice with PBS. The spheroids were then resuspended in 100 µL Accumax[3], incubated for 15 minutes at 37°C and washed twice with PBS. The pelleted cells were then incubated with Live/Dead Violet[4] solution (1 µL/1 mL PBS, Life Technologies) for 30 minutes on ice and washed again. The cells were fixed for 15 minutes at room temperature using fixation buffer diluted 1:1 with PBS (eBioscience), washed with PBS and stored at 4°C until analysis with flow cytometer.

Proportions of cell populations were measured using Fluorescence-Activated Cell Sorting (FACS). Briefly, the cell suspension was passed through a flow cytometer nozzle, one cell at a time, the forward and side scattered light, and fluorescence from stained cells, were detected and recorded. The experiments were performed in triplicate and 1.0×10^4 events were recorded for each tube.

The resulting data were analysed using FlowJo software. First, a gate (forward scatter vs. side scatter) was applied to remove debris. Second, clumps of cells were

[3]A cell dissociation solution used to dissolve cell clumps such as spheroids.

[4]The compound used to determine viability of cells prior to fixation. Dying cells lose their membrane integrity allowing for the compound to enter the cells. By reacting with free amines in the cell interior, Live/Dead Violet yields intense fluorescent staining.

excluded by applying another gate (forward scatter height vs. forward scatter width). Once single cells were identified for further analysis, the cells were segregated based on their fluorescence. Finally, the GFP- (control) and DsRed (resistant)-labelled cells were gated in the violet channel to identify the dead and live cells within each population.

2.3 Results

2.3.1 Characterisation of intrinsic radiosensitivity of cell lines under normoxia and hypoxia

To determine the intrinsic radiosensitivity of the PC3 Ctrl, PC3 Res, DU145 Ctrl and DU145 Res cell lines, we measured the clonogenic survival of exponentially growing cells following single doses of irradiation with 0, 2, 4 or 6 Gy. We confirmed that the PC3 Res and DU145 Res cell lines were significantly more radioresistant than the respective control cell lines under normoxic conditions (PC3: RPF = 1.18, P $<$ 0.05, Figure 2.1A; DU145: RPF = 1.14, P $<$ 0.05, Figure 2.1B). To test whether the

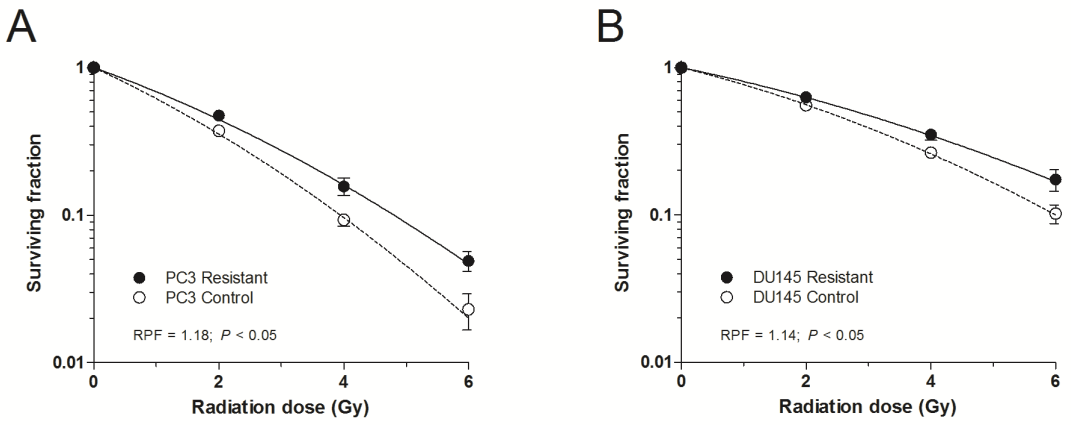

Figure 2.1: Radiation response of PC3 (A) and DU145 (B) cell lines under normoxia (20% O_2, 5% CO_2). Radiation survival was measured using clonogenics assays. Data represent mean ± SEM from 3 independent experiments performed in triplicate. RPF=radiation protection factor, calculated by measuring area under the curve. P $<$ 0.05 as calculated by a t-test from the AUC of each experiment.

differences in intrinsic radiosensitivity were maintained under low oxygen conditions, we repeated the experiment under hypoxia. The results show that although hypoxia decreases radiation sensitivity in all four cell lines, the relative difference in intrinsic radiosensitivity between the control and resistant cell lines was still present (PC3:

RPF = 1.11, P < 0.05, Figure 2.2; DU145: RPF = 1.60, P < 0.05, Figure 2.2B) with the RPF under hypoxia lower for the PC3 cells but significantly higher for the DU145 cells.

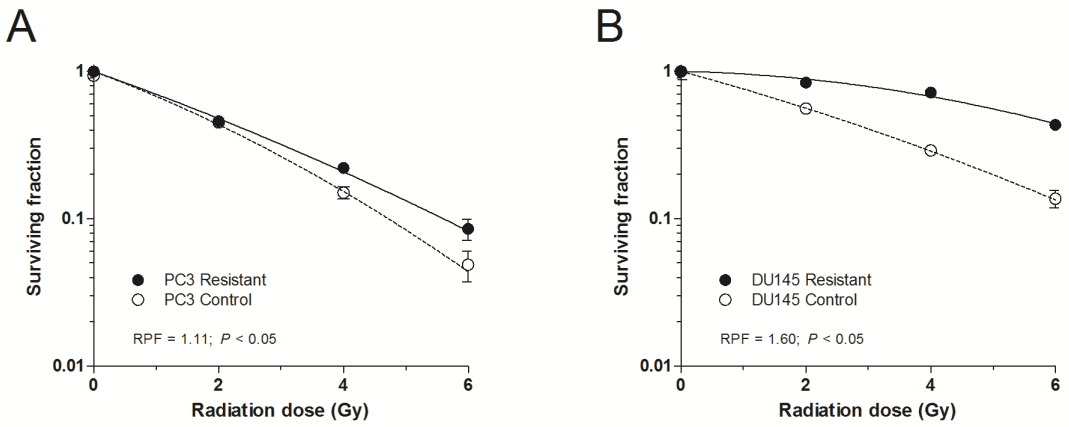

Figure 2.2: Radiation response of PC3 (A) and DU145 (B) cell lines under hypoxia (0.1% O_2, 5% CO_2). Radiation survival was measured using clonogenic assays and normalised to plating efficiency. Data represent mean ± SEM from 3 independent experiments. Statistical significance was evaluated using a Student t-test.

2.3.2 Radiation response in heterogeneous monolayers of tumour cells

To determine if cellular heterogeneity affects bulk radiation response in 2D we co-cultured control and resistant cells at different ratios and measured their proliferation following mock-irradiation or irradiation with a single dose of 6 Gy as described in Section 2.2.4. The results show that, for the mock-irradiated case, the growth dynamics of the homogeneous and heterogeneous cell populations in 2D were almost indistinguishable for the PC3 cells (Figure 2.3A) and very similar for the DU145 cells (Figure 2.3C). The results also suggest that cellular heterogeneity had little (PC3, Figure 2.3B) or almost no effect (DU145, Figure 2.3D) on bulk radiation response in 2D, on the timescale considered. Unfortunately, since the cells growing in monolayers quickly became confluent, we were not able to monitor their growth beyond day 4.

2.3.3 Optimal conditions for tumour spheroids formation

Since 2D monolayers did not provide an effective model system to measure interactions, we decided to grow 3D tumour spheroids containing two populations. The

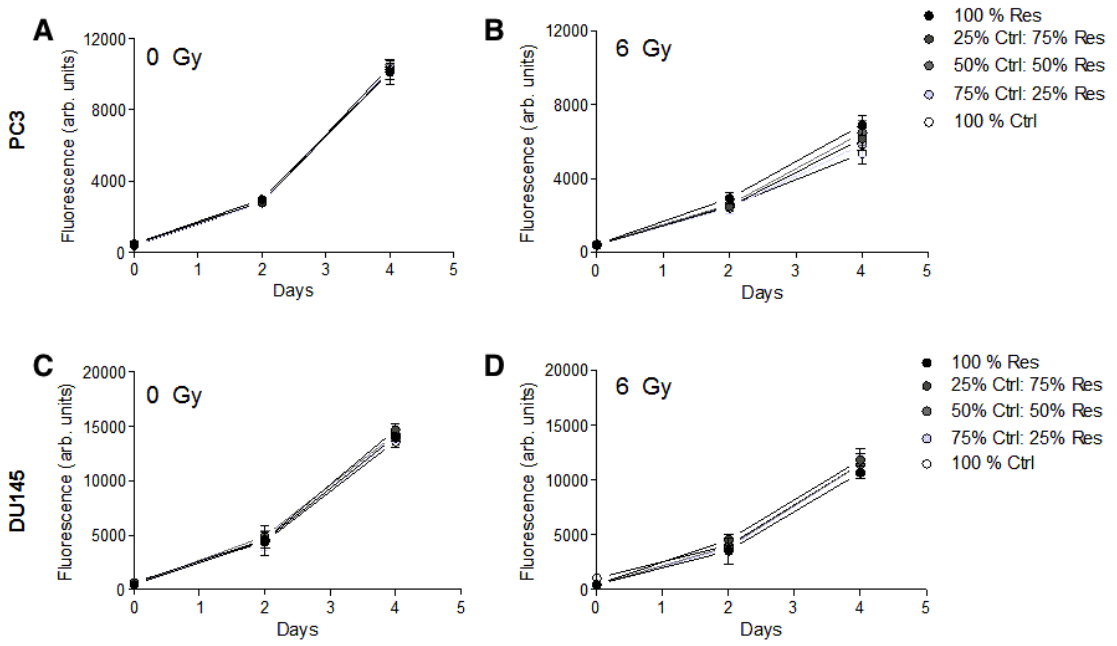

Figure 2.3: The growth of untreated (A and C) and irradiated (B and D) heterogeneous populations of PC3 and DU145 cells, respectively. Cellular proliferation was measured indirectly by uptake (arbitrary units) of a mitochondrial dye (Presto Blue), which is taken up by viable, proliferating cells. Data represent mean ± SD from 6 replicates for each cell line.

DU145 and PC3 cells failed to form spheroids in medium alone. It was necessary to add the basement membrane extract Matrigel to the medium to achieve spheroid formation (Figure 2.4). To determine the optimal concentration of Matrigel, the optimal medium type and the optimal initial cell density, the spheroids were cultured as described in Section 2.2.5 with different concentrations of Matrigel in three different cell culture mediums (DMEM, DMEM (Glutamax) and RPMI) at 1.0×10^3, 2.0×10^3 and 3.0×10^3 cells per well. The cells cultured at the Matrigel concentration of 5% formed the most compact spheroids (Fig. 2.5). The initial cell density of 1.0×10^3 cells per well was too low to form compact spheroids, whereas 3.0×10^3 cells per well led to spheroids too large to capture the exponential growth phase (results not shown). The concentration of 2.0×10^3 cells per well was found to be a suitable initial cell density. Although no difference was observed in spheroid formation for PC3 cells in DMEM *vs.* RPMI (Fig. 2.5), the DU145 cells formed spheroids that were more compact when cultured in DMEM (Glutamax) than those cultured in either DMEM or RPMI. Therefore spheroids were cultured in DMEM (Glutamax) for subsequent experiments.

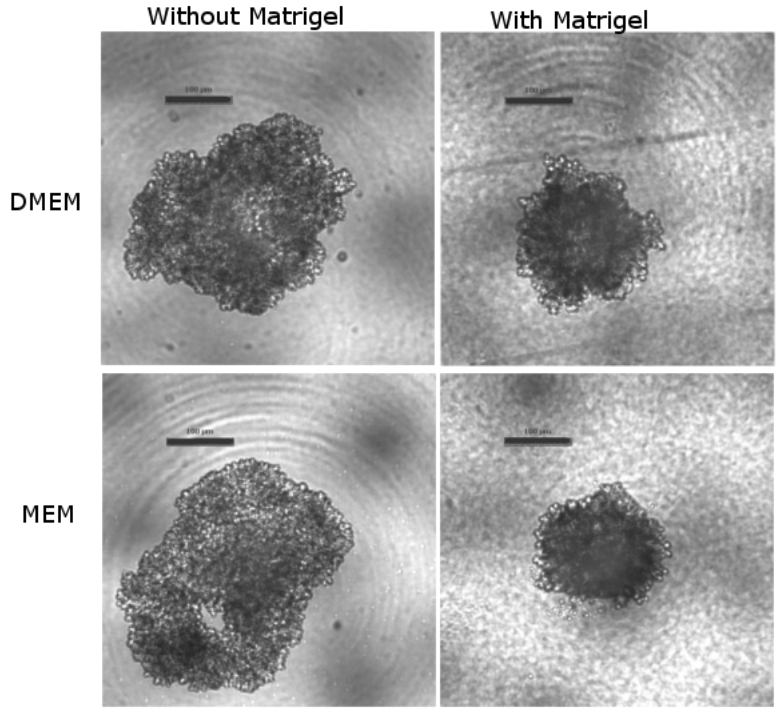

Figure 2.4: A typical set of experimental results showing that the PC3 cells do not form spheroids in the absence of Matrigel. Scale bar = 100 µm. DMEM and MEM are two different medium formulations.

2.3.4 Growth and radiation response of tumour spheroids

2.3.4.1 Homogeneous spheroids

To determine the growth and radiation response of homogeneous tumour spheroids, we generated spheroids composed of either PC3 Ctrl, PC3 Res, DU145 Ctrl or DU145 Res cells, and mock-irradiated them or irradiated them with a single dose of 6 Gy. We monitored their growth by measuring their volume using brightfield microscopy for either 15 days (PC3) or 30 days (DU145). The PC3 spheroids quickly lost their compactness and spheroidicity even in the absence of treatment (Figure 2.6). On the other hand, the DU145 spheroids remained compact and round even following radiation treatment (Figure 2.7). Therefore, we were able to monitor their growth over a longer time period than was possible for the PC3 spheroids.

The resistant cell lines were more aggressive in terms of growth than their respective control cell lines (Figure 2.8). The difference in size was marked for the PC3 cells. The resistant spheroids were twice as large as the controls on day 16 (Figure 2.8a). The DU145 Res spheroids appeared to increase in size up to the last day of imag-

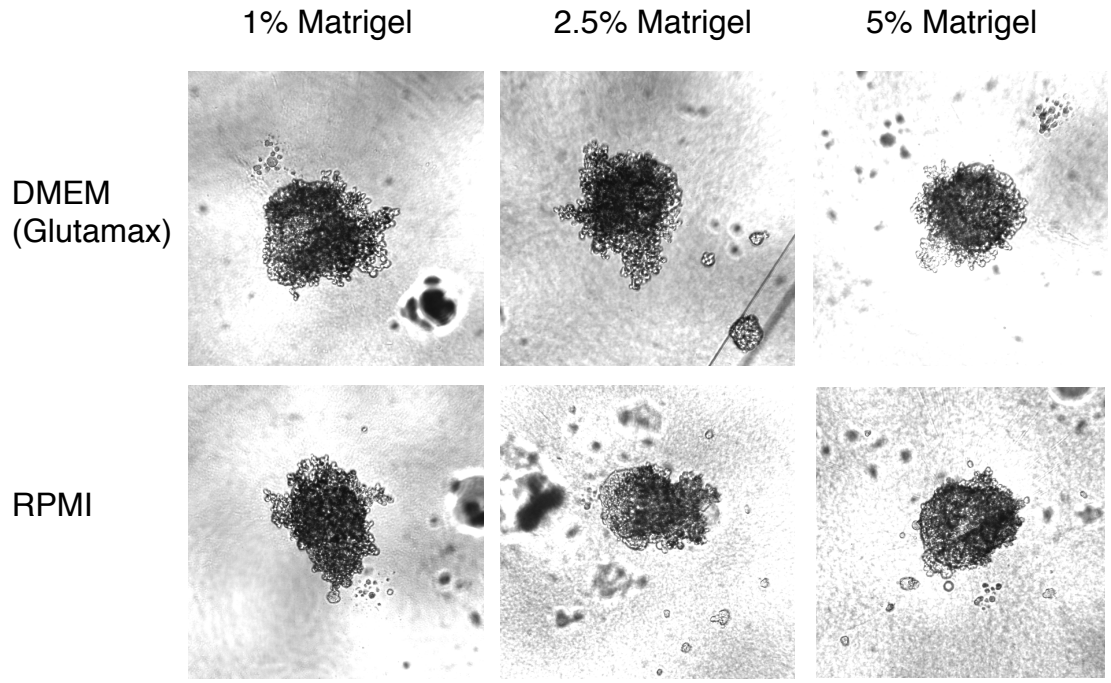

Figure 2.5: PC3 tumour spheroids obtained in different conditions. DMEM and RPMI are two different medium formulations.

ing when they reached a volume of approximately 0.8 mm^3. In contrast, the control spheroids plateaued at approximately 0.6 mm^3 around day 20 (Figure 2.8b).

The effects of a single dose of radiation (6 Gy) were more pronounced for the PC3 cell line, for which the sizes of the control and resistant spheroids were halved in comparison to the untreated case (Figure 2.8a). The DU145 cells appeared to be less sensitive to radiation. In particular, the growth curves of the resistant phenotype changed very little following treatment, whereas the DU145 Ctrl spheroids plateaued at sizes about 70% of their mock-irradiated size (Figure 2.8b).

2.3.4.2 Heterogeneous spheroids

We co-cultured the PC3 Ctrl and PC3 Res cells, and DU145 Ctrl and DU145 Res cells at different ratios (Ctrl:Res; 3:1, 1:1 and 1:3) to form spheroids. We either mock-irradiated the resulting spheroids or irradiated them with a single dose of 6 Gy, and monitored their growth as for the homogeneous spheroids case. The results suggest that the growth dynamics of the PC3 spheroids are affected by cellular heterogeneity in the absence of treatment as well as following irradiation (Figure 2.9a). A similar trend could be seen for the DU145 spheroids (Figure 2.9b). The mock-irradiated

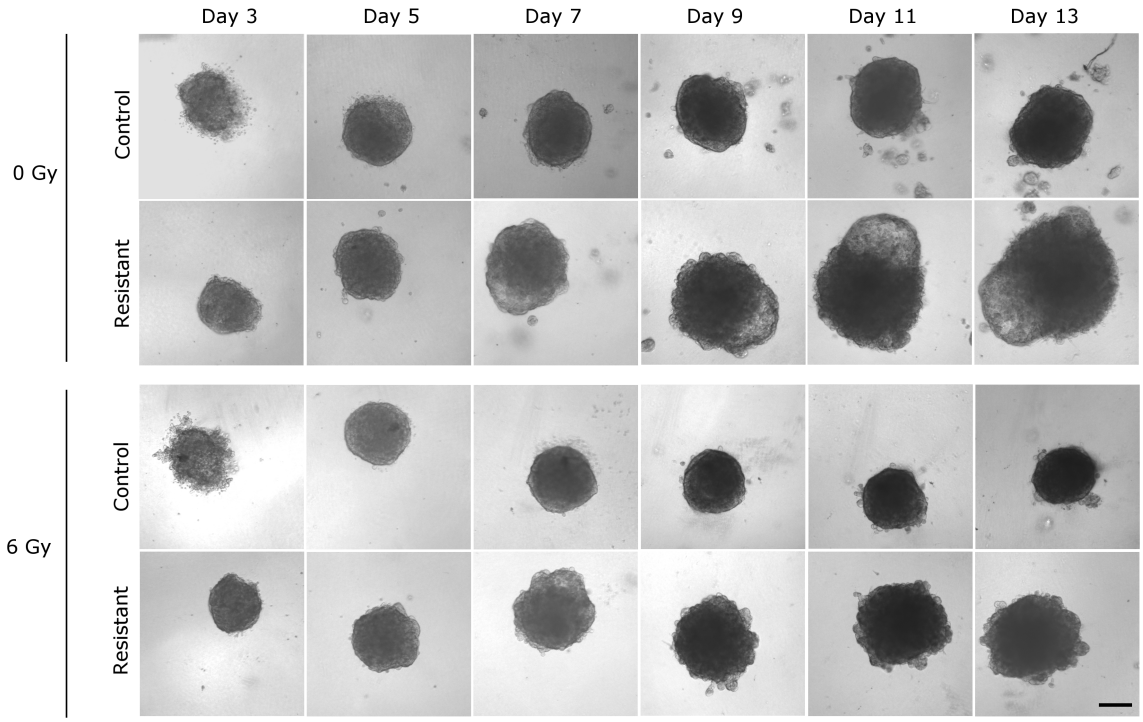

Figure 2.6: Representative images of PC3 spheroids (mock-irradiated or irradiated with a single dose of 6 Gy on day 3) taken on different days. Scale bar = 100 µm.

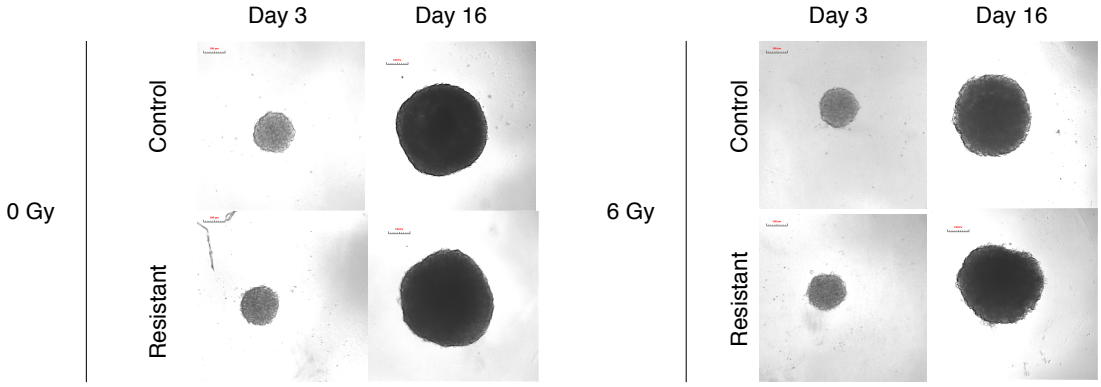

Figure 2.7: Representative images of DU145 spheroids (mock-irradiated or irradiated with a single dose of 6 Gy on day 3) taken on days 3 and 16. Scale bar = 100 µm.

DU145 spheroids seeded at a ratio 1:3 (Ctrl:Res) were larger than the homogeneous spheroids comprising either control or resistant cells. The homogeneous spheroids composed of the control cells, for either PC3 or DU145 cell lines, were the smallest of all cases considered and when the control and resistant cells were co-cultured we observed differences in their growth kinetics.

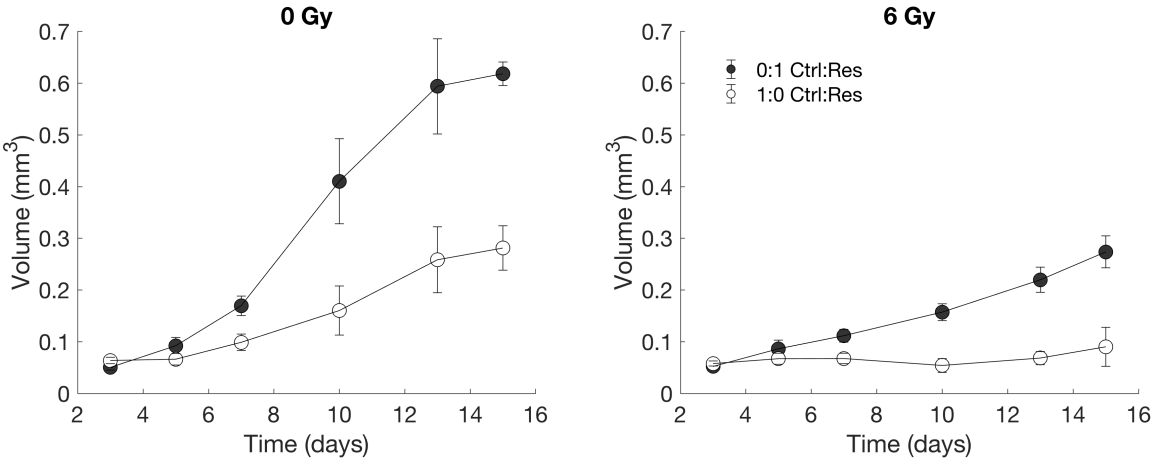

(a) PC3 homogeneous spheroids

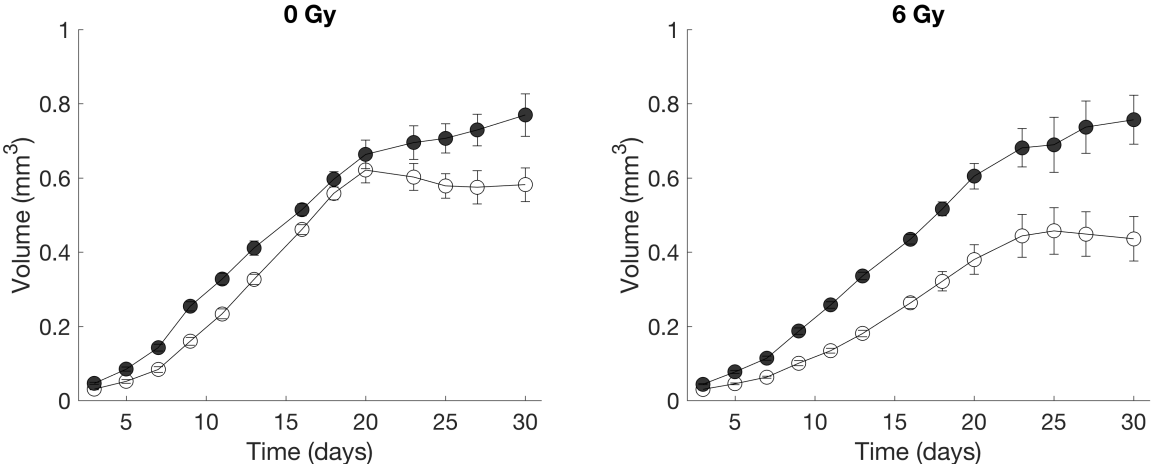

(b) DU145 homogeneous spheroids

Figure 2.8: Growth curves of homogeneous spheroids. Mock-irradiation and irradiation with a single dose of 6 Gy occurred on day 3 after seeding. Data represent mean, with 95% confidence intervals, based on 12 replicates from 2 independent experiments. The x-axis shows time after seeding.

2.3.5 Measurements of control and resistant cell populations in tumour spheroids

To determine how radiation affects intratumour kinetics we measured the proportion of control and resistant cells in heterogeneous tumour spheroids following mock-irradiation and irradiation with a single dose of 6 Gy. To demonstrate that flow cytometry can be used to separate different populations, we used FACS to identify fluorescence signals from unlabelled DU145 control and resistant cells, DU145-GFP (Ctrl) cells, DU145-DsRed (Res) cells and a 1:1 mix of fluorescently-labelled cells. Both channels accurately identified the GFP- and DsRed-labelled cells in homoge-

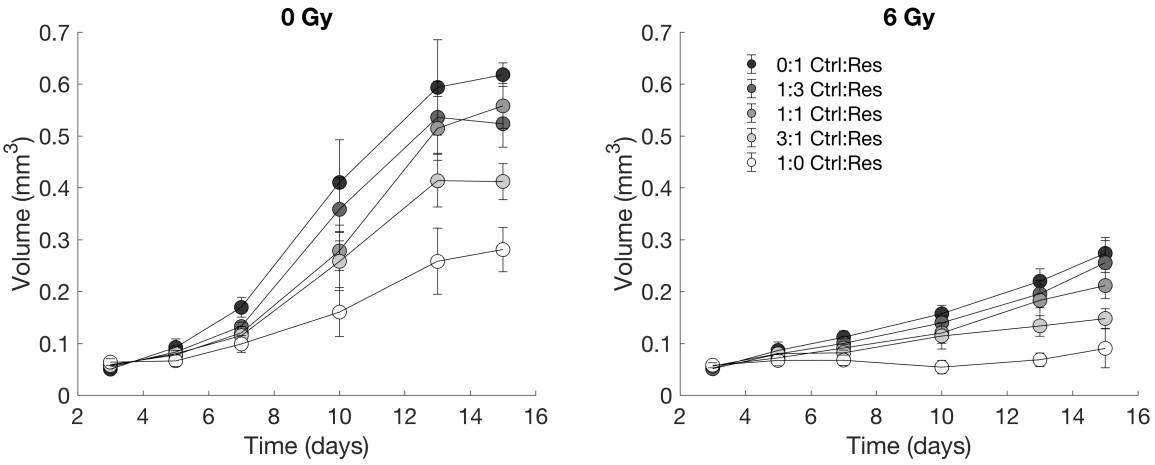

(a) PC3 heterogeneous spheroids.

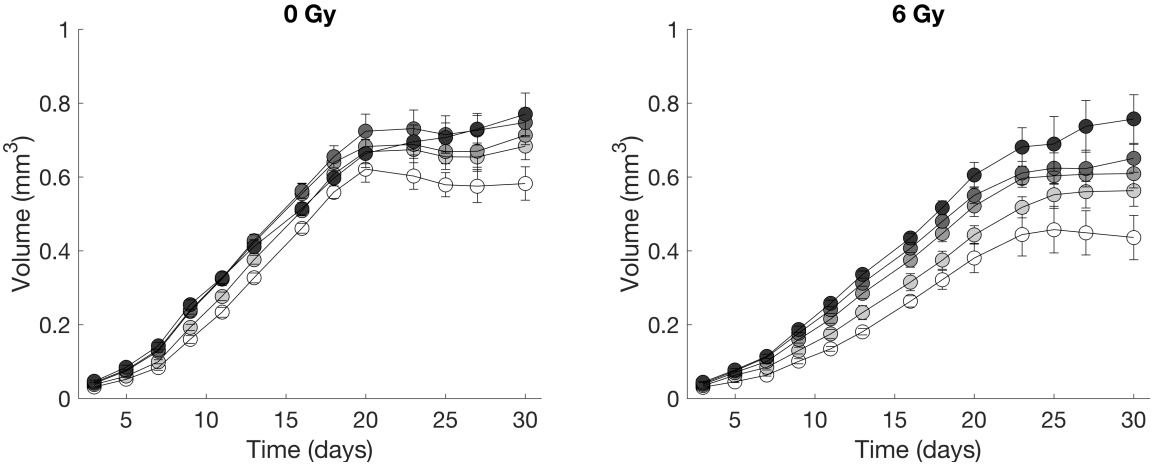

(b) DU145 heterogeneous spheroids.

Figure 2.9: Growth curves of heterogeneous spheroids. Data represent mean, with 95% confidence intervals, based on 12 replicates from 2 independent experiments.

neous and heterogeneous spheroids (Fig. 2.10). The GFP channel detected some unlabelled resistant cells but they constituted less than 0.1% of the total 10^4 cells. Importantly, none of the fluorescently-labelled cells were identified by the opposite channels.

Having confirmed that the method can distinguish between our two fluorescent populations, we generated heterogeneous PC3 and DU145 spheroids, containing fluorescent GFP control and DsRed resistant cells, and measured their composition on days 10 and 15 for the PC3 spheroids, and days 16 and 25 for the DU145 spheroids. The days of measurements were determined following an experimental design study described in Chapter 4.

As explained in Section 2.2.9, we collected 1.0×10^4 events for each sample. Fol-

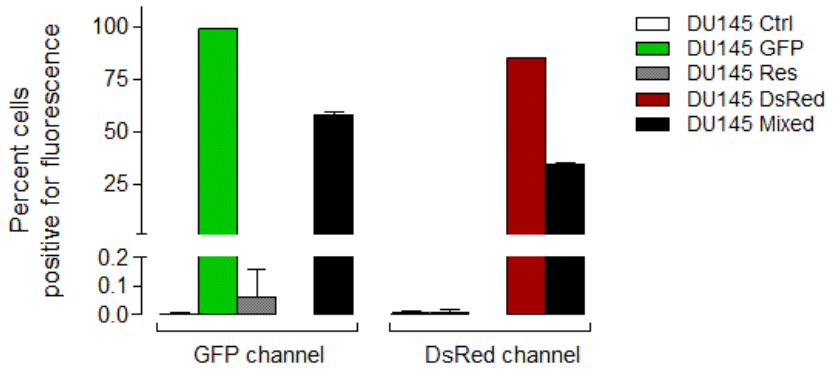

Figure 2.10: The proportions of different cell populations measured using the GFP and DsRed channels on a FACS machine.

lowing the gating procedures we found that the number of single PC3 cells available for further analysis was much higher for the non-irradiated spheroids. This number increased as the initial fraction of resistant cells increased. For example, on day 10, we found on average more than 7.0×10^3 single cells available for analysis from the non-irradiated spheroids and only about 4.0×10^3 cells from the irradiated spheroids. The difference was found to be statistically significant at the p=0.0001 level. Surprisingly, for the DU145 cells, we observed a significantly lower number of single cells available for analysis from the homogeneous resistant spheroids, both irradiated and non-irradiated.

We observed a shift in cellular composition of the PC3 spheroids in favour of the resistant population over time, suggesting that the resistant population was establishing itself as the dominant clone. (Table 2.1). The resistant cells constituted 43% of

Table 2.1: Proportions of PC3 control and resistant cells within heterogeneous spheroids measured on days 10 and 15. Data represent means ± 95% confidence intervals from experiments performed in triplicate.

Spheroids (Ctrl:Res)	0 Gy				6 Gy			
	day 10		day 15		day 10		day 15	
	Ctrl	Res	Ctrl	Res	Ctrl	Res	Ctrl	Res
1:0	**1.00**±0.00	**0.00**±0.00	**1.00**±0.00	**0.00**±0.00	**0.98**±0.01	**0.02**±0.01	**0.94**±0.01	**0.06**±0.01
3:1	**0.57**±0.01	**0.43**±0.01	**0.46**±0.05	**0.54**±0.05	**0.61**±0.01	**0.39**±0.01	**0.45**±0.02	**0.55**±0.02
1:1	**0.32**±0.02	**0.68**±0.02	**0.19**±0.01	**0.81**±0.01	**0.33**±0.02	**0.67**±0.02	**0.19**±0.03	**0.81**±0.03
1:3	**0.13**±0.01	**0.87**±0.01	**0.06**±0.01	**0.94**±0.01	**0.14**±0.00	**0.86**±0.00	**0.08**±0.01	**0.92**±0.01
0:1	**0.00**±0.00	**1.00**±0.00	**0.00**±0.00	**1.00**±0.00	**0.00**±0.00	**1.00**±0.00	**0.00**±0.00	**1.00**±0.00

the non-treated 3:1 (Ctrl:Res) spheroids on day 10 and 54% on day 15, 68% and 81% of the non-treated 1:1 spheroids, and 87% and 94% of the non-treated 1:3 spheroids on days 10 and 15 respectively. The proportions of the PC3 cell populations in the irradiated spheroids were similar to those in the non-irradiated spheroids.

Although irradiation did not change the control:resistant ratio much, the fraction of dead cells in both populations increased after treatment (Fig. 2.11). The ratio

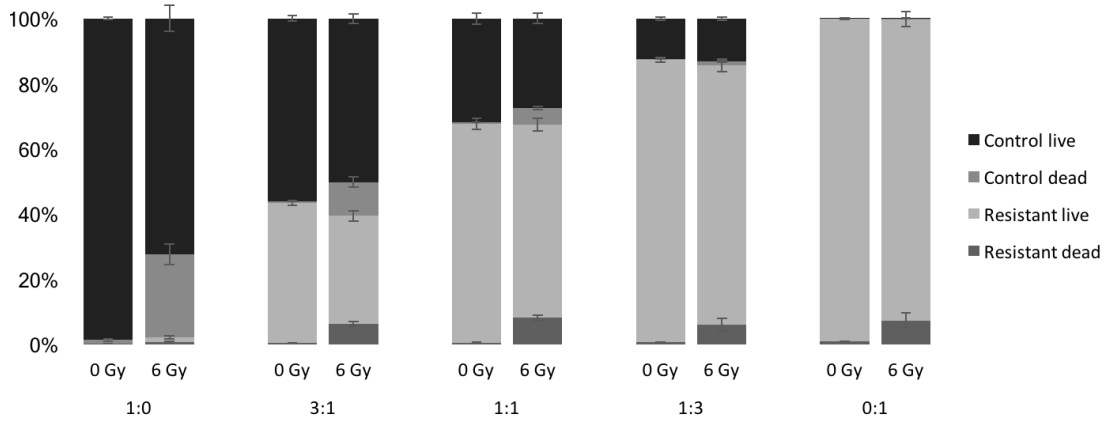

(a) Day 10

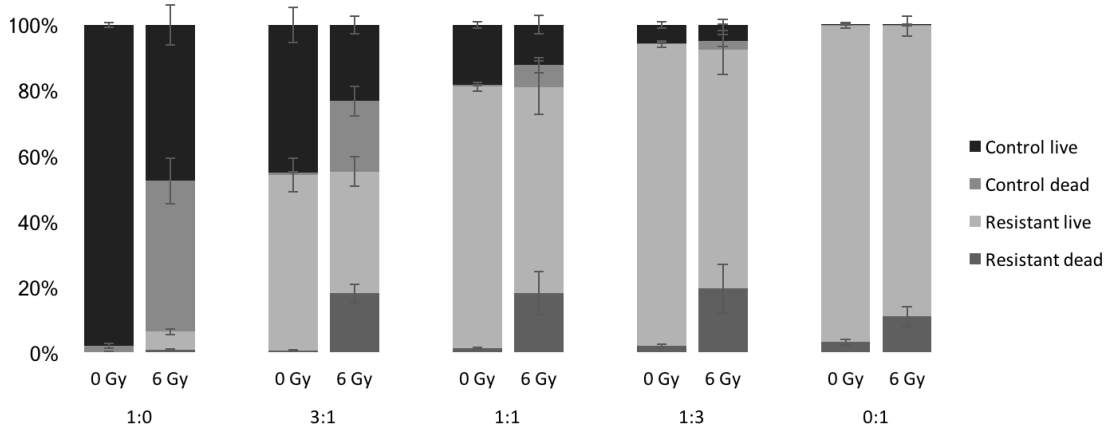

(b) Day 15

Figure 2.11: Proportions of different cell populations within heterogeneous PC3 spheroids on days 10 (a) and 15 (b). Data shown represent mean ± 95% confidence intervals from 3 independent samples.

of dead:live cells increased more markedly for the control population than for the resistant population, but in both cases the ratio was larger on day 15 than on day 10.

Conversely, the control cell population was dominant in the DU145 spheroids by day 16, clearly outnumbering the resistant population even when the initial composition was 1:3 in favour of resistant cells (Table 2.2). Although the data suggest that the fraction of resistant cells on day 25 was greater than that on day 16, the potential increase was within the 95% confidence intervals. The composition of control and resistant cells did not change following irradiation on the measured days, except for the 1:3 spheroids, for which the control population in irradiated spheroids was lower on day 16. However, by day 25, the fraction of the control cells increased, matching

Table 2.2: Proportions of DU145 control and resistant cells within heterogeneous spheroids measured on days 16 and 25. Data represent mean ± 95% confidence intervals from experiments performed in triplicate.

Spheroids (Ctrl:Res)	0 Gy				6 Gy			
	day 16		day 25		day 16		day 25	
	Ctrl	Res	Ctrl	Res	Ctrl	Res	Ctrl	Res
1:0	**1.00**±0.00	**0.00**±0.00	**0.99**±0.00	**0.01**±0.00	**0.10**±0.00	**0.00**±0.00	**1.00**±0.00	**0.00**±0.00
3:1	**0.97**±0.00	**0.03**±0.00	**0.95**±0.01	**0.05**±0.01	**0.96**±0.00	**0.04**±0.00	**0.96**±0.02	**0.04**±0.02
1:1	**0.94**±0.01	**0.06**±0.01	**0.91**±0.02	**0.09**±0.02	**0.91**±0.02	**0.09**±0.02	**0.90**±0.03	**0.10**±0.03
1:3	**0.86**±0.02	**0.14**±0.02	**0.81**±0.02	**0.19**±0.02	**0.75**±0.03	**0.25**±0.03	**0.80**±0.03	**0.20**±0.03
0:1	**0.00**±0.00	**1.00**±0.00	**0.00**±0.00	**1.00**±0.00	**0.01**±0.00	**0.99**±0.00	**0.01**±0.01	**0.99**±0.01

that for the non-irradiated spheroids. Whereas the dead:live ratio was slightly higher for the irradiated spheroids on day 16 as compared to the non-irradiated group for both control and resistant cells, the differences vanished by day 25 (see Fig. 2.12).

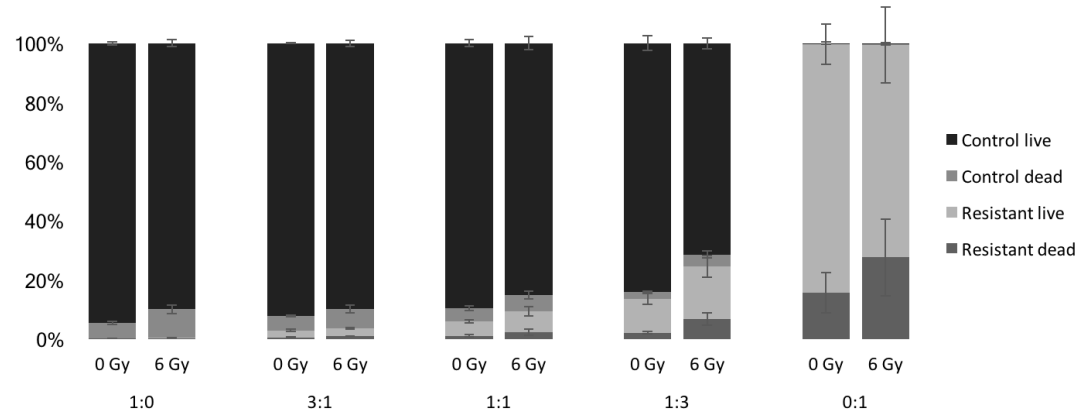

(a) Day 16

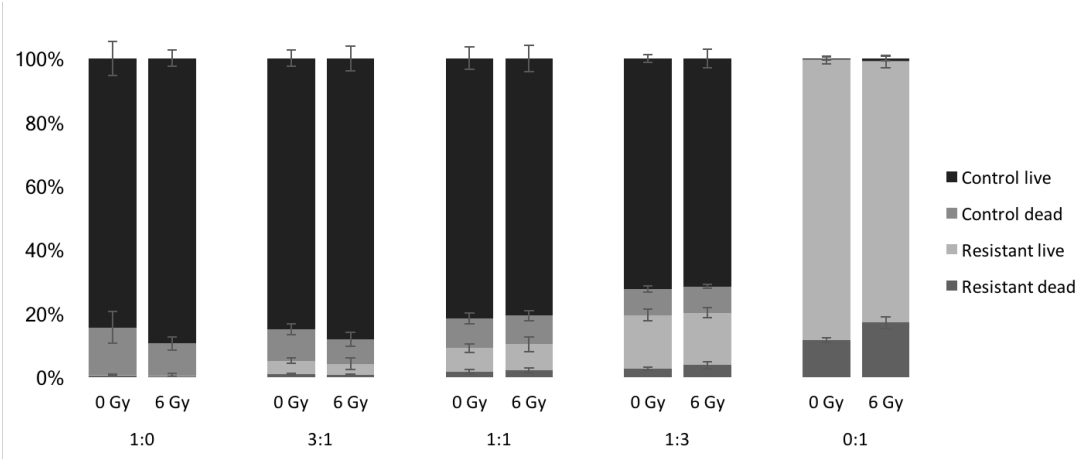

(b) Day 25

Figure 2.12: Proportions of different cell populations within heterogeneous DU145 spheroids on day 16 (a) and day 25 (b). Data shown represent mean ± 95% confidence intervals from 3 independent samples.

2.4 Discussion

In this chapter, we have described 2D and 3D *in vitro* models that enabled us to study the effect of intratumour heterogeneity on radiation response and potential interactions between two co-cultured cell populations with different radioresponsiveness. We have demonstrated that the resistant phenotypes had higher clonogenic surviving fractions than the control phenotypes, under normal and low oxygen conditions. We have exposed the shortcomings of the 2D model for our purposes and described a procedure for generating tumour spheroids composed of subpopulations of prostate cancer cell lines using a basement membrane extract Matrigel. Growth curves of the mixed spheroids revealed differences in 3D growth and radiation response of the control and resistant cell populations and suggested potential interactions between the clones. The presence of interclonal interactions was further evidenced by measurements of the proportions of the clones within heterogeneous spheroids. Although a single dose of radiation did not appear to significantly affect the composition of heterogeneous spheroids on the measurement days, the fraction of dead cells increased notably within each subpopulation.

Although *in vitro* monolayer models have been previously used to study the growth of heterogeneous cell cultures [130], one of their major disadvantages is that the cultures quickly reach confluency. As a result we could not monitor the growth of the co-cultured control and resistant populations beyond day 4 which was too short a timescale to observe any effect, if any effect was to be observed. A possible solution would be to passage the cells when they become confluent [130], but this disturbs the growth and alters any existing spatial distribution, which may be an important factor. Additionally, monolayer cultures provide an environment that is of limited relevance to *in vivo* tumours [69]. Most importantly, in many cases cells communicate via direct contact and such communication is impaired in monolayer cultures.

Our results show that the spheroids composed of only resistant cell lines grew faster and attained larger sizes than control spheroids. The differences between control and resistant spheroids in growth rates and maximum sizes were more pronounced for the PC3 cells. However, the PC3 spheroids were not grown for long enough to ensure that they reached their maximum size. The increased growth rate of the resistant PC3 cell line is consistent with other studies, which report faster growth of monolayer cultures and xenograft tumours composed of the PC3 resistant cells than the controls: the resistant cells were also more resistant to radiation, and showed increased invasive

potential [88]. The mechanism responsible for the increased growth rate and radiation resistance was shown to be overexpression of microRNA miR-95.

The fraction of resistant cells in PC3 spheroids increased markedly on day 10, as compared with the initial composition, and even further on day 15, for both non-irradiated and irradiated spheroids. This is perhaps not surprising since the resistant cells are more aggressive, as measured by the growth curves. The complexity of the growth kinetics of heterogeneous tumours has been demonstrated in the past. For example, Leith et al. [109] found that when two clones derived from human colon adenocarcinoma were mixed at extreme ratios (9:91 and 88:12) then the compositions remained stable. However, for the 50:50 ratio the composition changed drastically resulting in the approximately 10:90 split. In another study involving two clones derived from mouse mammary tumour, it was shown that for any initial composition, no matter how extreme, one clone always outgrew the other [130].

The effect of a single dose of 6 Gy was less severe for the DU145 spheroids than for the PC3 spheroids. We observed no differences in the composition on days 16 and 25 between the irradiated and non-irradiated spheroids. It future work, it would be informative to measure the proportions of the clones at some earlier time points. What is more surprising for the DU145 spheroids, is that although the resistant cells grew faster and were larger by the end of the experiments, the composition of the spheroids shifted overwhelmingly in favour of the control population, a phenomenon similar to that observed in [130]. The changes in the configuration of the DU145 spheroids are consistent with interactions between the control and resistant cells, which clearly benefited the former.

The effect of radiation on spheroid size could be observed on day 5 for the PC3 and day 7 for the DU145 cells. Following radiation damage, cells activate a DNA-damage response mechanism which comprises a very complex system of pathways and, depending on the extent of damage, the cell may undergo apoptosis, be repaired and resume cell cycle, or be temporarily blocked at one of the checkpoints [95]. The PC3 Res cells can escape the G2/M checkpoint due to upregulation of miR-95 [88]. We may ask whether the main reason of growth retardation following radiation damage was cell death or growth delay caused by the blockage of cell cycle progression due to cells being repaired. It is likely to be the combination of the two. As reported earlier, we noticed that, while applying the gate to remove debris from the FACS PC3 cell samples, we had to discard many more events for the samples from irradiated spheroids. We also noticed that as the number of resistant cells increased so did the number of cells available for further analysis. This indicates that there were

large quantities of debris, most likely from already disintegrated cells that had died following radiation damage, in addition to cells that were dying (but were still fairly compact) at the time of analysis.

We observed relatively large fractions of dead cells in the DU145 non-irradiated spheroids on day 16 that increased further on day 25. We believe that the spheroids might have developed hypoxic layers by that time and consequently necrotic cores in the centre. Hypoxia is a well documented phenomenon whereby poorly oxygenated tumours have to rely on diffusion to receive oxygen and nutrients [80]. As the tumour grows the cells in the centre do not receive enough oxygen and starve, forming a necrotic core. Necrotic core formation could explain the increased fraction of dead cells in untreated spheroids. Furthermore, we noticed that the number of cells rejected during the gating process of FACS analysis was much higher for the resistant homogeneous spheroids. This could also be explained by developing hypoxia leading to necrosis in the centre of the spheroids. If the DU145 Res spheroids were more susceptible to hypoxia, and in particular developed hypoxia earlier than the DU145 Ctrl spheroids, then this would give the control population a growth advantage leading to their clonal dominance.

In summary, we used 3D heterogeneous tumour spheroids to investigate potential interactions between two distinct clones derived from the same cell line. Our data for the PC3 spheroids do not provide compelling evidence that such interactions exist. However, the data for the DU145 spheroids, in particular the proportions measurements, suggest that the control and resistant clones may interact. In the chapters that follow, we resort to mathematical modelling and statistical inference techniques in order to determine the type of interactions and quantify their magnitude.

Chapter 3

Parameter inference and uncertainty quantification in a simple model of avascular tumour growth

3.1 Introduction

Mathematical models of biological systems are often formulated as systems of ordinary differential equations (ODEs) which contain parameters. Where possible, the parameters should be estimated from experimental data. The available dataset is usually a sample drawn from a population and may be incomplete. Moreover, biological systems are inherently noisy and the noise can arise in a number of ways. We can distinguish intrinsic variability arising due to stochastic processes present in otherwise identical cells, experimental and measurement errors occurring as a result of imperfections in experimental tools and measurement devices as well as imprecision of experimenters. Solving ODEs is often done numerically which means that the underlying mathematical model must be discretised which in turn introduces approximation errors. Moreover, the proposed model may be an inaccurate representation of the biological process considered. Therefore, it is clear that choosing an appropriate model and estimating its parameters is a challenging task.

ODE models have had a tremendous impact on qualitative understanding of biology. For example, the famous Lotka-Volterra equations have been used to describe the dynamics of systems comprising interacting species such as predator-prey interactions, but can be modified to model interactions such as competition or mutualism [134]. However, with the abundance of experimental data available, there is increasing pressure for such models to also have a quantitative impact. In particular, if we want to

use mathematical models to make critical decisions, such as what treatment protocol to give to a given patient, then we must be able to quantify the uncertainty associated with the model predictions.

The method of choice for parameter estimation in ODEs which are nonlinear in parameters has been nonlinear regression. Best estimates of model parameters are found by minimising a distance function (usually the sum of squared residuals) that relates model output and the data [13]. Although the main objective of nonlinear regression is to find point estimates of the parameters, it is equally important to assess how certain we are about them. In particular, predictions generated from parameterised models are in most cases critically dependent on the parameter values. Commonly, the uncertainty in estimated parameters is reflected by their 95% confidence intervals (CIs). The confidence intervals consist of the lower and upper bounds and define ranges in which we would expect our parameters to lie 95% of the time. It is important to stress that the meaning of the 95% CIs is not that there is the probability of 0.95 that our estimated parameters lie between the lower and upper bounds. Since parameters are considered to be unknown fixed quantities they either lie in the interval or they do not. However, if we repeated the experiment a large number of times and computed the 95% CIs for the parameters for each dataset we would expect to find the true value in 95% of all CIs constructed in this way.

Nonlinear regression is based on a set of assumptions and therefore its results, including CIs, might not be accurate if some of the assumptions are violated. For example, when computing CIs the intervals are always assumed to be symmetric and approximate or "asymptotic" [96]. To overcome these difficulties, simulation-based methods such as Monte Carlo simulations [156] or bootstrapping [96, 15] can be used.

With the Monte Carlo (MC) method a large number of noisy synthetic datasets are generated and the best parameter estimates for all of them are determined. Each synthetic dataset leads to a distinct parameter estimate. We determine the confidence intervals by analysing the distributions of the parameters estimated from the synthetic data. This method was used by Banks et al. [16] to analyse optimal design criteria for parameter estimation problems. They found that the standard errors based on the MC simulations were consistent with the standard errors based on the asymptotic theory.

Bootstrap, developed by Efron in 1979 [56], is a MC-based method for generating confidence intervals when we do not know much about the noise in the data. For dynamic models one constructs bootstrap datasets by adding noise to the dataset resulting from the best fit to the data. The noise is generated by sampling, with

replacement, from a set of residuals obtained from the best fit of the model to the available dataset. Bootstrap datasets constructed in this way are then used to produce a distribution of point estimates as for the MC method.

The bootstrap method has been shown to provide a better approximation to confidence intervals for parameters in dynamical systems than the asymptotic Fisher Information Matrix-based technique [96]. Banks and colleagues [15] also compared the bootstrap method with asymptotic theory by considering constant and non-constant variance data using the simple logistic population model. They concluded that for constant error model there is no advantage in using more computationally demanding bootstrap method over asymptotic theory. On the other hand, for proportional error model bootstrapping produced more accurate confidence intervals in certain cases.

Nonlinear regression and asymptotic, MC and bootstrap confidence intervals are all frequentist-type approaches for estimating parameters and confidence intervals. We also consider an alternative method that treats parameters as random variables. Underlying Bayesian inference is Bayes' theorem which allows us to update our prior belief about a parameter distribution as new evidence or data become available. In the context of parameter inference we can write Bayes' rule as

$$\pi(\theta|Y) = \frac{L(\theta|Y)\pi(\theta)}{\int L(\theta|Y)\pi(\theta)d\theta}, \tag{3.1}$$

where

- $\pi(\theta|Y)$ is the posterior distribution for θ,
- $L(\theta|Y)$ is the likelihood function,
- $\pi(\theta)$ is the prior distribution for θ and
- $\int L(\theta|Y)\pi(\theta)d\theta$ denotes the evidence.

Calculating the evidence (the term in the denominator of Equation (3.1)) is typically very challenging so, in most cases, this term is treated as a normalising constant. Then the problem reduces to computing $\pi(\theta|Y) \propto L(\theta|Y)\pi(\theta)$.

The prior $\pi(\theta)$ represents our belief about the possible ranges of parameter values θ before we observe data. Even if we know nothing about θ we can choose the prior to reflect this. This knowledge (or lack of it) is updated in light of observations and their probabilities for given θ which are encoded in the likelihood function. Since priors are chosen in a subjective manner this aspect of Bayesian inference has been occasionally criticised. On the other hand, one can argue that the ability to specify

any prior information about unknown parameters can lead to more accurate model calibration.

In most cases it is not possible to write analytical expressions for posterior distributions. As computers have become more powerful Markov chain Monte Carlo (MCMC) methods have been extensively utilised to sample from posterior distributions. In [86], Hines reviews MCMC algorithms such as Gibbs sampling and Metropolis-Hastings.

Recently, considerable research effort has focussed on developing methods that can deal with situations in which likelihood functions are too costly or impossible to evaluate. Such likelihood-free techniques are known as approximate Bayesian computation (ABC) methods [195, 181]. In general, ABC methods proceed in the following manner: sample a candidate parameter from the prior, generate a synthetic dataset using the sampled parameter, compute the discrepancy between the synthetic and observed datasets using some distance function and accept the candidate parameter if the discrepancy is within some tolerance. This process is repeated a large number of times and the accepted parameters are used to construct the approximate posterior distribution. The simplest ABC algorithm, ABC *rejection sampler* [158], proceeds in the way described above.

In this chapter, we use a logistic model to compare different methods for estimating model parameters and quantifying the uncertainty associated with these estimates. The techniques of interest include the asymptotic theory, MC simulations, bootstrapping and approximate Bayesian computation. The remainder of this chapter is organized as follows. In Section 3.2 we describe different techniques for uncertainty quantification from frequentist and Bayesian viewpoints. We apply these methods to a simple logistic model in Section 3.3 where we also assess the predictive power of the model for two synthetic datasets corresponding to measurements of tumour size with different growth dynamics. In Section 3.4 we apply the implemented techniques to our experimental data of homogeneous spheroids growth. The chapter ends in Section 3.5 where we present conclusions.

3.2 Methods

3.2.1 Mathematical and statistical models

We use the Verhulst logistic population model to describe the growth of tumour spheroids. The rate of change of the spheroid volume V at time t is given by

$$\frac{dV}{dt} = rV\left(1 - \frac{V}{K}\right), \quad \text{with} \quad V(t=0) = V_0, \tag{3.2}$$

where $r > 0$ represents the growth rate, $K > 0$ is the carrying capacity of the system and $V_0 > 0$ denotes the spheroid volume at $t = 0$. The analytical solution to the initial value problem (3.2) can be written

$$V(t) = \frac{V_0 K e^{rt}}{K + V_0(e^{rt} - 1)}. \tag{3.3}$$

We also require a statistical model to account for uncertainties associated with spheroid measurements. The constant error model assumes that the measurements are characterised by constant variance [15]. A common alternative, that is more appropriate for our data describing tumour growth, is the relative error model in which the measurement error is proportional to the size of measured quantity. Thus we assume that spheroid volume measurements at time t_i, with $i = 1, \ldots, N$ where N is the number of measurements, are generated by a statistical model given by

$$V_i = V(t_i; \theta^*) + \epsilon_i V(t_i; \theta^*) \tag{3.4}$$

where V_i are the observed values of spheroid volume at times t_i, $\theta^* = (r^*, K^*, V_0^*)$ are the true model parameters, $V(t_i; \theta^*)$ are the solutions of Eq. (3.2) and $\epsilon_i \sim \mathcal{N}(0, \sigma^2)$ where the standard deviation parameter σ represents the level of noise in the data.

3.2.2 Synthetic data

To compare different methods for parameter estimation and uncertainty quantification (described in the following sections), we use Eq. (3.2) to generate two synthetic datasets representing spheroid growth curves $V(t_i, \theta_1^*)$ and $V(t_i, \theta_2^*)$ for $\theta_1^* = (0.3, 1.0, 0.03)$ and $\theta_2^* = (0.1, 1.0, 0.03)$, respectively, and $t_i = \{3, 5, 7, 9, 11, 13, 15, 17, 19, 21, 23, 25, 27, 29, 31\}$. The former set describes fast growing spheroids whereas the latter set describes relatively slow growing spheroids. The growth curves $V(t_i, \theta_1^*)$ and $V(t_i, \theta_2^*)$ are then combined with Eq. (3.4) for $\sigma^* = \{0.01, 0.1, 0.2\}$ to generate *noisy* growth curves, six per condition, that are used to recover θ_1^* and θ_2^*.

3.2.3 Parameter estimation

Each of our noisy synthetic datasets consist of six growth curves. It is unclear whether we should compute the mean volume measurements at t_i when performing parameter inference or whether we should fit each growth curve separately. To determine which method allows us to recover parameter values with greater accuracy, we employ two nonlinear regression-based approaches (WLS and PEM) to estimate parameter values in the logistic model, both implemented within MATLAB [116].

3.2.3.1 Weighted least squares (WLS)

Here we fit the logistic model (3.2) to the data by minimising the weighted sum of squared residuals between the data and model outputs. That is we seek $\hat{\theta}_{WLS}$ such that

$$\hat{\theta}_{WLS} = \min_{\theta} \sum_{i=1}^{N} \frac{(\bar{V}_i - V(t_i;\theta))^2}{s_i^2} \tag{3.5}$$

where $\bar{V}_i$ is the mean and s_i is the standard deviation of the observations at time t_i. Weighting the data in this way ensures that the fit is not disproportionately influenced by more variable data. MATLAB functions *lsqnonlin* and *MultiStart* are used to find the best estimate for θ_1^* and θ_2^* for each noise level ($\sigma^* = \{0.01, 0.1, 0.2\}$). *lsqnonlin* is an implementation of the trust-region-reflective algorithm [46] which is an iterative optimisation technique. Since *lsqnonlin* is a local solver we use it in combination with *MultiStart* which runs the local solver from a number of randomly selected starting points within a prescribed region of parameter space, thus ensuring more thorough exploration of the parameter space.

3.2.3.2 Proportional error model (PEM)

In the WLS method we fit the model to the *average* volume measurements at t_i and use the corresponding standard deviations as weights. In contrast, in the PEM method we fit the model to each growth curve *separately* and then compute the average of parameter estimates across all six individual fits. Thus estimating $\hat{\theta}_{PEM}$ is split into two separate steps. We estimate $\hat{\theta}^j_{PEM}$, $j = 1, \ldots, 6$, for each growth curve and then compute

$$\hat{\theta}_{PEM} = \frac{1}{6} \sum_{j=1}^{6} \hat{\theta}^j_{PEM}. \tag{3.6}$$

To estimate $\hat{\theta}^j_{PEM}$ we use an iterative scheme [15]. We begin by estimating $\hat{\theta}^j$ for each growth curve by minimising the sum of squared residuals (3.5) with $s_i = 1$. Then, we define weights $\hat{w}_i^j$ as $\hat{w}_i^j = V^{-2}(t_i;\hat{\theta}^j)$ and estimate $\hat{\theta}^j_{PEM}$ by solving

$$\hat{\theta}^j_{PEM} = \min_{\theta} \sum_{i=1}^{N} \hat{w}_i^j (V_i - V(t_i;\hat{\theta}^j))^2. \tag{3.7}$$

We re-estimate $\hat{w}_i^j$ and $\hat{\theta}^j_{PEM}$ until convergence, that is until two successive estimates $\hat{\theta}^j_{PEM}$ are sufficiently close. Given $\hat{\theta}^j_{PEM}$, $\hat{\sigma}^j$ can be estimated via

$$\hat{\sigma}^j = \sqrt{\frac{SSR^j}{DF}}, \tag{3.8}$$

where

$$SSR^j = \sum_{i=1}^{N} \hat{w}_i^j (V_i^j - V(t_i; \hat{\theta}_{PEM}^j))^2 \tag{3.9}$$

and $DF = N - p$ where N is the number of data points and p is the number of parameters being estimated. As with $\hat{\theta}_{PEM}^j$, $\hat{\sigma}$ is then estimated via

$$\hat{\sigma} = \frac{1}{6} \sum_{j=1}^{6} \hat{\sigma}^j. \tag{3.10}$$

This method is implemented using MATLAB's *nlinfit* function. It uses the Levenberg-Marquardt nonlinear least squares algorithm [173] to estimate model parameters.

A graphical representation of the differences between the WLS and PEM methods is presented in Fig. 3.1.

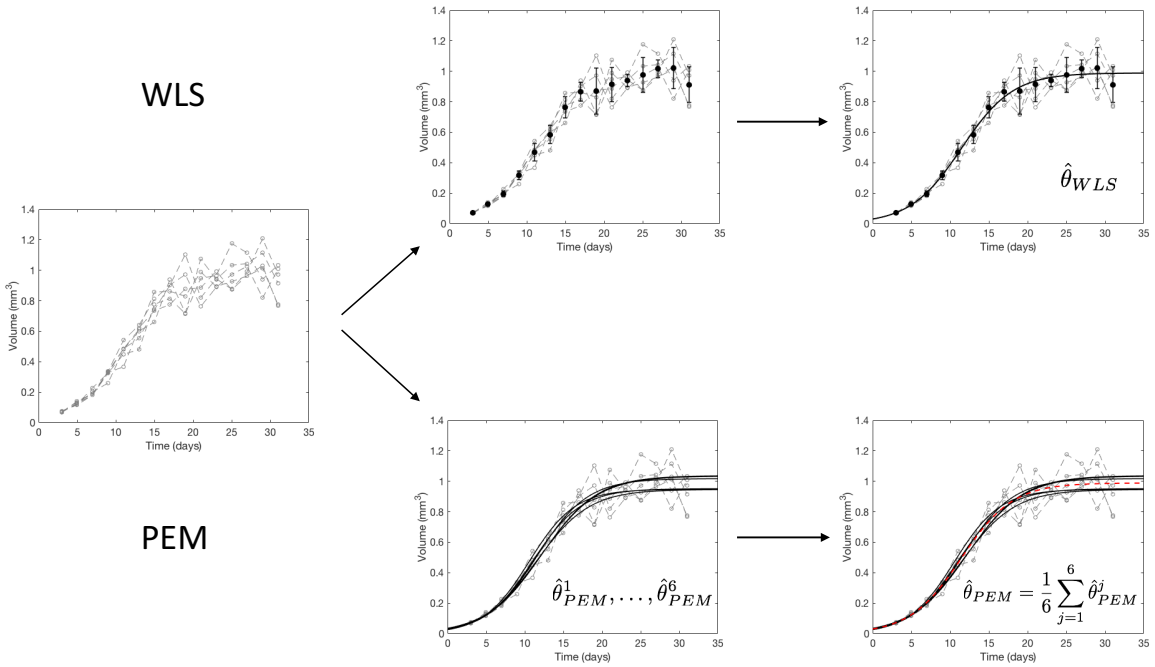

Figure 3.1: A diagram showing the differences between the WLS and PEM methods. In the WLS method we first compute the mean and standard deviation of the six noisy growth curves. Then we fit the model to the average data using the standard deviations as weights. In the PEM method we fit the model to each growth curve individually and then compute the average value of the parameters.

3.2.4 Confidence intervals

3.2.4.1 Asymptotic confidence intervals

In most parameter estimation problems the 95% confidence intervals are computed from the standard errors of the estimated parameters, that is

$$\hat{\theta}_i \pm t_{dist}(95\%, DF) SE(\hat{\theta}_i) \tag{3.11}$$

where

$$SE(\hat{\theta}_i) = \sqrt{\frac{SSR}{DF} Cov(i,i)}. \tag{3.12}$$

In Equations (3.11) and (3.12), $\hat{\theta}_i$ is the estimated value of the ith parameter, $t_{dist}(95\%, DF)$ is a value from the t distribution with 95% confidence and DF degrees of freedom, $SE(\hat{\theta}_i)$ represents the standard error of the ith parameter, SSR is the sum of squared residuals and $Cov(i,i)$ is the ith diagonal entry from the estimated covariance matrix for the fitted parameters. The asymptotic confidence intervals were computed with the MATLAB *nlparci* function.

3.2.4.2 Monte Carlo confidence intervals

To estimate the 95% CIs for the parameters $\hat{\theta}_{PEM}$ using the Monte Carlo (MC) method we used the point estimate to generate a "perfect" dataset to which we added random noise using the statistical model (3.4) with $\sigma = \hat{\sigma}$. Then, we used nonlinear regression again to estimate parameter values from the resulting noisy synthetic dataset. We repeated this process $M = 10^3$ times, each time generating a new random noise vector (see Fig. 3.2). In this way we derived a distribution of $\hat{\theta}^m_{MC}$ $(m = 1, ..., M)$ estimates.

We defined the lower and upper limits as the 2.5th and 97.5th percentiles of $\hat{\theta}^m_{MC}$ sorted in ascending order, respectively. We also defined the MC estimate as

$$\hat{\theta}_{MC} = \frac{1}{M} \sum_{m=1}^{M} \hat{\theta}^m_{MC}. \tag{3.13}$$

3.2.4.3 Bootstrap confidence intervals

In this work we adopted two bootstrap-based approaches to construct confidence intervals for the parameters estimated with the WLS fitting method. One method is based on sampling from a Gaussian distribution and the other on sampling with replacement from a set of standardised residuals (details included below). The main idea is to generate bootstrap data sets and estimate parameter values for each of them.

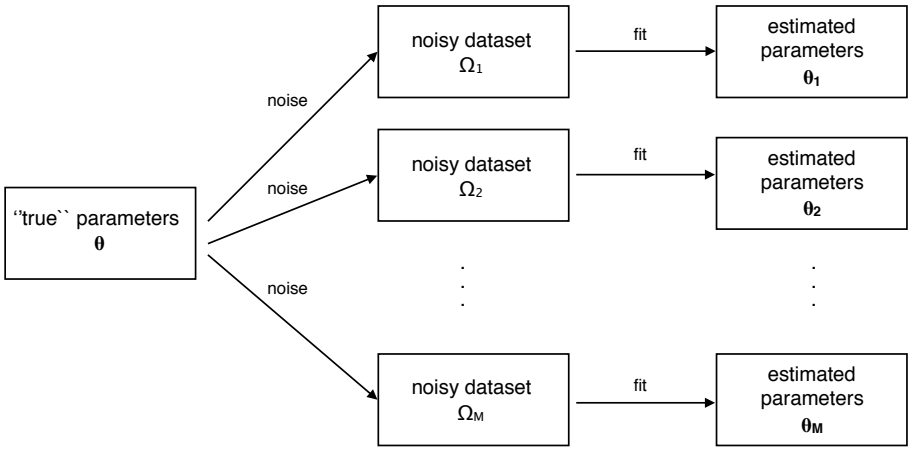

Figure 3.2: Diagram depicting the process of MC simulations.

The resulting distributions of parameter estimates can be used to obtain summary statistics as with the MC method.

Bootstrap based on standard deviations of observations (bootstrap_sd). Here we construct $M = 10^3$ bootstrap_sd datasets using the following formula

$$V_{m,i}^{bootsd} = \bar{V}_i + \bar{V}_i \epsilon_{m,i}^{bootsd} \tag{3.14}$$

where $\epsilon_{m,i}^{bootsd}$ is a random Gaussian number with zero mean and standard deviation s_i corresponding to the the observed standard deviation of V_i. For each bootstrap_sd dataset we find a corresponding parameter estimate $\hat{\theta}_{bootsd}^m$ using nonlinear regression. Then we compute the 95% CIs by the percentile method and the bootstrap_sd estimate as

$$\hat{\theta}_{bootsd} = \frac{1}{M} \sum_{m=1}^{M} \hat{\theta}_{bootsd}^m. \tag{3.15}$$

Bootstrap based on the residuals (bootstrap_res). An alternative, more traditional method to construct bootstrap estimates and confidence intervals is based on sampling with replacement from a set of residuals. Having obtained the WLS estimate $\hat{\theta}_{WLS}$ we define the standardised residuals $\bar{sr}_i$, as in [15], by

$$\bar{sr}_i = \frac{V_i - V(t_i; \hat{\theta}_{WLS})}{V(t_i; \hat{\theta}_{WLS})}. \tag{3.16}$$

Then we sample with replacement from the set $\{\bar{sr}_1, ..., \bar{sr}_N\}$ to obtain $M = 10^3$ bootstrap_res samples $\{sr_1^m, ..., sr_N^m\}$. The bootstrap_res samples are then used to

form M bootstrap_res datasets

$$V_{m,i}^{bootres} = V(t_i; \hat{\theta}_{WLS}) + V(t_i; \hat{\theta}_{WLS}) sr_j^m \tag{3.17}$$

where $j = 1, ..., N$. Each dataset is then fitted to the logistic model and the resulting distribution of parameter estimates used to construct the 95% CIs and $\hat{\theta}_{bootres}$ as explained previously.

3.2.4.4 Outliers

Outliers are data points which are distant from the other data points and have the potential to distort the data analysis process. They can occur due to chance, biological diversity or experimental error. Following Joshi et al. [96] we removed outliers from the distributions of parameter estimates in the following way. First, we divided the sorted parameter estimates into four equal quartiles separated by Q_i, $i = 0, 1, 2, 3, 4$, each containing 25% of the data. We defined the spread sp as $sp = Q_3 - Q_1$ and classified as outliers the values lying below $Q_1 - 1.5 \times sp$ and above $Q_3 + 1.5 \times sp$.

3.2.5 Approximate Bayesian computation

Bayesian inference methods have increased in popularity in the last decade. They offer a coherent and arguably more natural framework for parameter inference in inherently stochastic biological systems than frequentist-based approaches [111]. Approximate Bayesian computation algorithms are relatively simple to implement. The most basic ABC procedure, the rejection sampler algorithm [158], proceeds as follows.

RS1 Sample a candidate parameter θ^* from the prior $\pi(\theta)$.

RS2 Simulate a dataset D^* from the model $f(D|\theta^*)$.

RS3 Compare D^* with the experimental data D_0 using some distance function d and tolerance δ. If $d(D_0, D^*) \leq \delta$, accept θ^*, otherwise reject.

RS4 Return to **RS1**

The posterior distribution constructed with ABC algorithms is an approximation to the true posterior. In the limit as δ approaches zero this approximation should converge to the true posterior [111]. Here we used a slightly modified version of

the rejection sampler algorithm to infer the posterior distributions for θ. Instead of defining a fixed threshold value δ, we constructed a sequence of posteriors by starting with a large δ and decreased it as long as we were able to accept new parameters within a reasonable amount of computation time. The choices for δ were therefore heuristic. This enabled us to estimate the posterior much faster than by selecting δ a priori. Our method is thus a hybrid of the rejection sampler and ABC *sequential Monte Carlo* algorithm developed by Toni et al. [194].

We used the weighted sum of squared residuals defined in Equation (3.5) as our distance function, d. Thus D_0 is effectively represented by the average of the simulated/observed growth curves. Unless otherwise stated the prior distributions used for the logistic model parameters are: $\pi(r) = U(0,1)$, $\pi(K) = U(0,5)$ and $\pi(V_0) = U(0,0.1)$. From the approximated posterior distributions we computed the 95% credible intervals by the percentile method and parameter estimates $\hat{\theta}_{abc}$ by taking the mean values across the approximated marginal posteriors.

3.2.6 Predictive power analysis

We analysed the predictive power of the logistic model for the spheroids with large and small growth rates r and the noise level $\sigma^* = 0.1$. Following [20], the dataset corresponding to either fast (large r) or slow (small r) growing spheroids was split into the training set and the validation set. The training set consisted of the first n data points and was used to estimate the model parameters. Then the model was used to predict the remaining d data points which constitute the validation set. We defined a prediction as successful if the value predicted by the model was within one standard deviation of the data point considered. Formally, a prediction was classified as a success if

$$|V_{n+i}^{data} - V_{n+1}^{pred}| \leq s_{n+i}, \quad i = 1, 2, \ldots, d \tag{3.18}$$

where s_{n+i} is the standard deviation of the observed point V_{n+i}^{data} and V_{n+1}^{pred} is the $n + 1^{th}$ predicted point.

3.3 Results: synthetic data

3.3.1 Parameter estimation

We generated synthetic data for two sets of parameter values in the logistic model: $\theta_1^* = (r^* = 0.3, K^* = 1.0, V_0^* = 0.03)$ and $\theta_2^* = (r^* = 0.1, K^* = 1.0, V_0^* = 0.03)$, corresponding to fast and slow growing spheroids respectively. The mean values and

standard deviations of the 6 synthetic datasets are presented in Fig. 3.3 for both cases and for different noise levels ($\sigma^* = [0.01, 0.1, 0.2]$). Fig. 3.3 also shows the best fits curves obtained with the weighted least squares (WLS) and proportional error model (PEM) methods. The parameter values associated with the best fits are presented in Table 3.1.

As seen in Fig.3.3, the fast growing spheroids approach the saturation size within the time period considered ($T = 31$ [days]). Visual inspection reveals that the fits obtained with both methods are practically indistinguishable for the 1% and 10% noise levels. For the 20% noise level there is a slight difference between them. Variability in the estimated parameter values increases with noise levels but the estimates are in

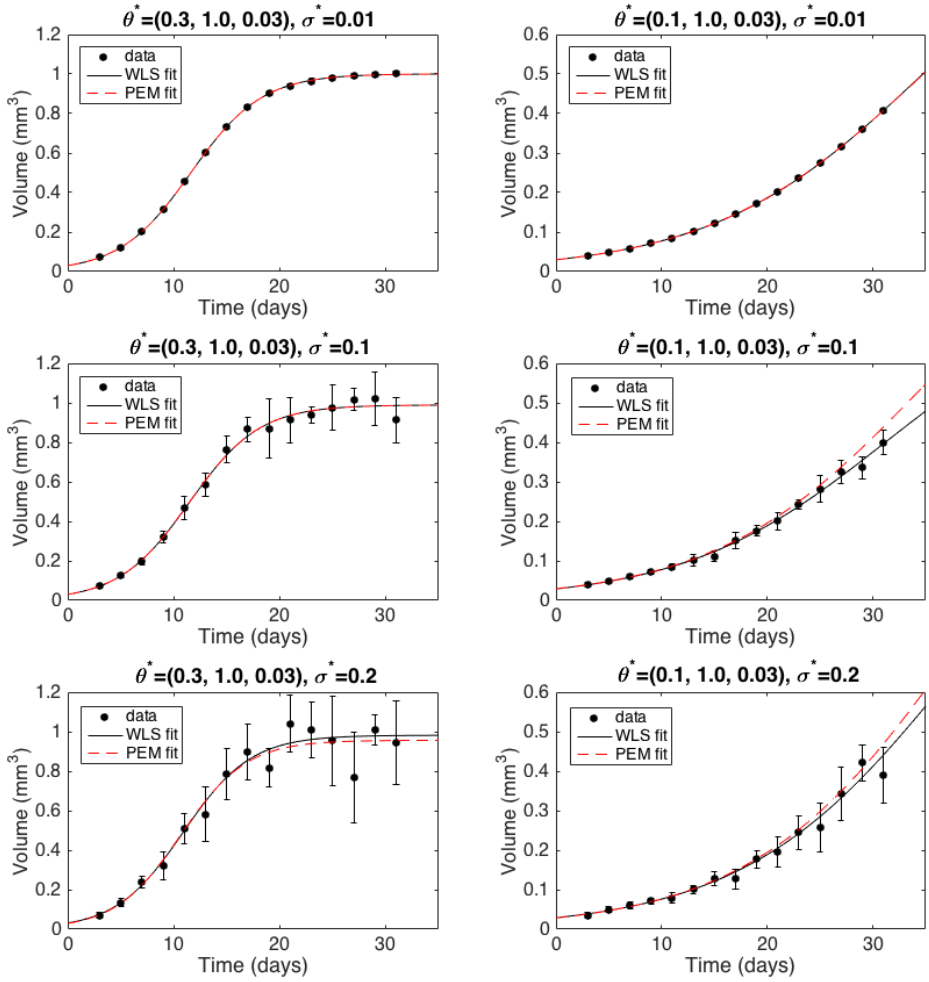

Figure 3.3: Noisy synthetic data and corresponding best fits to the logistic model. The best fits to the synthetic data for the fast (left column) and slow (right column) growing spheroids were obtained by applying the weighted least squares (solid black lines) and proportional error model (dashed red lines) methods. Data points represent mean$\pm$1$\times$standard deviation (SD) from six noisy growth curves.

Table 3.1: Comparison of the true parameter values (θ^*) and the best fit values obtained using the WLS ($\hat{\theta}_{WLS}$) and PEM ($\hat{\theta}_{PEM}$) methods.

	r [day^{-1}]	K [mm^3]	V_0 [mm^3]	σ
θ^*	0.3000	1.0000	0.0300	0.0100
$\hat{\theta}_{WLS}$	0.2983	1.0016	0.0303	
$\hat{\theta}_{PEM}$	0.2985	1.0008	0.0303	0.0089
θ^*	0.3000	1.0000	0.0300	0.1000
$\hat{\theta}_{WLS}$	0.3013	0.9891	0.0303	
$\hat{\theta}_{PEM}$	0.3014	0.9891	0.0305	0.1035
θ^*	0.3000	1.0000	0.0300	0.2000
$\hat{\theta}_{WLS}$	0.3140	0.9819	0.0310	
$\hat{\theta}_{PEM}$	0.3239	0.9566	0.0292	0.1842
θ^*	0.1000	1.0000	0.0300	0.0100
$\hat{\theta}_{WLS}$	0.1002	0.9981	0.0300	
$\hat{\theta}_{PEM}$	0.1007	0.9765	0.0299	0.0110
θ^*	0.1000	1.0000	0.0300	0.1000
$\hat{\theta}_{WLS}$	0.1053	0.7963	0.0291	
$\hat{\theta}_{PEM}$	0.1034	1.0632	0.0295	0.0978
θ^*	0.1000	1.0000	0.0300	0.2000
$\hat{\theta}_{WLS}$	0.1002	1.3143	0.0291	
$\hat{\theta}_{PEM}$	0.1021	1.4667	0.0285	0.1742

general good.

When $r^* = 0.1$ the growth rate is too slow for the system to attain its equilibrium value within the time considered (second column of Fig. 3.3). For $\sigma^* = 0.01$ the estimated parameters for both methods are reasonably close to the true values, with the weighted least squares providing more accurate estimates. For larger noise levels ($\sigma = 0.2$) the estimates of K are off by a significant amount for the WLS and PEM approaches. The fitted values for K are underestimated for the weighted least squares but overestimated for the individual fits approaches (10% noise). However, the PEM approach provides a good estimate for K with 10% noise present.

3.3.2 Confidence intervals

The asymptotic and bootstrap 95% CIs were constructed from the parameter estimates obtained with the weighted least squares fitting approach. The MC 95% CIs were generated from averaged parameter estimates resulting from the individual fits (PEM) method. Our findings are summarised in Figures 3.4 and 3.5 and Tables A.1–A.6.

In Figures 3.4 and 3.5 the vertical lines represent the normalised true values used to generate synthetic data. We used the following formula to restrict the values of r

to lie in the interval $(0, 1)$

$$r_{norm} = \frac{r^* - r_{min}}{r_{max} - r_{min}} \tag{3.19}$$

where r^* is the true parameter value, r_{min} is the lowest estimate of the lower 95% CIs limit for r and r_{max} is the largest estimate of the upper 95% CIs limit for r across all the methods used. We used similar formulae for the K and V_0 parameters.

Fig. 3.4 shows that for the fast growing spheroids the width of the CIs increases with increasing noise levels for all 3 parameters. In all cases, the asymptotic CIs are the most conservative and, by definition, symmetric. Although the bootstrap_sd CIs were constructed around the same parameter estimates as the asymptotic CIs, they are almost always the widest, the only exception being the MC CIs for K ($\sigma = 0.2$). Moreover, $\hat{\theta}_{bootsd}$ provides the least accurate estimates for θ of all methods considered. We also note that the simulation-based confidence intervals are not necessarily symmetric. In general, the parameter estimates and CIs obtained with the WLS and bootstrap_res methods are similar, with the latter being slightly wider and non-symmetric. In all cases and for all methods considered the true parameter values fall within the constructed confidence intervals.

In Fig. 3.5 we summarise the results of the confidence intervals analysis for the slow growing spheroids. We observe a similar trend as in the other case (asymptotic CIs are the most conservative and the bootstrap_sd CIs are almost always the widest). The width of the 95% CIs for the carrying capacity parameter K increases markedly as the noise level is increased from $\sigma = 0.01$ to $\sigma = 0.1$. Tables A.5 and A.6 reveal that the uncertainty associated with the estimates of K is very large. This is a direct consequence of our earlier observation that for the timescale of interest the slow growing spheroids remain in the exponential-linear growth phase. We also note that the lower limit of the asymptotic 95% CI for K with $\sigma = 0.2$ is negative which is clearly unrealistic.

Typical histograms obtained by constructing CIs using the Monte Carlo and bootstrap methods are shown in Fig. 3.6. The bootstrap_res-based histograms have the highest peaks and the lowest spread. The estimates $\hat{\theta}_{bootres}$ are also characterised by the smallest number of outliers of all methods considered (results not shown). The bootstrap_sd histograms are relatively wide and asymmetric, the asymmetry being particularly pronounced for the distribution of values of V_0.

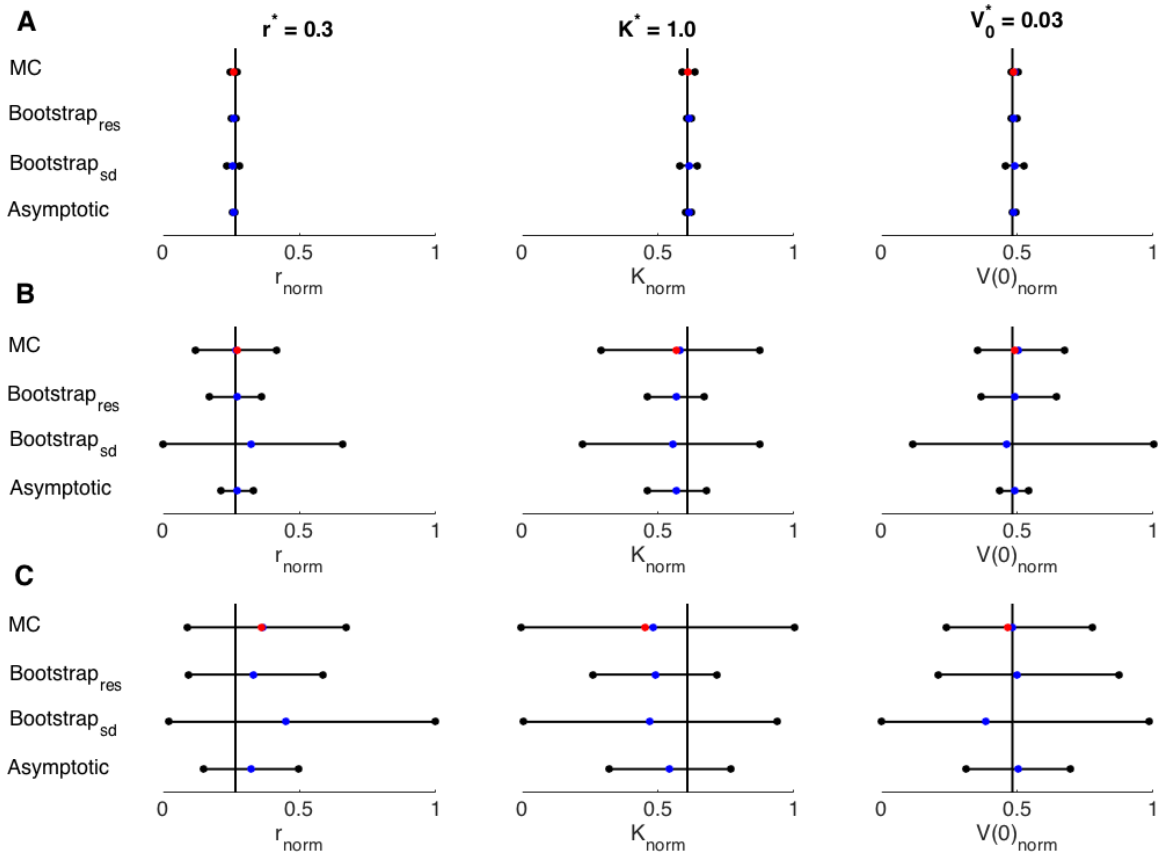

Figure 3.4: The normalised 95% asymptotic, bootstrap and Monte Carlo confidence intervals of the parameter estimates in the logistic model fitted to the fast growing spheroids data. The (normalised) parameter values used to generate the synthetic data are represented by vertical lines and the actual values are stated. The horizontal lines represent the 95% CIs with their lower and upper limits marked with black circles at both ends of the lines. The blue circles correspond to estimates of θ for a given method: i) $\hat{\theta}_{WLS}$ (asymptotic); ii) $\hat{\theta}_{bootsd}$ (bootstrap_sd); iii) $\hat{\theta}_{bootres}$ (bootstrap_res) and iv) $\hat{\theta}_{MC}$ (Monte Carlo). The red circles on the MC 95% CIs lines correspond to $\hat{\theta}_{PEM}$ (since MC CIs are based on this estimate). Each panel represents a different noise level in the synthetic data: A) $\sigma = 0.01$; B) $\sigma = 0.1$; C) $\sigma = 0.2$.

3.3.3 Posterior distributions of model parameters

The approximate posterior distributions for the fast and slow growing synthetic spheroids are shown in Figures 3.7 and 3.8 respectively. We also included $\hat{\theta}_{abc}$ and corresponding 95% credible intervals in Tables A.1–A.6. We note that the values of $\hat{\theta}_{abc}$ and $\hat{\theta}_{WLS}$ are identical in all but one case. The exception is for the slow growing spheroids case with $\sigma = 0.2$ (Table A.6). The good agreement between the results obtained with the ABC and WLS methods is due to our choice of the distance function d. If d is the weighted sum of squared residuals and summary statistics are used rather than raw data in step **RS3** of the rejection sampler algorithm, the ABC

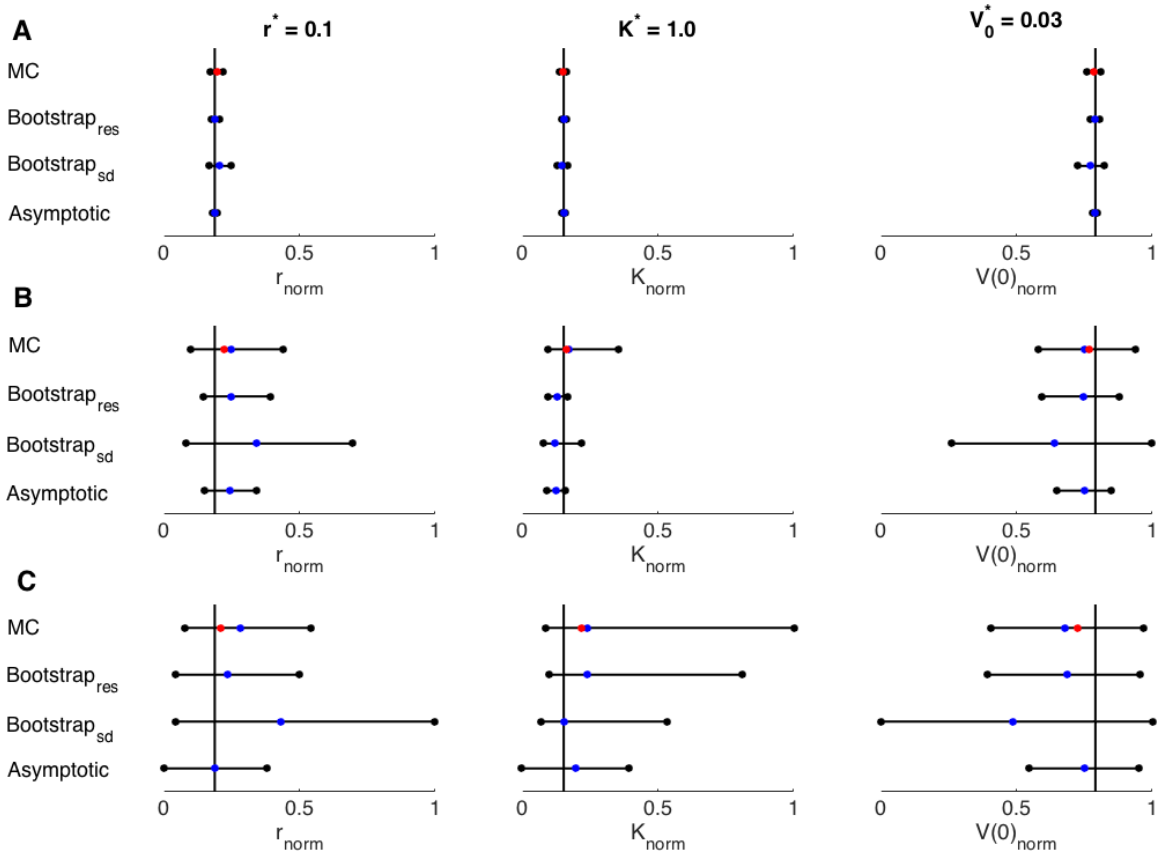

Figure 3.5: The normalised 95% asymptotic, bootstrap and Monte Carlo confidence intervals of the parameter estimates in the logistic model fitted to the fast growing spheroids data. See the legend of Fig. 3.4 for more details.

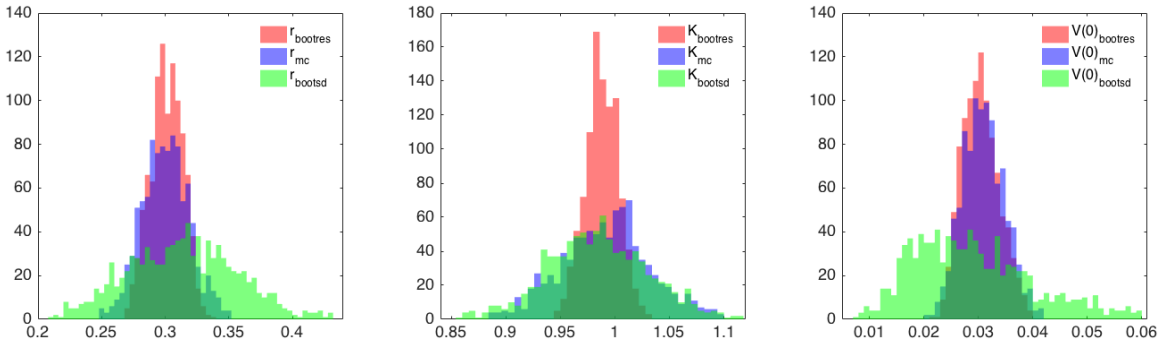

Figure 3.6: A representative example of the histograms describing distributions of parameters generated with the bootstrap and MC simulations. Parameter values used to generate synthetic data: $\theta^* = (0.3, 1.0, 0.03)$, $\sigma = 0.1$.

and WLS methods generate similar results.

However, the 95% credible intervals constructed for $\hat{\theta}_{abc}$ are extremely tight. In fact, the width of the credible intervals depends critically on the value of the tolerance δ. As we decrease the value of δ to obtain approximate posterior distributions, the

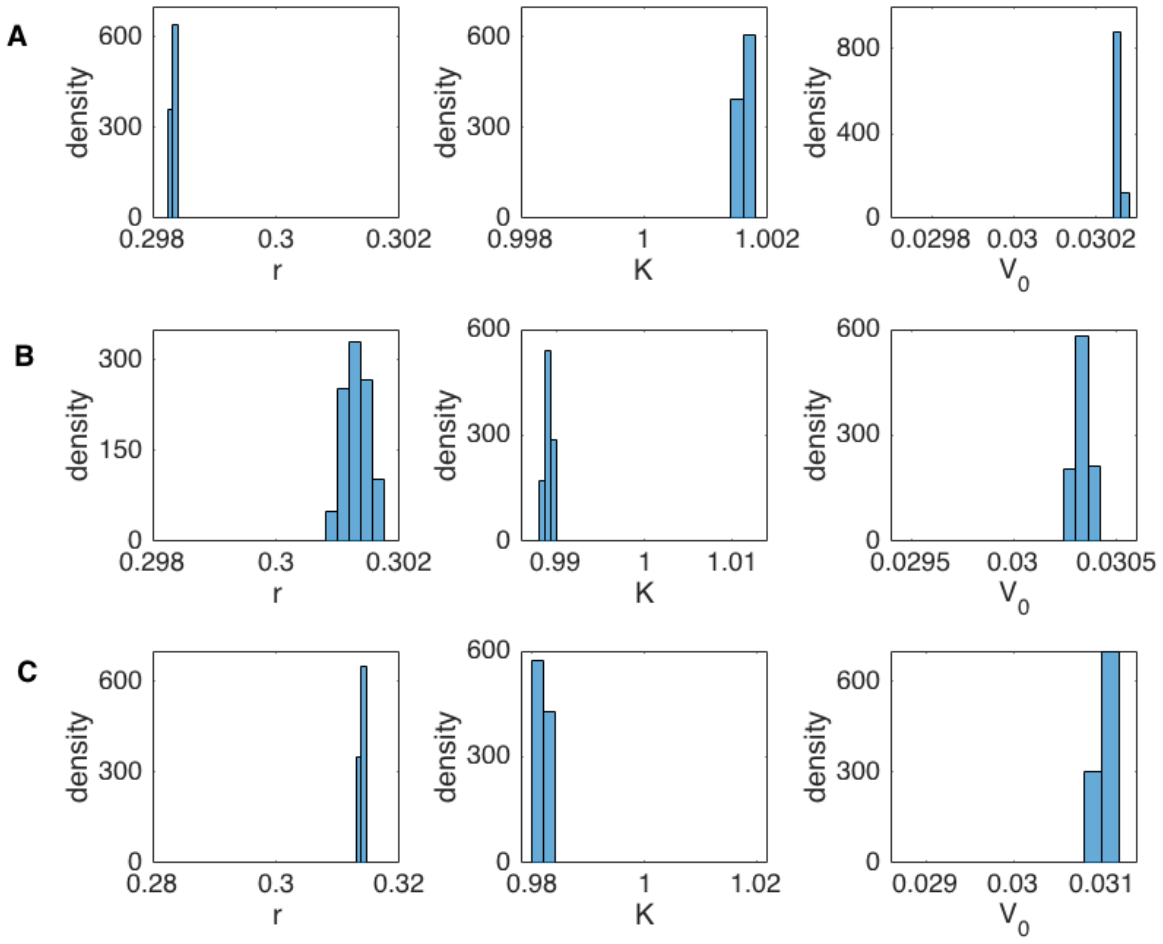

Figure 3.7: Posterior distributions of the logistic model parameters inferred for the fast growing spheroids data. Histograms showing approximated posterior distributions of parameters r, K and V_0 for different noise levels: A) $\sigma = 0.01$; B) $\sigma = 0.1$; C) $\sigma = 0.2$. The values used to generate the synthetic data: $r^* = 0.3$, $K^* = 1.0$ and $V_0^* = 0.03$.

range of accepted particles also decreases. This is exemplified in Figure 3.9 where we present scatter plots of the accepted parameter values for decreasing values of δ. For $\delta = 30$ the ranges of r, K and V_0 are quite wide (blue dots). When $\delta = 2.3$ these ranges are very narrow (green dots). We also note that, since the distance function d in the ABC algorithm is the same as the objective function (3.5), the minimum value of δ should be the same as the value of SSR for $\hat{\theta}_{WLS}$.

3.3.4 Model predictions for synthetic data

To assess the predictive power of the logistic model for the fast and slow growing spheroids we systematically decreased the size of the training dataset used to estimate the model parameters and used the remaining data points for validation. As explained

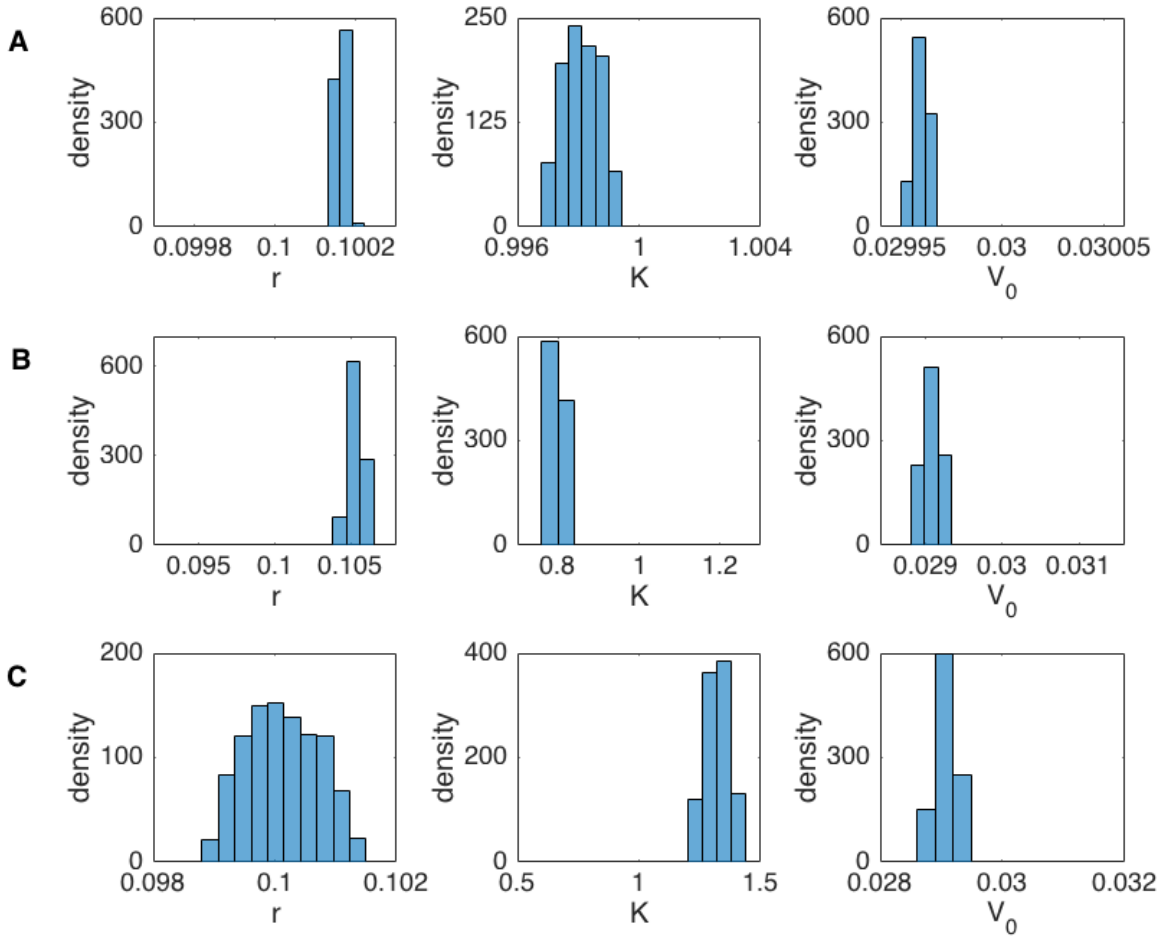

Figure 3.8: Posterior distributions of the logistic model parameters inferred for the slow growing spheroids data. Histograms showing approximated posterior distributions of parameters r, K and V_0 for different noise levels: A) $\sigma = 0.01$; B) $\sigma = 0.1$; C) $\sigma = 0.2$. The values used to generate the synthetic data: $r^* = 0.1$, $K^* = 1.0$ and $V_0^* = 0.03$.

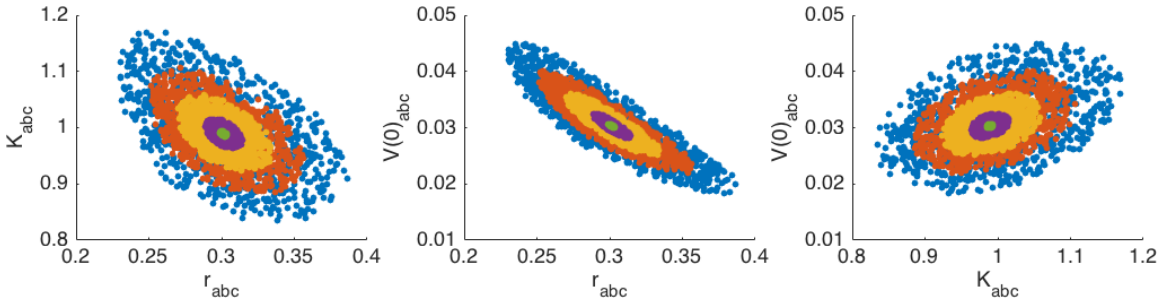

Figure 3.9: The effect of decreasing the tolerance δ on the joint distributions of the parameter values for the logistic model when $\theta^* = (0.3, 1.0, 0.03)$ and $\sigma^* = 0.1$. The values of $\delta = 30, 15, 7, 3, 2.3$ correspond to the blue, orange, yellow, purple and green dots respectively.

in the methods section, we defined a given prediction a success if the distance between

the data point V_{n+i}^{data} and its model prediction V_{n+i}^{pred} falls within one standard deviation of V_{n+i}^{data}.

In Figures 3.10 and 3.11 we show the results of our analysis for $\theta^* = (0.1, 1.0, 0.03)$ with $\sigma^* = 0.1$ and $\theta^* = (0.3, 1.0, 0.03)$ with $\sigma^* = 0.1$. The black circles represent the training set and the red circles represent the validation set. Parameter estimation was performed by the WLS minimisation method on $n = 14, ..., 3$ data points. The resulting curves were plotted on top of the training data (black solid lines) and forecast onto the validation data (red dotted lines). We summarise these results in Figure 3.12 where the blue and red colours correspond to successful or failed predictions respectively.

It is evident from Figures 3.10 and 3.12a that the model predictions for the slow growing spheroids are widely inaccurate if fewer than 8 data points were used for the training set. For $n = 7$ the model did not accurately predict any of the data points, successfully forecasting only 2, 2, 3 and 1 data points for $n = 6, 5, 4$ and 3 respectively. The model failed to predict either of the 2 validation points for $n = 13$. The last data point corresponding to V_{15} was successfully predicted only once when $n = 14$.

For the fast growing spheroids the predictions were much better. Visual inspection of Figure 3.11 reveals that only when $n = 3$ the predicted data was far from the validation data. As shown in Figure 3.12b the prediction rate is much higher (at most 2 data points not successfully predicted for $n \geq 6$). For this dataset, when $n = 4$ the prediction rate was 100% dropping to 0% for $n = 3$.

As noted previously, our approximations to the posterior distribution depend on the value of the tolerance δ. Since the model predictions depend on the approximation to the posterior, they also depend on the value of δ. In Figure 3.13 we generate predictions by running Monte Carlo simulations for every point in the approximated posterior distribution for θ for different values of δ based on $n = 8$ training points. As expected, the predictions become narrower as the tolerance δ decreases. However, as δ becomes smaller, our predictions fail to capture data points from the validation set. Due to deterministic form of our distance function d used in the ABC algorithm, the method fails to capture stochastic behaviour as $\delta \to \infty$.

3.4 Results: application to experimental data

In this section we apply the inference techniques introduced in Section 3.2 to our experimental data describing the growth dynamics of the homogeneous DU145 Ctrl,

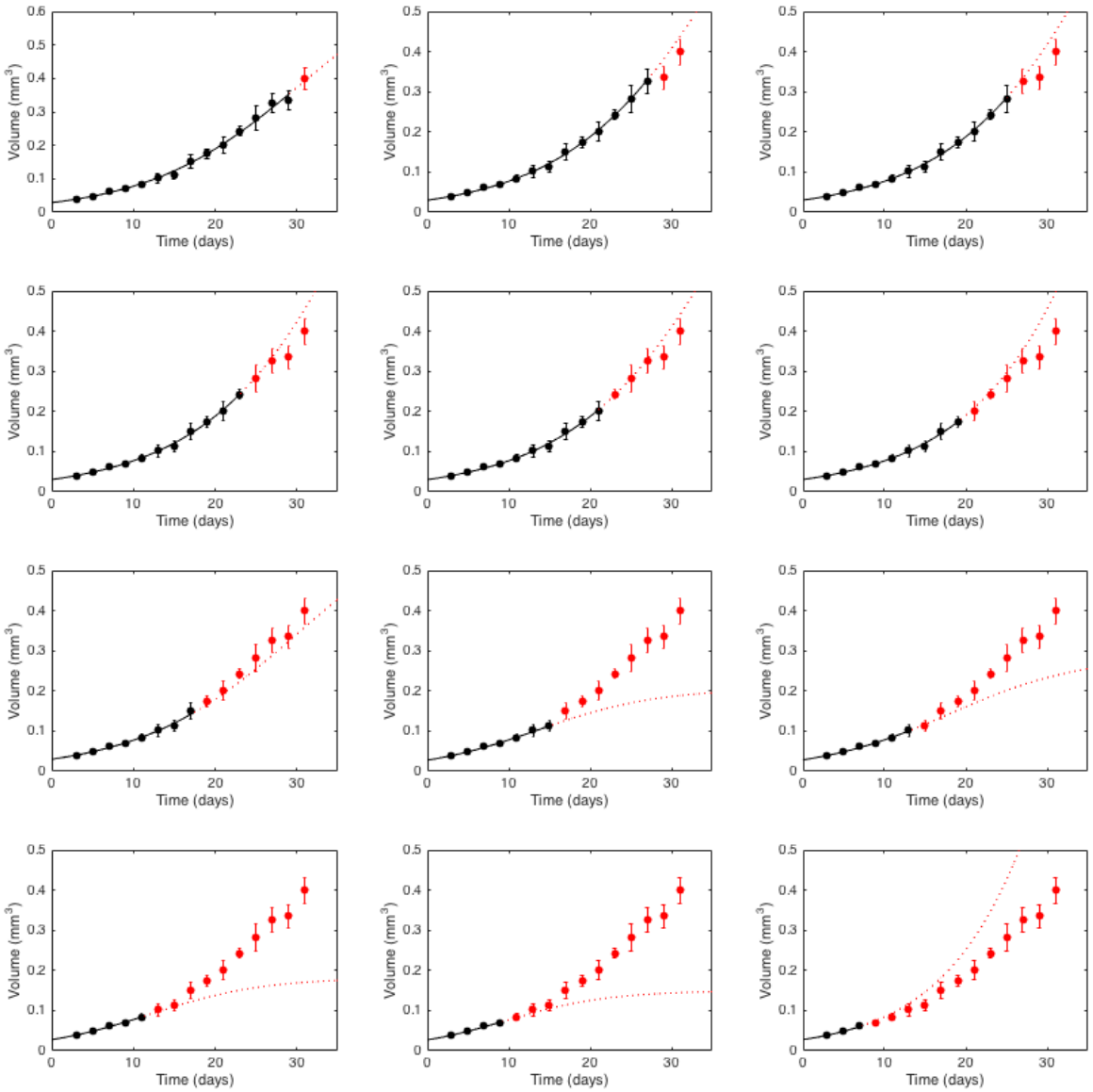

Figure 3.10: The predictive power of the logistic model for the slow growing spheroids. Parameter values: $\theta^* = (r^*, K^*, V_0^*) = (0.1, 1.0, 0.03)$ and $\sigma = 0.1$. The black circles and lines represent the training sets and best fits based on these sets, respectively. The red circles and dashed lines correspond to the validation sets and model predictions, respectively.

DU145 Res, PC3 Ctrl and PC3 Res tumour spheroids. In what follows, the parameter values are estimated using the WLS and PEM fitting methods and their uncertainty is assessed by constructing the 95% confidence intervals using the asymptotic, bootstrap and Monte Carlo methods. As in the previous section, the construction of the asymptotic and bootstrap CIs is based on $\hat{\theta}_{WLS}$ and the uncertainty in $\hat{\theta}_{PEM}$ is assessed using the MC 95% CIs. We also use the sequential rejection sampler algorithm to approximate the posterior distribution of the parameters.

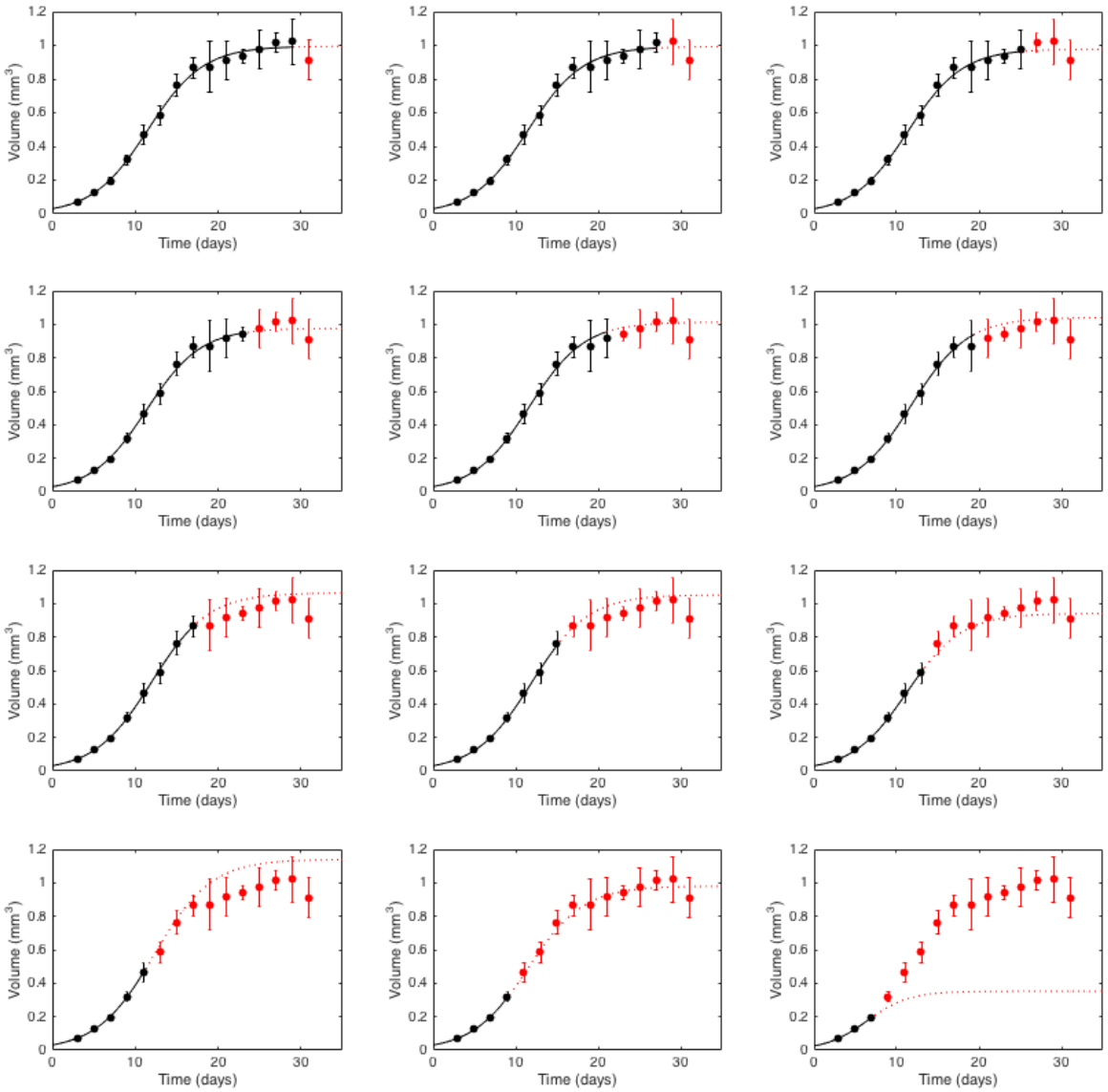

Figure 3.11: The predictive power of the logistic model for the fast growing spheroids. Parameter values: $\theta^* = (r^*, K^*, V_0^*) = (0.3, 1.0, 0.03)$ and $\sigma = 0.1$. The black circles and lines represent the training sets and best fits based on these sets, respectively. The red circles and dashed lines correspond to the validation sets and model predictions, respectively.

3.4.1 DU145 homogeneous spheroids

The spheroids composed of the DU145 cells (see Figures 3.14a and 3.14b) appear to have reached (DU145 Ctrl) or approached (DU145 Res) their maximum sizes on the time scales of experiments (30 days). They growth dynamics are characterised by initial exponential growth followed by a linear growth phase and a plateau, such dynamics are commonly observed in avascular tumours and multicellular tumour spheroids [182].

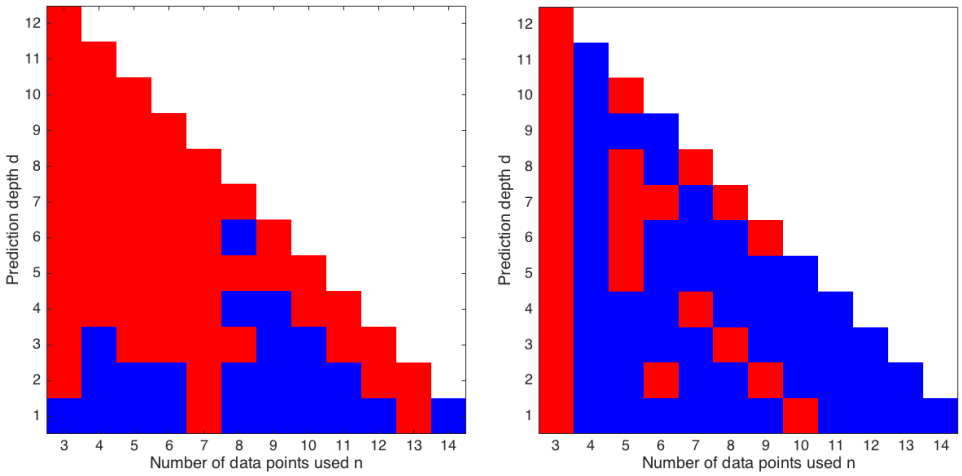

(a) $\theta^* = (0.1, 1.0, 0.03)$, $\sigma = 0.1$ **(b)** $\theta^* = (0.3, 1.0, 0.03)$, $\sigma = 0.1$

Figure 3.12: Matrices summarising the predictive power of the logistic model for the slow and fast growing synthetic spheroids. The blue and red squares corresponds to successful or failed predictions at depth d using n data points to parameterise the model, respectively.

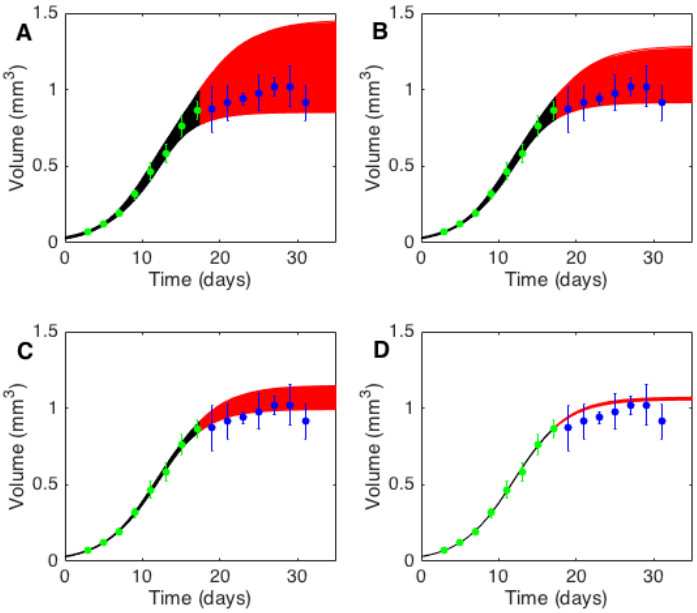

Figure 3.13: A typical example of the predictive power of the logistic model within the ABC framework. Parameter values: $\theta^* = (r^*, K^*, V_0^*) = (0.3, 1.0, 0.03)$, $\sigma = 0.1$, A) $\delta = 5$, B) $\delta = 2.5$, C) $\delta = 1$, D) $\delta = 0.63$. The green circles represent the data points in the training set used to approximate the posterior distribution of θ and the black lines corresponding simulated curves generated by the MC simulations. The blue circles correspond to the validation set and the red lines are the predictions based on the posterior.

The best WLS and PEM fits are similar for the DU145 Ctrl spheroids (Figure 3.14a) but for the DU145 Res spheroids (Figure 3.14b) differ slightly. The early data points were captured very well but the later observations show increased vari-

ability which affected the fitting results. In particular the data suggest that after reaching a maximum size at around $t = 20$ [days] the DU145 Ctrl spheroids slightly decreased in size settling at just below 0.6 mm^3. The model estimates of the carrying capacity were $\hat{K}_{WLS} = 0.6256$ mm^3 and $\hat{K}_{PEM} = 0.6183$ mm^3 (Table 3.2) and so the value of K might have been slightly overestimated. The opposite is true for the

Table 3.2: The best fit parameter values obtained using the WLS and PEM methods for the DU145 control and resistant spheroids.

	r [days^{-1}]	K [mm^3]	V_0 [mm^3]	σ
$\hat{\theta}_{WLS}$ (ctrl)	0.3150	0.6256	0.0117	
$\hat{\theta}_{PEM}$ (ctrl)	0.3182	0.6183	0.0115	0.0735
$\hat{\theta}_{WLS}$ (res)	0.3010	0.6940	0.0208	
$\hat{\theta}_{PEM}$ (res)	0.3080	0.7148	0.0201	0.0749

resistant spheroids where both fits underestimate the carrying capacity K. Based on the estimated parameters we conclude that the control spheroids grow slightly faster but have a smaller carrying capacity than the resistant spheroids (Table 3.2). We also report that the estimates of the proportional error model parameter σ suggest that the noise present in the data is respectively 7.35% and 7.49% for the control and resistant spheroids.

The 95% CIs for the parameter estimates are summarised in Fig. 3.15 (numerical values are provided in Table A.9). A trend similar to that observed in the synthetic data analysis is apparent. The bootstrap_sd CIs are the most generous and the estimate $\hat{\theta}_{bootsd}$ significantly differs from the other estimates. The asymptotic and MC CIs are similar which is perhaps surprising since for the fast growing synthetic spheroids the MC CIs were much wider than the asymptotic CIs (Fig. 3.4). The

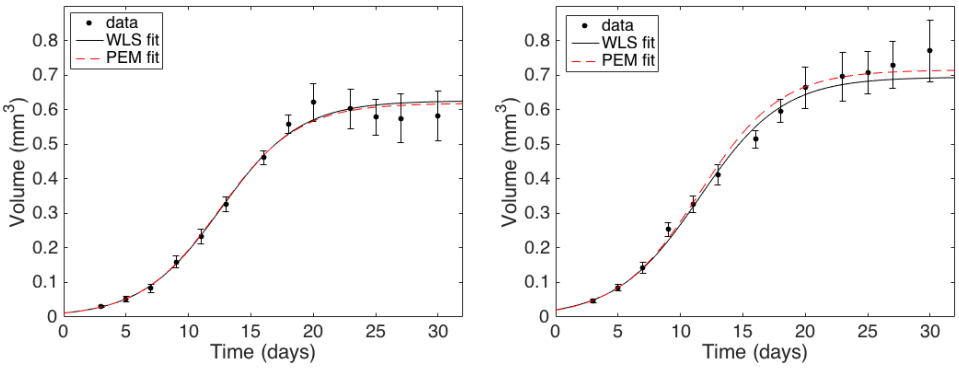

(a) DU145 ctrl **(b)** DU145 res

Figure 3.14: Best fits of the logistic model to the DU145 control and resistant spheroids data. Data shown as mean±1×SD.

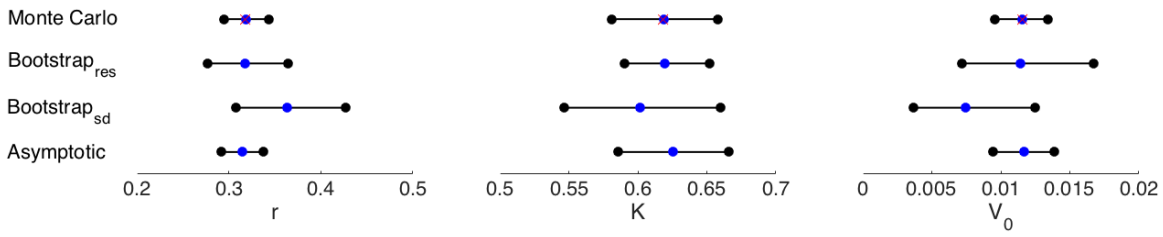

(a) DU145 ctrl

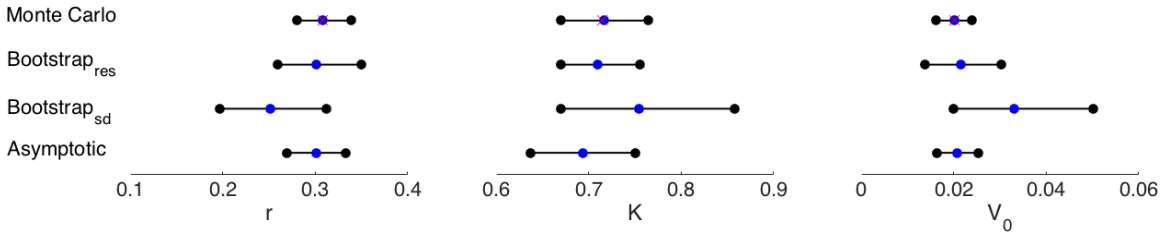

(b) DU145 res

Figure 3.15: 95% confidence intervals for the parameter values estimated from the DU145 control and resistant data.

confidence intervals obtained with the bootstrap_res method are narrower for the K parameter but suggest more uncertainty in the r and V_0 estimates when compared with the asymptotic and MC approaches.

Finally, the approximate marginal posterior distributions for the parameters obtained using the ABC method are presented in Fig. 3.16. As noted previously, the ABC parameter estimates are identical to those obtained using the WLS fitting procedure (Tables A.9 and A.10).

3.4.2 PC3 homogeneous spheroids

The data for the PC3 spheroids are less complete than for the DU145 spheroids (please see Chapter 2 for details). As a result we were not able to fit the logistic model (3.2) to the PC3 Ctrl data, in particular it was not possible to obtain reliable estimates of the carrying capacity parameter K. Therefore we decided that the exponential model is more appropriate to describe this data as it can be considered a special case of the logistic model in which $K \to \infty$. The exponential model is given by

$$\frac{dV}{dt} = rV \quad \text{with} \quad V(0) = V_0 \tag{3.20}$$

with solution

$$V(t) = V_0 e^{rt}. \tag{3.21}$$

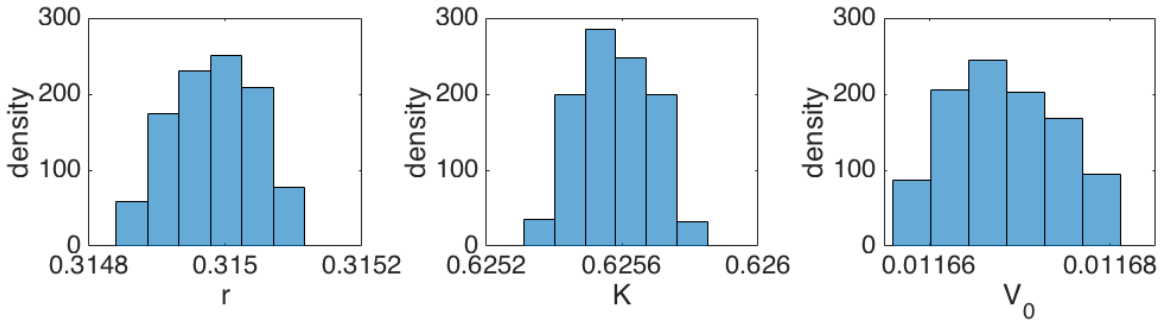

(a) DU145 ctrl

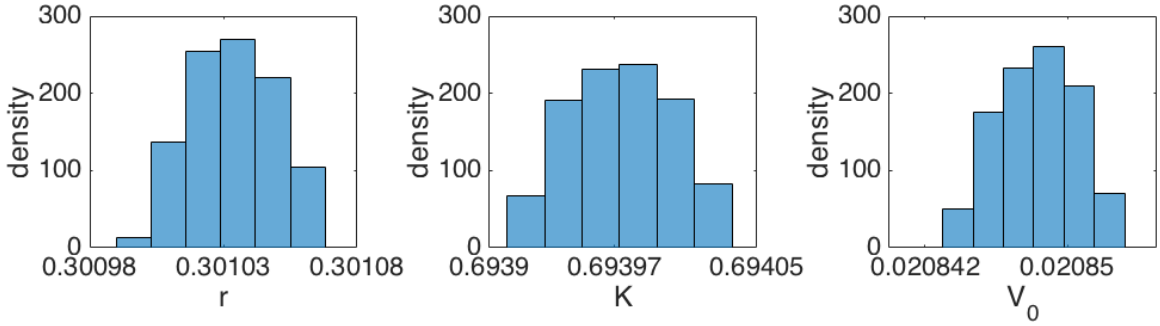

(b) DU145 res

Figure 3.16: The approximate marginal posterior distributions for the DU145 control and resistant homogeneous spheroids.

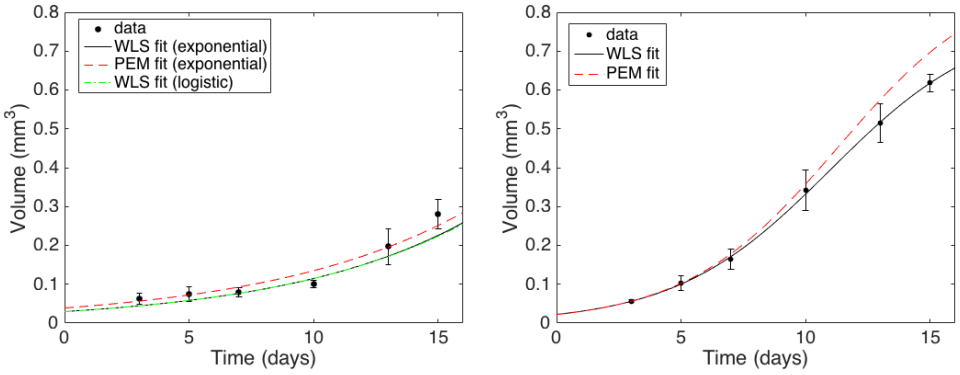

(a) PC3 ctrl **(b)** PC3 res

Figure 3.17: Best fits of the logistic and exponential models to the PC3 control data and the logistic model to the PC3 resistant data. Data shown as mean±1×SD.

We fitted the model (3.20) to the PC3 Ctrl data and the resulting best fit curves are shown in Fig. 3.17a along with the WLS fit to the logistic model, with the corresponding estimated parameter values being reported in Table 3.3. We note that the WLS and PEM methods yield different results when applied to the exponential model. We note also that the estimates of r and V_0 are almost identical for the WLS method

Table 3.3: The best fit parameter values obtained by fitting the exponential and logistic models to the PC3 control data and the logistic model to the PC3 resistant data using the WLS and PEM methods. Note that the logistic model was fitted to the PC3 Ctrl data using only the WLS method.

	r [days^{-1}]	K [mm^3]	V_0 [mm^3]	σ
$\hat{\theta}_{WLS}$ (ctrl, exp)	0.1353	-	0.0297	
$\hat{\theta}_{WLS}$ (ctrl, log)	0.1376	5.0000	0.0296	
$\hat{\theta}_{PEM}$ (ctrl, exp)	0.1243	-	0.0389	0.1835
$\hat{\theta}_{WLS}$ (res, log)	0.3218	0.7873	0.0224	
$\hat{\theta}_{PEM}$ (res, log)	0.3269	0.9052	0.0220	0.0850

applied to the exponential and logistic models. On the other hand, the PC3 Res data could be fit to the logistic model even though a limited number of data points were available. The WLS-best fit curve appears to fit the data with higher accuracy than that obtained with the PEM method (Fig. 3.17b), leading to markedly different estimates for K. Comparing the estimated parameter values between the control and resistant cell lines, it can be seen that resistant spheroids grow almost 3 times faster than the control spheroids (Table 3.3). The estimated noise levels associated with the PC3 Ctrl spheroids measurements are much larger than that associated with the other cell lines ($\hat{\sigma} \approx 0.18$).

The parameter estimates for the PC3 Ctrl data are associated with large uncertainties whereas the parameter values for the PC3 Res data appear to be well estimated (Fig. 3.18). In particular, the width of the asymptotic 95% confidence intervals is markedly different for the two cell lines. However, the approximate posterior distributions suggest that the parameters were estimated with high accuracy (Fig. 3.19).

3.5 Discussion

In this chapter we have developed methodology for parameter estimation and uncertainty quantification for a simple model of tumour growth. We demonstrated the use of two different nonlinear regression-based methods and an approximate Bayesian computation-based method to infer parameter values in a nonlinear model using synthetic and experimental data. We also considered a number of techniques to construct confidence intervals around estimated parameters and presented a framework for assessing the predictive power of a tumour growth model.

As argued in [140], one of the main objectives of mathematical and computational modelling is to describe, explain and predict the outcomes of the processes being mod-

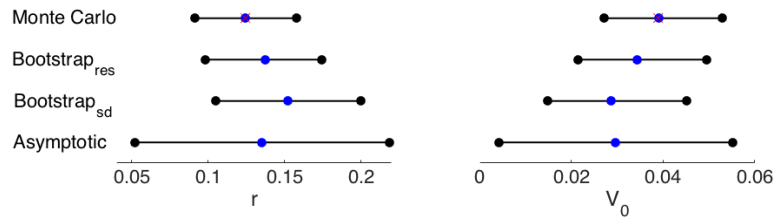

(a) PC3 ctrl

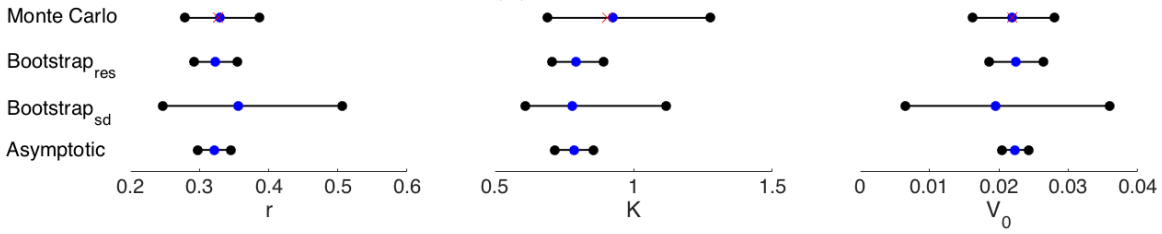

(b) PC3 res

Figure 3.18: 95% confidence intervals for the parameter values estimated from the PC3 control and resistant data fitted to the exponential and logistic models respectively.

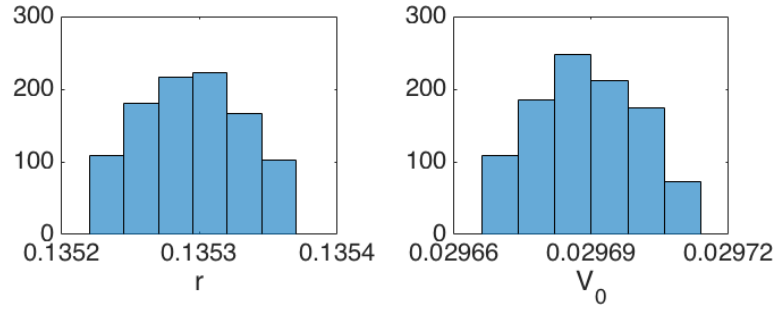

(a) PC3 ctrl

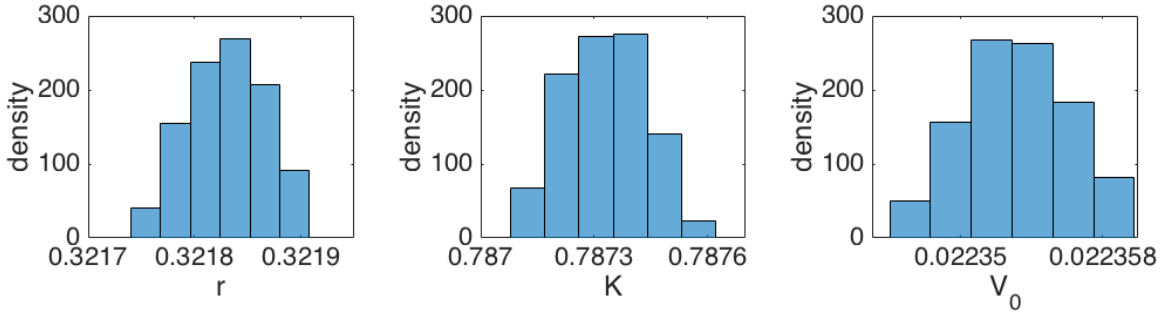

(b) PC3 res

Figure 3.19: The approximate marginal posterior distributions for the PC3 control and resistant data fitted to the exponential and logistic models respectively.

elled. Nowadays, these processes can be of critical importance and include simulations of cancer treatment among other phenomena. In order to consider mathematical and computational models as predictive tools in cancer research and treatment we must be able to accurately estimate parameter values in such models, or at least quantify

uncertainties in them and the resulting predictions of quantities of interest, such as a patient's response to radiation.

Since the asymptotic confidence intervals, the most commonly used method to quantify uncertainty in estimated parameters, are based on a number of simplifications they are only approximately correct and always symmetric which may lead to unrealistic ranges. Therefore, we compared the asymptotic CIs to other methods for uncertainty quantification such as Monte Carlo simulations and bootstrapping. The asymptotic CIs were previously compared to CIs constructed by Monte Carlo simulations to investigate the performance of different optimal experimental design criteria [16]. The two methods were found to provide consistent results. Uncertainty quantification using the asymptotic theory was also examined in contrast to bootstrapping [96, 15] and the latter method was found to provide a useful tool for construction of CIs.

In this work, we provided a more complete comparison of the asymptotic, Monte Carlo and bootstrap methods applied to the same problem, than the previously reported work. In addition, we considered two different bootstrap techniques, one based on sampling from a distribution [96] and one based on sampling with replacement from a set of residuals [15]. The former was found to provide results inconsistent with the other methods and therefore we refrain from using it in our future analyses. The asymptotic and bootstrap_res methods emerged as two most accurate techniques for uncertainty quantification as the MC methods often yielded CIs which were unnecessarily generous. The asymptotic method is always computationally faster than bootstrapping but has some limitations, as discussed earlier. We recommend using both the asymptotic and bootstrap_res methods if possible as they are both distinctive techniques and their accuracy depends on models and available data.

In addition to estimating parameters using nonlinear regression we also performed Bayesian inference using an ABC algorithm. We found little value in doing so for the logistic model in this case; the ABC method was computationally demanding and led to the same parameter estimates as the WLS method which is readily explained by the fact that we used as the distance function the weighted sum of squared residuals (3.5). Although other authors used similar distance functions in their work (e.g., [194]), we note that a statistical model such as that given by Eq. (3.4) should be used instead to account for uncertainty associated with measurement errors. Thus we recommend that the ABC inference should be repeated in the future. For a comprehensive tutorial on Bayesian inference in tumour growth models we refer the reader to [47].

The results of the predictive power analysis of the logistic model need to be interpreted with caution. Although the faster growing spheroids could be predicted with higher accuracy these results are not generalisable and the analysis should be repeated for multiple datasets before meaningful conclusions can be drawn.

Finally, we note that the proportional error assumption adopted in this work needs to be validated. The error model can have a significant impact on the analysis of descriptive and predictive capabilities of mathematical models. Benzekry et al. [20] used statistical analysis to determine an appropriate error model in their study. They found that the proportional error model was correct if the tumour volume was above some threshold value. Below this value, a constant error model was used.

Chapter 4

Mathematical modelling of biological interactions in heterogeneous tumour spheroids

4.1 Introduction

In this chapter we aim to establish if two cell populations with different radiation sensitivities interact with each other when co-cultured to form heterogeneous tumour spheroids. Our objective is to determine the nature of these interactions and whether they change following exposure to a single dose of radiation. We use a Lotka-Volterra-type model consisting of two coupled nonlinear ODEs describing growth kinetics between two cell populations. ODEs have been used previously to model the growth of heterogeneous tumours. Michelson et al. [123] presented and analysed three nested models of two cell populations restricted by logistic growth. The first model assumed no interactions between the populations, the second model introduced a competitive interaction term, and the third model added another term allowing one population to emerge from the other. Steady state analysis revealed that all three models lead to different dynamics. Michelson and Leith later used the models to demonstrate that the competitive advantage predicted by the models changes following radiation injury to the stroma in which the heterogeneous tumours grow [121], and to study the response of tumours to chemotherapy treatment [122]. ODE-based models were also used to study drug response of heterogeneous tumours consisting of cells with different sensitivities to the drug [143] and to explore the impact of natural selection on cancer development [135].

The models described above focused on competitive interactions between cell populations. Although cells compete for limited resources they can also interact in other

direct and/or indirect ways. Our model allows us to describe most biological interactions observed in ecology. In what follows, we first introduce and analyse a Lotka-Volterra model which we use to model the growth of heterogeneous tumour spheroids. We show that it is not possible to infer the values of the interaction parameters using measurements of spheroid volume alone. We proceed to determine what additional data are needed to determine the parameter values by considering synthetic data. We investigate whether fixing the kinetic parameters for each subpopulation leads to more accurate estimates of the interaction terms as compared to pooling the data together. Finally, we compare the values of the interaction parameters in the Lotka-Volterra model, for irradiated and non-irradiated PC3 and DU145 spheroids.

4.2 Mathematical model for heterogeneous avascular tumour growth

The growth and interactions between the control and resistant cell populations, that are co-cultured to form heterogeneous spheroids, are modelled as a Lotka-Volterra system whose evolution can be described by the following system of ordinary differential equations:

$$\begin{aligned} \frac{dV_C}{dt} &= r_C V_C \left(1 - \frac{V_C}{K_C} - \lambda_R \frac{V_R}{K_C}\right), \\ \frac{dV_R}{dt} &= r_R V_R \left(1 - \frac{V_R}{K_R} - \lambda_C \frac{V_C}{K_R}\right). \end{aligned} \tag{4.1}$$

In Eqs. (4.1), the dependent variables $V_C(t)$ and $V_R(t)$ represent the volumes of the control and resistant cell populations, respectively. The positive parameters r_C and r_R are the intrinsic growth rates, and thus the terms $r_C V_C$ and $r_R V_R$ represent the Malthusian growth of each population of cells. The quadratic terms, $r_C V_C^2/K_C$ and $r_R V_R^2/K_R$, describe *intraspecific* competition between cells where the positive parameters K_C and K_R are the carrying capacities of the control and resistant cell populations, respectively. The parameters λ_C and λ_R respectively measure the effect that the control cells have on the resistant cells, and the resistant cells have on the control cells. Thus the terms $r_C \lambda_R V_C V_R/K_C$ and $r_r \lambda_C V_C V_R/K_R$ describe *interspecific* competition between the two populations. In the absence of prior knowledge of the nature of interactions between the two cell populations, we do not restrict λ_C and λ_R to be positive or negative. Thus depending on the signs of λ_C and λ_R we can distinguish six types of interactions: these are summarised in Table 4.1. Clearly,

Table 4.1: Potential interactions between tumour cell populations. The table provides a summary of biological effects that the control and resistant cell populations can have on each other together with corresponding signs of the parameters λ_C and λ_R in Eqs. (4.1).

Effect control cells have on resistant cells	**Effect resistant cells have on control cells**	**Sign of λ_C**	**Sign of λ_R**	**Type of interaction**
Detrimental	Detrimental	+	+	***Competition***
Detrimental	No effect	+	0	***Amensalism***
Detrimental	Beneficial	+	-	***Antagonism***
No effect	No effect	0	0	***Neutralism***
No effect	Beneficial	0	-	***Commensalism***
Beneficial	Beneficial	-	-	***Mutualism***

if $\lambda_C = \lambda_R = 0$, Eqs. (4.1) reduce to two uncoupled logistic equations similar to Eq. (3.2). In order to arrive at a well defined initial value problem the system (4.1) must be supplemented by appropriate initial conditions: $V_C(t = 0) = V_C(0)$ and $V_R(t = 0) = V_R(0)$. Eqs. (4.1) have four equilibrium points, including one in which the two populations coexist (please see Sec. B.1 for more details).

In the case of a homogeneous spheroid, the growth of which is modelled with Eq. (3.2), there is an obvious physical interpretation of the carrying capacity parameter K—it is the maximum size of the spheroid supported by its environment. In the case of a heterogeneous spheroid, such as that modelled with Eqs. (4.1), it is not possible to capture the spheroid's saturation size in a single parameter or even expression. Various interactions existing between co-cultured cell populations manifest themselves in a multitude of possible growth regimes. Nonetheless, our intuition dictates that we can consider some obvious cases. Let us first denote the carrying capacity of a heterogeneous spheroid, when it exists, by K_T. Then if $\lambda_C = \lambda_R = 0$ then $K_T = K_C + K_R$. In the case of competition, when $\lambda_C > 0$ and $\lambda_R > 0$, we would expect $K_T < K_C + K_R$. Similarly, when the populations support each other, that is when $\lambda_C < 0$ and $\lambda_R < 0$ (mutualism), we would expect to observe $K_T > K_C + K_R$.

There is a close relationship between the carrying capacity parameter K in the logistic equation (3.2) and its equilibrium solution—K is the equation's steady state. Similarly, equilibrium solutions of Eqs. (4.1) can be thought of as saturation sizes of heterogeneous spheroids. After all, we are interested in what happens to $V_C + V_R$ as $t \to \infty$. As shown in Appendix B.1, Eqs. (4.1) have four steady states. Three of them are trivial—if either population is absent then K_T will be equal to the carrying capacity of the present population. Clearly, if $V_C = V_R = 0$ then $K_T = 0$. The fourth, non-trivial steady state given by Eqs. (B.3) exists and is biologically relevant for different groupings of λ_C, K_C and K_R, and λ_R, K_C and K_R (see Eqs. (B.1)).

Various cases are captured in Fig. B.1. In terms of the carrying capacities of the control and resistant populations, for this non-trivial steady state we have

$$V_C + V_R = \frac{K_C(1-\lambda_C) + K_R(1-\lambda_R)}{1-\lambda_C\lambda_R}. \tag{4.2}$$

In some situations, it will be more convenient to rewrite Eqs. (4.1) as

$$\begin{aligned} \frac{dV_C}{dt} &= V_C\left[r_C\left(1-\frac{V_C}{K_C}\right) - \eta_R V_R\right], \\ \frac{dV_R}{dt} &= V_R\left[r_R\left(1-\frac{V_R}{K_R}\right) - \eta_C V_C\right], \end{aligned} \tag{4.3}$$

where we have redefined the interaction coefficients as $\eta_R \equiv r_C\lambda_R/K_C$ and $\eta_C \equiv r_R\lambda_C/K_R$. By doing so we eliminate the dependence of the interaction parameters on the growth rate and carrying capacity parameters which makes it easier to interpret the inference results.

4.3 Case study: experimental design I

4.3.1 Introduction

We have previously collected volume measurements of heterogeneous spheroids which were seeded with different initial proportions of control and resistant cells (Chapter 2). In this section, we conduct a parameter recovery study to gain understanding of the extent to which we can determine the type and strength of interactions between the cell populations, by using only the data representing total spheroid volume. To this end, we combine Eqs. (4.1) with a statistical model describing measurement error to generate noisy synthetic data representing the growth of heterogeneous spheroids and then re-estimate the values of the interaction parameters by minimising the sum of weighted squared residuals.

4.3.2 Methods

4.3.2.1 Synthetic data

We generated synthetic spheroids composed of hypothetical cell lines with growth kinetics similar to those of the PC3 Ctrl, PC3 Res, DU145 Ctrl and DU145 Res cells examined in Chapter 3. In particular, we used Eqs. (4.1) to generate *in silico* heterogeneous spheroids that were seeded at the ratio 1:1. The synthetic cell lines were assigned the values shown in Table 4.2. Please note that asterisks denote parameter

values used to generate synthetic data. The values of the interaction coefficients selected for this study are shown in Table 4.3 and the corresponding growth curves are presented in Fig. 4.1.

Since we only measured the total volume of the heterogeneous spheroids, as opposed to the volumes of the control and resistant cell populations, we extracted similar data from the *in silico* experiments. Accordingly, after solving Eqs. (4.1), we recorded $V(t) = V_C(t) + V_R(t)$ at discrete time points, corresponding to those at which the experimental data were collected. Therefore, $V(t_i)$ were recorded at $t_i = (3, 5, 7, 10, 13, 15)$ for the synthetic PC3 spheroids, and at $t_i = (3, 5, 7, 9, 11, 13, 16, 18, 20, 23, 25, 27, 30)$ for the synthetic DU145 spheroids.

Table 4.2: Parameter values assigned to the hypothetical cell lines used to generate synthetic data.

	r_C^* (day^{-1})	K_C^* (mm^3)	$V_C^*(0)$ (mm^3)	r_R^* (day^{-1})	K_R^* (mm^3)	$V_R^*(0)$ (mm^3)
PC3	0.22	0.48	0.03	0.48	0.67	0.01
DU145	0.32	0.62	0.015	0.30	0.70	0.02

Table 4.3: Values of the interaction parameters λ_C and λ_R used to generate synthetic data.

λ_C^*	0.5	0.5	1.2	1.2
λ_R^*	0.5	1.2	0.5	-0.5

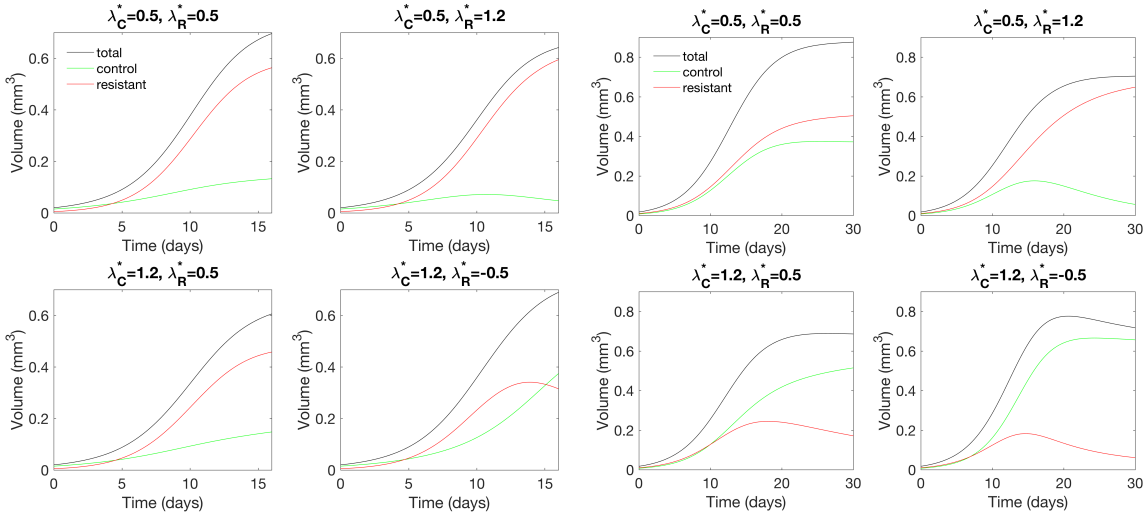

(a) Synthetic PC3 growth curves **(b)** Synthetic DU145 growth curves

Figure 4.1: Synthetic growth curves resulting from solving the Lotka-Volterra model (4.1) with the parameter values as in Tables 4.2 and 4.3.

4.3.2.2 Statistical noise model

In addition to studying the effect of different values of the interaction parameters, we considered the effect of different noise levels in the data on our ability to recover λ_C and λ_R. In line with our assumption that the measurement error is proportional to the spheroid volume, we generated noisy synthetic data using a statistical model given by

$$V_i^{data} = V^{model}(t_i;\theta^*) + \epsilon_i V^{model}(t_i;\theta^*) \tag{4.4}$$

where $\epsilon_i \sim \mathcal{N}(0,\sigma^2)$ and $i = 1,\ldots,N$ where N is the number measurements. In Eq. (4.4), V_i^{data} represent the total volume measurements of a synthetic spheroid at t_i, and $V^{model}(t_i;\theta^*) = V_C^{model}(t_i;\theta^*) + V_R^{model}(t_i;\theta^*)$, where $V_C^{model}(t_i;\theta^*)$ and $V_R^{model}(t_i;\theta^*)$ are the solutions of Eqs. (4.1) at t_i for a given $\theta^* = (\lambda_C^*, \lambda_R^*)$. To account for different levels of noise in the synthetic data the simulations were repeated three times for standard deviation $\sigma^* = 0.05, 0.1$ and 0.2.

4.3.2.3 Parameter estimation

The kinetic parameters in Eqs. (4.1) were fixed at the values stated in Table 4.2. Once the noisy synthetic data were generated, the values of λ_C and λ_R were forgotten and re-estimated. We estimated the parameter values by minimising the weighted sum of squared residuals. In more detail, we sought to identify $\hat{\theta} = (\hat{\lambda}_C, \hat{\lambda}_R)$ minimising the expression

$$\sum_{i=1}^{N} w_i^{-2}(V_i^{data} - V^{model}(t_i;\hat{\theta}))^2, \tag{4.5}$$

where $w_i = V^{model}(t_i;\hat{\theta})$. We use "hats" over parameters to distinguish between the values used to generate data and the estimated values. To find $\hat{\lambda}_C$ and $\hat{\lambda}_R$ we employed MATLAB's *MultiStart* function with *lsqnonlin* (trust-region-reflective algorithm) as the local solver. The asymptotic 95% confidence intervals for $\hat{\lambda}_C$ and $\hat{\lambda}_R$ were calculated, as described in Chapter 3, using *nlparci* function. When performing nonlinear regression, the bounds imposed on the estimated values of λ_C and λ_R were set to $LB = -5$ and $UB = 5$ where LB and UB denote the lower and upper bounds respectively.

4.3.3 Results

We generated 100 noisy (5%, 10% and 20% noise) synthetic datasets for each pair of interaction parameters (Table 4.3) for both PC3 and DU145 cell lines (Table 4.2), re-estimated the interaction parameters in each case and computed the 95% asymptotic

CIs for the estimates. In Fig. 4.2 we show the estimated values for the PC3 heterogeneous 1:1 (control:resistant) spheroids generated with $\lambda_C^* = 0.5$ and $\lambda_R^* = 0.5$. The accuracy of the estimated parameters clearly decreases as the noise level in the data increases. The estimates of λ_C appear to be more accurate than those of λ_R and the 95% CIs of the former are narrower than those of the latter. However, even for low noise levels, the values of λ_C and λ_R are very inaccurate with high degrees of uncertainty as measured by the CIs. Almost identical results were observed for the other pairs of λ_C and λ_R (not shown).

Fig. 4.3 shows corresponding results for the DU145 spheroids obtained with ($\lambda_C^* = 0.5, \lambda_R^* = 1.2$) (Fig. 4.3a) and ($\lambda_C^* = 1.2, \lambda_R^* = -0.5$) (Fig. 4.3b) pairs. As before, the accuracy decreases and CIs become wider as the noise levels are increased. However, our ability to recover λ_C and λ_R clearly depends on their values used to generated the data. For the ($\lambda_C^* = 0.5, \lambda_R^* = 1.2$) pair, the estimates are unreliable with large uncertainties even for the 5% noise level. On the other hand, the estimates are highly accurate for the ($\lambda_C^* = 1.2, \lambda_R^* = -0.5$) pair even when the noise in data is 10% but this accuracy decreases significantly for the 20% noise. For the other values of λ_C and λ_R the estimates were similar to those presented in Fig. 4.3a suggesting that antagonistic interactions are easier to detect than the competitive ones with the given

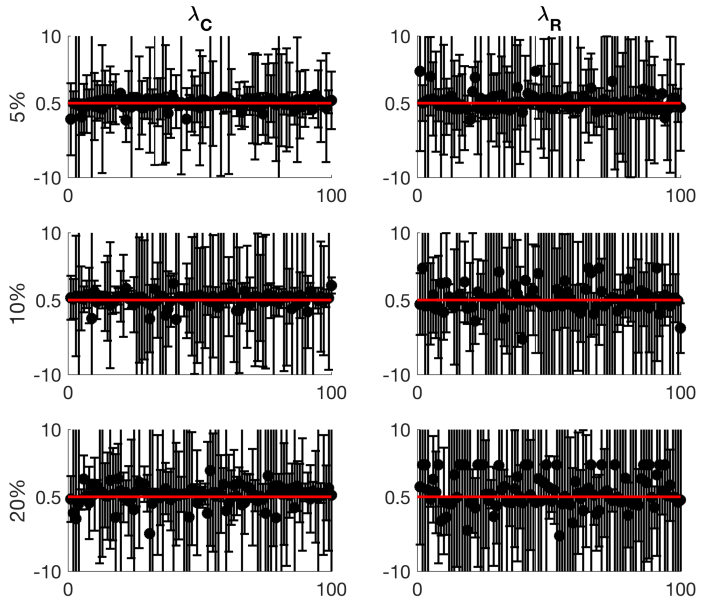

Figure 4.2: Estimated values of the interaction parameters for the synthetic PC3 spheroids data. Circles show point estimates and error bars corresponding 95% CIs of the interaction parameters resulting from fitting the Lotka-Volterra model to 100 noisy synthetic PC3 datasets with different noise levels (5%, 10% and 20%). Red lines show the values used to generate the data: $\lambda_C^* = 0.5$ and $\lambda_R^* = 0.5$, other values as in Table 4.2.

data.

These results indicate that spheroid volume data are not sufficient to reliably estimate the interaction parameters and that we require more information about the spheroid growth. In the next section, we determine if collecting data on the proportions of control and resistant cells is sufficient to estimate λ_C and λ_R more accurately and when these data should be collected to maximise information content.

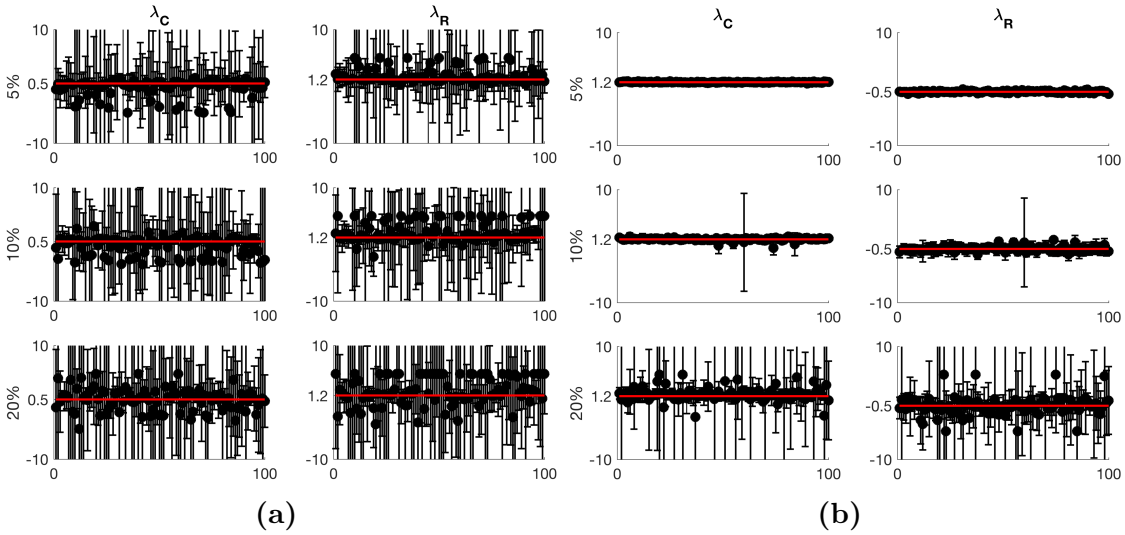

Figure 4.3: Estimated values of the interaction parameters for the synthetic DU145 spheroids data. Circles show point estimates and error bars corresponding 95% CIs of the interaction parameters resulting from fitting the Lotka-Volterra model to 100 noisy synthetic DU145 datasets with different noise levels (5%, 10% and 20%). Red lines show the values used to generate the data: $\lambda_C^* = 0.5$ and $\lambda_R^* = 1.2$ (a), $\lambda_C^* = 1.2$ and $\lambda_R^* = -0.5$ (b), other values as in Table 4.2.

4.4 Case study: experimental design II

4.4.1 Introduction

In the previous section, we showed that the total volume measurements of heterogeneous spheroids were not sufficient to reliably infer the values of the interaction parameters in the Lotka-Volterra model (4.1). As described in Chapter 2, it is possible to estimate the proportions of the control and resistant cells in heterogeneous spheroids by dissociating the spheroids and sorting the fluorescently-labelled cells. If we know the proportions of the control and resistant cells and the spheroid volume at a given time point then we can estimate the respective volumes of the control and resistant cell populations. Since collecting data on the proportions of the two cell

populations is costly and time-consuming, we aim to minimise the burden associated with conducting the experiment whilst insisting on collecting enough data to reliably estimate λ_C and λ_R for both cell lines. With this in mind, we conduct an experimental design study to determine at what time points we should collect the proportions data.

4.4.2 Methods

We used Eqs. (4.1) to generate synthetic data as before, supplementing data on total spheroid volumes at times $t_i (i = 1, 2, \ldots, N_{tot})$ with additional proportions data at times $t_j (j = 1, 2, \ldots, N_{props})$. The combinations of time points at which the proportions data were recorded (henceforth referred to as *cases*) are shown in Table 4.4. We then used the proportions and total volume data to estimate respective

Table 4.4: Cases used for the experimental design study. The second and third columns indicate the days on which the proportions data were collected for the PC3 and DU145 synthetic spheroids, respectively.

Case #	PC3	DU145
1	3	3
2	5	5
3	7	7
4	10	9
5	13	11
6	15	13
7	3,5,7	16
8	5,10	18
9	5,15	20
10	7,10	23
11	7,13	25
12	10,15	27
13	5,10,15	30
14	10,13	3,5,7
15	13,15	9,11,13
16	3,5,7,10,13,15	16,18,20
17		13,16
18		16,20
19		16,25
20		3,5,7,9,11,13,16,18,20,23,25,27,30

volumes of the control and resistant cell populations at times t_j and amended the minimisation function accordingly.

4.4.3 Results

In Fig. 4.4 we summarise the study results for the datasets generated with $\lambda_C^* = 0.5$ and $\lambda_R^* = 0.5$. The results for other combinations of λ_C and λ_R are very similar for both cell lines so we refrain from discussing them here. Fig. 4.4 shows that increasing the noise levels leads to less accurate estimates of the interaction parameters and greater variation in the estimated values for both cell lines. There is a clear tendency to overestimate both parameters as noise levels increase. In general, data on the proportions of control and resistant cells collected at later time points lead to more

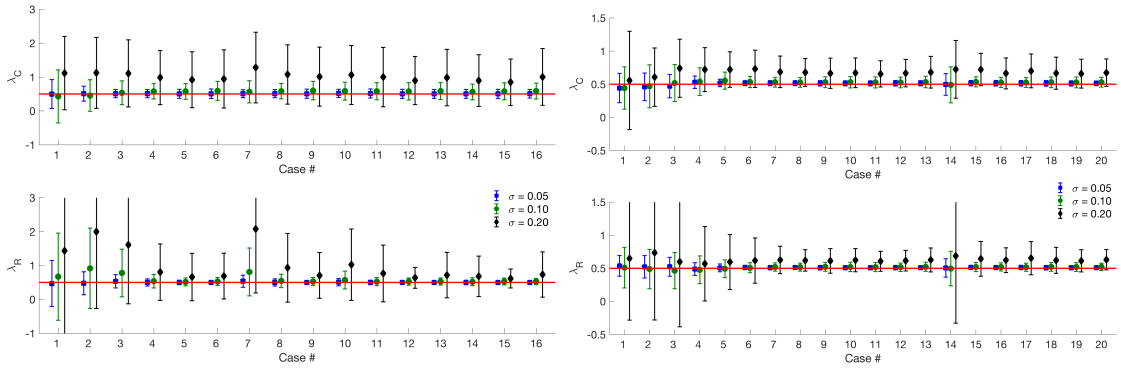

(a) PC3 **(b)** DU145

Figure 4.4: Point estimates of the interaction parameters. Data show means±1×SD of the point estimates of the interaction parameters obtained by fitting the Lotka-Volterra model to 100 PC3 (a) and DU145 (b) synthetic datasets using different cases. The markers are colour-coded based on the noise level present in the data: 5% (blue squares), 10% (green circles) and 20% (black diamonds). Red lines show the parameter values used to generate the data ($\lambda_C^* = 0.5$ and $\lambda_R^* = 0.5$ for both cell lines).

accurate parameter estimates and less variation. In particular, collecting these data on days 3, 5 or 7 (cases 1, 2 and 3 respectively) leads to large variations even when the noise is 5%. Moreover, collecting the proportions data on days 3, 5 *and* 7 (cases 7 and 14 for PC3 and DU145 respectively) leads to worse estimates than collecting only one data point after this initial growth period. Overall, it seems that the proportions data recorded from day 10 (case 4) for the PC3 spheroids and day 16 (case 7) for the DU145 spheroids generate estimates of λ_C and λ_R that have comparable accuracy to those obtained with the best case scenarios that correspond to collecting the data on the same days as spheroid volumes (cases 16 and 20 for the PC3 and DU145 respectively). Together, these results indicate that collecting the additional data on later time points is more important than choosing particular days. This conclusion is not affected for either cell line if the number of noisy synthetic datasets is increased from 100 to 1000 (data not shown). Based on this study, we chose to collect the proportions data on days 10 and 15 (case 12) in the PC3 spheroids, and days 16 and 25 in the DU145 spheroids (case 19). We found that these choices provide an acceptable balance between the burden associated with conducting the experiment and accuracy of the estimated parameters.

To determine how our choices of days on which to collect the proportions data affect the uncertainties in the estimated parameters, we provide representative plots showing individual point estimates with the corresponding 95% CIs for both cell lines in Fig. 4.5. As expected, the CIs become wider as we increase the noise but the

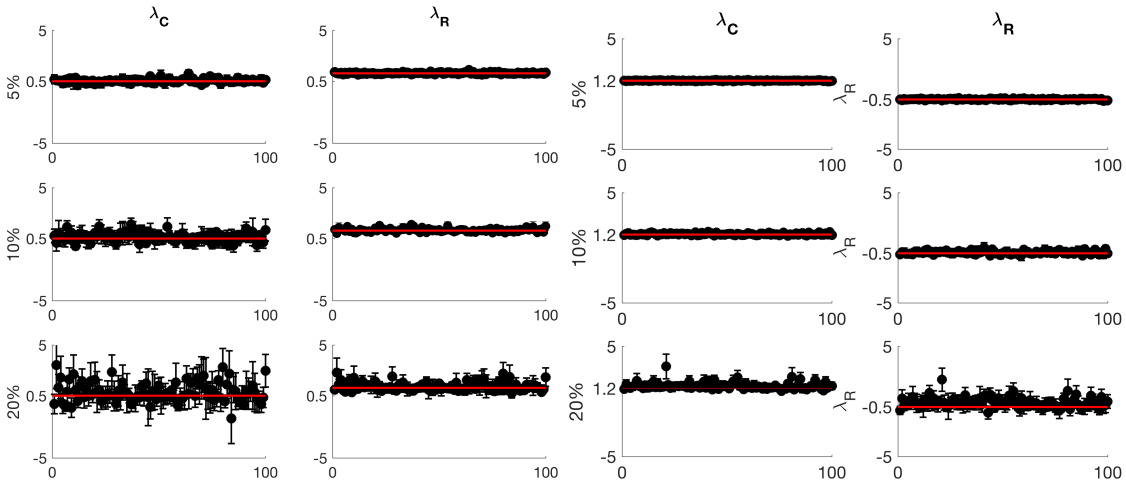

(a) PC3 **(b)** DU145

Figure 4.5: Estimates and 95% CIs of λ_C and λ_R obtained by fitting the Lotka-Volterra model to 100 noisy PC3 and DU145 synthetic datasets using cases 12 (proportions data recorded on days 10 and 15) and 19 (proportions data recorded on days 16 and 25), respectively. Red lines show parameter values used to generated the data: $\lambda_C^* = 0.5$, $\lambda_R^* = 0.5$ for PC3 and $\lambda_C^* = 1.2$, $\lambda_R^* = -0.5$ for DU145 spheroids.

estimates are generally consistent and highly accurate. The estimates of λ_C for the PC3 data and λ_R for the DU145 data with 20% noise are less precise than in other cases and some of them appear to have a different sign to the sign of the underlying parameter value used to generate the data. We found an interesting correlation between the level of uncertainty associated with the estimates of interaction parameters and the proportion of control and resistant cells: if the volume of the resistant population ($V_R(t)$) is higher than the volume of the control population ($V_C(t)$) then we can estimate the effect that the resistant cells have on the control cells (λ_R) with higher accuracy than the effect of the control cells on the resistant population (λ_C). The opposite is also true. To illustrate this point, let us consider Figs. 4.1 and 4.5. When $\lambda_C = 0.5$ and $\lambda_R = 0.5$ the volume of the PC3 resistant population is higher than the volume of the PC3 control population (Fig. 4.1a). The estimates of λ_R are more precise than those of λ_C in this case (Fig. 4.5a). Conversely, for $\lambda_C^* = 1.2$ and $\lambda_R^* = -0.5$ the control population is dominant in the DU145 spheroids (Fig. 4.1b) and the estimates of λ_C are more accurate (Fig. 4.5b). We found similar correlations for other combinations of the interaction parameters.

4.5 Case study: fitting protocols

4.5.1 Introduction

In Section 4.4 we conducted a case study to determine at what time points we should collect the data on the proportions of the control and resistant cell populations. Since our main objective was to estimate the values of λ_C and λ_R in Eqs. (4.1), we assumed that the values of the other model parameters were known. In this section we investigate three alternative ways of estimating all model parameters.

4.5.2 Methods

4.5.2.1 Synthetic data

The synthetic data were generated as described in Section 4.4.2. In addition to the total volume of spheroids $V(t_i)$, we assumed the volumes of the control and resistant cell populations $V_C(t_j)$ and $V_R(t_j)$ to be known on days 10 and 15 for the PC3 spheroids, and on days 16 and 25 for the DU145 spheroids. In this case study, our *in silico* spheroids were seeded at the ratios 1:0, 3:1, 1:1, 1:3 and 0:1. To generate the data we used the parameter values stated in Table 4.2, and fixed $\lambda_C^* = 1.2$ and $\lambda_R^* = 0.5$. After noise was added to the dataset, we forgot all parameter values and proceeded to re-estimate them by minimising the weighted sum of squared residuals (as described previously) following the fitting protocols presented below.

4.5.2.2 Two-step fitting protocol

The main assumption of the two-step protocol is that the growth kinetics parameters, r_k, K_k and $V_k(0)$ where k denotes either PC3 Ctrl, PC3 Res, DU145 Ctrl or DU145 Res, are intrinsic to the given cell line, and do not change even if the cell populations are co-cultured. This allows us to estimate their values using volume measurements of homogeneous spheroids data. Additionally, we assume that λ_C and λ_R depend on the initial proportions of the control and resistant cells. In other words, we assume that the type of interactions between two cell populations is conditioned on the initial make up of the spheroid.

Under these assumptions, the two-step fitting protocol proceeds as follows:

(1) Estimate the values of r_C, K_C and $V_C(0)$ using the logistic model (3.2) and the volume measurements data of the homogeneous control 1:0 spheroids.

(2) Estimate the values of r_R, K_R and $V_R(0)$ using the logistic model (3.2) and the volume measurements data of the homogeneous resistant 0:1 spheroids.

(3) Fix r_C, K_C, $V_C(0)$, r_R, K_R and $V_R(0)$ in the Lotka-Volterra model (4.1) to the values obtained in steps 1 and 2.

(4) Estimate the values of $\lambda_C^{3:1}$ and $\lambda_R^{3:1}$ in the Lotka-Volterra model (4.1) using the volume measurements and proportions of the control and resistant cell populations data for the heterogeneous 3:1 spheroids.

(5) Repeat step 4 to estimate $(\lambda_C^{1:1}, \lambda_R^{1:1})$ and $(\lambda_C^{1:3}, \lambda_R^{1:3})$ using the corresponding data.

We emphasise here that the parameter $V_k(0)$ is understood to describe the initial volume of a spheroid consisting of 1000 cells of type k. This assumption allows us to prescribe the initial conditions when solving Eqs. (4.1), as a pair $(\gamma V_C(0), (1-\gamma)V_R(0))$, where γ is the initial proportion of the control cell population in the spheroid. $V_k(0)$ represents the volume of a homogeneous spheroid containing 1000 cells.

4.5.2.3 Two-step fitting protocol with data on proportions pooled

This protocol is similar to that described above. The kinetic parameters are estimated separately for both cell lines using data from homogeneous spheroids, and held fixed in Eqs. (4.1). In the second step, the data from heterogeneous 3:1, 1:1 and 1:3 spheroids are pooled and only one pair of (λ_C, λ_R) estimates is found. The assumption underlying this protocol is that the interactions coefficient are independent of the initial composition of the spheroid.

4.5.2.4 Pooled data fitting protocol

This fitting protocol was designed to find the values of the parameters in Eqs. (4.1) that minimised the weighted sum of squared residuals across all five datasets.

4.5.3 Results

4.5.3.1 Intrinsic parameters

Fig. 4.6 shows the best point estimates with the corresponding 95% CIs of the parameters r_C, K_C, $V_C(0)$, r_R, K_R and $V_R(0)$ obtained using the two-step and pooled fitting protocols for the synthetic PC3 and DU145 spheroids data with 10% noise (the corresponding results for 5% and 20% noise are presented in Appendix: see Figs. B.2 and B.3). To make the comparison of the estimated parameters easier for all three fitting protocols we also computed the means and standard deviations of the estimates

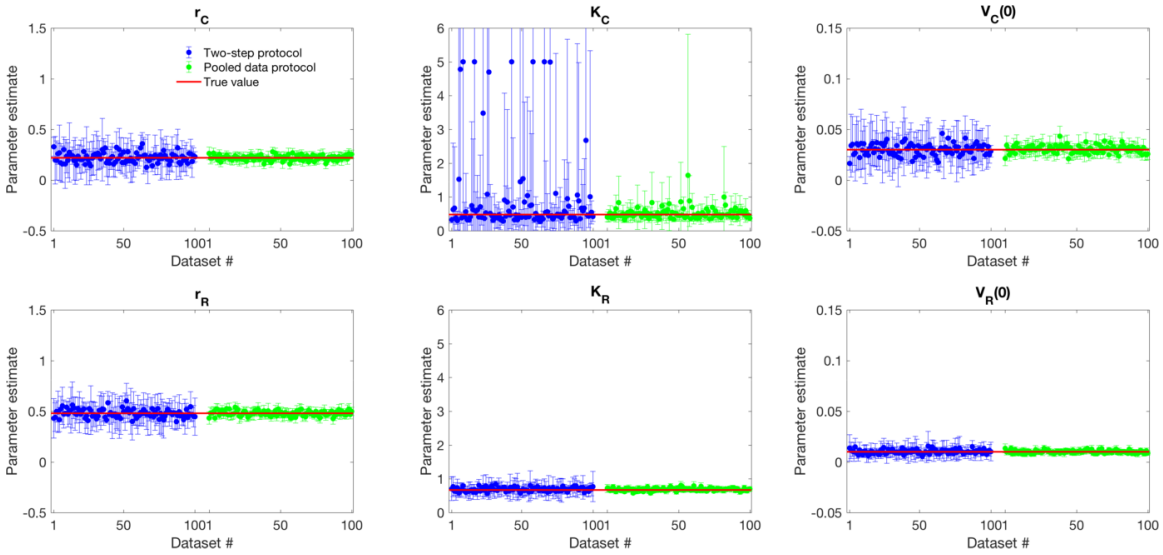

(a) PC3: 10% noise.

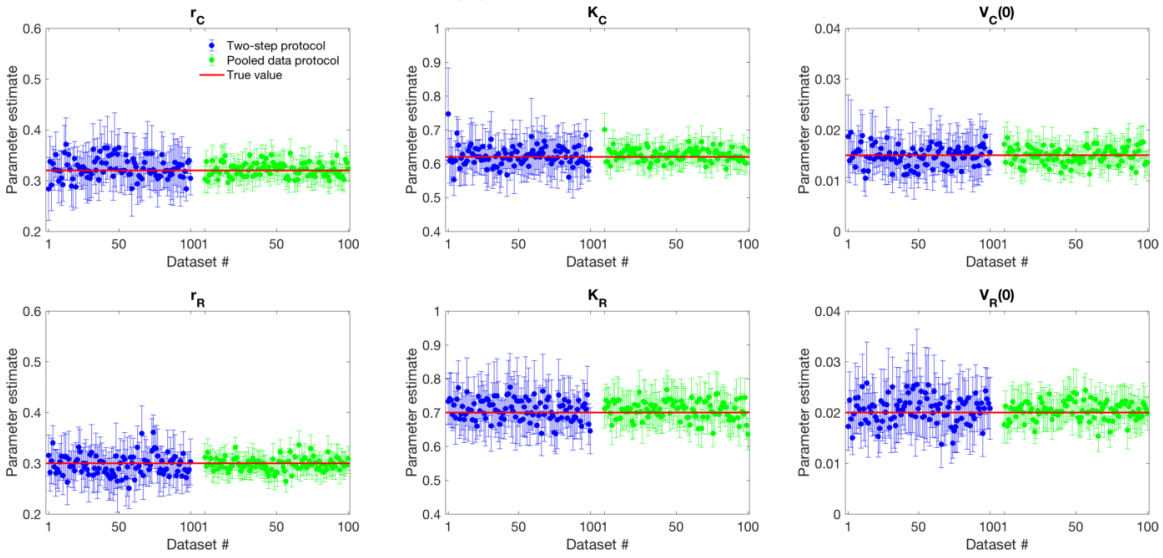

(b) DU145: 10% noise.

Figure 4.6: Estimated values of the parameters r_C, K_C, $V_C(0)$, r_R, K_R and $V_R(0)$ with 95% CIs for the synthetic PC3 (a) and DU145 (b) spheroids data with 10% noise. Blue circles show the values estimated using the two-step protocol. Green circles show the values estimated using the pooled data protocol. Red lines correspond to the "true" values used to generate the data.

(Figs. 4.7a, B.4 for PC3 and Figs. 4.7b, B.5 for DU145 data). These figures show that increasing noise levels typically leads to less accurate estimates, larger CIs and larger variation in the estimated values. The parameters also tend to be overestimated. When the noise is 5%, the estimates of r, K and $V(0)$ are very accurate with low variation and narrow confidence intervals. The only exception is the parameter K for the PC3 control spheroids for which some two-step protocol estimates are markedly

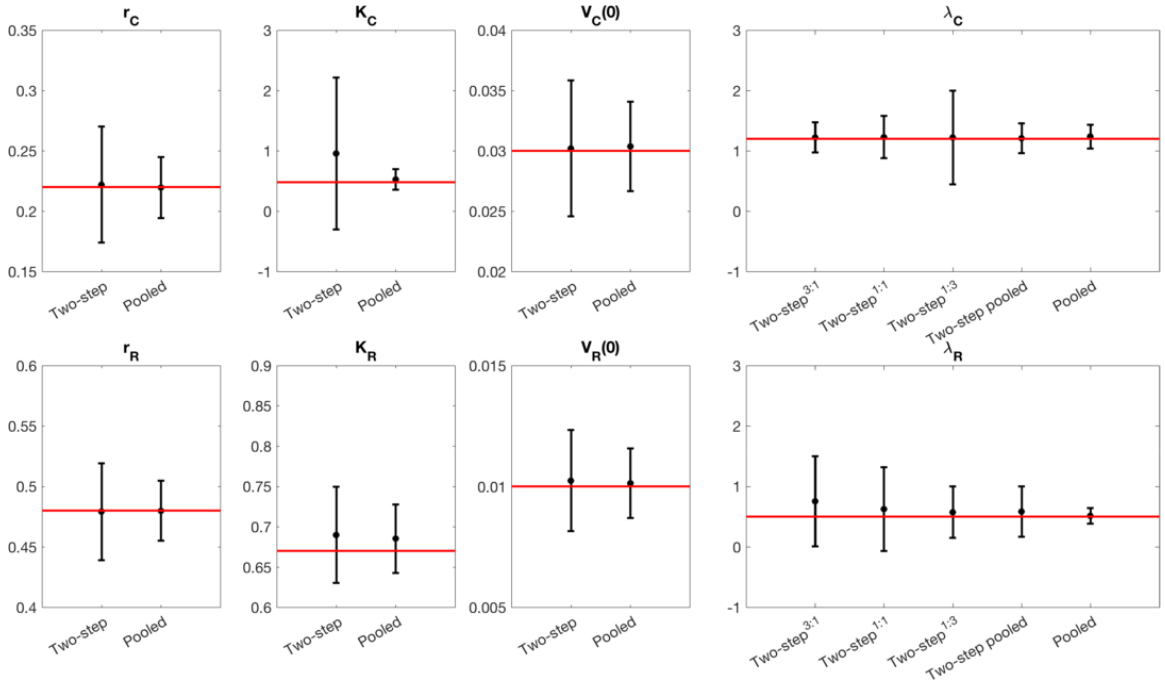

(a) PC3: 10% noise

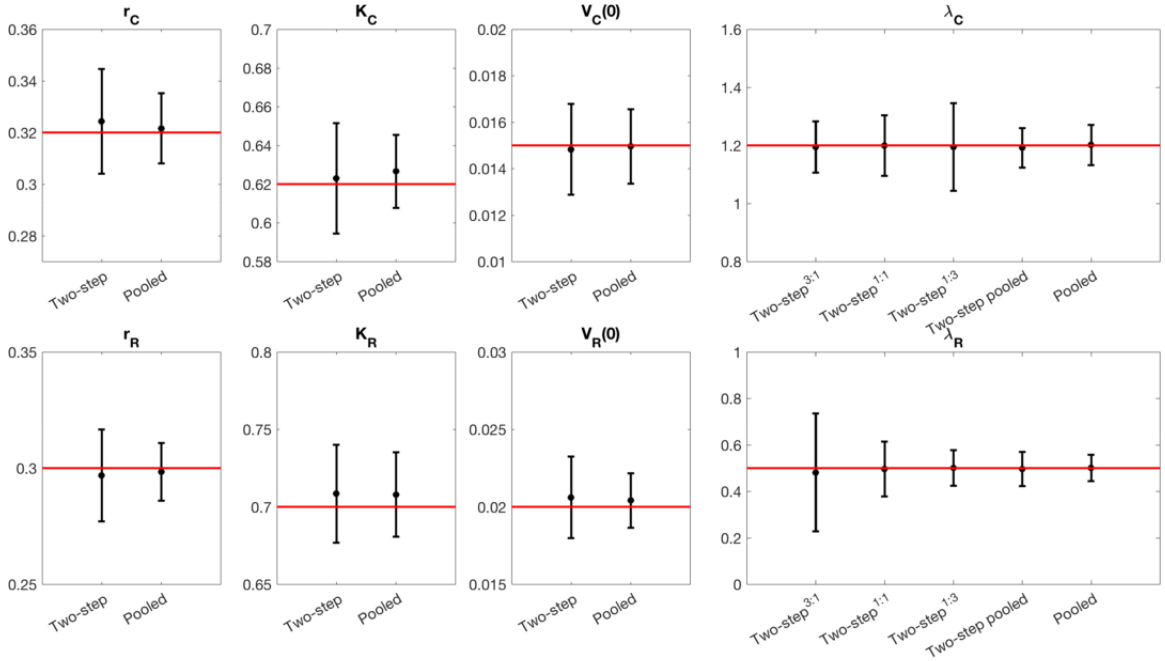

(b) DU145: 10% noise

Figure 4.7: Comparison of estimated parameter values in the Lotka-Volterra model (4.1) obtained by fitting the model to the synthetic PC3 (a) and DU145 (b) spheroids data with 10% noise using the three fitting protocols. The values shown represent the mean$\pm$1$\times$SD from 100 datasets. The values used to generate the data are represented by red horizontal lines.

overestimated and have wide CIs (Fig. B.4a). The PC3 estimates of K_C become much less accurate for larger noise often reaching the upper bound imposed on this parameter (Figs. 4.6a and B.2b). The parameters estimated with the data containing 10% noise are also adequate with low variation but when the noise is increased to 20% the estimates of the carrying capacity in particular are significantly overestimated.

For both PC3 and DU145 spheroids, the pooled protocol estimates of the intrinsic parameters are more accurate and associated with lower uncertainties and variability than the estimates obtained with the two-step fitting protocol. The differences are more pronounced for the PC3 cell line.

4.5.3.2 Interaction parameters

The mean values of the estimated PC3 interaction parameters are shown in Figs. 4.7a (10% noise) and B.4 (5% and 20% noise). Corresponding individual estimates with 95% CIs are shown in Figs. 4.8a and B.6. We note that the CIs and variations about the means increase as the noise level increases. We we were able to estimate λ_R with greater accuracy since, for parameter values used to generate the data, the volume of the resistant cell population was larger than the volume of the control cells (see Fig. 4.1a).

The two-step protocol estimates were acceptable for the 5% noise data but their accuracy dropped significantly for larger noise. In particular, the estimates of $\lambda_C^{1:3}$ and all three estimates of λ_R showed wide confidence intervals when the noise reached 20%.

The two-step pooled and pooled fitting protocols were similar and had comparable uncertainties. Nonetheless, for about a sixth of the synthetic datasets these uncertainties grew significantly for 20% noise (Fig B.6b).

In comparison, the estimates of λ_C and λ_R were more accurate for the synthetic DU145 spheroids (Figs. 4.8b, B.7, 4.7b and B.5). We observed a similar trend as for the PC3 cells—the accuracy of our estimates was correlated to the relative volume of the control and resistant cell populations. Although the differences in the uncertainties of the estimates across the three fitting protocols were less dramatic than those for the PC3 cells, the two-step pooled and pooled fitting protocols led to narrower confidence intervals than the two-step protocol.

4.5.3.3 Goodness of fit comparison

In addition to inspecting parameter estimates and their corresponding uncertainties, we also compared the three fitting protocols in terms of their goodness of fit. We

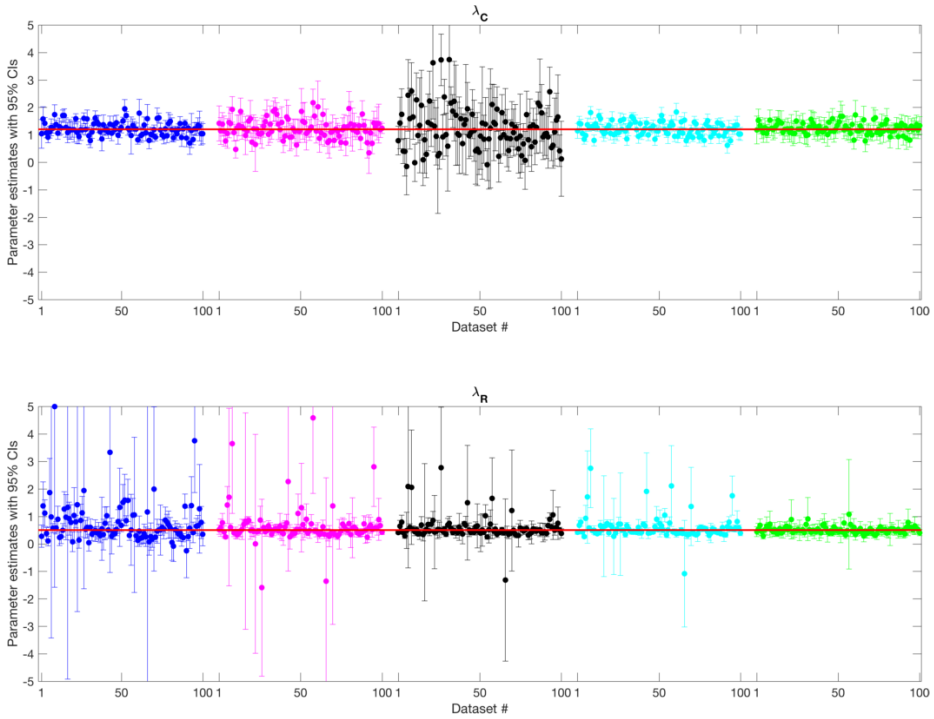

(a) PC3: 10% noise

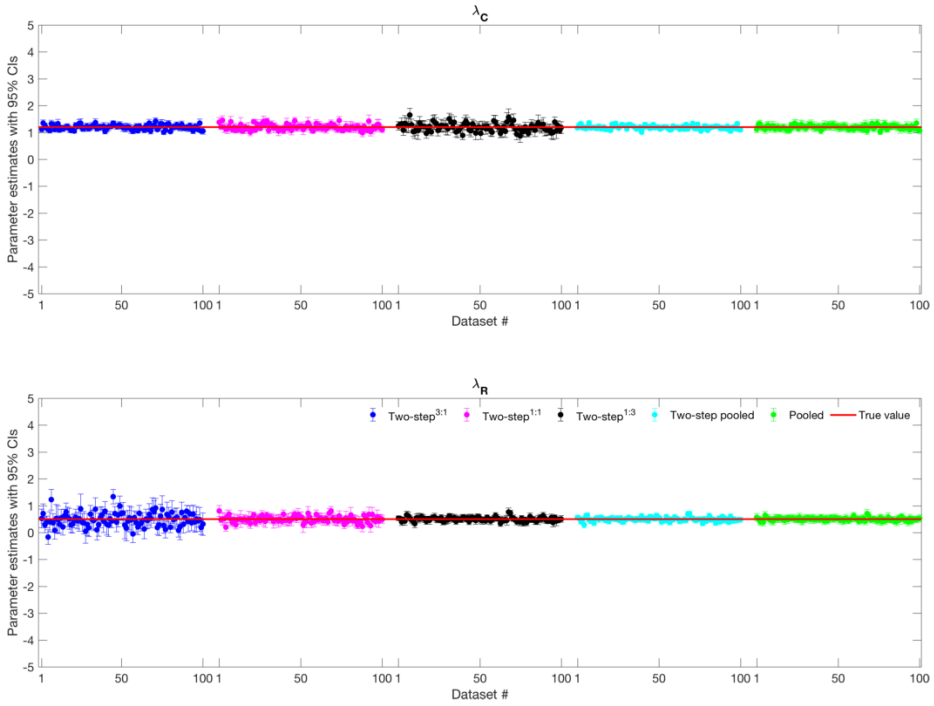

(b) DU145: 10% noise

Figure 4.8: Estimated values with 95% CIs of the interaction parameters λ_C and λ_R for the synthetic PC3 (a) and DU145 (b) spheroids with 10% noise obtained using the three fitting protocols.

quantified the goodness of fit as the mean weighted sum of squared residuals (WSSR) of parameter estimates from 100 noisy datasets. We computed the mean WSSR together with the 95% CIs for the three fitting protocols and for each noise level. We present the results in Fig. 4.9.

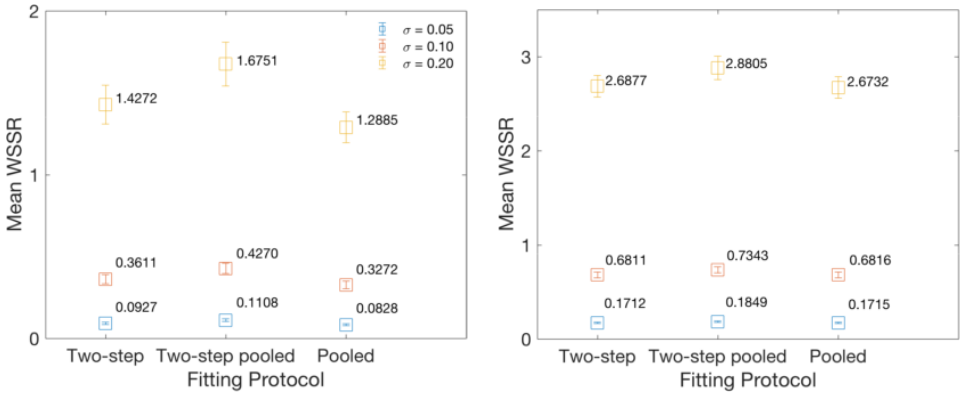

(a) PC3 **(b)** DU145

Figure 4.9: Comparison of the weighted sums of squared residuals obtained by fitting the Lotka-Volterra model (4.1) to synthetic PC3 (a) and DU145 (b) spheroids data using the three fitting protocols for different noise levels.

As seen in Fig. 4.9a, the pooled data protocol provided the lowest mean WSSR for all noise levels for the synthetic PC3 spheroids, followed by the two-step protocol. The largest mean WSSR was obtained for the two-step pooled protocol. In contrast, for the DU145 synthetic spheroids (Figure 4.9b), the lowest values of the mean WSSR were recorded for the two-step protocol for the 5% and 10% noise levels. These were, however, very close to the values of the mean WSSR obtained for the pooled protocol, which also led to the lowest mean WSSR for the 20% noise level. As with the PC3s, the two-step pooled fitting protocol provided the largest mean WSSR in all cases.

4.5.3.4 Estimating noise levels

In the previous sections we showed that our ability to estimate model parameters depends on the noise level present in the data. Therefore, it is important that any fitting protocol should accurately estimate the noise level. In Table 4.5 we report the values of σ used to generate noisy synthetic PC3 and DU145 spheroids data, together with the estimates of σ obtained with the three fitting protocols. The estimates of σ were computed using Equation (3.8). All three fitting protocols yielded reasonable estimates of the noise with low variance. Both two-step fitting protocols tended to overestimate the noise, whereas the pooled protocol underestimated σ. Once again,

the latter protocol provided the most accurate predictions of the parameter being estimated.

Table 4.5: Estimated values of σ, corresponding to the noise level in the synthetic PC3 and DU145 spheroids data for the three fitting protocols. The values shown represent means±1SD based on a sample of size 100.

	σ	0.05	0.10	0.20
PC3	Two-step	0.0546 ± 0.0103	0.1077 ± 0.0208	0.2137 ± 0.0436
	Two-step pooled	0.0562 ± 0.0101	0.1102 ± 0.0204	0.2178 ± 0.0428
	Pooled	0.0486 ± 0.0083	0.0966 ± 0.0173	0.1915 ± 0.0350
DU145	Two-step	0.0510 ± 0.0059	0.1017 ± 0.0116	0.2021 ± 0.0224
	Two-step pooled	0.0514 ± 0.0060	0.1025 ± 0.0118	0.2031 ± 0.0227
	Pooled	0.0495 ± 0.0057	0.0987 ± 0.0113	0.1956 ± 0.0218

4.6 Application: parameter inference for heterogeneous PC3 and DU145 tumour spheroids

4.6.1 Introduction

In Section 4.3 we established that the total volume measurements of heterogeneous spheroids do not provide sufficient information to accurately estimate the values of the interaction parameters in Eqs. (4.1). We found that the accuracy could be notably improved if we measured the proportions of the control and resistant cell populations on days 10 and 15 for the PC3 spheroids, and days 16 and 25 for the DU145 spheroids. Therefore, we conducted an experiment to determine these proportions on the given days for each cell line. Briefly, we grew spheroids composed of different ratios of fluorescently-labelled control and resistant cells, we dissociated the spheroids on the desired days to form single cell suspensions and separated them into the two cell types for counting using flow cytometry (for details, see Chapter 2).

In Section 4.5 we compared three distinct protocols for estimating the parameter values in Eqs. (4.1). We now use the knowledge gained from these case studies to perform parameter inference using *real experimental data*. To do so, we use the three fitting protocols described earlier, together with the total volume measurements and the proportions of the control and resistant cells data, collected for the PC3 and DU145 spheroids. Since we are interested in directly comparing the interaction coefficients, in what follows we use Eqs. (4.3).

4.6.2 Results

4.6.2.1 PC3 untreated heterogeneous tumour spheroids

The estimates of the growth rate and carrying capacity for the control cell population differed markedly for the two-step and pooled fitting protocols (Table 4.6). The value

Table 4.6: Parameter estimates and 95% CIs resulting from fitting the Lotka-Volterra model (4.3) to the PC3 spheroids data using the two-step, two-step pooled and pooled fitting protocols.

	Two-step fp	**Two-step pooled fp**	**Pooled fp**
r_C	**0.180** (0.093,0.267)	**0.180** (0.093,0.267)	**0.236** (0.201,0.271)
K_C	**0.918** (-1.229,3.065)	**0.918** (-1.229,3.065)	**0.473** (0.342,0.604)
$V_C(\mathbf{o})$	**0.036** (0.024,0.047)	**0.036** (0.024,0.047)	**0.031** (0.026,0.036)
r_R	**0.396** (0.342,0.451)	**0.396** (0.342,0.451)	**0.401** (0.366,0.436)
K_R	**0.788** (0.620,0.956)	**0.788** (0.620,0.956)	**0.773** (0.673,0.873)
$V_R(\mathbf{o})$	**0.016** (0.012,0.020)	**0.016** (0.012,0.020)	**0.015** (0.012,0.018)
η_C	**0.652** (0.520,0.784)$^{3:1}$ **0.731** (0.593,0.868)$^{1:1}$ **0.850** (0.406,1.292)$^{1:3}$	**0.679** (0.580,0.777)	**0.655** (0.434,0.875)
η_R	**0.110** (-0.060,0.280)$^{3:1}$ **0.256** (0.123,0.320)$^{1:1}$ **0.275** (0.201,0.349)$^{1:3}$	**0.247** (0.198,0.296)	**0.480** (0.363,0.597)
σ	0.247	0.247	0.241
WSSR	25.998	26.245	24.982

of r_C obtained with the pooled protocol was notably larger than the value obtained for the homogeneous 1:0 spheroids data alone. The best point estimate of K_C for the two-step fitting protocols was almost twice as large as for the pooled protocol. However, its confidence intervals were wide. Moreover, the 95% CIs for the estimates of r_C and K_C obtained with the pooled protocol did not include the best point estimates obtained with the two-step fitting methods. Interestingly, the estimates of $V_C(0)$, the volume of a spheroid composed of 1000 control cells at time $t = 0$, were about twice as large as the estimates of $V_R(0)$, even when using the pooled fitting protocol. We also observed that the confidence intervals for the intrinsic parameters were wider when using the two-step fitting protocols.

As seen in Table 4.6, all three fitting protocols predicted that the interaction between the control and resistant cells was competitive (see Table 4.1 for explanation). In more detail, the control cell population exerted a stronger competitive effect on the resistant cell population than vice versa ($\eta_C > \eta_R$). The magnitude of the two-step protocol estimates of η_C and η_R increased with the initial number of resistant cells. The uncertainty in the estimated values improved as the initial proportion of the cell population corresponding to the given interaction coefficient increased. In other

words, the more control (resistant) cells at time $t = 0$, the more confidence in the estimate of the effect that the control (resistant) cells have on the resistant (control) cells—we observed similar phenomenon in Section 4.5. The estimate of η_R obtained with the pooled protocol was clearly larger than any other estimate of this parameter. Moreover, the 95% CIs for the pooled protocol estimate of η_R did not capture any of the best point estimates obtained with the two-step fitting protocols, nor did they overlap with the confidence intervals for these estimates.

We also observed that the estimates of the noise present in the data were decidedly higher than we anticipated, exceeding 24% which corresponds to the estimates of σ in Table 4.6.

Fig. 4.10 shows the data collected for the PC3 heterogeneous spheroids together with the best fits obtained from the different fitting protocols. On the timescale of the

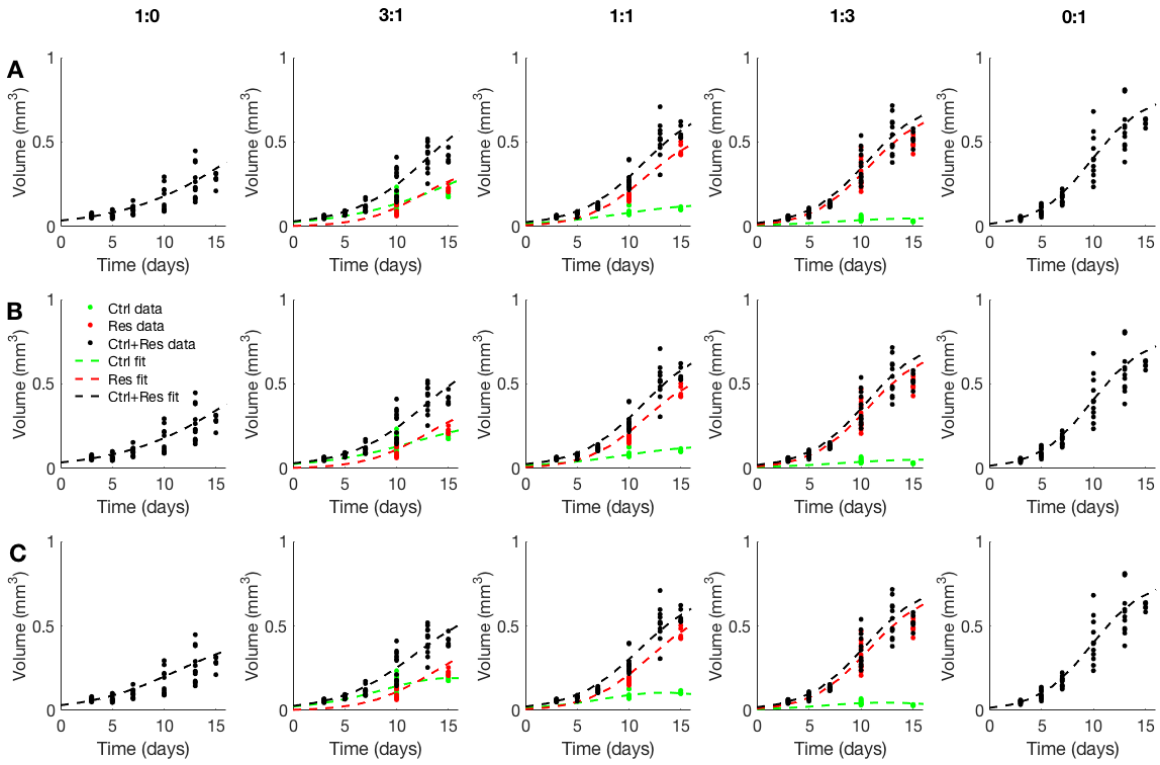

Figure 4.10: Best fits to the untreated PC3 heterogeneous spheroids data obtained with the two-step (A), two-step pooled (B) and pooled (C) fitting protocols.

available data, the fits look similar suggesting that the resistant cells are dominant. The resistant population had much higher initial growth rate, which suggested that it would outgrow the control cells in the long term. However, for both two-step fitting protocols, the model predicted that for the 3:1 and 1:1 spheroids the control cells would dominate in the long term (Fig. 4.11).

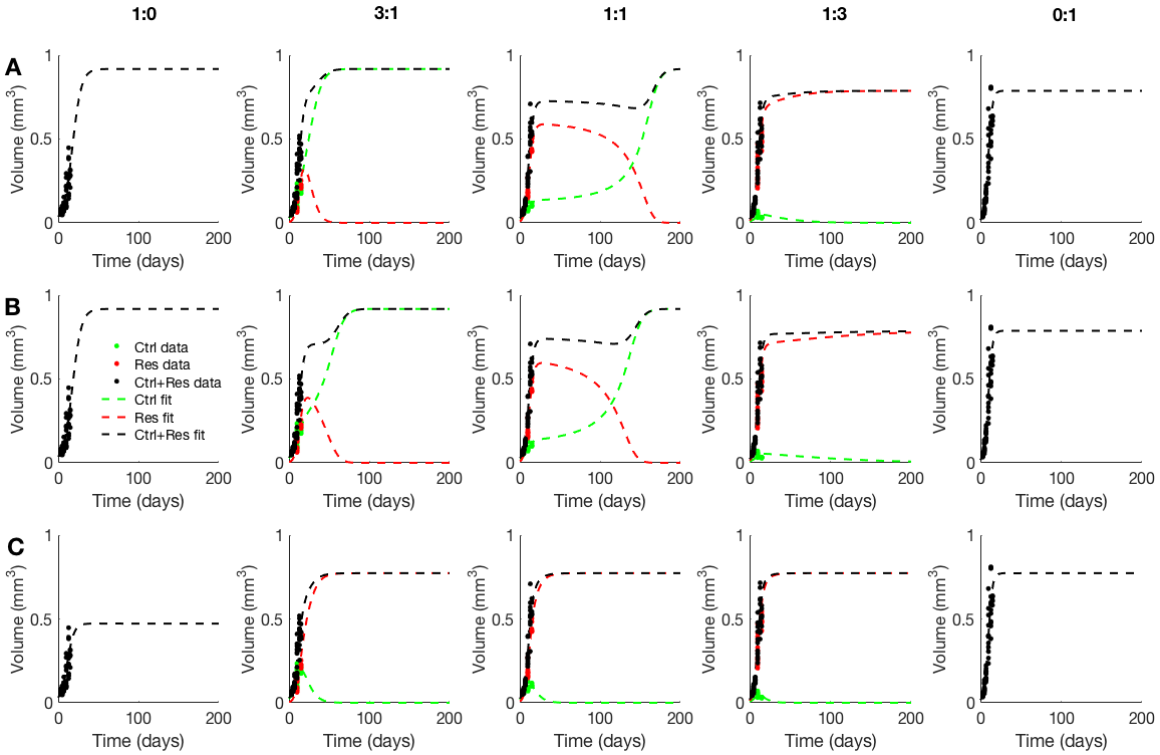

Figure 4.11: Best fits to the untreated PC3 heterogeneous spheroids data obtained with the two-step (A), two-step pooled (B) and pooled (C) fitting protocols shown on a longer timescale.

4.6.2.2 DU145 untreated heterogeneous tumour spheroids

Although the estimates of the intrinsic parameter values for the DU145 spheroids were similar for the two-step and pooled fitting protocols, their 95% CIs overlaped only for the estimates of K_C (Table 4.7). The estimates of η_C and η_R imply that interactions between the control and resistant cell populations are *antagonistic*. The data suggest that the control population had a strong detrimental effect on the resistant cells, whereas the latter provided support for the controls. The strength of the inhibitory interactions experienced by the resistant population decreased as the initial number of resistant cells grew. Pooling all the data yielded estimates for η_C and η_R that were lower in magnitude than estimates provided by the two-step protocols. The noise levels in the data were estimated to be around 20%, and as expected the lowest sum of squared weighted residuals was achieved with the pooled protocol.

Fig. 4.12 shows the DU145 spheroids data with the best fits obtained by using the pooled protocol. The fits obtained with the two-step protocols look similar (not shown). As expected based on the values of η_C and η_R, the control cell population quickly dominated the resistant cells. However, as can be seen from Fig. 4.12, the

Table 4.7: Parameter estimates and 95% CIs resulting from fitting the Lotka-Volterra model (4.3) to the DU145 spheroids data using the two-step, two-step pooled and pooled fitting protocols.

	Two-step fp	**Two-step pooled fp**	**Pooled fp**
r_C	**0.314** (0.303,0.325)	**0.314** (0.303,0.325)	**0.356** (0.343,0.370)
K_C	**0.623** (0.604,0.642)	**0.623** (0.604,0.642)	**0.605** (0.590,0.621)
$V_C(\mathbf{o})$	**0.012** (0.011,0.013)	**0.012** (0.011,0.013)	**0.010** (0.009,0.011)
r_R	**0.306** (0.295,0.318)	**0.306** (0.295,0.318)	**0.251** (0.236,0.265)
K_R	**0.722** (0.702,0.741)	**0.722** (0.702,0.741)	**0.802** (0.756,0.849)
$V_R(\mathbf{o})$	**0.020** (0.019,0.022)	**0.020** (0.019,0.022)	**0.027** (0.025,0.030)
η_C	**0.670** (0.656,0.724)$^{3:1}$ **0.647** (0.611,0.683)$^{1:1}$ **0.547** (0.512,0.583)$^{1:3}$	**0.644** (0.623,0.665)	**0.536** (0.504,567)
η_R	**-0.183** (-0.330,-0.036)$^{3:1}$ **-0.237** (-0.324,-0.149)$^{1:1}$ **-0.217** (-0.269,-0.165)$^{1:3}$	**-0.154** (-0.189,-0.118)	**-0.102** (-0.159,-0.044)
σ	0.196	0.204	0.194
WSSR	34.940	38.247	34.427

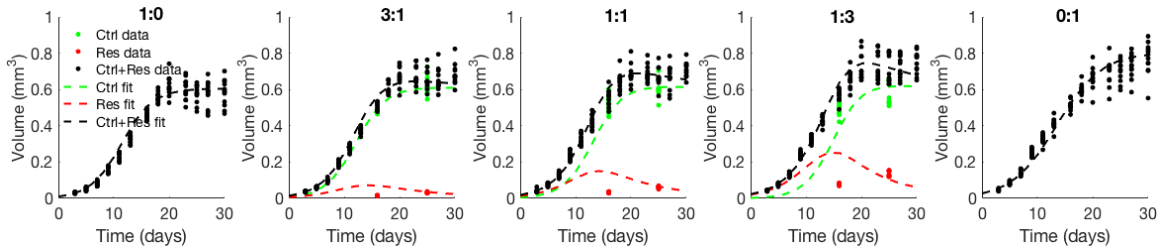

Figure 4.12: Best fits to the non-irradiated DU145 heterogeneous spheroids data obtained with the pooled fitting protocol.

model did not describe the data very well. In particular, the predicted volume of the resistant population at $t = 16$ days appears to diverge from the observed values as the initial number of the resistant cells increase.

4.6.2.3 PC3 irradiated heterogeneous tumour spheroids

To determine whether the type and strength of interactions were affected by radiation, we fitted Eqs. (4.3) to kinetic data from heterogeneous spheroids irradiated with a single dose of 6 Gy on day 3. Since it was not possible to obtain meaningful estimates of the carrying capacity parameter for the irradiated 1:0 spheroids data, we were unable to use the two-step fitting protocols. The pooled protocol estimates are shown in Table 4.8. Table 4.8 suggests that there is competition between the control and resistant cell populations Although competitive interactions were predicted for the non-irradiated PC3 spheroids (Table 4.6), its nature seems to shift following irradiation. The resistant population appears to have stronger competitive effect on

Table 4.8: Estimated parameters with 95% CIs obtained by fitting Eqs. (4.3) to the growth data of the heterogeneous PC3 spheroids irradiated with a single dose of 6 Gy. The parameters were estimated using the pooled fitting protocol.

r_C	**0.112** (0.054,0.169)
K_C	**0.117** (0.087,0.146)
$V_C(\mathbf{o})$	**0.051** (0.043,0.059)
r_R	**0.217** (0.169,0.265)
K_R	**0.393** (0.261,0.526)
$V_R(\mathbf{o})$	**0.031** (0.026,0.037)
η_C	**0.516** (0.026,1.006)
η_R	**0.586** (0.199,0.974)
σ	0.215
WSSR	19.370

the control population following irradiation. However, the wide 95% CIs mean that we are unable to draw strong conclusions about these changes.

Irradiation had a significant effect on the values of the initial growth rate and carrying capacity for both cell populations. Direct comparison of the pooled protocol estimates shows that the values of the initial growth rates of the control and resistant cell populations were halved following irradiation, and the value of the carrying capacity parameter was halved for the resistant population and reduced by a factor of 4 for the control population.

As shown in Fig. 4.13, the resistant population became the dominant one following irradiation.

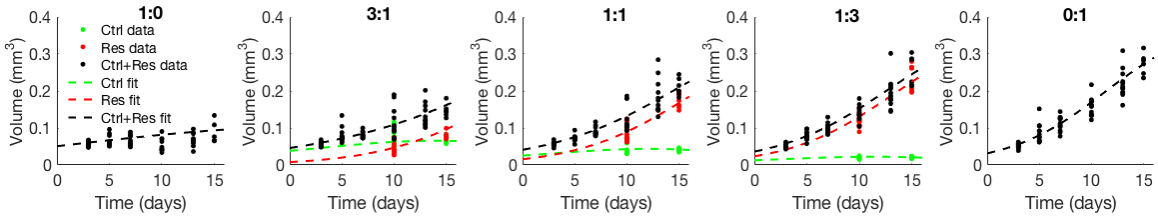

Figure 4.13: Best fits to the PC3 irradiated heterogeneous spheroids data obtained with the pooled fitting protocol.

4.6.2.4 DU145 irradiated heterogeneous tumour spheroids

The parameter estimates for the irradiated DU145 spheroids were similar across the three fitting methods with narrower confidence intervals (Tab. 4.9). A single dose of radiation seemed to have little effect on the resistant population but a significant effect on the initial growth rate and carrying capacity of the control cells. Surprisingly,

Table 4.9: Estimated parameter values in the Lotka-Volterra model (4.3) for the DU145 spheroids irradiated with a single dose of 6 Gy data.

	Two-step fp	Two-step pooled fp	Pooled fp
r_C	**0.222** (0.211,0.234)	**0.222** (0.211,0.234)	**0.253** (0.242,0.265)
K_C	**0.516** (0.486,0.546)	**0.516** (0.486,0.546)	**0.496** (0.480,0.513)
$V_C(\mathbf{o})$	**0.016** (0.014,0.017)	**0.016** (0.014,0.017)	**0.015** (0.013,0.016)
r_R	**0.249** (0.239,0.259)	**0.249** (0.239,0.259)	**0.195** (0.183,0.207)
K_R	**0.754** (0.728,0.779)	**0.754** (0.728,0.779)	**0.924** (0.838,1.009)
$V_R(\mathbf{o})$	**0.023** (0.022,0.025)	**0.023** (0.022,0.025)	**0.032** (0.029,0.035)
η_C	**0.860** (0.813,0.907)$^{3:1}$ **0.716** (0.674,0.759)$^{1:1}$ **0.623** (0.580,0.667)$^{1:3}$	**0.740** (0.711,0.769)	**0.594** (0.555,0.632)
η_R	**-0.500** (-0.645,-0.356)$^{3:1}$ **-0.457** (-0.529,-0.385)$^{1:1}$ **-0.417** (-0.462,-0.371)$^{1:3}$	**-0.369** (-0.402,-0.336)	**-0.329** (-0.388,-0.269)
σ	0.204	0.217	0.202
WSSR	37.857	42.969	37.344

the value of the carrying capacity for the resistant cells increased following irradiation, though the 95% CIs overlapped for all fitting protocols. As for the untreated spheroids, the data suggest antagonistic interactions between the two cell populations. However, the strength of these interactions increased substantially, with the resistant cells becoming more supportive of the control cells following treatment. We also noted that, following irradiation, the magnitude of the beneficial effect decreased with the increasing initial proportion of the resistant cells—the trend opposite to what we observed in the absence of radiation. Due to the nature of interactions, the control cell population quickly become dominant within the heterogeneous spheroids (Fig. 4.14).

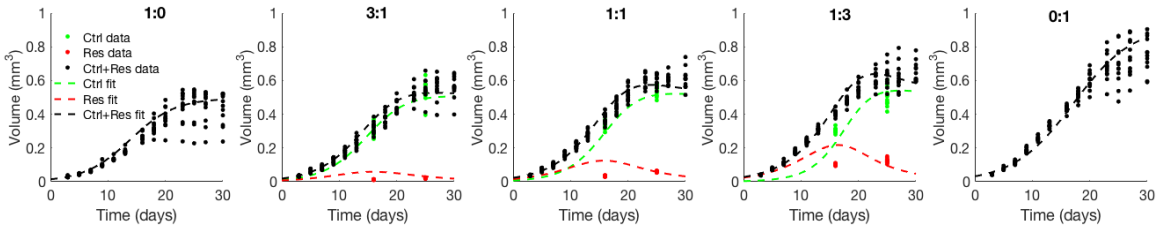

Figure 4.14: Best fits to the DU145 irradiated heterogeneous spheroids data obtained with the pooled fitting protocol.

4.7 Discussion

The present study was designed to elucidate the interactions between two populations of tumour cells when they are co-cultured. Pairs of cell populations with different

radiosensitivity were chosen in order to determine whether the nature of interactions between the two cell types changes following exposure to a single round of radiotherapy. Our findings indicate that the control and resistant PC3 cell populations compete with each other and that competition persists after radiation. Interactions between the control and resistant DU145 cell lines were found to be antagonistic. In particular, the control population appeared to have a pernicious effect on the resistant cells, whereas the latter seemed to have a beneficial effect on the former. These interactions did not seem to change following exposure to a single dose of radiotherapy.

We used a Lotka-Volterra-type equations to model the interactions between the control and resistant clones for two main reasons. Firstly, the model can be fit to our experimental data. Secondly, the model can exhibit a wide range of interactions between the two cell populations. However, as we saw in Section 4.6, the model did not describe the DU145 heterogeneous spheroids data particularly well. A possible explanation for the observed discrepancies may be the fact that the model is too simple to adequately represent such a complex phenomena as the growth of heterogeneous spheroids.

The experimental design case studies provided valuable insight into our ability to estimate parameters. Initially, we measured only the total volumes of heterogeneous spheroids. A parameter recovery simulation study, reported in Section 4.3, revealed that these data were not sufficient to estimate the interaction coefficients.

After learning that additional data were required we designed an experiment to determine the proportions of control and resistant cells. As shown in Section 4.4, the additional data significantly improve the accuracy of estimated parameters. As collecting data on proportions is costly and time-consuming, we sought to identify the minimum number of time points (and times) at which proportions data should be collected in order to generate accurate and reliable estimates of all model parameters.

Having demonstrated using synthetic data the feasibility of recovering parameter estimates from the new data, we then considered several different ways of fitting the model to the data. A distinctive feature of the two-step protocol is that it provides a single set of interaction parameter for each condition (3:1, 1:1 and 1:3). Its implicit assumption is that the interactions depend on the initial composition of the spheroid. In both two-step fitting protocols the parameters intrinsic to each cell population (r, K and $V(0)$) are estimated first, and then fixed in Eqs. (4.1) and (4.3). Clearly, these best point estimates are associated with some uncertainty. The main disadvantage of these methods is that the uncertainties are not propagated through the model when estimating the interaction parameters. To address this issue, we designed the pooled

protocol, which aggregated all data, and was found to provide the most accurate estimates with relatively low uncertainties.

One of the obvious limitations of the parameter recovery approach is that we had to be very selective in choosing the parameter values to generate synthetic data. For practical reasons, we could not consider all possible types of interactions or sets of time points at which to collect proportions data. However, our choices were always guided by experimental protocols and particular problems that we have investigated. Another limitation of our approach is that we assumed a multiplicative error model to explain measurement noise in our data. This assumption requires further investigation. Additionally, we did not consider uncertainties in measuring the proportions of the cell populations, even though they contribute to the noise in the data.

Overall, all three fitting protocols yielded similar conclusions, though the pooled protocol seemed to offer the highest level of confidence. Not only did it lead to narrow confidence intervals, but as shown in Section 4.5, it estimated parameter values with highest accuracy. The most notable disagreement between the two-step and pooled fitting protocols was perhaps for the estimates of K_C for the untreated PC3 spheroids (Table 4.6). However, these results were consistent with the results of the case study in Section 4.5 where K_C tended to be overestimated when using the two-step protocols. One explanation for this behaviour could be that the data collected for the PC3 Ctrl homogeneous spheroids show that the spheroids were still in the exponential phase of growth. With such data it is often difficult to estimate the carrying capacity. However, when the datasets obtained for the spheroids seeded at different proportions of control and resistant cells were used in the fitting process the estimates of K_C became more accurate.

Another problem with the PC3 spheroids data was that the two datasets, which came from two independent experiments (see Chapter 2 for details), presented markedly different behaviour. Additionally, for one of them we had to stop imaging on day 13, whereas for the other imaging ended on day 15, which led to less data points being available on day 15. Since our goal was to estimate population parameters, rather than sample parameters, we decided to use both datasets together. We note, however, that a more suitable approach to parameter estimation in this case would be mixed effect population modelling or hierarchical Bayesian inference.

To determine if the types of interactions changed following radiation we fitted the irradiated spheroids data by the same model as the non-irradiated data. Modelling the radiation explicitly in this case was not warranted. The spheroids were irradiated with a single dose of 6 Gy on day 3 after seeding. Thus by observing their dynamics

we were able to determine the types of interactions between the subpopulations, at least on the timescale of available data.

Chapter 5

Cellular automaton model of avascular tumour growth

5.1 Introduction

In Chapter 2 we reported the results of a series of experiments in which two cell populations were co-cultured to form heterogeneous tumour spheroids. In Chapters 3 and 4 we developed and applied methodology to mathematically model the growth of these spheroids and infer parameter values in the proposed models. By fitting a Lotka-Volterra interactions model to our data we concluded that the PC3 subpopulations competed with each other when co-cultured, whereas the DU145 subpopulations exhibited antagonistic interactions. Since we used spatially averaged models we could not infer whether the interactions were *indirect*, in the form of competition for space and nutrients, or *direct*, in the form of cell-cell communication.

In order to determine how our co-cultured subpopulations interact we now develop a spatially resolved cellular automaton (CA) model. Such agent-based models are well suited to describe interactions between individual cells. Agent-based models can be classified as being on- or off-lattice. The former are generally easier to implement but are constrained by the structure of the lattice on which they reside. Examples of on-lattice models include CA and Potts models [162]. Off-lattice models are not confined to a uniform grid which enables modelling cell movement in any direction. However, such models tend to be harder to implement [162]. Nonetheless, both types of spatially resolved models can be coupled to differential equations typically used to describe nutrient concentrations and other continuous processes.

Despite being relatively easy to implement, CA models are powerful tools for describing nonlinear dynamics in spatio-temporal systems. CA models have been extensively used to model various aspects of tumour development that include the

effect of nutrients on avascular tumour growth [65, 75], tumour response to treatment [55, 202, 161, 61, 153], tumour invasion [147, 94] or the effect of angiogenesis and vascular remodelling on the dynamics of tumour and normal cells [1]. Many CA models of avascular tumour growth are coupled to reaction-diffusion equations describing the concentration nutrients such as oxygen [65, 75]. Such models, generate tumours with commonly observed structure including a central necrotic core surrounded by a layer of viable but resting cells and an outer rim of proliferating cells. These morphologies have also been reproduced by models that do not consider nutrients explicitly assuming instead that a cell can proliferate only if it is located a certain distance from the spheroid boundary [55, 202]. While these models save computational time (because reaction-diffusion equations describing nutrient concentrations do not have to be solved) they are less physically realistic. Nonetheless, many CA models have been shown to replicate common tumour growth laws such as Gompertz growth [159, 65, 161].

One of the biggest advantages of CA models is that they treat each cell as an individual entity and allow description of cellular or even subcellular processes. Most often, each lattice site can be occupied by only one cell (e.g., [1, 75]) but this assumption can be relaxed by allowing multiple cells to reside at a grid site [150, 11]. Depending on the model's purpose, different levels of detail can be included. Enderling et al. [61] modelled cancer stem cells and cancer non-stem cells allowing them to become quiescent if there was no space for them to divide. Gerlee and Anderson [75] assumed that cancer cells could be in one of three states: proliferating, quiescent or dead. Powathil et al. [153] used a system of ODEs to track cycle phase of each individual cell.

A major consideration with on-lattice modelling of cell division is where to place a newly created cell. Some authors allow a cell to divide only if there is an empty site in the nearest neighbourhood [75] or within some distance ρ from the dividing cell [153]. These approaches create a proliferating rim that can be only ρ cells thick. Alternatively, if every cell has equal probability of division at any given time, each newly created cell may be placed in the nearest available free space which can be far from its parent [136]. These approaches require modification for inhomogeneous cell populations as they artificially rearrange spatial configurations within tumours. Other models allow a dividing cell to push neighbouring cells away in order to divide [202]. Similarly, the removal of dead cells, in particular from the necrotic core, is an important aspect of the design of CA models. Often, it is the mechanism that controls growth saturation or tumour shrinkage and cell shifting algorithms have been

widely used to regulate tumour size [136]. Care is needed when implementing cell division and death algorithms as CA models exhibit inherent anisotropies caused by the regularity of the lattice on which they are based [54, 201].

Here, we develop a CA model of avascular tumour growth coupled to a reaction-diffusion equation describing nutrient concentration. The model can be used to simulate the growth of homogeneous and heterogeneous spheroids. We describe the CA model and investigate relationships between its parameters and those in the spatially averaged logistic model presented in Chapter 3 by fitting the latter to synthetic data generated with the CA model for a range of parameter values. The remainder of this chapter is organised as follows. In Section 5.2 we describe the CA model, in Section 5.3 we investigate how its parameters affect the parameters in the logistic model and we summarise this chapter in Section 5.4.

5.2 Model description

Our hybrid model of avascular tumour growth is assumed to replicate the changes in the size and structure of a 2D cross-section through a 3D tumour spheroid suspended in culture medium. The model couples a set of automaton elements arranged on a regular, two-dimensional grid to a PDE describing the distribution of a growth-rate-limiting nutrient which is supplied from the culture medium surrounding the spheroid. Each automaton can be occupied either by a tumour cell or culture medium. We consider oxygen to be the single, growth-rate-limiting nutrient and thus model its concentration explicitly. All model simulations are initialised by placing a circular cluster of cells in the centre of the grid: this imitates seeding a spheroid in a Petri dish. The cells consume oxygen as it diffuses from the medium and divide. As the spheroid grows, less oxygen diffuses into its centre and when the oxygen concentration drops below a threshold value the cells there become quiescent. As the spheroid grows further, and even less oxygen is available for the cells in the centre, quiescent cells die via necrosis and the resulting necrotic debris is transported away from the spheroid. This simple model does not take into account the intricate mechanisms involved in tumour growth but allows us to study the impact of model parameters on spheroid dynamics. It can be readily extended to model the growth of heterogeneous spheroids consisting of multiple cell lines with distinct growth dynamics and to test hypotheses about their potential interactions. Our strategy is to keep the model as simple as possible while including enough detail to explain the observed behaviour. Engelberg et al. [62] have previously identified nine axioms essential to explain the growth of

EMT6 tumour spheroids. These included nutrient consumption, change of state based on nutrient availability, cell movement, proliferation, death and removal of necrotic debris: our model incorporates all of these features to varying degrees.

Below, we present a computer algorithm used to implement the CA model. In the remainder of this section, we describe the algorithm in more detail.

(1) *Initialisation* ($t = 0$). We assign values to all parameters (see Table 5.1 and Section 5.2.3), initialise the spatial distribution of oxygen on the discretised spatial domain that has the same size as the grid containing cells (Section 5.2.2), place a circular cluster of proliferating cells in the centre of the computational grid (other sites of the grid are assumed to contain culture medium), assign cell cycle duration times to the proliferating cells and set $t = \tau$ where τ is the length of our computational step.

(2) *Nutrient consumption.* We update oxygen concentration field by solving a reaction-diffusion equation where culture medium acts as source and cells act as sinks.

(3) *Update cell states.* We update cellular states based on the renewed oxygen distribution (Section 5.2.1.1).

(4) *Update cell cycle times.* The cell cycle duration counter of each proliferating cell is decreased by the amount that depends on the number of neighbours of that cell (Fig. 5.3).

(5) *Cell division.* If the updated cell cycle counter of a proliferating cells is reduced to zero the cell divides (Section 5.2.1.2). Cell division is performed asynchronously.

(6) *Cell lysis.* Necrotic cells are removed from the grid with a rate p_{lys} (Section 5.2.1.3). Cell lysis is performed asynchronously.

(7) *Update time.* Increase time t by computational step τ and if $t < T$, where T is the total simulation time, repeat steps (2)–(7).

A flowchart summarising our model is shown in Fig. 5.1.

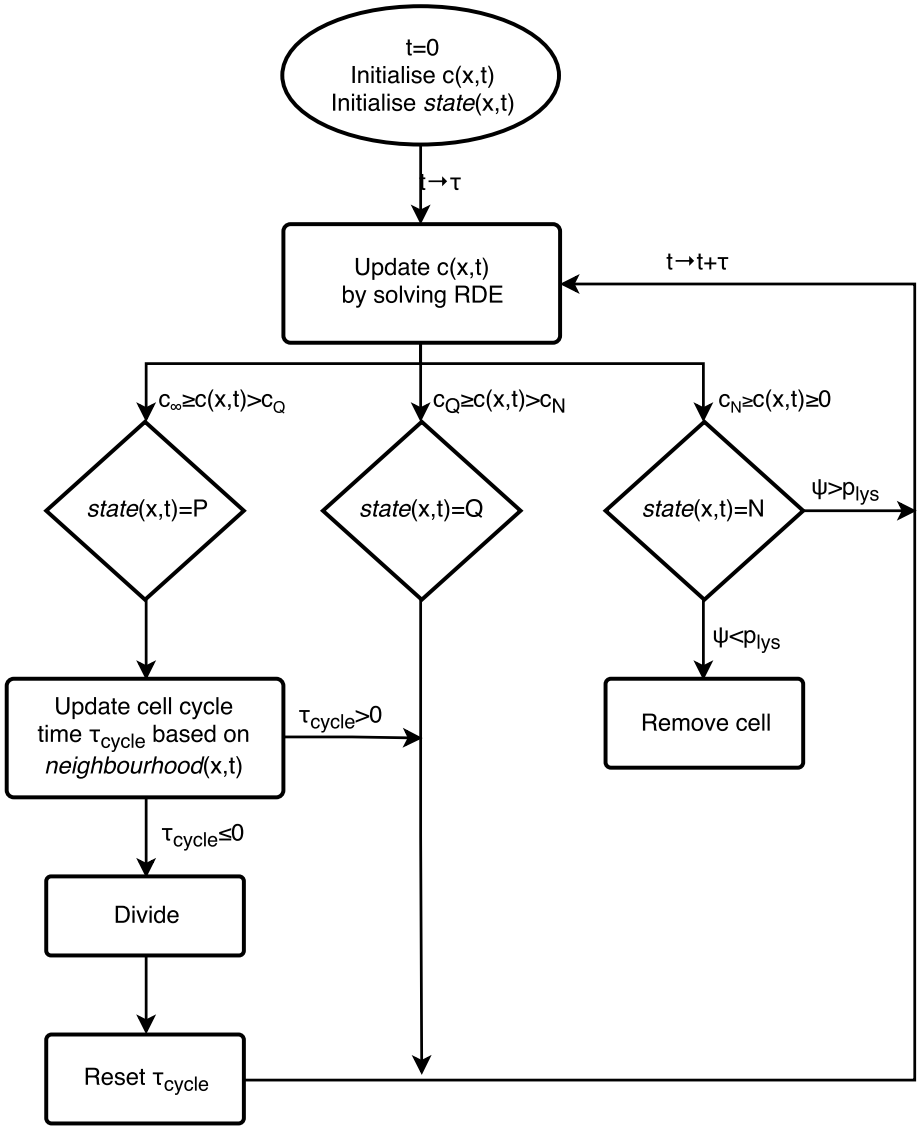

Figure 5.1: Flowchart corresponding to the algorithm used to implement the CA model.

5.2.1 Cellular automaton model

The automaton elements are arranged on an $N \times N$ lattice in a two-dimensional discrete space. The size of each element is equal to an average size of a PC3 cell (18 µm). Each automaton at location $\mathbf{x}$ and time t can be considered a dynamical variable with a *state*, *properties* and *neighbourhood*. We allow each element to assume one of four states: proliferating cell ($\mathcal{P}$), quiescent cell ($\mathcal{Q}$), necrotic cell ($\mathcal{N}$) or empty ($\mathcal{E}$). Empty automata contain culture medium. The set of states $\{\mathcal{P}, \mathcal{Q}, \mathcal{N}\}$ enables us to represent commonly observed features of tumour spheroids which include the formation of quiescent/hypoxic and necrotic regions in response to oxygen levels [203]. We define quiescent cells to be viable cells that are not actively progressing through the cell cycle. These cells are in the G_0 phase and awaiting restoration of favourable conditions so that they can re-enter the cell cycle.

The properties of CA elements are closely related to their states. Properties of interest include O_2 concentration, requirements and consumption rate, the number of neighbours, proliferation time and the probability of lysis.

The two most commonly used neighbourhoods in CA models are the von Neumann [159, 75, 174] and Moore [61, 161, 153] neighbourhoods (Fig. 5.2). The number and location of neighbours can have a significant impact on cell-cell communication. Tzedakis et al. [196] have previously demonstrated that the Moore neighbourhood can minimise artefacts associated with lattice anisotropies. Therefore, we use the first order Moore neighbourhood so that, in a 2-D setting, every cell can communicate with 8 neighbours.

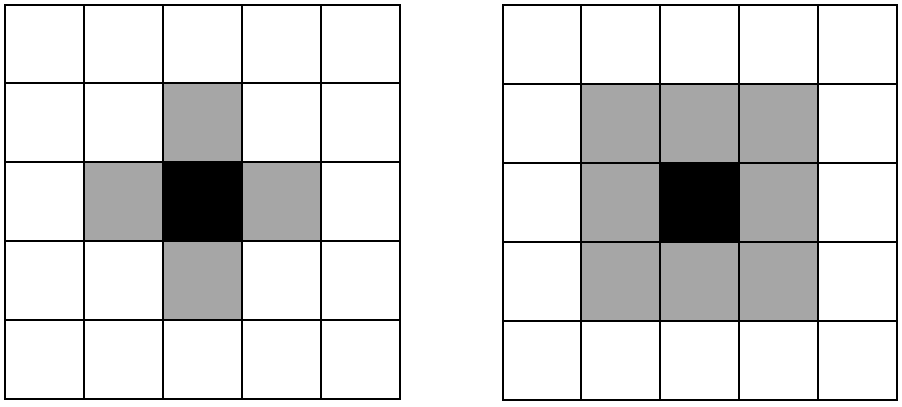

(a) First order von Neumann neighbourhood

(b) First order Moore neighbourhood

Figure 5.2: Two most commonly used types of neighbourhoods in CA models.

5.2.1.1 Rules for specifying cell state

If an automaton site at location $\mathbf{x}$ and time t contains a cell then its state $S(\mathbf{x}, t)$ is determined by the concentration of O_2, $c(\mathbf{x}, t)$, at that location. In particular, if we denote by c_∞ the background O_2 concentration, by $c_\mathcal{Q}$ and $c_\mathcal{N}$ the threshold O_2 levels below which cells become quiescent and necrotic, respectively, then we have:

- $c_\infty \geq c(\mathbf{x}, t) > c_Q \implies S(\mathbf{x}, t) = P$,
- $c_Q \geq c(\mathbf{x}, t) > c_N \implies S(\mathbf{x}, t) = Q$,
- $c_N \geq c(\mathbf{x}, t) \geq 0 \implies S(\mathbf{x}, t) = N$.

A cell can switch between proliferating and quiescent states if O_2 levels change but necrotic cells cannot change their state.

In turn, the O_2 consumption rate $\kappa(\mathbf{x}, t)$ depends upon the nature and state of the automaton at a given location, creating a feedback loop. Proliferating and quiescent cells consume oxygen at rates $\kappa_\mathcal{P}$ and $\kappa_\mathcal{Q}$, respectively, where $\kappa_\mathcal{P} > \kappa_\mathcal{Q} > 0$. Although in theory O_2 concentration could become negative (see Section 5.2.2), in practice this does not happen in our model because cells residing in low but nonzero O_2 conditions become necrotic and do not consume O_2.

5.2.1.2 Cell division

Every cell initially placed on the grid has $S(\mathbf{x}, t) = \mathcal{P}$ and is assigned a uniformly distributed random number τ_{cycle} from the set $(0, \bar{\tau}_{cycle})$ representing the time until cell division. $\bar{\tau}_{cycle}$ represents the mean cell cycle duration time for a given cell population. After each discrete CA time step of duration τ, τ_{cycle} of each proliferating cell is reduced by an amount that depends on its local *neighbourhood* (Fig. 5.3). This mechanism imitates contact inhibition of proliferation, a well known feature of 2D and 3D cell aggregates [106]. Unlike Jagiella et al. [93] who assumed that a cell cycles only if it is located within a given distance from the spheroid boundary, here the cell makes this decision based on local information. Gerle and Anderson [75] modelled contact inhibition in a similar way but they assumed that a cell would remain in a proliferating state only if it had less than 4 neighbours (they used von Neumann neighbourhood). Consequently, the proliferating rim in their model was only one cell thick. Similar assumptions were made in [62] and [61].

We asynchronously loop over all proliferating cells and when $\tau_{cycle} \leq 0$ the cell produces an offspring. The states of both cells are set to $\mathcal{P}$ and new values of τ_{cycle}

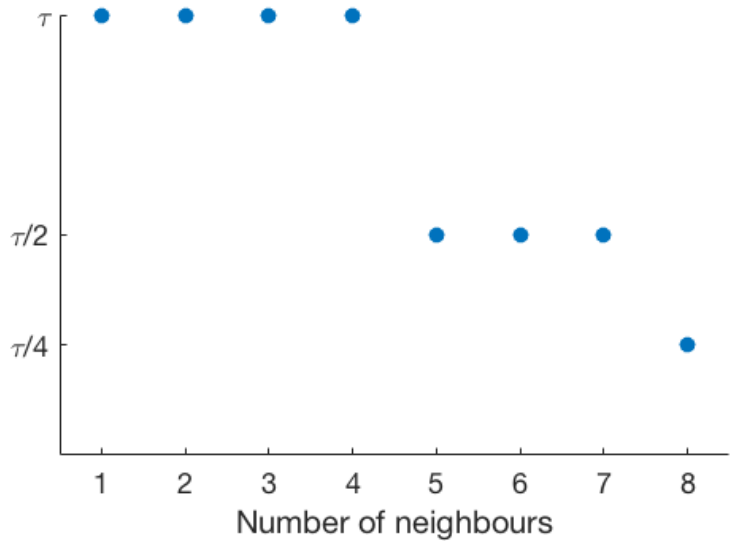

Figure 5.3: The amount by which τ_{cycle} for a given cell is reduced after each computational step of length τ as a function of the number of the cell's neighbours.

for each cell are drawn from a Gaussian distribution with mean $\bar{\tau}_{cycle}$ and standard deviation σ_{cycle}. One cell occupies the same position as the parent cell, the other is placed on the grid according to the division algorithm (DA) described below.

DA1: If free space is available in the first order Moore neighbourhood of the parent then the new cell is placed into the site that has maximum number of neighbours.

DA2: Otherwise, a cell chain is shifted from the parent towards the spheroid boundary by repeating the following steps until an empty cell is encountered:

DA2.1 distances in all 8 directions (N,NE,E,SE,S,SW,W,NW) from the current cell to the nearest empty site are computed;

DA2.2 the directions are sorted from the shortest to the longest distance to the empty site;

DA2.3 the cell is shifted by one site in the direction with the lowest distance.

DA3: Steps DA2.1-DA2.3 are repeated until the current cells reaches an empty site.

This algorithm shifts a chain of cells towards the spheroid's boundary and mimics the way in which growing cells exert mechanical stress on their neighbours to generate spheroid expansion. We illustrate how the algorithm works in Fig. 5.4. The dividing parent cell (P) pushes cells 1, 2 and 3 outwards in the direction determined by the division algorithm to create space for its daughter (D). In contrast to Zacharaki et

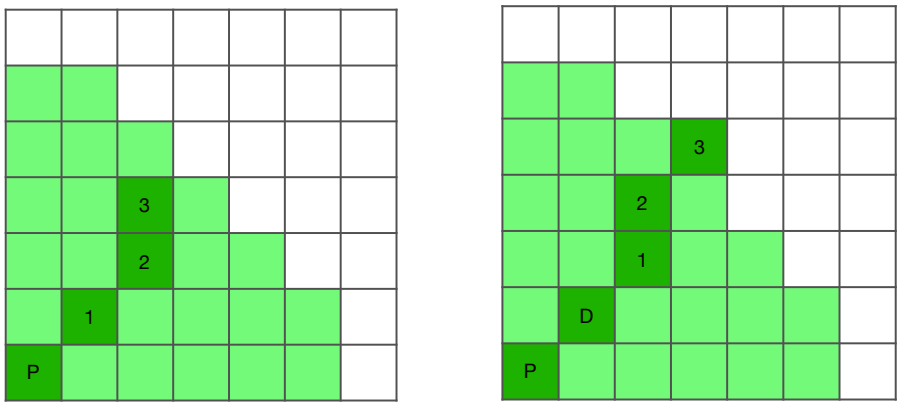

Figure 5.4: Chain shifting following a cell division event. State of the grid before (a) and after (b) division. Green cells are proliferating and white cells are empty.

al. [202] who shifted the cell chain in a random direction, we assume that the chain is pushed along the path of least resistance.

5.2.1.3 Cell death and lysis

A cell becomes necrotic if the oxygen concentration at its location falls below a threshold value $c_{\mathcal{N}}$. Necrotic cells can be lysed with probability p_{lys}. At each computational step we asynchronously loop over all necrotic cells and generate a random number $\psi \sim U(0,1)$ for each of them. If $\psi < p_{lys}$ then the cell is removed from the grid and a chain of cells is shifted from the spheroid boundary towards the location of the removed cell. In Fig. 5.5 we show how the algorithm shifts cells 1, 2, 3, 4 and 5 following lysis of cell R. In order to preserve spheroidicity we select the cell on the boundary that is located furthest away from the spheroid centre (or choose randomly if multiple cells lie at the same distance from the centre). The resulting cell rearrangement occurs within one computational step. This assumption was made to keep the model simple and ensure that the spheroid remains approximately spherical.

5.2.2 Oxygen dynamics

Following [75, 153, 44], a reaction-diffusion equation (RDE) models the concentration of oxygen within our simulation domain. If we denote the oxygen concentration at location $\mathbf{x}$ and time t by $c(\mathbf{x}, t)$ then its rate of change is given by

$$\frac{\partial c(\mathbf{x}, t)}{\partial t} = D\nabla^2 c(\mathbf{x}, t) - \kappa(\mathbf{x}, t)\mathbb{1}(\mathbf{x}, t), \tag{5.1}$$

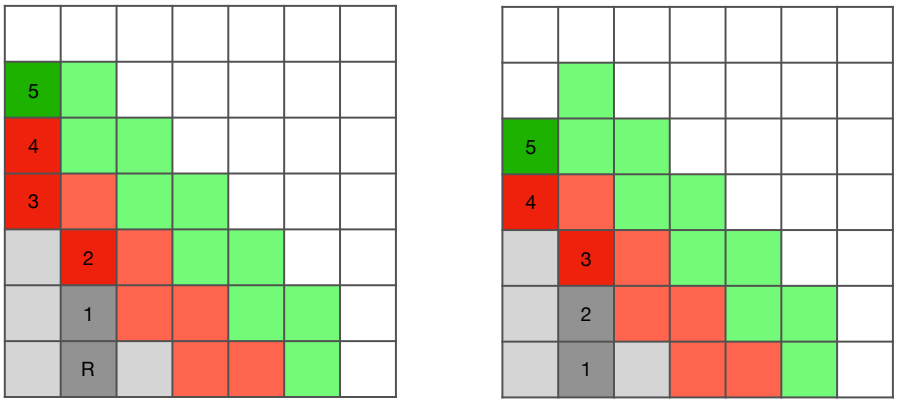

(a) **(b)**

Figure 5.5: Chain shifting following lysis. State of the grid before (a) and after (b) cell removal. Green cells are proliferating, red cells are quiescent, grey cells are necrotic and white cells are empty.

where D is the (constant) oxygen diffusion coefficient, $\kappa(\mathbf{x}, t)$ is the oxygen consumption rate and

$$\mathbb{1}(\mathbf{x}, t) = \begin{cases} 1 & \text{if } \mathbf{x} \text{ is occupied by a proliferating or quiescent cell} \\ 0 & \text{otherwise.} \end{cases}$$

Equation (5.1) is supplemented by the following initial and boundary conditions

$$c(x, y, 0) = c_\infty, \tag{5.2}$$

$$c(0, y, t) = c(L, y, t) = c(x, 0, t) = c(x, L, t) = c_\infty \tag{5.3}$$

where L is the domain length and c_∞ is the background O_2 concentration. Equations (5.1)–(5.3) describe a situation in which O_2 diffuses from the boundaries of a Petri dish (where it is maintained at fixed levels) into the culture medium and spheroid where it is consumed by tumour cells.

5.2.2.1 Nondimensionalisation

In order to simplify model simulations and analysis we nondimensionalised equations (5.1)–(5.3) by substituting

$$c = \tilde{c}c_0, \quad t = \tilde{t}t_0, \quad x = \tilde{x}x_0, \quad y = \tilde{y}y_0,$$

choosing

$$c_0 = c_\infty, \quad x_0 = y_0 = L, \quad t_0 = \frac{L^2}{D}$$

and defining

$$\tilde{\kappa} = \frac{L^2 \kappa}{D c_\infty}$$

where L is a typical length scale, here equal to the length of the computational domain. We can think of t_0 as the time scale for the diffusion process to affect the entire computational domain. Scaling O_2 concentration by its background level implies that $\tilde{c} \in (0, 1)$.

The dimensionless form of the equation describing oxygen concentration is thus given by

$$\frac{\partial c(\mathbf{x}, t)}{\partial t} = \nabla^2 c(\mathbf{x}, t) - \kappa(\mathbf{x}, t) \mathbb{1}(\mathbf{x}, t) \tag{5.4}$$

with the initial and boundary conditions

$$c(x, y, 0) = 1, \quad c(0, y, t) = c(1, y, t) = c(x, 0, t) = c(x, 1, t) = 1 \tag{5.5}$$

where henceforth tildes are dropped for convenience. In what follows, we will refer to dimensionless variables unless otherwise stated.

5.2.2.2 Numerical scheme

We construct approximate solution to equations (5.4) and (5.5) by discretising the computational domain and replacing partial derivatives with their finite difference approximations. The computational domain is replaced by a regular $N \times N$ grid of points, with constant spacing Δx. At a fixed t, the spatial derivatives are approximated by the second order symmetric finite difference formulae

$$\frac{\partial^2 c}{\partial x^2} \approx \frac{c(x + \Delta x, y, t) - 2c(x, y, t) + c(x - \Delta x, y, t)}{(\Delta x)^2}$$

and

$$\frac{\partial^2 c}{\partial y^2} \approx \frac{c(x, y + \Delta x, t) - 2c(x, y, t) + c(x, y - \Delta x, t)}{(\Delta x)^2}.$$

The time derivative was approximated with the first order forward difference formula

$$\frac{\partial c}{\partial t} \approx \frac{c(x, y, t + \Delta t) - c(x, y, t)}{\Delta t}$$

where Δt is the timestep. Under these assumptions, our explicit iterative finite difference scheme for approximating the solution to equation (5.4) is given by

$$\begin{aligned} c(x_i, y_j, t_{k+1}) = c(x_i, y_j, t_k) + \frac{\Delta t}{(\Delta x)^2} [c(x_{i+1}, y_j, t_k) + c(x_{i-1}, y_j, t_k) \\ + c(x_i, y_{j+1}, t_k) + c(x_i, y_{j-1}, t_k) - 4c(x_i, y_j, t_k)] - \Delta t \kappa \end{aligned} \tag{5.6}$$

for $i, j = 1, \ldots, N-2$ and $k = 0, \ldots, T$ with

$$c(x_i, y_j, t_0) = 1$$

and

$$c(x_0, y_j, t_k) = c(x_{N-1}, y_j, t_k) = c(x_i, y_0, t_k) = c(x_i, y_{N-1}, t_k) = 1.$$

In order for this numerical scheme to be stable we require that $\Delta t \leq \frac{(\Delta x)^2}{4}$.

5.2.3 Model parameters

5.2.3.1 Computational grid

The CA lattice on which the cells reside is the same size as the grid on which we solve the RDE for the O_2 concentration. In both cases $N = 200$. We consider the consequences of refining the grid on which the oxygen equation is solved in Appendix C.1. An average size of a PC3 cell, l_{PC3}, was estimated to be 0.0018 cm [137]. Thus our domain has the size of $L \times L$ (0.36 cm $\times$ 0.36 cm). Since we nondimensionalised the model parameters, both the cell size and grid spacing in the numerical scheme for solving equation (5.4) have the same size $\Delta x = 0.005$. To satisfy the stability condition for our numerical scheme we set $\Delta t = 6.25 \times 10^{-7}$.

5.2.3.2 Cell cycle duration

We estimated cell cycle times for the PC3 Ctrl and PC3 Res cell populations by seeding a small number of exponentially growing cells in a Petri dish and allowing them expand for 48 hours. We then counted the number of viable cells and estimated their doubling times using the exponential model. If we denote by N_0 the number of cells at $t = 0$ and by N_{48} the number of cells at $t = 48$ (hours) then the growth rate k (h^{-1}) in the exponential model ($N_t = N_0 e^{kt}$) can be estimated by

$$k = \frac{\log\left(\frac{N_{48}}{N_0}\right)}{48}$$

and the doubling time is given by $t_d = \frac{\log(2)}{k}$ hours. The average cell cycle time of the PC3 Ctrl was estimated to be $\bar{\tau}_{cycle} = 18.3$ h with standard deviation $\sigma_{cycle} = 1.4$ h. The PC3 Res cells divided faster with mean $\bar{\tau}_{cycle} = 16.9$ h and standard deviation $\sigma_{cycle} = 0.9$ h. These estimates were based on six independent measurements.

Table 5.1: Summary of parameters used in the simulations.

Parameter	Description	Value	Units	Ref.
l_{PC3}	Cell size	0.0018	cm	[137]
L	Domain length	0.36	cm	Estimated
$\bar{\tau}^{Ctrl}_{cycle}(\sigma^{Ctrl}_{cycle})$	Average cell cycle duration and corresponding standard deviation for the PC3 Ctrl cells	18.3(1.4)	h	Estimated
$\bar{\tau}^{Res}_{cycle}(\sigma^{Res}_{cycle})$	Average cell cycle duration and corresponding standard deviation for the PC3 Res cells	16.9(0.9)	h	Estimated
c_∞	Background O_2 concentration	2.8×10^{-7}	mol cm^{-3}	[68]
D	O_2 diffusion constant	1.8×10^{-5}	cm^2 s^{-1}	[81]
c_Q	Proliferation O_2 concentration threshold	$(0, 2.8 \times 10^{-7})$	mol cm^{-3}	Estimated
c_N	Quiescence O_2 concentration threshold	$(0, c_Q)$	mol cm^{-3}	Estimated
κ	O_2 consumption rate of proliferating cells	$(1.0 \times 10^{-9}, 1.0 \times 10^{-8})$	mol cm^{-3} s^{-1}	[68]
κ_Q	O_2 consumption rate of quiescent cells	0.5κ	mol cm^{-3} s^{-1}	Estimated
p_{lys}	Rate of lysis	$(0, 0.5)$	h^{-1}	Estimated

5.2.3.3 Oxygen concentration

In the absence of direct measurements of the O_2 concentration in culture medium we used the estimate reported in [68] and set the background O_2 concentration to $c_\infty = 2.8 \times 10^{-7}$ mol cm^{-3}. The O_2 diffusion constant within a growing spheroid was set to $D = 1.8 \times 10^{-5}$ cm^2 s^{-1} [81]. Since the diffusion of O_2 in culture medium is likely to be higher than within the spheroid [93], we assumed that the concentration of O_2 within the medium was replenished on a faster timescale than within the spheroid. In practice this means that O_2 levels in the culture medium were held constant at the background O_2 concentration c_∞. Proliferating cells were assumed to consume oxygen with rate κ. Quiescent cells also consume oxygen but at a lower rate $\kappa_Q = 0.5 \times \kappa$.

Oxygen consumption measurements of the PC3 Ctrl and PC3 Res cells cultured in monolayers revealed that the Ctrl cells consume more oxygen than Res cells by a factor of 1.4[1]. As shown previously, cells in tumour spheroids are known to consume less oxygen than in monolayers [68]. In the absence of estimates of the O_2 consumption rates of the PC3 spheroids, we treated κ as a free parameter and explored its influence on spheroid growth. Based on the results of the experiments to determine O_2 consumption rates in monolayers we considered different values of κ for control and resistant cells. The values of $c_{\mathcal{Q}}$ and $c_{\mathcal{N}}$ were also difficult to estimate and so we treated them as free parameters too.

[1]Measurements were performed and kindly provided by Dr Pavitra Kannan

5.3 Relationship between model parameters at micro- and macro-scale levels

With the recent increase in computational power the interest in individual cell models has also risen [162]. This prompted some researchers to explore the relationships between agent-based models and more traditional continuum models. Among others, Anderson et al. [10] presented continuum and discrete models of tumour invasion. Drasdo described an off-lattice model of cell population growth in monolayers as a cellular automaton, and then derived a continuum equation based on the latter [54]. Byrne and Drasdo compared simulations of an off-lattice and cellular automaton models to corresponding continuum descriptions of cell population growth [37]. Here we investigate how changes in parameter values at the level of single cells affect the behaviour at the macroscale. In particular, we investigate the relationship between the CA model parameters κ, p_{lys}, c_Q and c_N, and the logistic model parameters r and K.

A single realisation of the CA model described in the previous section can be time consuming. Analysing the model requires a large number of realisations with different parameter values. Moreover, since the model is stochastic, multiple realisations using identical parameter values can lead to variable outcomes. Thus in this section, we first determine the level of variability associated with the CA model of homogeneous spheroid growth. Then we use the CA model to generate synthetic data which we fit to the logistic model. In this way, we aim to establish relationships between the cell-scale parameters that characterise the CA and macroscale parameters associated with the logistic growth model.

5.3.1 Variability in the CA model of homogeneous spheroid growth

Typical results from the CA model are shown in Fig. 5.6. In Fig. 5.6a, we show the spatial distributions of spheroids measured on different days. Initially, all cells are proliferating but on day 5 there is a central necrotic core surrounded by a layer of quiescent cells and a rim of proliferating cells. On day 30, the necrotic core is very large and it appears that the spheroid size and composition reached their equilibria.

To assess variability across multiple realisations of the CA model with identical parameter values, we performed 100 realisations of the model and plotted the volumes of the necrotic region, the combined volumes of the necrotic and quiescent regions, as well as the total spheroids volumes in the form of box and whisker plots (Fig. 5.6b).

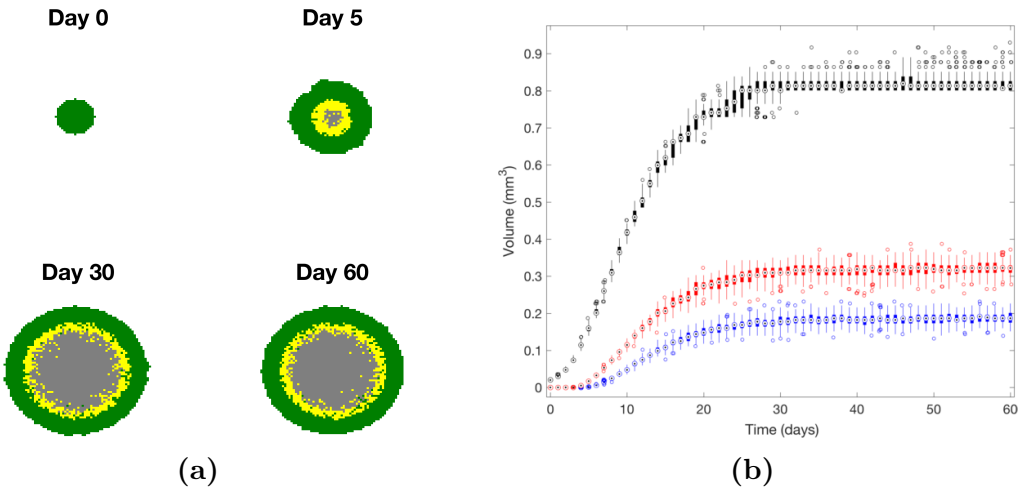

(a) (b)

Figure 5.6: Typical results from simulations of the 2D CA model showing spatial distributions of spheroids on different days from a single realisation of the model (a) and growth curves obtained from 100 realisations (b). In (a), the proliferating cells are green, quiescent cells are yellow and necrotic cells are grey. Plot (b) shows the total volumes of spheroids (black), the volumes of necrotic regions (blue) and the combined volumes of the necrotic and quiescent regions (red). The circled dots represent the median values, the boxes represent the interquartile ranges and the whiskers extending from the boxes mark the min. and max. values. The empty circles represent outliers. Spheroid volumes were estimated using the formula described in Section 2.2.8. Parameter values used to generate the data: $\bar{\tau}_{cycle} = 18.3$, $\kappa = 150$, $p_{lys} = 0.015$, $c_{\mathcal{Q}} = 0.8$ and $c_{\mathcal{N}} = 0.775$. Other parameter values as in Table 5.1.

The volumes of the synthetic spheroids were estimated using the same formula as that used to estimate the volumes of experimental spheroids (see Chapter 2 for more details). We measured the volumes at 24-hour intervals for 60 days.

For the given set of parameter values (see Fig. 5.6b and Table 5.1), the initial exponential growth of the spheroids gave way to linear growth and then plateaued at about day 30. Hypoxic cells appeared after about day 4 and necrotic cells shortly afterwards. The rapid onset of hypoxia and necrosis is due to relatively large and similar values of c_Q and c_N. As the size of the spheroids reached saturation the sizes of the necrotic and quiescent regions also plateaued. The equilibrium size is attained when the rate at which cells in the proliferating rim balances the rate at which cell debris is removed from the necrotic core.

Variability across different replicates was initially very low but increased as the spheroids grew, becoming stable at the saturation size (Fig. 5.6b). Although the volumes of necrotic and combined necrotic and quiescent regions seemed to follow Gaussian distribution, the values representing total spheroids volumes appeared to be negatively skewed at equilibrium. In particular, there was a clear lower bound for

the saturation size of volume V but much more variability at the upper bound with a few outliers (black box plots, Fig. 5.6b).

5.3.2 Fitting logistic model to CA spheroid growth curves

With the exception of a few outliers, the reproducibility of the stochastic CA model is high (Fig. 5.6b). However, since our objective is to estimate parameter values in the logistic model using CA growth curves, we must also establish the level of variability in the estimated parameters. In this section, we use nonlinear regression to fit the logistic model to each of the 100 synthetic growth curves summarised in Fig. 5.6b. We faced a number of options such as whether to apply a weighting scheme for the data, and whether to fix the initial condition $V(0)$ or treat it as a free parameter. The parameter $V(0)$ is known for the synthetic data as it corresponds to the volume of a spheroid on day 0. Since all simulations begin from placing a circular cluster of cells of radius 9 cells in the centre of the grid there is no variability in the spheroid size at $t = 0$. However, when performing *in vitro* experiments the spheroid volume is not known at $t = 0$ because it takes approximately three days for spheroids to form following seeding. We could have started measuring the volume from day 3 but the composition of heterogeneous spheroids would have changed by then. These deliberations led us to consider four regression models:

(A) fix $V(0)$ as a constant and estimate the growth rate r and carrying capacity K parameters without weighting data;

(B) estimate $V(0)$, r and K without weighting data;

(C) fix $V(0)$ as a constant and estimate r and K parameters with weighted data;

(D) estimate $V(0)$, r and K with weighted data.

The parameter values were estimated by minimising the weighted sum of squared residuals between CA synthetic data and logistic model outputs (see Chapter 4 for details). In cases where data were not weighted we fixed the weights $\hat{w}_i = 1$ for $i = 1, 2, \ldots, N$ where N is the number of available data points.

The results of the inference process are summarised in Fig. 5.7. Regression without weighting scheme (cases A and B) led to lower estimates of r and higher estimates of K and $V(0)$ than when data were weighted (cases C and D). The lowest estimate of r was achieved for the unweighted data model with three free parameters (case B), with the histogram peaking at $r \approx 0.25$ day^{-1}. This model also led to the

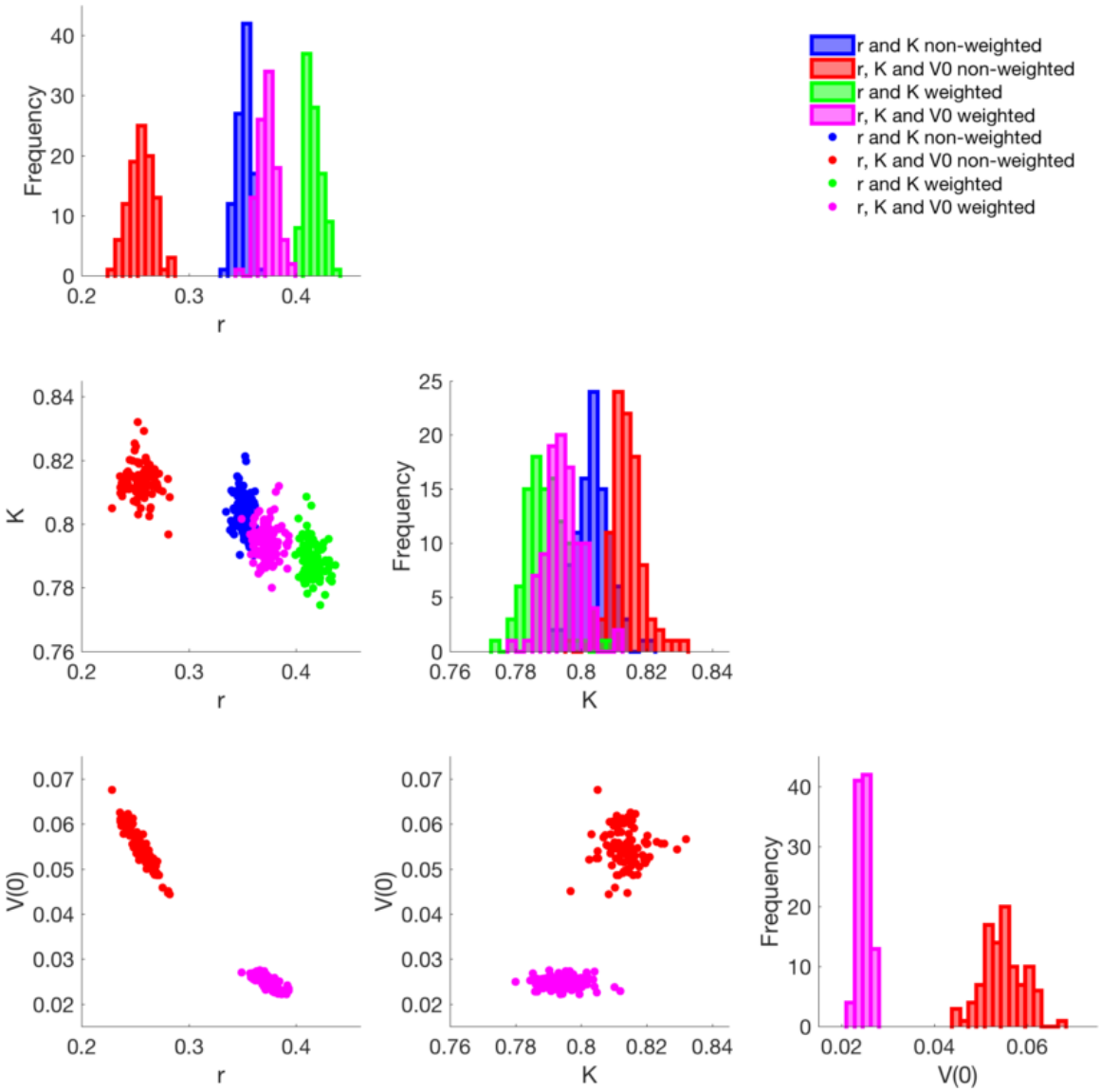

Figure 5.7: Distributions of and pairwise correlations between estimates of r, K and $V(0)$ in the logistic model for each of 100 CA growth curves for different regression models described in the text.

largest and perhaps most accurate estimate of K. It can be seen in Fig. 5.8 that the resulting growth curve (red dashed line) appears to go straight through the data at the saturation size, unlike other curves which lie below the data. The linear phase of the growth and transition to plateau are also described better than by any other model. On the other hand, the curve does not represent the data well in the initial stages of growth. The estimate of $V(0)$ is almost three times larger than its true value ($V^*(0) \approx 0.02$; Fig. 5.7). We also note a correlation between the estimates of r and $V(0)$, regardless of the weighting scheme used. Inaccurate representation of the data

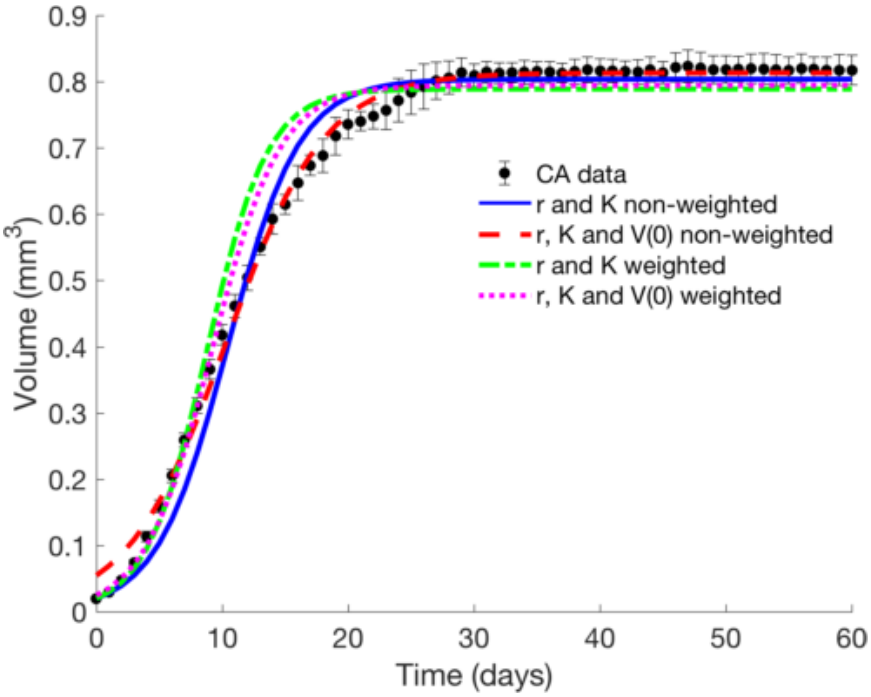

Figure 5.8: Best fits to the CA spheroid growth curves obtained with the four fitting methods. All the data were used to find the best parameter values. The CA data is represented as mean $\pm 1 \times$SD.

in the early stages of growth suggests that the estimates of r are also questionable when the three parameter model is fit to unweighted data (case B).

Fixing $V(0) = V^*(0)$ led to larger estimates of r and slightly lower K for the non-weighted data model (case A;blue histograms, Fig. 5.7). Although the first few days of the growth are described well by the resulting curve, it does not capture the linear growth phase well (blue curve, Fig. 5.8).

Deploying a weighting scheme (cases C and D) resulted in larger estimates of r and lower estimates of K. In these cases, we consider relative rather than absolute vertical distances between the CA data and fitted curve. Consequently, we treat all data points with equal importance as opposed to giving more significance to data points with higher residuals. Visual inspection of Fig. 5.6b suggests that the average amount of scatter increases with spheroid volume. Thus using a weighting scheme here is justified and more appropriate than not weighting the data.

The estimates of K are very similar for both weighted data models (Fig. 5.7). However, the histograms of estimates of r barely overlap and achieve peaks at approximately 0.38 and 0.42 (day^{-1}) for cases C and D, respectively. Additionally, when $V(0)$ is treated as a free parameter its estimates are slightly larger than $V^*(0)$, even though the scatter is lower than with the non-weighted data scheme. Both methods

with weighted data capture the initial stages of growth very well but overestimate the volume at the transition from linear growth to equilibrium (Fig. 5.8).

As noted before, the variance associated with CA spheroid measurements increases with spheroid size (except of the transition from linear growth to equilibrium where the scatter appears to be larger than anywhere else along the curve; Fig. 5.6b). Since our goal is to accurately estimate parameter values in the logistic model, fixing $V(0) = V^*(0)$ is appropriate as we eliminate uncertainty associated with this parameter. We cannot apply the same logic to the carrying capacity parameter K due to variability in volume measurements at the equilibrium size (Fig. 5.6b). As a result, the appropriate model in these circumstances seems to be regression with weighted data and two free parameters r and K (case C).

Interestingly, the method that appears to be most appropriate leads to the largest error as measured by the sum of squared residuals between CA volume data and best estimated growth curves (Fig. 5.9, C). The lowest errors were observed for what is

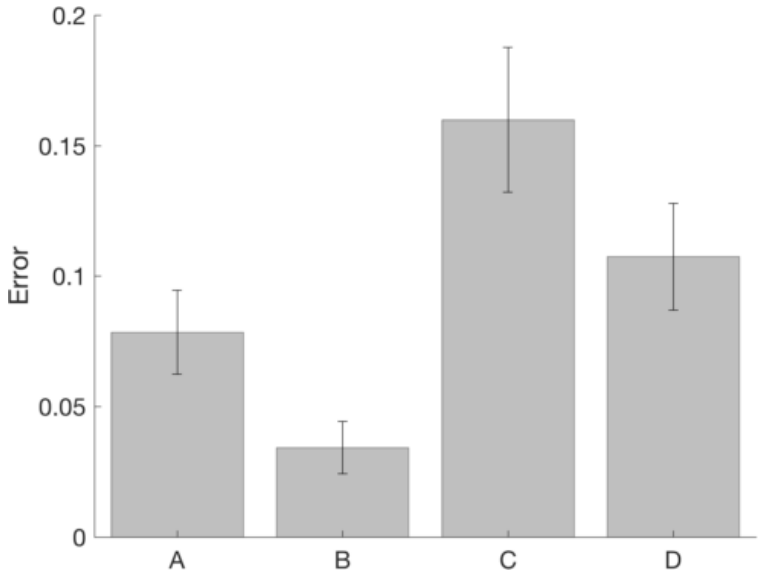

Figure 5.9: Errors (sums of squared residuals) associated with the four models: A) r and K non-weighted; B) r, K and $V(0)$ non-weighted; C) r and K weighted; D) r, K and $V(0)$ weighted. Bars represent the mean values from 100 replicates and error bars show 1×SD.

arguably least appropriate model where we estimated all three parameters without a weighting scheme (Fig. 5.9, B). Overall, regression with weighted data led to larger errors than without weighting as did fixing $V(0)$. The latter observation is unsurprising as estimating three rather than two parameters often leads to a better fit. In such cases, in order to discriminate between different models, we can employ Akaike's

Information Criterion (AIC) method. The AIC equation is given by

$$AIC = N \cdot \ln\left(\frac{WSSR}{N}\right) + 2P \tag{5.7}$$

where N is the number of data points, $WSSR$ the weighted sum of squared residuals and P is the number of parameters being estimated. The model with the smallest AIC value is most likely to be correct. As can be seen in Table 5.2, the smallest value of AIC was obtained for the two-parameter model with weighted data (case C). This result confirms that it is the most appropriate method to estimate parameter values.

Table 5.2: AIC values for different regression models. Labels as in legend of Fig. 5.9.

Method	A	B	C	D
AIC value	-4.0×10^4	-4.5×10^4	-3.0×10^4	-3.1×10^4

In summary, we have shown that choices made when fitting the logistic model to CA generated growth curves can have a significant effect on the estimated parameter values.

Since one of our objectives was to determine the level of reproducibility of our stochastic CA model of homogeneous spheroid growth, we examined in more detail

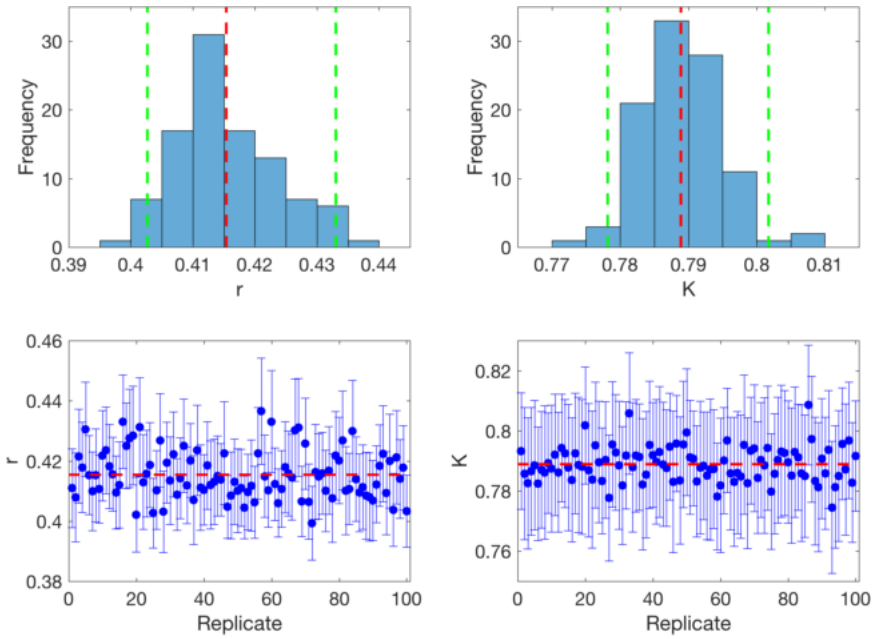

Figure 5.10: Estimated parameter values in the logistic model obtained with weighted-data regression for r and K. Red dashed lines show the mean value and green dashed lines show the 95% credible intervals. In the lower panel, the circles represent best estimated values and error bars show the 95% confidence intervals associated with each point estimate.

the estimated parameter values obtained with weighted-data regression for two parameters (case C; Fig. 5.10). Although some variability is clearly present (95% of the estimates of r lie between 0.40 and 0.43 (day^{-1}), and 95% of the estimates of K lie between 0.78 and 0.80 (mm^3)), the 95% confidence intervals associated with each estimate are narrow and most of the estimated values are clustered around the mean.

5.3.3 Relationships between CA and logistic model parameters

5.3.3.1 Oxygen consumption and lysis

Having established the level of reproducibility of the stochastic CA model of homogeneous spheroid growth, we now aim to establish the relationship between parameters in the CA and logistic models. We start by considering the effect that varying the oxygen consumption rate κ and probability of lysis p_{lys} have on the growth rate r and carrying capacity K. We then examine the impact of varying the O_2 concentration thresholds $c_{\mathcal{Q}}$ and $c_{\mathcal{N}}$ on the logistic model parameters.

To study how κ and p_{lys} affect r and K we set $\bar{\tau}_{cycle} = 18.3$, $\sigma_{cycle} = 1.4$, $c_{\mathcal{Q}} = 0.9$, $c_{\mathcal{N}} = 0.85$ and generated synthetic growth curves using the CA model for $\kappa = \{100, 150, 200, 250\}$ and $p_{lys} = \{0.005, 0.01, 0.015, 0.02\}$. We ran the model for 100 days and measured spheroid volumes at 24-hour time intervals. We then used the volume measurements to estimate parameter values in the logistic model. The parameter values chosen for this study led to spheroids that reached equilibrium sizes in the range 0.15–3.2 mm^3 and both quiescent and necrotic regions appeared within the growth period (Fig. C.2, appendix).

Our deliberations in the previous section led us to conclude that the most appropriate way to perform regression is to fix $V(0) = V^*(0)$, weight the data and estimate r and K only. In Fig. 5.11 we show the values estimated using this method. The uncertainty associated with the estimates of r and K, as measured by the 95% CIs, was reasonably low which is unsurprising given the amount of available data.

Fig. 5.11 reveals some interesting relationships between parameters in the CA and logistic models. The top panel shows a clear trend, with the growth rate r increasing approximately linearly with the probability of lysis p_{lys}. At the same time, increasing κ led to lower estimates of r. To explain these relationships we first observe that, for a given value of κ and with the O_2 thresholds $c_{\mathcal{Q}}$ and $c_{\mathcal{N}}$ fixed, spheroid growth is similar until necrotic cells begin to appear. Only when there are spheroid regions in which $c(\mathbf{x}, t) < c_{\mathcal{N}}$ does the effect of p_{lys} become apparent. As κ increases, all else

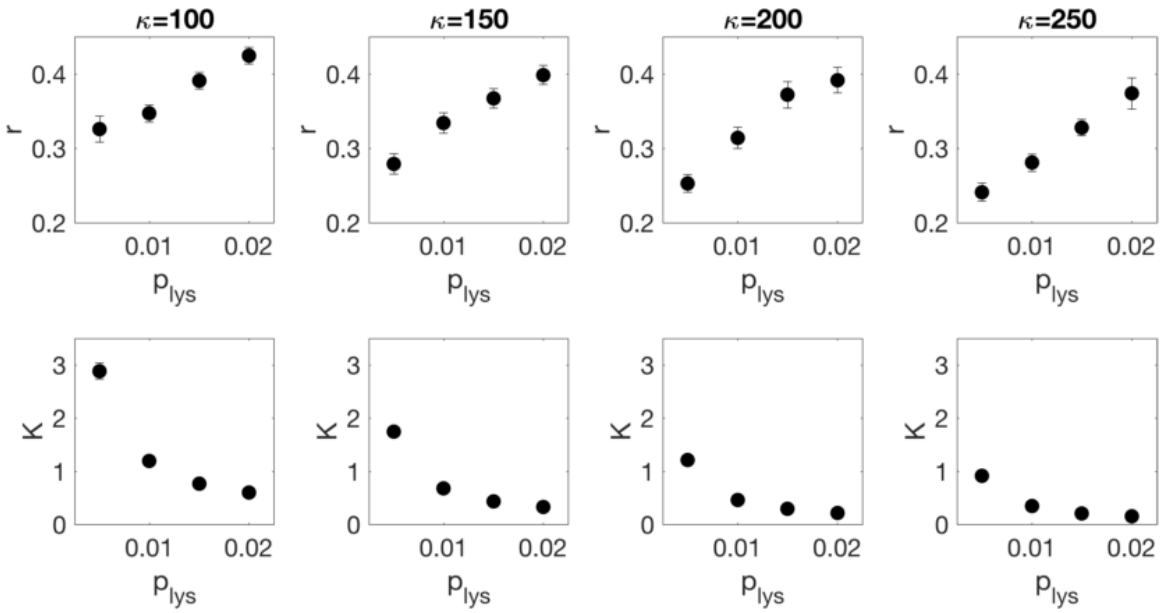

Figure 5.11: Estimated parameter values in the logistic model using CA growth curves generated for a range of (κ, p_{lys})-pairs. The parameters r and K were estimated using weighted-data regression with $V(0) = V^*(0)$. The circles represent best point estimates and the error bars 95% CIs.

being equal, the onset of hypoxia and necrosis occur sooner and at smaller spheroid volumes than for cells with lower O_2 requirements. For example, when $\kappa = 100$ quiescent cells appeared between days 2 and 3, and necrotic cells appeared between days 6 and 7 (Fig. 5.12a). In contrast, raising the cellular O_2 consumption rate from $\kappa = 100$ to $\kappa = 250$ while holding $c_{\mathcal{Q}}$ and $c_{\mathcal{N}}$ fixed led to cells becoming hypoxic on the first day of spheroid growth with necrosis beginning on day 4 (Fig. 5.12b). Consequently, for higher κ, growth retardation occurs sooner which is manifested in lower estimates of the growth rate r.

Similarly, cells that consume O_2 at a higher rate in order to proliferate and maintain life functions form smaller spheroids as O_2 levels are depleted more rapidly than for cells requiring less O_2. Proliferating cells at the spheroid surface consume oxygen at such a high rate that not enough oxygen reaches the spheroid centre. As a result, spheroids composed of cells with relatively low values of κ have higher carrying capacities than spheroids consisting of cells with relatively high O_2 consumption rates (bottom half, Fig. 5.11). These observations are consistent with experimental results. The PC3 Ctrl cells, shown to consume more O_2 than the PC3 Res cells, had lower growth rate and carrying capacity (Table 6.1).

Increasing the rate of lysis also led to smaller spheroids (bottom half, Fig. 5.11). Once necrosis begins, the rate of cellular disintegration and removal of necrotic debris

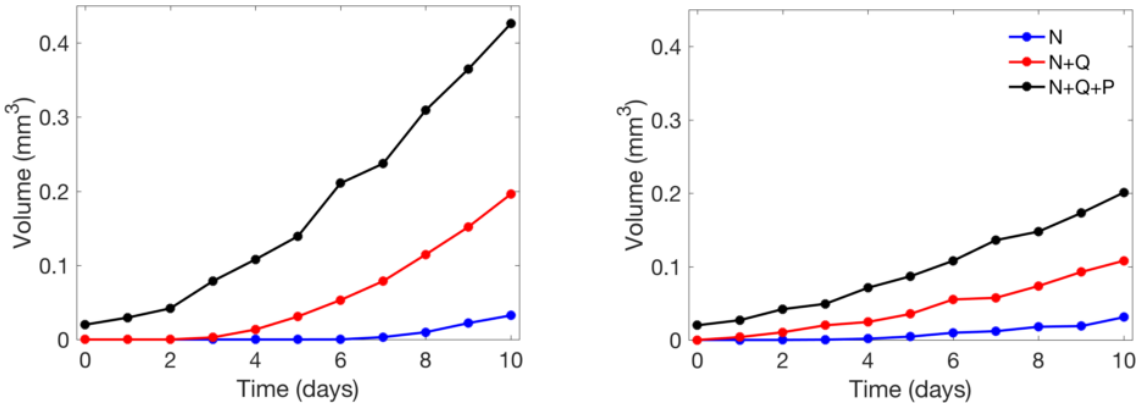

(a) $\kappa = 100$ **(b)** $\kappa = 250$

Figure 5.12: Synthetic growth curves showing initial stages of spheroid growth with $p_{lys} = 0.005$, $\kappa = 100$ (a) and $\kappa = 250$ (b).

are controlled by the parameter p_{lys}. The higher its value the faster necrotic debris is removed from the spheroid. In such cases, the carrying capacity is achieved more rapidly for higher p_{lys} and such spheroids are smaller than those with lower values of p_{lys}. Since the growth rate r regulates the rate of approach to the steady state—larger r implies more rapid approach to equilibrium—its values increase with p_{lys} (top half, Fig. 5.11). An examination of the spatial distribution of spheroids when they reached quasi-steady state revealed that the sizes of their necrotic cores (and hence the overall tumour volume) varied with p_{lys}. In particular, the necrotic cores were smaller for higher values of p_{lys}. For example, with $\kappa = 100$ as we varied p_{lys} the ratio of the radius of the necrotic core to the total spheroid radius decreased from ≈ 0.74 for $p_{lys} = 0.005$ to ≈ 0.48 for $p_{lys} = 0.02$ (Fig. 5.13). At the same time, the radii of quiescent and proliferating layers remained similar.

In summary, both κ and p_{lys} influence K: κ controls K by regulating the onset of hypoxia and necrosis while p_{lys} controls K by regulating the size of the necrotic core.

In the previous section we considered four different ways to perform regression for a single set of parameter values. In order to determine whether our conclusions are valid for other parameter sets we estimated the parameters in the logistic model using all four regression models for the CA growth curves generated in this section. As before, fitting for r, K and $V(0)$ without weighting the data led to the lowest estimates of r and highest estimates of K and $V(0)$, though the estimates of K were very similar for all methods (Fig. C.3, appendix). Weighted-data regression with $V(0) = V^*(0)$ led to the highest estimates of r and the other two methods to intermediate ones. The errors were also distributed in a similar way, with the seemingly most appropriate

method leading to the largest errors (Fig. C.4, appendix).

5.3.3.2 Oxygen-dependent transition thresholds

Recall that the parameters $c_{\mathcal{Q}}$ and $c_{\mathcal{N}}$ denote the threshold oxygen concentrations at which cells become quiescent and necrotic, respectively. In order to investigate the impact of varying $c_{\mathcal{Q}}$ and $c_{\mathcal{N}}$ on the fitted values of the growth rate r and the carrying capacity K in the logistic model, we fixed $\kappa = 190$, $p_{lys} = 0.015$ and generated growth curves from the CA model for a range of values of $c_{\mathcal{Q}}$ and $c_{\mathcal{N}}$. Our synthetic spheroids were grown for 60 days by which time they reached saturation size and showed hypoxia and necrosis.

Fig. 5.14 summarises the estimates of r and K obtained with two-parameter weighted-data regression (see Fig. C.5 for growth curves and best fits). The estimates of r increased with $c_{\mathcal{N}}$ but decreased with $c_{\mathcal{Q}}$, with a sharp drop at the transition from $c_{\mathcal{Q}} = 0.8$ to $c_{\mathcal{Q}} = 0.9$. The estimated values of K decreased approximately linearly as either threshold value was varied.

To explain these results we first note that the parameter $c_{\mathcal{Q}}$ controls the onset of hypoxia. For low values of $c_{\mathcal{Q}}$ hypoxia occurs later than for high values (note that initially all cells are proliferating). For example, increasing $c_{\mathcal{Q}}$ from $c_{\mathcal{Q}} = 0.2$ to $c_{\mathcal{Q}} = 0.9$ with $c_{\mathcal{N}} = 0.1$ reduced the time of hypoxia onset from day 8 to day 1 (Fig. 5.15a). Surprisingly, the time of necrosis onset increased from day 9 to day 26 at the same time. To explain this we first note that when the quiescence threshold

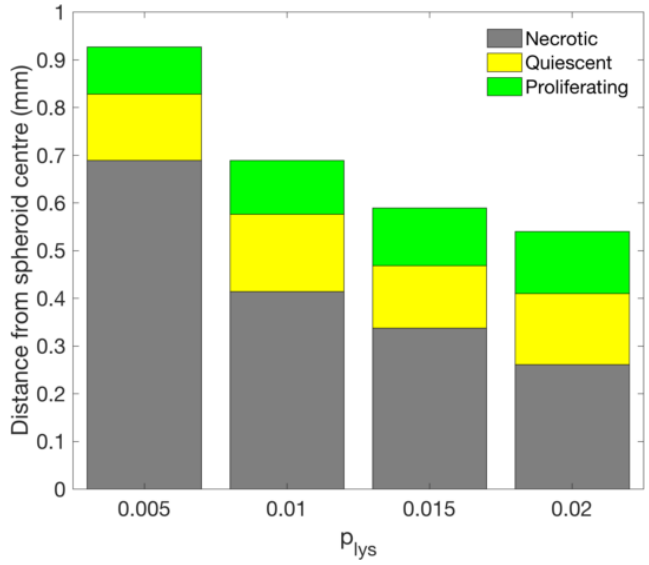

Figure 5.13: Spatial distributions of CA spheroids measured along spheroid radius for $\kappa = 100$ at saturation size.

is low a spheroid develops a thick proliferating rim before cells become hypoxic. As $c_{\mathcal{Q}}$ becomes larger, hypoxic cells appear sooner and the thickness of the proliferating rim decreases at the expense of quiescent layer. Since quiescent cells consume less oxygen than proliferating cells, it takes more time for oxygen levels to be depleted below $c_{\mathcal{N}}$ when cells become necrotic (see Fig. 5.15a). In Fig. 5.15b we show how the composition of the spheroids changes when they reach their carrying capacity (on day 60) as $c_{\mathcal{Q}}$ varies. The relative (and absolute, not shown) size of the hypoxic/quiescent layer increases with $c_{\mathcal{Q}}$ at the expense of the necrotic core and proliferating rim both of which decrease.

As the fraction of proliferating cells decreases with increasing $c_{\mathcal{Q}}$, the average spheroid growth rate must also decrease. The parameter r represents the intrinsic spheroid growth rate during the initial stages of growth, when the ratio $V(t)/K << 1$.

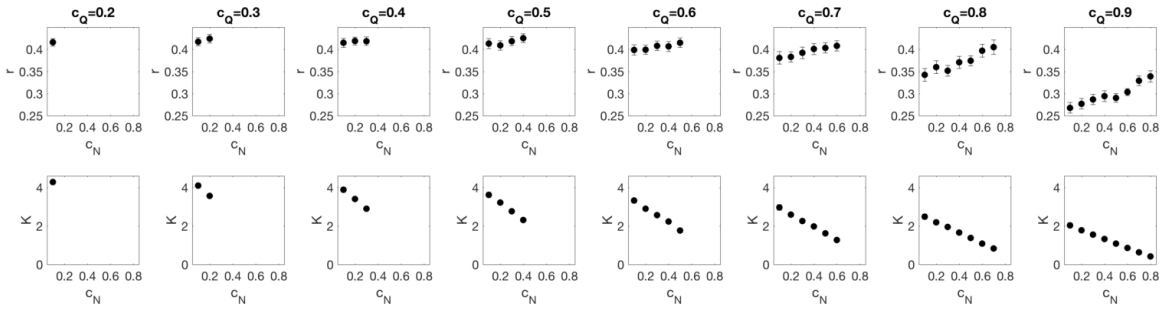

Figure 5.14: Parameter values in the logistic model estimated from a range of CA growth curves for different $(c_{\mathcal{Q}}, c_{\mathcal{N}})$-pairs. The parameters r and K were estimated using weighted-data regression with $V(0) = V^*(0)$. The circles represent best point estimates and the error bars 95% CIs.

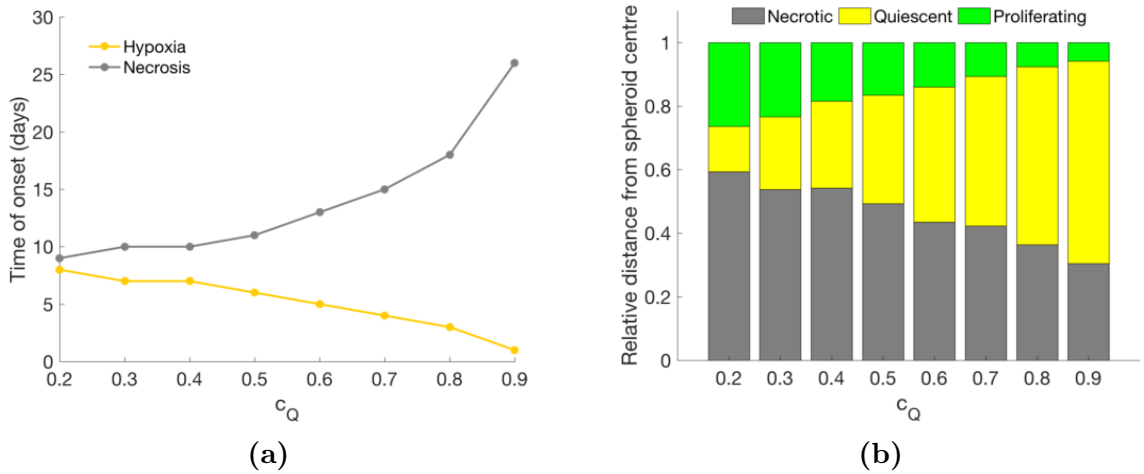

Figure 5.15: Time of hypoxia and necrosis onset (a) and relative spheroid compositions at growth saturation (b) for different values of $c_{\mathcal{Q}}$ and $c_{\mathcal{N}} = 0.1$.

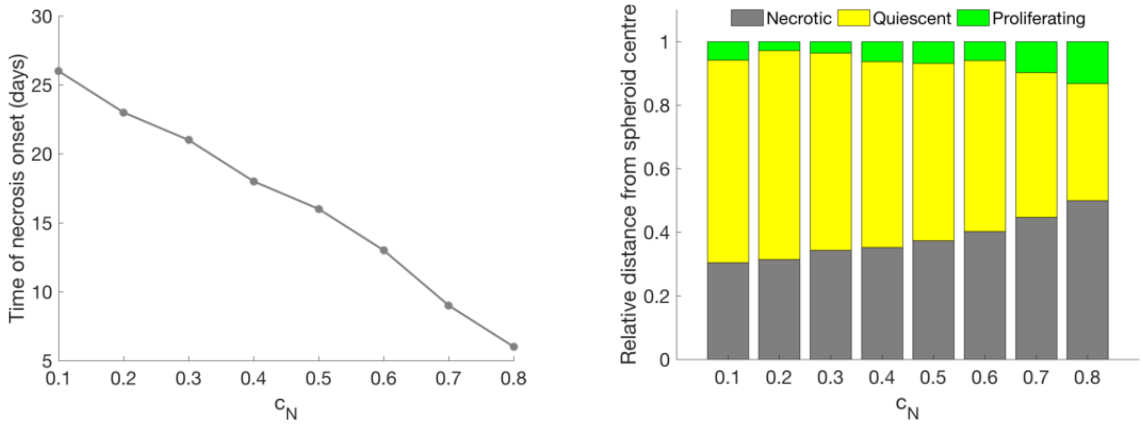

(a) **(b)**

Figure 5.16: Time of necrosis onset (a) and relative spheroid compositions at growth saturation (b) for different values of $c_{\mathcal{N}}$ and $c_{\mathcal{Q}} = 0.9$.

The transition from a proliferating to quiescent state for $c_{\mathcal{Q}} = 0.8$ occurred on day 3 whereas for $c_{\mathcal{Q}} = 0.9$ it occurred on day 1, which could explain the sharp fall in the estimates of r between these two cases (Fig. 5.14). The effect that $c_{\mathcal{Q}}$ has on r is, in some ways, similar to the effect that κ has on r. Both parameters determine the onset of quiescence. The smaller fraction of proliferating cells also explains the drop in the estimates of K for higher values of $c_{\mathcal{Q}}$.

Whereas $c_{\mathcal{Q}}$ controls the transition from proliferation to quiescence, $c_{\mathcal{N}}$ determines the onset of necrosis. When $c_{\mathcal{N}} = 0.1$ for fixed $c_{\mathcal{Q}} = 0.9$ necrotic cells first appear on day 26. Increasing $c_{\mathcal{N}}$ led to a marked reduction in the time of necrosis onset (Fig. 5.16a). When $c_{\mathcal{N}} = 0.8$, necrosis emerges as early as day 6. The sooner necrosis began to develop the larger the *relative* size of the necrotic core was observed (Fig. 5.16b). However, the *absolute* size of the necrotic core remained constant across all values of $c_{\mathcal{N}}$ (data not shown). The relative and absolute sizes of the quiescent zone decreased at the same time and no clear trend was observed for the proliferating rim. As reported earlier, the size of the necrotic core is controlled by the rate of lysis, p_{lys}, whereas the parameter $c_{\mathcal{N}}$ affects the stage of growth at which necrosis occurs. For a fixed value of $c_{\mathcal{Q}}$, quiescence emerges at the same time (and volume), regardless of the value of $c_{\mathcal{N}}$. If $c_{\mathcal{N}}$ is low, the spheroid grows for a longer period of time than when $c_{\mathcal{N}}$ is high because necrosis onset is delayed (Fig. 5.16a). Once necrosis is initiated, the size of the necrotic core is controlled by the rate of lysis. Thus the spheroids with delayed necrosis onset are larger and as a result the estimates of K decrease with increasing $c_{\mathcal{N}}$. Similarly, growth saturation of spheroids with higher values of $c_{\mathcal{N}}$ is reached faster than for lower values of $c_{\mathcal{N}}$ (see Fig. C.5). As the parameter r

in the logistic model influences the rate at which spheroids approach their carrying capacity, the estimates of r increase with $c_{\mathcal{N}}$ (top half, Fig. 5.14).

When investigating the role of factors, such as the doubling time, clonogenic capacity, diameter of viable cells, cell line, packing density and initial spheroid growth rate, on the saturation sizes of spheroids from 15 different cell lines, Freyer [67] did not find any correlation between these factors and saturation sizes, except of the size at which necrosis initially developed. Since the onset of necrosis depends on the availability of metabolites (such as oxygen), Freyer hypothesised that the relationship between spheroid saturation size and the size at which necrosis initially developed could be explained by cellular differences in metabolite consumption rate and sensitivity to its low levels. To determine whether our model reproduces this relationship (and to confirm Freyer's hypothesis), we plotted spheroid saturation volumes as a function of spheroid volume at the onset of necrosis for different values of $c_{\mathcal{N}}$ (Fig. 5.17a) and for different values of κ (Fig. 5.17b). We found a clear positive correlation between the two variables in both cases.

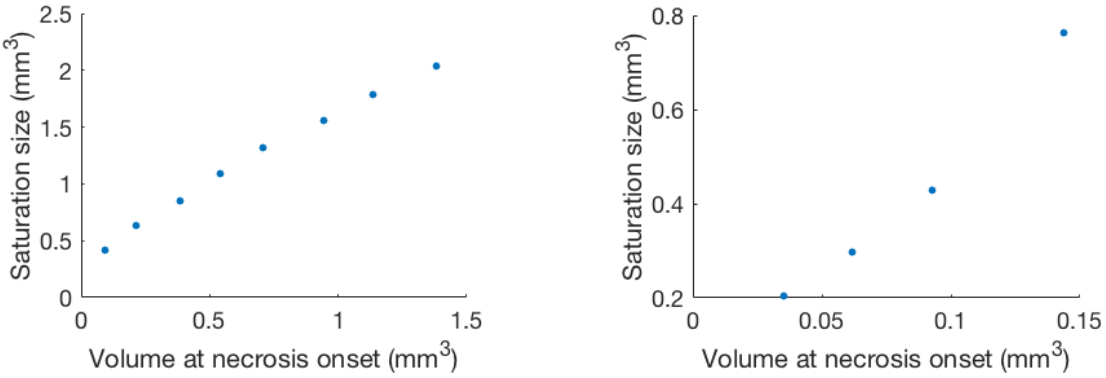

Figure 5.17: Correlations between volumes at necrosis onset and at saturation size of spheroids generated for different values of $c_{\mathcal{N}}$ (a) and κ (b).

5.4 Summary

In this chapter, we presented a hybrid model of tumour spheroid growth in which a stochastic cellular automaton model describing cell proliferation and death is coupled to a PDE for the oxygen distribution. Most of the model parameters were estimated from our *in vitro* experiments or from existing literature. The model was used to establish relationships between four parameters in the CA model (the oxygen consumption rate κ, the probability of lysis p_{lys} and the oxygen concentration thresholds

$c_{\mathcal{Q}}$, $c_{\mathcal{N}}$ at which cells become quiescent and necrotic), and the growth rate and carrying capacity parameters in the logistic model of tumour growth. To determine how CA model parameters affected logistic model parameters, we fitted the latter to synthetic growth curves generated with the former, using four different regression models (Figs. 5.11, 5.14 and C.3). We found that the choice of regression model had a significant impact on the estimated values. We also found that the growth rate r in the logistic model increased with the probability of lysis and the oxygen concentration threshold at which cells become necrotic $c_{\mathcal{N}}$, and decreased with the oxygen consumption rate κ and oxygen quiescence threshold $c_{\mathcal{Q}}$. Predictably, estimates of the carrying capacity parameter K decreased for increasing values of all four CA model parameters considered.

Due to time limitations, we used only one realisation of our stochastic model for each set of parameter values when investigating the relationship between the CA and logistic models parameters. In future work it would be useful to perform multiple realisations of the model for each set of values in the CA model. Nonetheless, the trends revealed by our analyses were as expected. We reported that the estimated values of the intrinsic growth rate parameter r in the logistic model increased with the probability of lysis p_{lys} and necrosis oxygen concentration threshold $c_{\mathcal{N}}$. The parameter $c_{\mathcal{N}}$ controls the time and spheroid size at which necrosis emerges and p_{lys} controls the size of the necrotic core and the rate at which saturation size is attained. Increasing either $c_{\mathcal{N}}$ or p_{lys} leads to smaller spheroids but also reduces the time at which growth saturation is reached. Thus the parameter r in the logistic model controls not only the growth rate at the initial stages of growth but also the rate at which the saturation size is attained.

Our work highlights the importance of choosing an appropriate regression model when fitting models to data. In this chapter, we considered four regression models that differed in weighting schemes and number of parameters. We concluded that, for the examples considered here, using a weighting scheme was appropriate because the scatter in the data increased with spheroid size. We also decided to fix the value of $V(0)$ since, for the CA model, this value was known. However, weighting the data and fixing $V(0)$ led to large errors and simulation results that did not describe the data well (at late stages of growth). The implications of this work strengthen the results obtained in Chapters 3 and 4 where we fitted the logistic model to spheroid growth data without knowing the value of $V(0)$. Since we used the same weighting scheme there as in this chapter, we can be reasonably confident that our estimates of

$V(0)$ and r were more accurate than they would have been had we not weighted the data.

In the next chapter, we extend our CA model to test hypotheses about the modes of interaction between control and resistant cell populations in heterogeneous tumour spheroids.

Chapter 6

Cellular automaton model of avascular heterogeneous tumour growth

6.1 Introduction

In this chapter, we extend the CA model of avascular tumour growth from Chapter 5 to investigate the growth of heterogeneous spheroids obtained by co-culturing two populations of PC3 cancer cells with different growth kinetics. Our objective is to test hypotheses regarding interactions between the co-cultured cell populations. We first use the Lotka-Volterra model to show that the two clones compete when co-cultured. We then use the CA model with the goal to establish whether the competition is indirect (via competition for resources) or direct (via cell-cell communication). We proceed by first estimating parameter values in the CA model of homogeneous tumour growth for each cell population separately using the experimental data from homogeneous spheroids. Then, we fix the estimated values in the CA model of heterogeneous tumour growth and predict the growth of heterogeneous spheroids assuming that there are no direct interactions between the two cell types (our null hypothesis). Our reasoning is that if the CA model predictions agree with the experimental data then it indicates that we can explain the differences in the growth of heterogeneous spheroids by competition of resources alone. However, if the experimental data cannot be reproduced by the model, then it suggests the existence of cell-cell communication between the cell populations and we can reject the null hypothesis. Our strategy is summarised in a diagram presented in Fig. 6.1. We note that this method depends on our ability to accurately estimate parameter values in the CA model. We also make an implicit assumption that the parameter values estimated for homogeneous spheroids do not

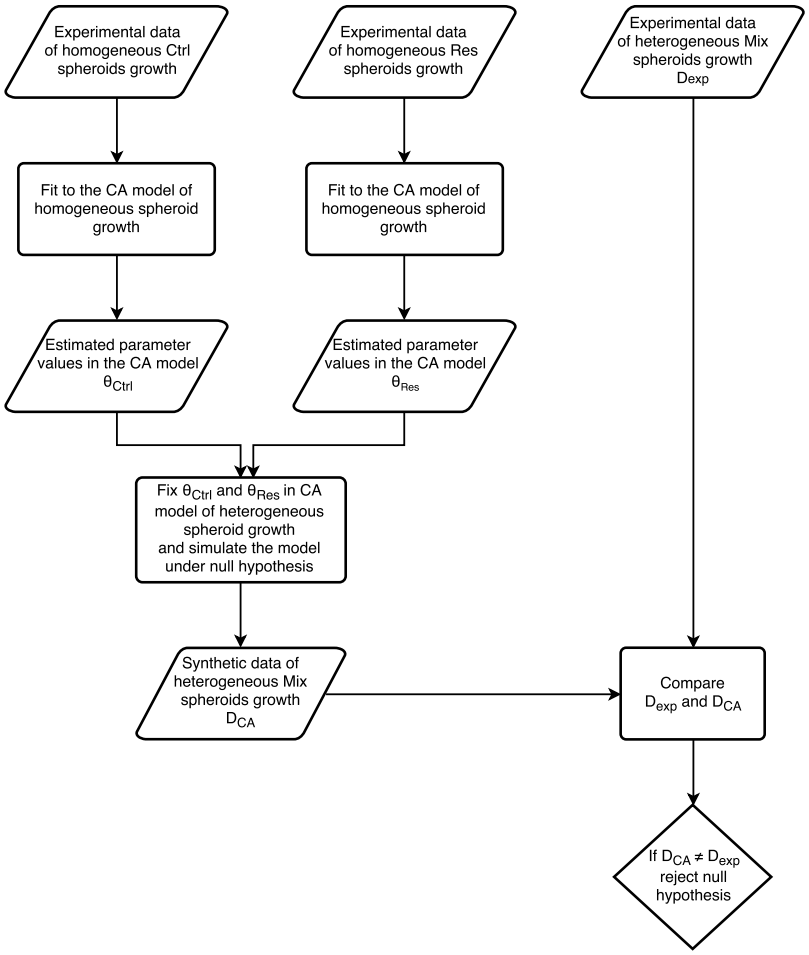

Figure 6.1: A diagram depicting our strategy to test the null hypothesis that the co-cultured PC3 cell populations do not interact directly.

change in heterogeneous spheroids for either cell population.

An additional aim of this chapter is to establish how well the Lotka-Volterra model describes growth curves from CA-derived heterogeneous spheroids data. In particular, we use the Lotka-Volterra model to determine the type and magnitude of interclonal interactions in the CA model under the null hypothesis that there is no cross-talk between the clones.

The remainder of this chapter is structured as follows: in Section 6.2 we describe experimental data of PC3 spheroid growth; in Section 6.3 we estimate parameter values in the CA model of homogeneous spheroid growth, in Section 6.4 we use the CA model to simulate the growth of heterogeneous spheroids; and in Section 6.5 we fit the Lotka-Volterra model to the synthetic growth curves generated in Section 6.4.

6.2 Experimental data from PC3 spheroids

When optimising conditions for spheroid formation in Chapter 2 we tested different types of culture medium, all of which were characterised by relatively high glucose content. Our aim was to reduce the impact of variables such as glucose levels that can affect spheroid growth. In order to mimic growth conditions that occur *in vivo*, the PC3 spheroids considered in this chapter were grown in culture medium with lower glucose levels. Below, we summarise these data. We note that all data presented in this chapter were collected and kindly provided by Dr Pavitra Kannan.

Volume measurements of control, resistant and mixed (1:1) spheroids were collected on days 3, 5, 10, 12, 15, 17 and 19. Proportions of the control and resistant populations in mixed spheroids were collected on days 5, 10, 15 and 19. The time points were determined using an experimental design study with synthetic data as described in Chapter 4. The resulting growth curves and proportion measurements were used to estimate parameter values in the Lotka-Volterra model (Eqs. [4.3]). In Fig. 6.2, we show the data and the corresponding best fits. The estimated parameter values are presented in Table 6.1.

The spheroids presented here were grown for longer than the PC3 spheroids described in Chapter 2 and they attained larger sizes (black box plots, Fig. 6.2). The control spheroids reached volumes of approximately 0.8 mm^3 by day 19 whereas the resistant spheroids grew to almost 2 mm^3 in volume. The growth of the heterogeneous spheroids was similar to that of the resistant ones, and the resistant population became dominant over time (Fig. 6.2c). Surprisingly, the PC3 spheroids grew better in low glucose conditions than when glucose levels were high and abundant. Although the spheroids were larger in low glucose, the trends observed for spheroids grown in high glucose medium were preserved: resistant spheroids grew faster than control spheroids, and attained much larger sizes; the growth of spheroids mixed at the 1:1 ratio was very similar to that of homogeneous resistant spheroids, and the resistant population established itself as the dominant clone in the heterogeneous spheroids.

We fitted the Lotka-Volterra model [4.3] to the spheroid data using the two-step and pooled data fitting protocols (see Chapter 4 for details). The estimated values were very similar for both methods. As for the PC3 spheroids grown in high glucose, we found that the growth rate and carrying capacity of the resistant population were higher than for the control cells. Based on our estimates of η_C and η_R we conclude that the control and resistant cells compete and that the control population has a stronger effect on the resistant population than the other way around.

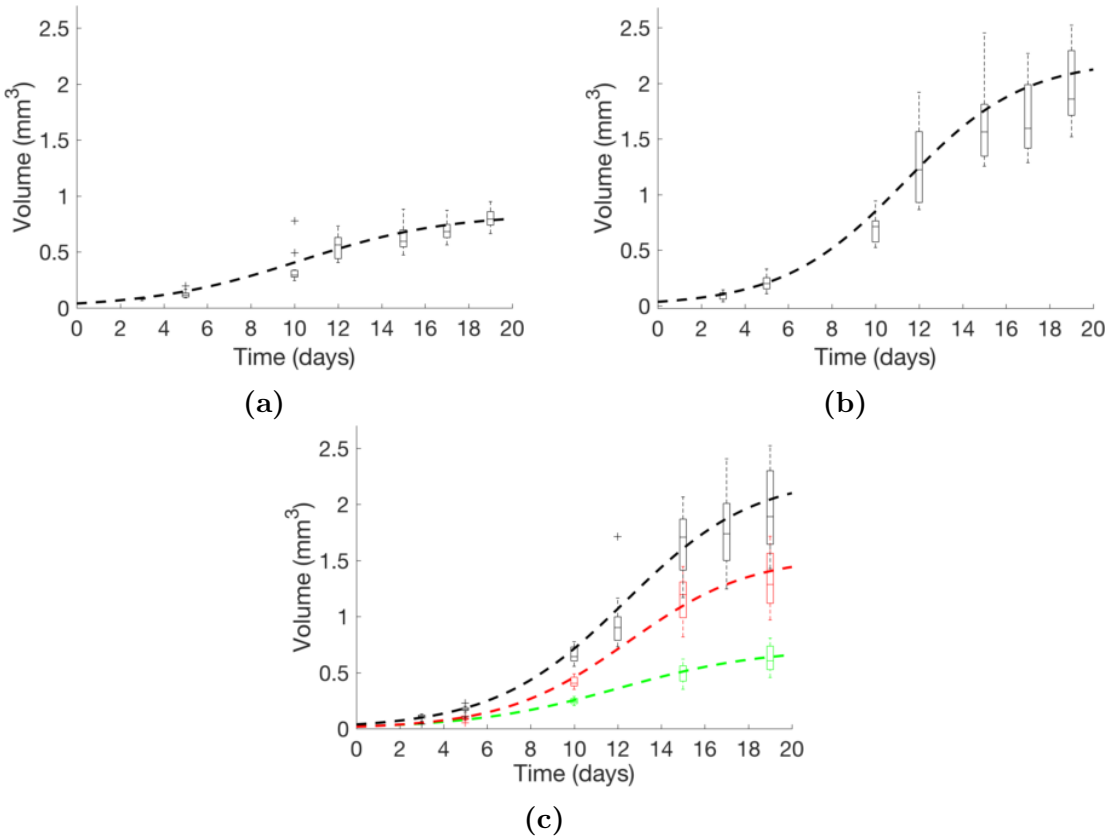

Figure 6.2: Experimental volume measurements and best fits to the growth curves data describing PC3 spheroids grown in low glucose conditions. Control (a), resistant (b) and mixed (c) PC3 spheroids and corresponding fits by the Lotka-Volterra model. Black box plots show the total volume measurements and dashed lines best fit curves. In (c), red and green box plots and dashed lines show the volumes of resistant and control clones, respectively.

Table 6.1: Parameter estimates in the Lotka-Volterra model [4.3] for the PC3 spheroids grown in low glucose conditions. Data show point estimates and corresponding 95% confidence intervals.

	Two-step protocol	**Pooled data protocol**
$\mathbf{r_C}$ **(day^{-1})**	**0.316** (0.272,0.360)	**0.293** (0.263,0.323)
$\mathbf{K_C}$ **(mm^3)**	**0.822** (0.722,0.922)	**0.843** (0.754,0.933)
$\mathbf{V_C(0)}$ **(mm^3)**	**0.034** (0.027,0.041)	**0.040** (0.033,0.047)
$\mathbf{r_R}$ **(day^{-1})**	**0.377** (0.325,0.428)	**0.363** (0.339,0.386)
$\mathbf{K_R}$ **(mm^3)**	**2.084** (1.782,2.386)	**2.217** (2.000,2.433)
$\mathbf{V_R(0)}$ **(mm^3)**	**0.037** (0.027,0.047)	**0.036** (0.032,0.042)
η_C	**0.178** (0.150,0.206)	**0.159** (0.112,0.206)
η_R	**0.035** (0.017,0.052)	**0.027** (0.001,0.053)

Images, taken on days 5 and 12, showing cross-sections of spheroids stained with different markers are presented in Fig. 6.3. Briefly, the control, resistant and mixed spheroids were stained with hematoxylin and eosin (H/E) to discriminate between

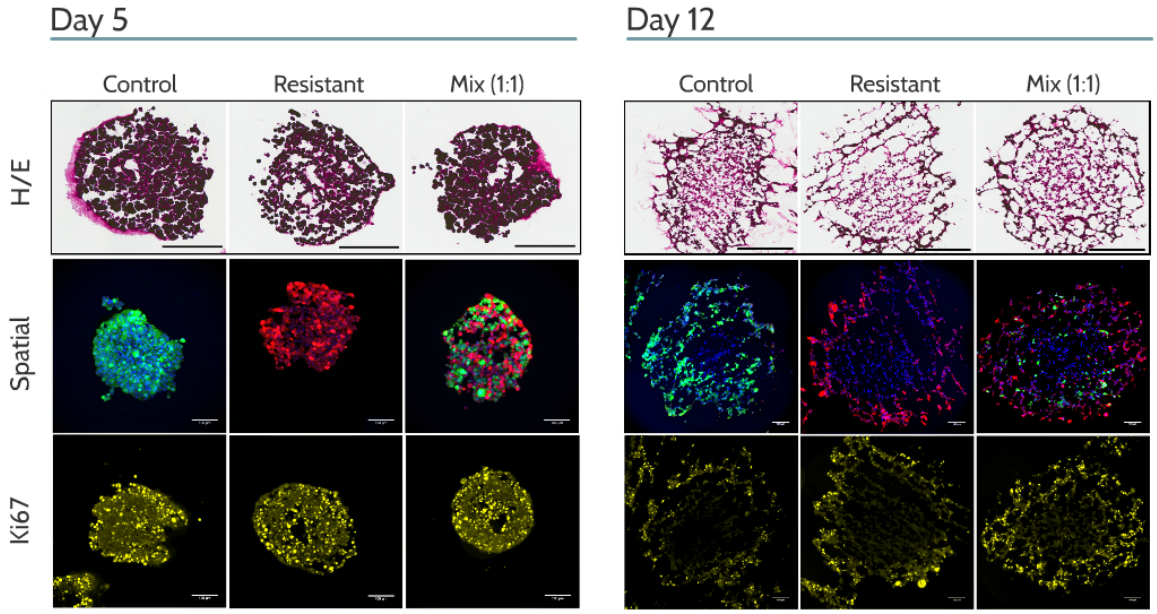

Figure 6.3: Images showing spatial distribution of stained PC3 spheroids (data collected and provided by Dr Pavitra Kannan).

viable and necrotic cells (top panel, Fig. 6.3). Hematoxylin binds to nucleic acids and stains cell nuclei in dark purple. Eosin stains cytoplasm and stromal components in pink. The middle panel of Fig. 6.3 shows the spatial distribution of fluorescently-labelled control (GFP-green) and resistant (DsRed-red) cells. The spheroids presented in the bottom panel of Fig. 6.3 were stained with the proliferation marker antigen Ki67 which is present in actively cycling cells and absent from quiescent cells.

H/E staining suggests that all cells within the spheroids were intact and viable on day 5. Ki67 staining shows that many cells actively participated in the cell cycle but proliferating cells were mainly concentrated at spheroid boundaries. We note also that the control and resistant cells were well mixed within heterogeneous spheroids on day 5.

On day 12, viable cells in the homogeneous and heterogeneous spheroids were mainly located at the spheroid boundaries, with the centres occupied by necrotic cells and debris. Ki67 staining indicates that many of these viable cells were actively dividing. The proliferating rim of the heterogeneous spheroids appear to be thicker than for the homogeneous spheroids. The images showing spatial composition on day 12 are consistent with the proportion measurements which showed that the resistant cells become dominant over time. However, the spatial images also reveal that the resistant cells were concentrated at the spheroid boundary while the control cells were located between the layer of resistant population and the necrotic core.

6.3 Parameter estimation in CA model of homogeneous spheroid growth

The main objective of this chapter is to determine whether the interactions occurring between the PC3 cell populations that have been co-cultured to form tumour spheroids are direct or indirect. In other words, we aim to establish whether competition predicted with the Lotka-Volterra model is due to competition for space and nutrients or direct cell-cell communication. To address this question, we start by estimating parameter values in the CA model for the control and resistant cell populations separately. We then use these parameter values to simulate the growth of heterogeneous spheroids under the null hypothesis which states that the two populations do not interact directly (see diagram in Fig. 6.1). If we recover the data observed *in vitro* then we will fail to reject the null hypothesis, concluding that direct communication is not necessary to explain the data.

Unfortunately, the quality of the images showing the spatial distribution of PC3 spheroids presented in the previous section is too poor for us to extract and quantify spatial information about the spheroids for use in the parameter inference process. Consequently, we use the growth curves of the homogeneous spheroids only, and consider the spatial information in a qualitative rather than quantitative manner.

6.3.1 ABC inference in the CA model using synthetic growth curves

Te determine if it is possible to infer the values of κ, p_{lys}, $c_{\mathcal{Q}}$ and $c_{\mathcal{N}}$ in the CA model of homogeneous tumour growth using only the growth curves data, we generate synthetic growth curves using the CA model and attempt to recover the four parameters using ABC inference.

Briefly, 100 growth curves were generated with the CA model for $\kappa = 154$, $p_{lys} = 0.015$, $c_{\mathcal{Q}} = 0.8$ and $c_{\mathcal{N}} = 0.775$. Volume data were collected every day until day 34, by which time the spheroids had attained saturation sizes of approximately 0.8 mm^3 (see Fig. 5.6b in Chapter 5). To ensure that $c_{\mathcal{Q}} > c_{\mathcal{N}}$, we estimated $c_{\mathcal{Q}}$ and $A = c_{\mathcal{N}}/c_{\mathcal{Q}}$ rather than $c_{\mathcal{Q}}$ and $c_{\mathcal{N}}$, noting that here $A = 0.969$. The values of κ, p_{lys}, $c_{\mathcal{Q}}$ and A were inferred with the rejection sampler algorithm described in Section 3.2.5. We used the weighted sum of squared residuals between the growth curves and model outputs as our distance function d in the ABC algorithm. The prior distributions for the parameters are given by: $\pi(\kappa) = U(0, 1800)$, $\pi(p_{lys}) = U(0, 0.25)$, $\pi(c_{\mathcal{Q}}) = U(0, 1)$ and $\pi(A) = U(0, 1)$, where U denotes a uniform distribution. We performed 5×10^4

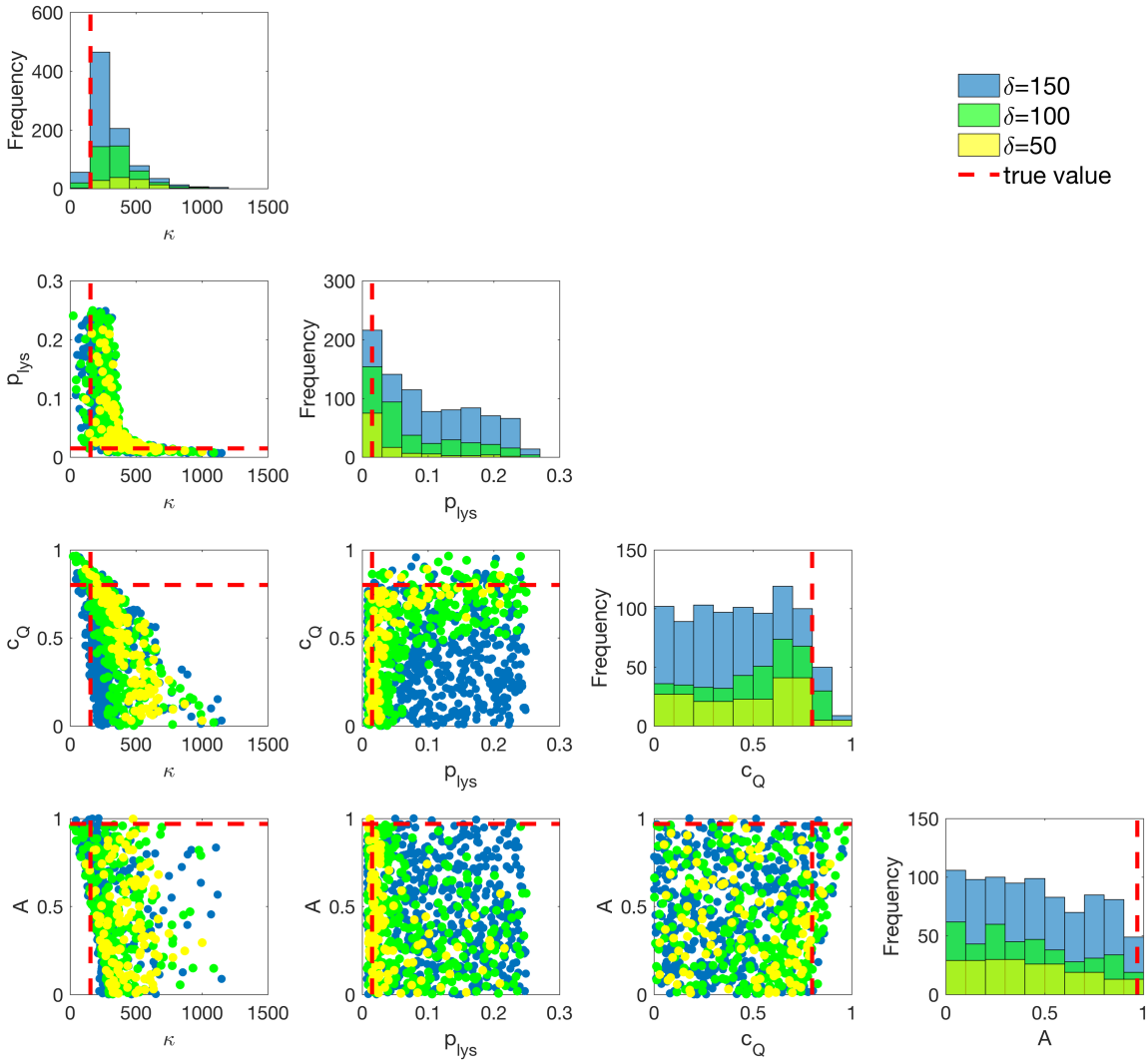

Figure 6.4: Posterior probability distributions and pairwise correlations between CA model parameters. Histograms show approximate posterior distributions and scatter plots show pairwise correlations between estimated parameters for different values of the tolerance δ. The red dashed lines indicate the true values of the parameters used to generate the data.

realisations of the rejection sampler algorithm and considered the effect of different values of tolerance δ on the results.

The estimated posterior distributions of κ, p_{lys}, $c_{\mathcal{Q}}$ and A are presented in Fig. 6.4 together with pairwise correlations between the estimated parameters. As seen in the figure, we were unable to recover true values of the parameters. Although decreasing the tolerance δ led to histograms approaching the true value of p_{lys}, the histograms for κ were skewed to the right of the true value and the histograms for $c_{\mathcal{Q}}$ and A remained approximately flat.

Since we could not infer all four parameters using growth curves data we decided to infer one of them. Therefore, we fixed the values of κ, p_{lys} and $c_{\mathcal{N}}$, and estimated $c_{\mathcal{Q}}$ alone. The posterior distributions of $c_{\mathcal{Q}}$ for decreasing values of tolerance δ are shown in Fig. 6.5. In this case, the histograms clearly approach the true value of $c_{\mathcal{Q}}$ as $\delta \to 0$. We repeated the inference process for κ holding the values of other parameters fixed,

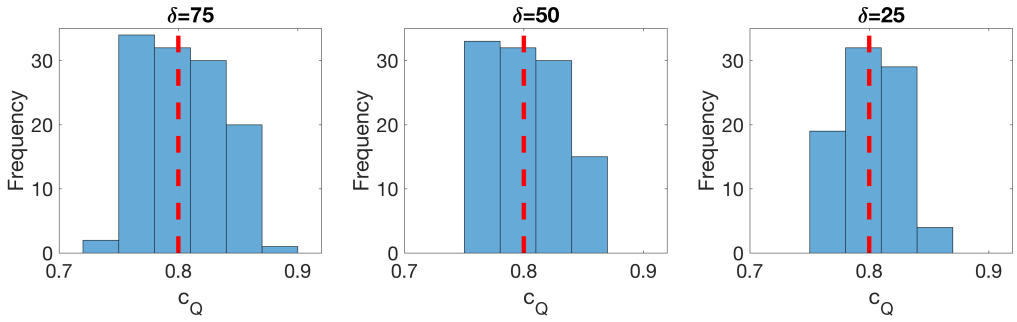

Figure 6.5: Posterior probability distributions of $c_{\mathcal{Q}}$ for different values of tolerance δ. The rejection sampler algorithm was used to recover the value of $c_{\mathcal{Q}}$ while other parameter values were held fixed: $\kappa = 154$, $p_{lys} = 0.015$, $c_{\mathcal{N}} = 0.775$.

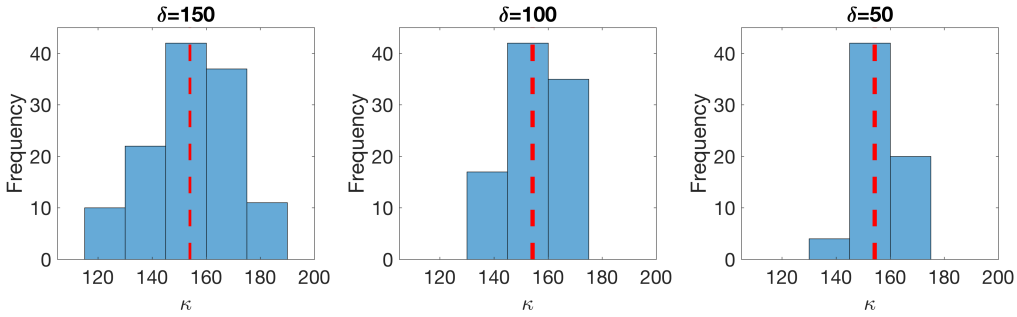

Figure 6.6: Posterior probability distributions of κ for different values of tolerance δ. The rejection sampler algorithm was used to recover the value of κ while other parameter values were held fixed: $p_{lys} = 0.015$, $c_{\mathcal{Q}} = 0.8$, $c_{\mathcal{N}} = 0.775$.

and found that the histograms of posterior distributions also approached the true value as $\delta \to 0$ (Fig. 6.6).

We then attempted to recover both κ and $c_{\mathcal{Q}}$ at the same time. In Fig. 6.7, we show the posteriors and correlations between the parameters. Inferring both κ and $c_{\mathcal{Q}}$ simultaneously is clearly not possible. We also identified strong correlations between κ and $c_{\mathcal{Q}}$.

Taken together, the data in Figures 6.4 and 6.7 suggest that the CA model in its current form (with κ, p_{lys}, $c_{\mathcal{Q}}$ and $c_{\mathcal{N}}$ as free parameters) is not identifiable from growth curves alone. We discuss this point further in the next section.

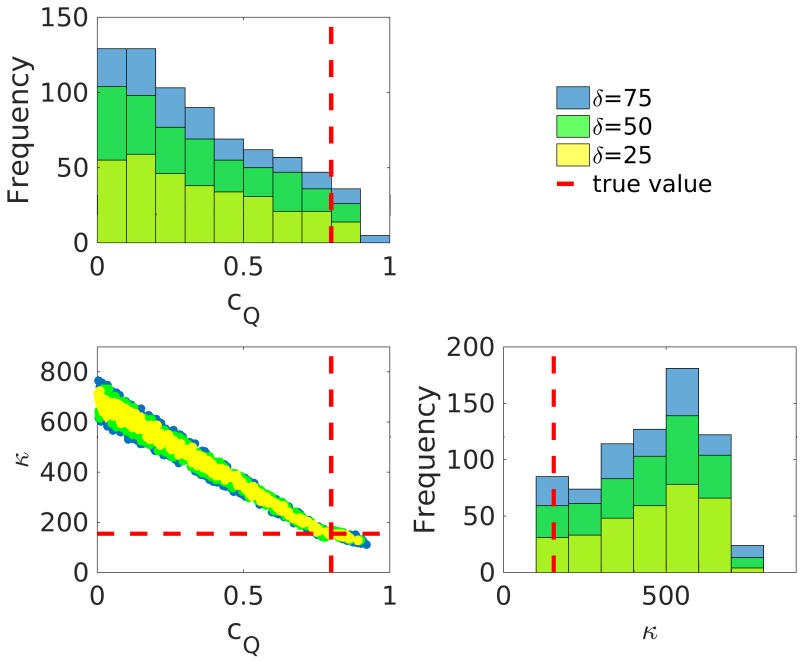

Figure 6.7: Posterior probability distributions and correlations between $c_{\mathcal{Q}}$ and κ for different values of tolerance δ. The rejection sampler algorithm was used to recover the value of κ and $c_{\mathcal{Q}}$ while other parameter values were held fixed: $p_{lys} = 0.015$, $c_{\mathcal{N}} = 0.775$.

6.3.2 Parameter sensitivity analysis

As shown in the previous section, it is not possible to infer the values of all four parameters in the CA model of homogeneous tumour growth using only the growth curves data. Unfortunately, the quality of the experimental images prevents us from extracting and quantifying spatial information from them. Instead we identify combinations of parameter values (κ, p_{lys}, $c_{\mathcal{Q}}$ and $c_{\mathcal{N}}$) that lead to acceptable agreement with the experimental PC3 growth curves of homogeneous spheroids (Fig. 6.2). We then compare the spatial distributions of the synthetic spheroids obtained in this way to the experimental images (Fig. 6.3) and select those which give the best agreement (by visual inspection). We note that this method does not allow us to exhaustively search the parameter space or to find the best set of parameters matching the data. However, it enables us to identify several candidate control and resistant spheroids.

The method that we employ involves performing a parameter sweep for a range of values for κ, p_{lys}, $c_{\mathcal{Q}}$, $c_{\mathcal{N}}$ and selecting those combinations that match the data best in the least squares sense. We perform the parameter sweep for both control and resistant homogeneous spheroids. We also aim to select those combinations that lead to diverse spatial compositions and, in so doing, to explore a larger range of potential

candidate models (i.e., specific sets of parameter values in the CA model). For each parameter, we consider ranges of values that are compatible with the observed data, our previous simulations and empirical observations.

The range of values of p_{lys}, $c_{\mathcal{Q}}$ and $c_{\mathcal{N}}$ that we use are identical for both cell lines but we consider different values of κ to reflect the differences in O_2 consumption rates for the control and resistant cells observed in monolayers. Thus we consider $p_{lys} = \{0.0025, 0.005, 0.01, 0.015, 0.02\}$, $c_{\mathcal{Q}} = \{0.3, 0.35, \ldots, 0.9, 0.95\}$, $c_{\mathcal{N}} = c_{\mathcal{Q}} - 0.05$ and $c_{\mathcal{N}} = c_{\mathcal{Q}} - 0.025$. The choice for $c_{\mathcal{N}}$ was motivated by the observation that the hypoxic layer was always very thin[1] and for that to occur the difference between the hypoxic and necrotic thresholds must be small. For the O_2 consumption rate we set $\kappa = \{100, 150, 200, 250\}$ for the PC3 Ctrl cells and $\kappa = \{25, 85, 170, 250\}$ for the PC3 Res cells. Other parameter values, such as cell cycle duration for each cell population, were set as in Table 5.1. For each combination of parameters the model was run for 20 days and the resulting growth curves were compared to either the PC3 Ctrl or PC3 Res growth data.

In Fig. 6.8 we present contour plots showing the mean squared errors (MSEs) between the growth curves generated with the CA model for a range of parameter values described in the previous paragraph and the PC3 Ctrl growth curves. In all four contour plots we observe a valley corresponding to low values of MSE. As the value of κ increases, this valley shifts towards the bottom of each plot which corresponds to lower values of $c_{\mathcal{Q}}$ (and consequently $c_{\mathcal{N}}$). This dependency was also observed in Section 6.3.1 when we performed ABC inference for $c_{\mathcal{Q}}$ and κ (Fig. 6.7). The larger the value of κ the lower the value of $c_{\mathcal{Q}}$ has to be in order to maintain low MSE. This suggests that the model may not be identifiable. As shown in the previous section, both κ and $c_{\mathcal{Q}}$ control the onset of hypoxia. In theory we could achieve a good agreement with the growth curves data by setting $\kappa \to \infty$ and $c_{\mathcal{Q}} \to 0$. In practice however, there is clearly an upper limit to the value of κ for which all the available oxygen is consumed by the cells that are present at $t = 0$. For our model that limit is $\kappa \approx 1800$ (7.0×10^{-8} mol cm^3 s^{-1}). On the other hand, we could also obtain low MSE if $\kappa \to 0$ and $c_{\mathcal{Q}} \to 1$. However, previous measurements of cellular oxygen consumption rates in spheroids suggest that the lower limit could be set at $\kappa \approx 25$ (1.0×10^{-9} mol cm^3 s^{-1}) [68]. These arguments enable us to restrict the possible range of κ to $\kappa \in (25, 1800)$. Although for each value of κ in this range we can find values of $c_{\mathcal{Q}}$ that will yield similar growth curves, the resulting spheroids can be distinguished by their spatial distributions. To illustrate this point, we set

[1]Private communication with Dr Pavitra Kannan

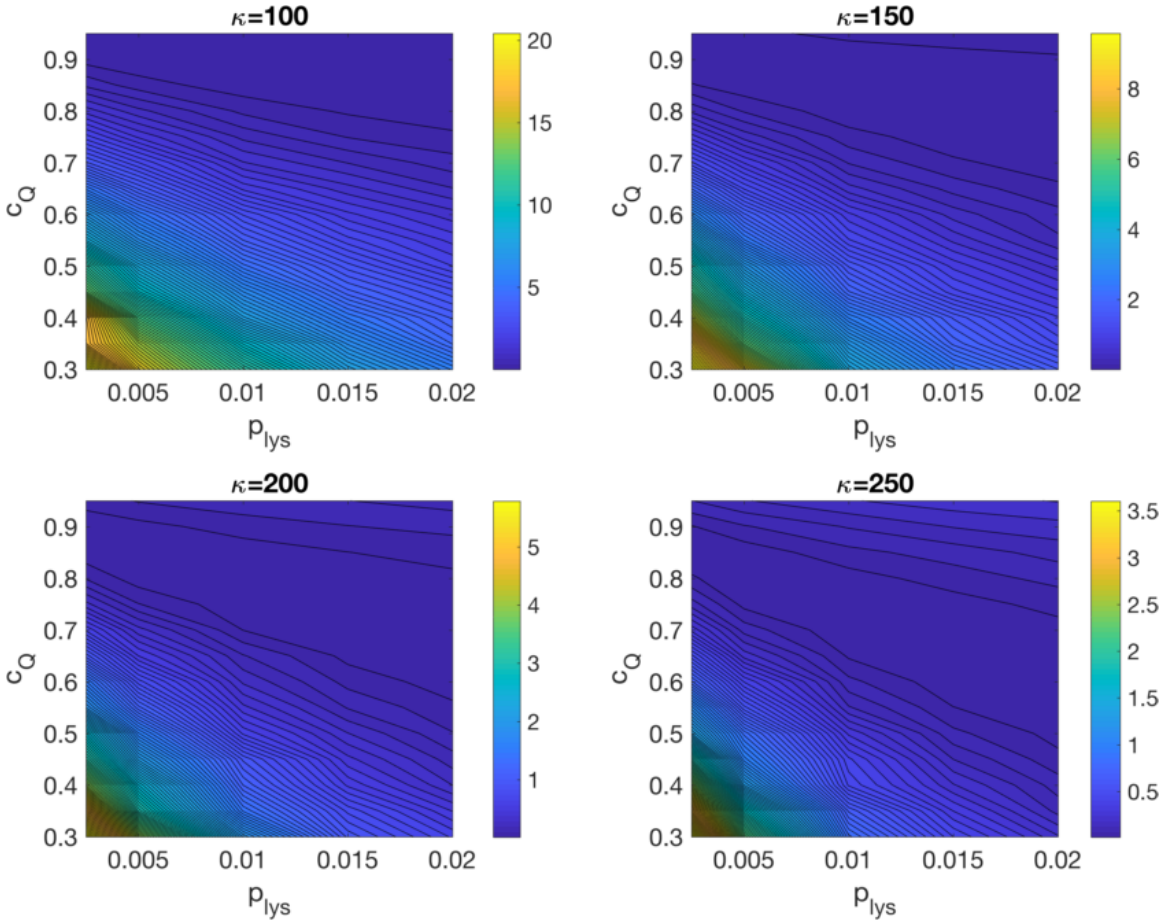

Figure 6.8: The mean squared errors (MSEs) between the volume measurements of the PC3 Ctrl spheroids and synthetic spheroids generated with the CA model for a range of κ, p_{lys}, $c_{\mathcal{Q}}$ and $c_{\mathcal{N}} = c_{\mathcal{Q}} - 0.05$.

$p_{lys} = 0.015$, $c_{\mathcal{N}} = c_{\mathcal{Q}} - 0.05$ and plotted MSEs as a function of κ and $c_{\mathcal{Q}}$ (Fig. 6.9a). For each value of κ we identified the value of $c_{\mathcal{Q}}$ that led to the lowest MSE and plotted spatial distributions of the resulting spheroids on day 7 (Fig. 6.9b). As expected, the sizes of the necrotic core and proliferating rim increased with κ whereas the size of the quiescent layer decreased. In the limited time we were unable to determine whether the value of the necrotic threshold $c_{\mathcal{N}}$ could be adjusted in a way that would allow us to achieve not only similar volumes but also similar spheroid compositions for different $(\kappa, c_{\mathcal{Q}})$ pairs. In conclusion, if we use only growth curves data then the model is not identifiable. We would have to either fix κ or the threshold values $c_{\mathcal{Q}}$ and $c_{\mathcal{N}}$ in order to uniquely identify parameter values. Alternatively, with better quality spatial data we should be able to infer three of the parameters (either $c_{\mathcal{Q}}$ or $c_{\mathcal{N}}$ would probably have to be fixed).

Returning to Fig. 6.8, we note that the low-MSE regions extend beyond the min-

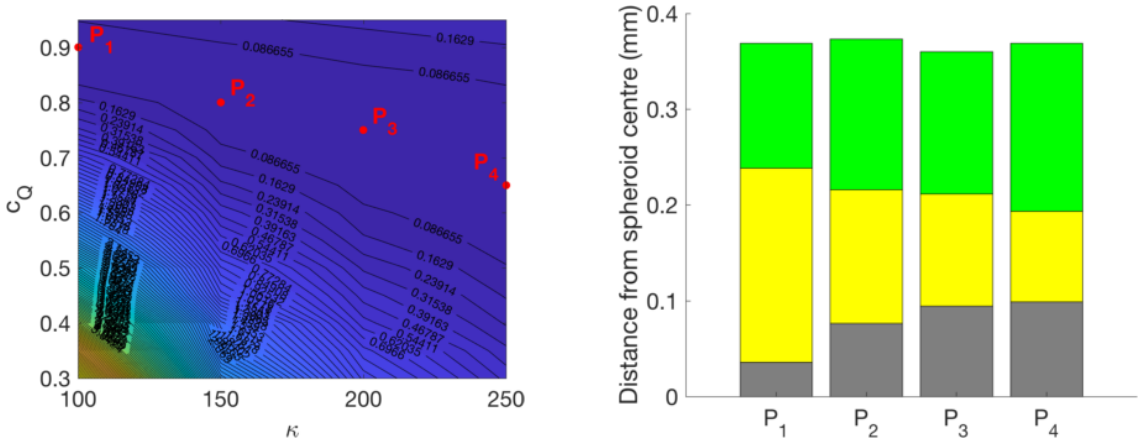

(a) **(b)**

Figure 6.9: The lowest MSEs between volume measurements of the synthetic and experimental PC3 Ctrl spheroids for each value of κ and corresponding spatial distributions of the spheroids on day 7. The red dots on the contour plot show the lowest MSEs (points P_1, P_2, P_3 and P_4) for each value of κ (a). In (b), we show the spatial distributions of the synthetic spheroids corresponding to points P_1, P_2, P_3 and P_4 measured along the spheroids' radii. Parameter values: $p_{lys} = 0.015$, $c_{\mathcal{N}} = c_{\mathcal{Q}} - 0.05$.

imum value $p_{lys} = 0.0025$ and maximum value $p_{lys} = 0.02$. Thus we would expect good agreement with the growth curves data either for (lower p_{lys} and higher $c_{\mathcal{Q}}$) or (higher p_{lys} and lower $c_{\mathcal{Q}}$). However, based on previous model simulations and empirical observations, we note that for $p_{lys} < 0.0025$ spheroids do not reach a saturation size within the timescale of experiments. Additionally, simulations with $p_{lys} > 0.02$ tend to generate spheroids with necrotic cores that are smaller than those observed *in vitro*. Taken together, these observations enable us to constrain the possible values of p_{lys}.

The MSE contour plots for the case with $c_{\mathcal{N}} = c_{\mathcal{Q}} - 0.025$ and for the PC3 Res spheroids follow similar trends (data not shown). In Fig. 6.10 we show a zoomed-in version of Fig. 6.8 focusing on regions with low MSEs. For each value of κ we identified the minimum MSE with a red dot. We repeated this procedure for the case with $c_{\mathcal{N}} = c_{\mathcal{Q}} - 0.025$ and for the PC3 Res spheroids, thus identifying 16 points in total, 8 for each cell line. We then selected 2 sets of parameter values from each cell line for further studies. These are summarised in Table 6.2. We denoted by C_i and R_i, $i = \{1, 2\}$, the sets of parameter values for the control and resistant cells, respectively. For the synthetic control spheroids we selected one set with low value of κ and high value of $c_{\mathcal{Q}}$ which corresponds to cells with relatively low oxygen consumption rate but relatively high quiescence threshold (C_1) and one set with a high oxygen consumption rate but higher tolerance for low-oxygen conditions (C_2).

Table 6.2: Parameter values for the synthetic control and resistant cells selected for further study.

	κ	$\mathbf{p_{lys}}$	$\mathbf{c_{\mathcal{Q}}}$	$\mathbf{c_{\mathcal{N}}}$
$\mathbf{C_1}$	100	0.01	0.9	0.85
$\mathbf{C_2}$	250	0.015	0.65	0.6
$\mathbf{R_1}$	25	0.015	0.95	0.925
$\mathbf{R_2}$	170	0.015	0.55	0.525

In Fig. 6.11 we show the compositions of the synthetic C_1 and C_2 spheroids at different stages of growth. Although the volumes of both spheroids were very similar within the first 20 days of growth, C_1 continued to grow until day 40 reaching a saturation size of approximately 1.2 mm^3. The growth of C_2 settled around day 25 at approximately 0.8 mm^3. Both spheroids developed quiescent regions very early but C_2 showed evidence of necrosis from day 5. The proliferating rim of C_2 was wider but its quiescent region thinner than that of C_1. In both cases, the necrotic core

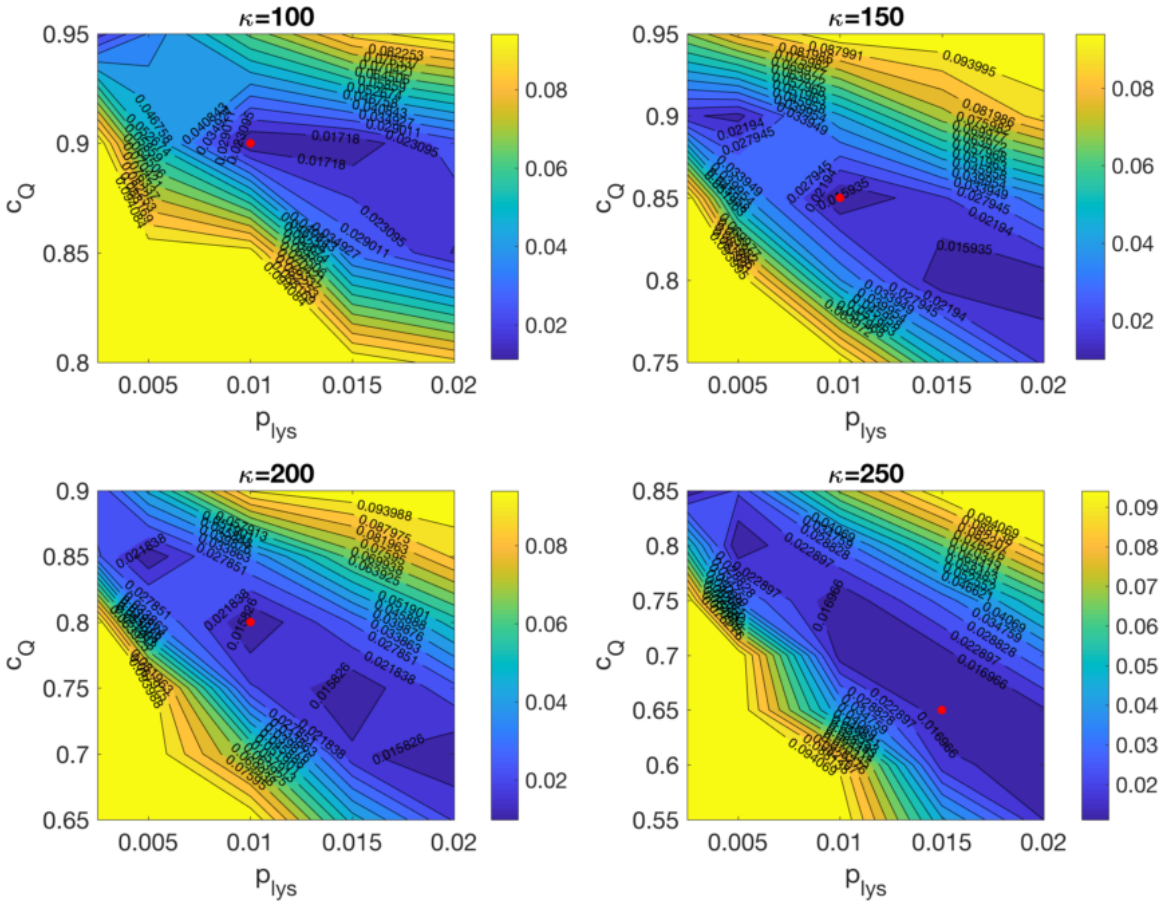

Figure 6.10: Zoomed-in version of plots from Fig. 6.8. Red dots show the points with minimum MSE for each value of κ.

reached a substantial size, occupying a large proportion of both spheroids. Although the volume fraction of the necrotic core was initially larger for C_2, at the saturation size was the same for both spheroids. When we contrast these images with those of *in vitro* PC3 Ctrl spheroids (Fig. 6.3) we see that C_1 seems to be a better match on day 5. Most of the proliferating cells are concentrated at the outer spheroid boundary and the interior seems to be occupied by quiescent. On day 12, the PC3 Ctrl spheroids had extensive necrosis, surrounded by a thin rim of viable cells, some of which were dividing. Slightly larger necrotic core would suggest that perhaps C_2 was a better match here.

The compositions of the resistant spheroids selected for further study, R_1 and R_2 (Table 6.2), were also very different despite similar growth kinetics see (Fig. 6.12). Both spheroids grew almost identically until day 25, after which R_2 settled at a slightly higher volume than R_1 of 2.4 mm^3. Characterised by a low oxygen consumption rate and high transition thresholds, R_1 showed quiescent cells on day 5. At the same time (and volume), all cells in R_2, with a significantly higher value of κ and lower values of $c_{\mathcal{Q}}$ and $c_{\mathcal{N}}$, were still in proliferating state. The Ki67 images of the PC3 Res spheroids (Fig. 6.3) suggest that the distribution of cycling cells was more uniform than in the PC3 Ctrl spheroids on day 5. All cells seemed to be viable (H/E staining) and there was no evidence of hypoxia. On day 12, however, R_2 had a large necrotic core, significantly larger than R_1. Its proliferating rim was visibly thicker with quiescence occupying little spheroid volume, a trend that was maintained until saturation size was reached. The quiescent cells in R_1 occupied about 40% of its volume which

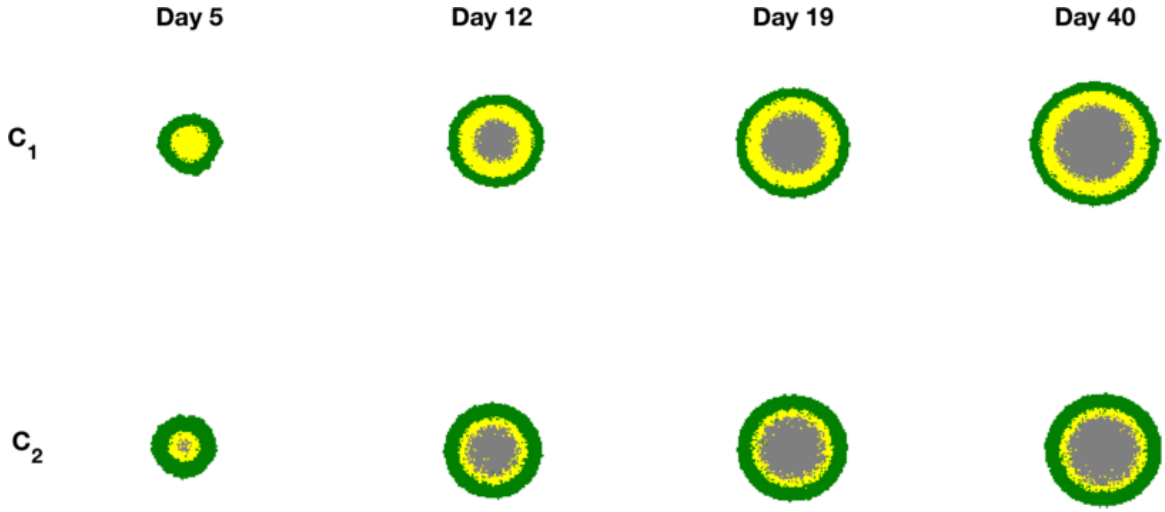

Figure 6.11: Spatial distribution of C_1 and C_2 spheroids. Green cells are proliferating, yellow cells are quiescent and grey cells are necrotic. See Table 6.2 for parameter values.

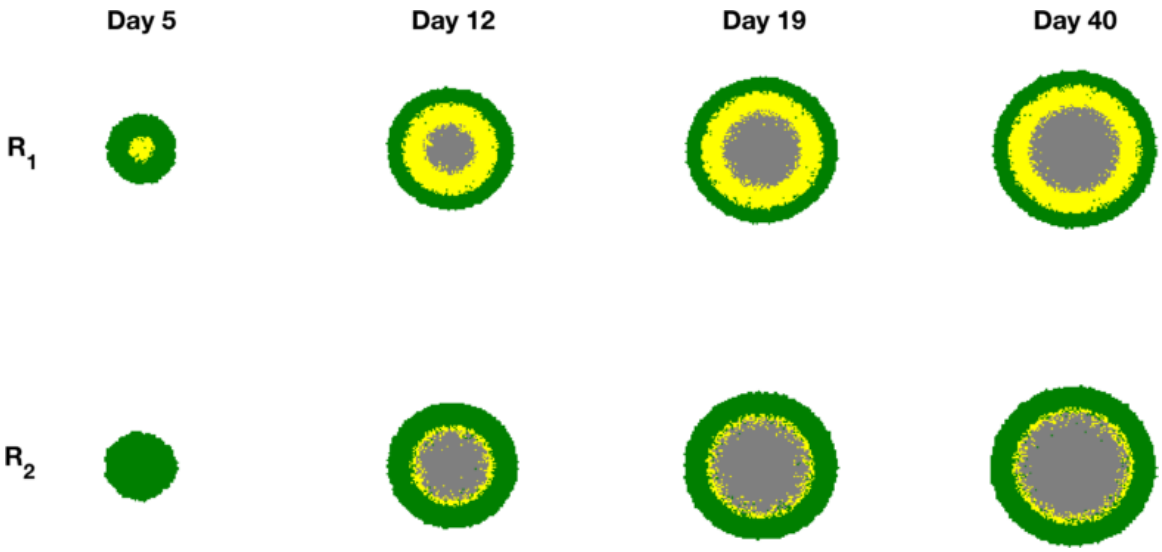

Figure 6.12: Spatial distribution of R_1 and R_2 spheroids. Green cells are proliferating, yellow cells are quiescent and grey cells are necrotic. See Table 6.2 for parameter values.

was surprising considering small difference between $c_{\mathcal{Q}}$ and $c_{\mathcal{N}}$. This difference was, however, balanced by low oxygen consumption rate which had the effect of delaying the onset of necrosis. In PC3 Res spheroids, proliferation on day 12 was clearly limited to a thin rim of cells on the spheroid boundary. These images also suggest the existence of a large necrotic core, an observation more consistent with R_2.

6.4 Simulations of the growth of heterogeneous spheroids

In the previous section, we attempted to infer the parameter values in the CA model of homogeneous tumour growth for the PC3 Ctrl and PC3 Res homogeneous spheroids described in Section 6.2. Since we were unable to uniquely estimate the parameter values, we identified candidate *in silico* CA spheroids: C_1, C_2, R_1 and R_2 (Table 6.2) that provided a good agreement with the experimental data. In this section, we aim to determine if co-culturing the control (C_1 and C_2) and resistant (R_1 and R_2) cell populations *in silico* can reproduce the growth of the experimental heterogeneous PC3 spheroids under the null hypothesis (no cross-talk between the clones). We used the CA model of heterogeneous tumour growth to generate synthetic spheroids by seeding the control (C_1 and C_2) and resistant (R_1 and R_2) cells at the 3:1, 1:1 and 1:3 ratios. The spheroids were grown for 60 days, 10 realisations being generated for each condition. We neglected direct interactions between the control and resistant

clones. The only differences between them were: cell cycle time, rate of lysis, oxygen consumption rate and the oxygen thresholds at which they become quiescent and necrotic. Below, we discuss the results of simulations of the C_1R_2 heterogeneous spheroids growth. The corresponding results for the C_1R_1, C_2R_1 and C_2R_2 spheroids are presented in Appendix D.

6.4.1 C_1R_2 spheroids

We begin our discussion by presenting simulation results for heterogeneous spheroids composed of C_1 and R_2 cells. In Fig. 6.13a, we show the growth curves of the C_1R_2 and PC3 spheroids. In Section 6.2 we only presented the growth curves and Lotka-Volterra model fits to the heterogeneous PC3 spheroids mixed at the 1:1 (Ctrl:Res) ratio because we do not have proportion measurements for the 3:1 and 1:3 conditions. However, we have the growth curves of the 3:1 and 1:3 spheroids and thus compare them to the CA model simulations. Interestingly, we note that the 3:1 spheroids were larger than any other spheroids from day 12 onwards and that the growth of the heterogeneous spheroids was similar to the growth of the resistant spheroids.

As expected, the growth of the homogeneous spheroids was well described by the CA model (green and red curves, Fig. 6.13a). The growth curves of the PC3 1:3 spheroids (magenta) were also predicted accurately but the growth curves of the PC3 3:1 and PC3 1:1 spheroids were not (blue and black). Fig. 6.13b shows the growth of

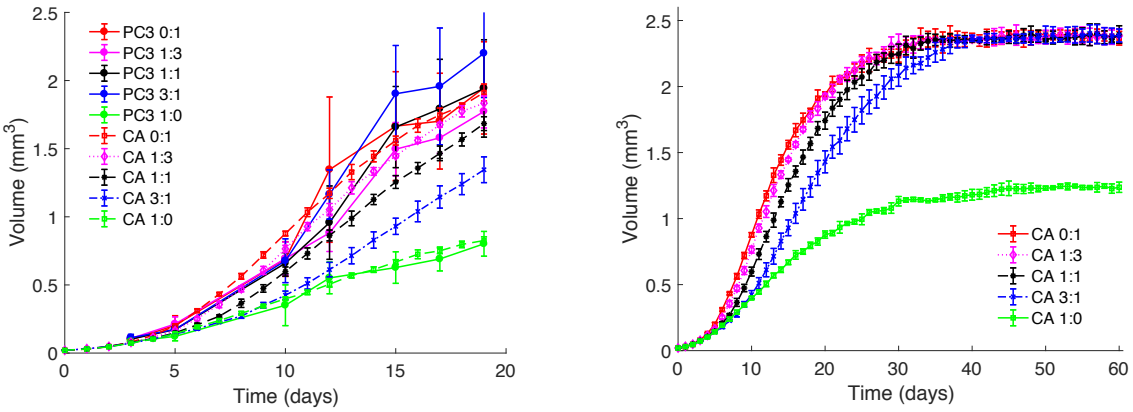

Figure 6.13: Growth curves of heterogeneous C_1R_2 spheroids. Comparison of the growth curves of the heterogeneous *in vitro* PC3 and *in silico* C_1R_2 spheroids co-cultured at different ratios of control and resistant cells **(a)**; and long-term behaviour of the C_1R_2 spheroids **(b)**. Data points show the mean±1×SD from 12 independent experiments (PC3 spheroids) or 10 realisations of the CA model. For the parameter values used to generate the C_1R_2 spheroids see Tables 6.2 and 5.1.

the CA spheroids over a period of 60 days. Initially, the spheroids containing a larger fraction of the resistant cells grew faster but by day 40 all except for the homogeneous control spheroids reached a similar saturation volume, of approximately 2.5 mm^3. The control spheroids also reached an equilibrium volume of approximately 1 mm^3. Thus Fig. 6.13 suggests that the growth of the heterogeneous spheroids was dominated by the resistant cells.

Indeed, inspection of the composition of the heterogeneous spheroids reveals that the resistant clone quickly became dominant (Fig. 6.14). The figure shows snapshots of cross-sections of the heterogeneous C_1R_2 spheroids at different time points. Although all cells within the heterogeneous spheroids were initially dividing, the control cells in the 3:1 and 1:1 spheroids had formed a necrotic core surrounded by a layer of quiescent cells and an outer rim of proliferating cells by day 5. Any resistant cells within the spheroids remained proliferating. The early formation of necrotic and quiescent regions of the C_1 cells was due to their high sensitivity to low oxygen conditions ($c_{\mathcal{Q}} = 0.9$, $c_{\mathcal{N}} = 0.85$). In contrast, hypoxia and necrosis for the R_2 cells began when the oxygen concentration dropped to 55% and 52.5% of its background levels, respectively. Thus by day 12 the R_2 cells were also quiescent and necrotic, and had become the dominant clone. The larger the initial proportion of resistant cells, the more rapidly they outgrew the control cells. This explains the growth delay between days 4 and 40 of the heterogeneous spheroids (Fig. 6.13b). No control cells

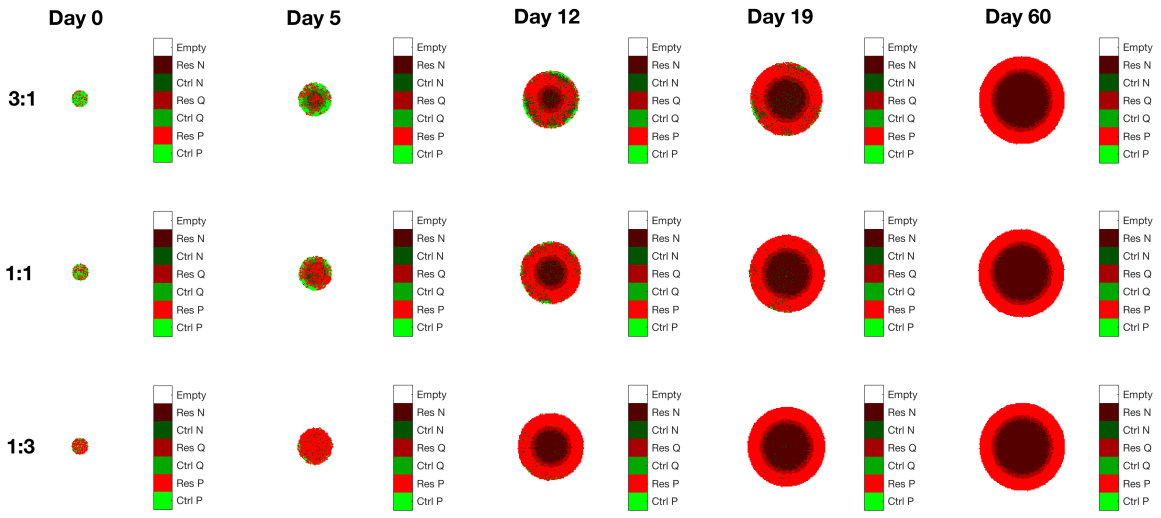

Figure 6.14: Cross-sections through the heterogeneous C_1R_2 spheroids. Shades of green and red represent control and resistant cells, respectively. Light shades correspond to proliferating, darker shades to quiescent and the darkest shades to necrotic cells. For the parameter values used to generate the C_1R_2 spheroids see Tables 6.2 and 5.1.

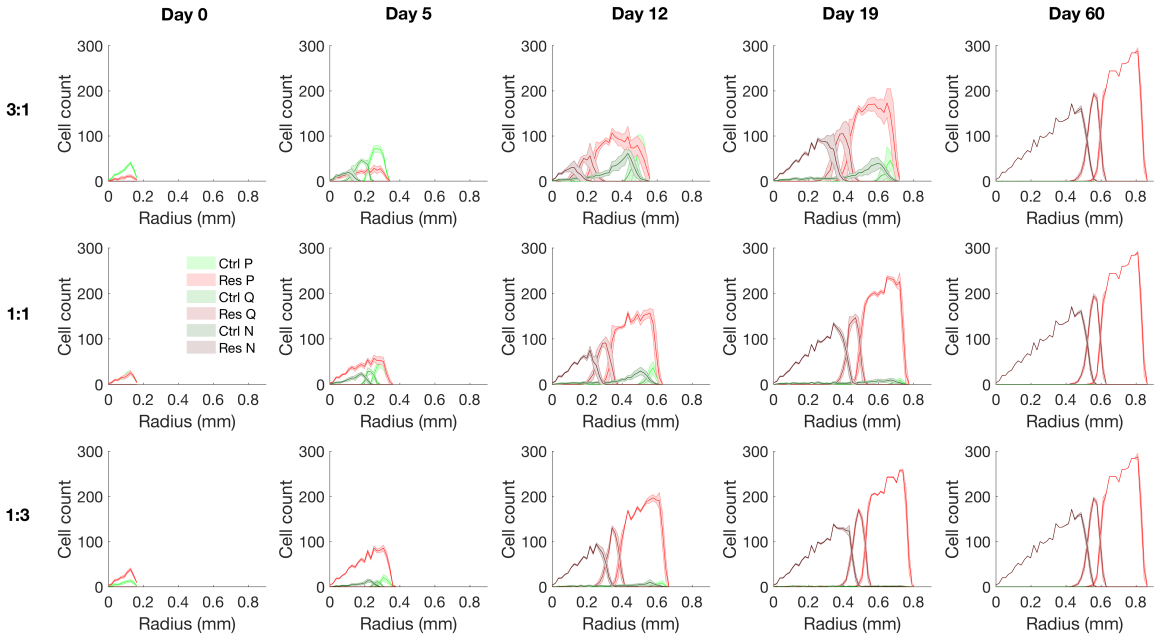

Figure 6.15: Series of plots showing how the spatial distribution of heterogeneous C_1R_2 spheroids changes over time. Plots show the number of control and resistant cells in different states (proliferating, quiescent or necrotic) on cross-sections of spheroids as a function of their radius. Solid lines show the mean and the shaded error bars 1×SD based on 10 realisations of the CA model.

were present in the spheroids on day 60 and their composition was similar to that of homogeneous resistant spheroids at growth saturation (Fig. 6.12).

Since the snapshots presented in Fig. 6.14 show spheroid compositions from one realisation of the model, in Fig. 6.15 we show cellular composition of the C_1R_2 spheroids averaged over 10 realisations of the model as a function of spheroid radius. Surprisingly, the variation in spatial composition of heterogeneous spheroids was quite low across multiple realisations of the model, in particular, when one of the clones was clearly dominant.

A qualitative comparison of the experimental images showing spatial distribution of the PC3 1:1 spheroids (Fig. 6.3) with the cross-sections of the C_1R_2 1:1 spheroids (Figures 6.14 and 6.15) on days 5 and 12 reveals that the combination of the C_1 and R_2 cells under the no cross-talk assumption does not explain the growth of the PC3 heterogeneous spheroids. The spatial images suggest that the majority of both control and resistant cells were in the proliferating state on day 5, whereas many C_1 cells were already quiescent or necrotic. On day 12, the C_1R_2 1:1 spheroids had a substantial necrotic core surrounded by a thin layer of quiescent cells and a thick rim of dividing R_2 cells mixed with necrotic and hypoxic C_1 cells and a few pockets of

proliferating C_1 cells. Although the bulk spatial distribution of the C_1R_2 spheroids is similar to the PC3 spheroids bulk composition, the control cells in the latter are located within the proliferating rim of the dominant resistant clone rather than on its outer boundary. Thus the C_1R_2 spheroids do not explain the growth curves or spatial composition of the PC3 heterogeneous spheroids well.

6.4.2 Growth curves of heterogeneous spheroids

The comparisons of the growth curves of the experimental PC3 spheroids and the *in silico* C_1R_1, C_2R_1 and C_2R_2 spheroids are presented in Figs. D.1, D.3 and D.5, respectively. As expected, the growth curves of all homogeneous *in silico* spheroids describe the corresponding growth curves of the homogeneous PC3 spheroids well. The growth curves of the heterogeneous C_2R_2 spheroids were very similar to those of the C_1R_2 spheroids: they captured the growth of the 1:3 condition well, but underestimated the growth of the 3:1 and 1:1 conditions (Figs. D.5 and 6.13). Whereas, in the long term, the growth curves of the heterogeneous C_1R_2 and C_2R_2 spheroids approach those of the homogeneous resistant spheroids, the growth curves of the C_1R_1 and C_2R_1 spheroids show the opposite trend: they approach the growth curves of the homogeneous control spheroids (Figs. D.1 and D.3). As a result, the growth curves of the heterogeneous C_1R_1 and C_2R_1 spheroids significantly underestimate the growth of the corresponding experimental PC3 spheroids.

6.4.3 Compositions of heterogeneous spheroids

The spatial distributions of the *in silico* C_1R_1, C_2R_1 and C_2R_2 spheroids are presented in Figs. D.2, D.4 and D.6, respectively. Unsurprisingly, since the growth curves of the C_2R_2 and C_1R_2 spheroids were very similar, their spatial composition also show similar trends: the resistant population became dominant for all three initial conditions (3:1, 1:1 and 1:3; Figs. 6.15 and D.6). However, unlike in the C_1R_2 spheroids, the proportions of the control and resistant cells in the C_2R_2 1:1 spheroids showed a much better agreement with the measured proportions in the experimental PC3 1:1 spheroids (Fig. 6.16). The growth of the heterogeneous C_2R_1 spheroids became rapidly dominated by the control population, even for the initial 1:3 composition (Fig. D.4).

Whereas the C_1R_2, C_2R_1 and C_2R_2 spheroids conform to the competitive exclusion principle, which states that two populations cannot coexist if they compete for the same limiting resources, leading to the extinction of one of the competitors, the

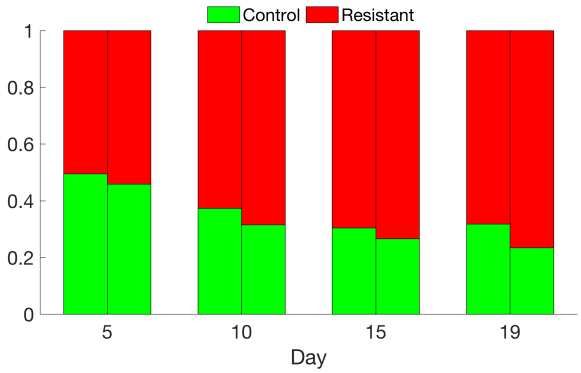

Figure 6.16: Proportions of the control and resistant cells in the heterogeneous PC3 and C_2R_2 spheroids. The first bar for each day shows the proportion of control and resistant cells in the PC3 1:1 spheroids. The second bar shows corresponding proportions in the C_2R_2 spheroids.

C_1R_1 spheroids appear to refute this principle. The spatial composition of the C_1R_1 spheroids remained approximately constant within the timescale considered (60 days; Fig. D.2). To determine if the initial proportions of the C_1 and R_1 cells in the heterogeneous spheroids would be preserved on a longer timescale, we simulated the CA model for 200 days. Our simulations confirmed that, when co-cultured, the C_1 and R_1 cells could stably coexist at their initial compositions (data not shown).

The dominance of the R_2 cells in the C_1R_2 and C_2R_2 spheroids can be explained by their relatively low sensitivity to changing oxygen levels: the quiescence and necrosis oxygen threshold values for this population were $c_{\mathcal{Q}} = 0.55$ and $c_{\mathcal{N}} = 0.525$, respectively (see Table 6.2 for comparison with other synthetic cell lines). Similarly, the C_1 cells were dominant in the C_1R_1 spheroids because they had lower values of $c_{\mathcal{Q}}$ and $c_{\mathcal{N}}$ than the R_1 cells. The coexistence of the C_1 and R_1 cells in the C_1R_1 spheroids could be explained by the balance between the properties of these cells: the resistant cells divide faster than the control cells (see Table 5.1) but the latter have lower sensitivity to low oxygen conditions (Table 6.2).

In summary, none of the candidate *in silico* spheroids considered in this section explained the experimental PC3 spheroids data. Although the growth curves of the C_2R_2 1:3 spheroids and the proportions of the control and resistant cells in the C_2R_2 1:1 spheroids closely matched the corresponding experimental data, the 3:1 and 1:1 growth curves and the spatial compositions were not described well.

6.5 Lotka-Volterra model for *in silico* data from heterogeneous CA spheroids

In Sections 6.3 and 6.4, we used the CA model to generate *in silico* homogeneous and heterogeneous spheroids composed of control (C_1 and C_2) and resistant (R_1 and R_2) cell lines seeded at the 1:0, 3:1, 1:1, 1:3 and 0:1 ratios. All spheroids (C_1R_1, C_1R_2, C_2R_1 and C_2R_2) were generated under the null hypothesis which states the co-cultured cell populations do not interact directly but compete for space and nutrients. In this section, we fit the Lotka-Volterra model (4.3) to the data describing these *in silico* spheroids to establish if the Lotka-Volterra model can consistently predict the correct type of interactions between co-cultured clones.

The CA growth curves data were fitted using the three protocols described in Chapter 4. However, here we fixed the values of $V_C(0) = V_C^*(0)$ and $V_R(0) = V_R^*(0)$. Briefly, the two-step fitting protocol involves estimating parameter values for the homogeneous spheroids separately, fixing these parameter values for each population and then estimating the interaction terms for each heterogeneous spheroid. In the two-step pooled data protocol we again estimate parameter values for the homogeneous spheroids separately but in the second step of the protocol we pool the data for the growth of the heterogeneous spheroids and find a single pair of interaction parameters that best fit all data. Finally, the pooled data protocol involves finding a set of parameter values that best fit all data in one step. We estimate the volumes of the control and resistant populations based on the total spheroid volume measurements and the proportion of control and resistant cells on a cross-section of the spheroid.

Tables D.1, D.2, D.3 and D.4 show the best point estimates and the 95% confidence intervals for the Lotka-Volterra model parameters for the C_1R_2, C_2R_2, C_2R_1 and C_1R_1 spheroids, respectively. The tables also show the estimated level of noise in the data (σ) and errors as measured by the weighted sum of squared residuals (WSSR). Figures D.7, D.8, D.9 and D.10 show the corresponding best fitted curves to each dataset. Below, we summarise our findings.

In general, the 95% confidence intervals were very narrow due to the large number of data points available for the inference process (the data were recorded every day even though they are plotted at 5-day intervals for clarity of the figures).

In most cases, the estimates of the growth rate for the control cells were lower than those for the resistant cells, a result which is consistent with the estimates for the PC3 spheroids (Table 6.1). The only exceptions were the estimates obtained with the pooled data protocol for the C_2R_1 and C_1R_1 spheroids (Tables D.3 and D.4). All

synthetic control and resistant cells had higher growth rates than the corresponding PC3 cells, except for the growth rates of the R_1 cells estimated with the pooled data protocol.

The estimates of the carrying capacity were generally accurate, as assessed by visual inspection, except for those obtained using the pooled data protocol for the C_1R_1 spheroids which clearly underestimated the saturation volume (Fig. D.10). Compared to the PC3 homogeneous spheroids, the estimated saturation volumes of the synthetic spheroids were generally larger. However, no clear patterns were observed, with different fitting protocols giving different values.

The ability of the Lotka-Volterra model to describe the growth curves from the CA simulations was strongly dependent on the CA data. Recall that the two-step fitting protocols involve estimating the growth rate and carrying capacity parameters in the logistic model using homogeneous spheroids growth data. As noted in Chapter 5, it can be difficult to accurately capture the growth curve of a synthetic spheroid with the logistic model (Fig. 5.8). Here, too, the ability of the logistic model to accurately describe the growth of homogeneous spheroids was limited (e.g., Fig. D.7). Similarly, describing the volumes of heterogeneous spheroids by the Lotka-Volterra model was not always successful. For example, the growth of the C_2R_2 spheroids was well described by the Lotka-Volterra model (Fig. D.8) but not that of the C_1R_1 spheroids, particularly for the two-step fitting protocols (Fig. D.10).

The Lotka-Volterra model predicted competitive interactions for all heterogeneous spheroids. The only exceptions were the estimates for the C_1R_2 and C_2R_1 spheroids obtained with the two-step protocol (Tables D.1 and D.3). In these cases, the model predicted antagonistic interactions. However, the negative values of $\eta_{C1}^{1:1}$ and $\eta_{C1}^{1:3}$ in the C_1R_2 spheroids, and $\eta_{R1}^{1:1}$ and $\eta_{R1}^{1:3}$ in the C_2R_1 spheroids are due to incorrect fits to the data. For example, Fig. D.7 shows that the fits to the 1:1 and 1:3 spheroids data with the two-step protocol significantly overestimate the volume. In particular, the model is unable to capture the growth of the resistant cells (and consequently the total volume since the resistant clone is dominant). The model predicts that the volume of the resistant cells increases rapidly beyond its carrying capacity and then decreases and stabilises. This behaviour contradicts the CA data which reveal that the resistant clone quickly outgrows the control cells and then approaches its saturation volume albeit in a more controlled way. Since the volume of the resistant population is, at some point, estimated by the model to be larger than its carrying capacity, the estimated values of $\eta_{C1}^{1:1}$ and $\eta_{C1}^{1:3}$ are negative. In other words, the resistant cells could not have grown beyond their carrying capacity unless the control population

supported their growth. The negative values of $\eta_{R1}^{1:1}$ and $\eta_{R1}^{1:3}$ in the C_2R_1 spheroids arise in a similar manner. Fig. D.9 shows that, the model predicted that the control cells in the 1:1 and 1:3 spheroids would grow beyond their carrying capacity, then decrease in size and finally plateau. For this to happen, the control cells must receive support from the resistant population (i.e., $\eta_{R1}^{1:1}$ and $\eta_{R1}^{1:3}$ are negative).

Comparison of the interaction parameter estimates reveals that the magnitude of the competitive effect that the control cells had on the resistant cells was larger in all cases except for the C_1R_2 spheroids. Both two-step fitting protocols predicted that $\eta_{C1} < \eta_{R2}$ in the C_1R_2 spheroids. However, the pooled protocol predicted the reverse (Table D.1). Interestingly, for all cases except the C_1R_2 spheroids, the oxygen consumption rate of the control population was higher than that of the resistant population, suggesting that cells that consume more oxygen have a stronger competitive effect on the cells that consume relatively less oxygen. This observation is consistent with the PC3 spheroids data: the control cells that consume more oxygen in monolayers were found to have a stronger competitive effect on the resistant cells which consume less oxygen in monolayers (Table 6.1). To test this hypothesis, we simulated the growth of spheroids where the only difference between the control and resistant population was the oxygen consumption rate. We set $\bar{\tau}_{cycle} = 16.9$, σ^2_{cycle}, $p_{lys} = 0.015$, $c_{\mathcal{Q}} = 0.8$, $c_{\mathcal{N}} = 0.75$ for both cell populations, and $\kappa = 155$ and $\kappa = 50$ for the control and resistant cells, respectively. The growth curves show that the homogeneous spheroids plateaued around day 35 with the resistant spheroids attaining an equilibrium volume five times larger than that for the control spheroids (Fig. 6.17). The growth of the heterogeneous spheroids did not equilibrate on the timescale considered (200 days); the spheroids continued to increase in size, with those initially containing more resistant cells displaying more aggressive growth. Spatial distributions show that the resistant clone became dominant in all spheroids, even those initially containing 75% control cells (Fig. 6.18). Thus it appears that lower oxygen consumption rate gives the resistant population competitive advantage. However, this observation is not reflected in the estimates of the interaction parameters in the Lotka-Volterra model. The estimates from the pooled data protocol are $\eta_C = 0.411$ and $\eta_R = 0.079$. These are similar for all fitting protocols (data not shown), suggesting that the control population has a stronger competitive effect on the resistant cells than the other way around. Although the estimates of the growth rate are similar for both populations ($r_C = 0.460$ and $r_R = 0.473$; pooled data protocol), the estimates of the carrying capacity for the resistant cells are much higher ($K_C = 1.129$ and $K_R = 5.909$; pooled data protocol). Consequently, it appears that the intrinsic growth kinetics (r and K)

are more important for the long term composition of spheroids than the interaction parameters.

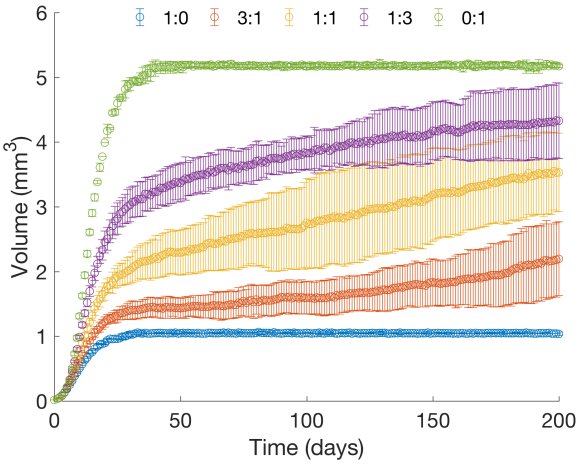

Figure 6.17: Growth curves of heterogeneous *in silico* spheroids in which the co-cultured cell populations differ only by the oxygen consumption rates generated with the CA model with the following parameter values: $\bar{\tau}_{cycle} = 16.9$, σ^2_{cycle}, $p_{lys} = 0.015$, $c_{\mathcal{Q}} = 0.8$, $c_{\mathcal{N}} = 0.75$ for both cell populations; $\kappa = 155$ and $\kappa = 50$ for the control and resistant cells, respectively. 10 realisations of the CA model were performed for each initial condition.

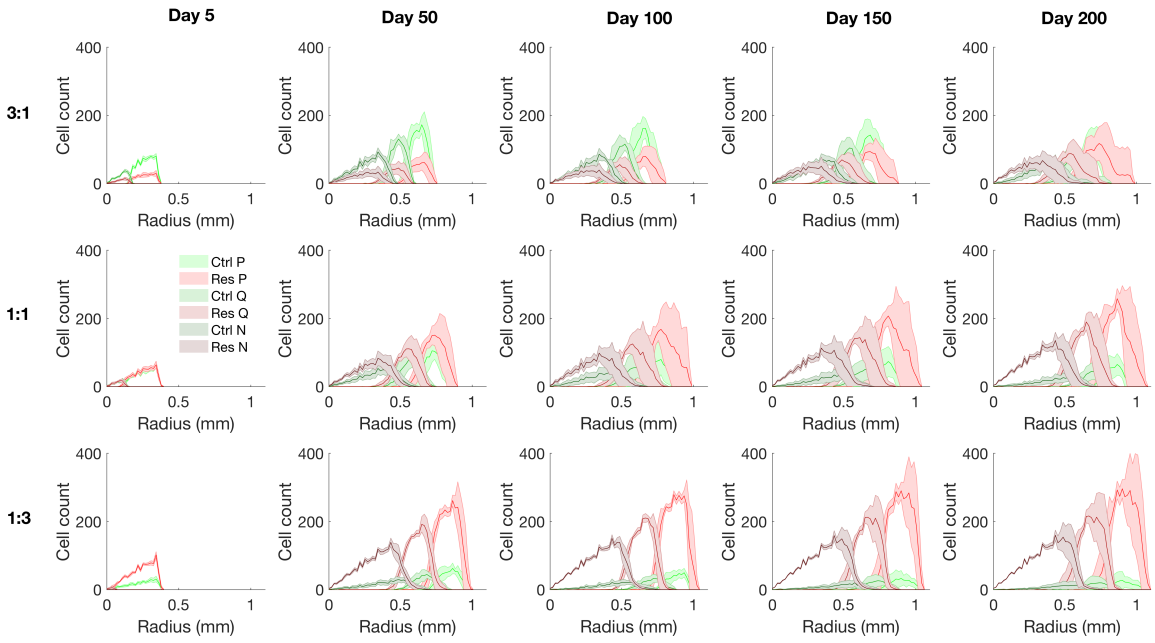

Figure 6.18: Spatial distributions of heterogeneous *in silico* spheroids in which the co-cultured populations differ only by the oxygen consumption rates generated with the CA model with the following parameter values: $\bar{\tau}_{cycle} = 16.9$, σ^2_{cycle}, $p_{lys} = 0.015$, $c_{\mathcal{Q}} = 0.8$, $c_{\mathcal{N}} = 0.75$ for both cell populations; $\kappa = 155$ and $\kappa = 50$ for the control and resistant cells, respectively. 10 realisations of the CA model were performed for each initial condition.

6.6 Discussion

Our main aim in this chapter was to determine whether the competitive interactions between two co-cultured PC3 cell populations were due to indirect competition for resources, or whether direct communication was needed in order to explain the experimental PC3 data presented in Section 6.2. Our strategy involved first estimating parameter values in the CA model of homogeneous spheroid growth for both cell populations separately. We then simulated the growth of heterogeneous spheroids using the model with the parameter values for each population fixed assuming that there is no cross-talk between the two populations. If we could not reproduce the heterogeneous spheroids growth data then we would reject this null hypothesis and deduce instead that the two populations must interact directly. In Section 6.2, we introduced the experimental data, fit the Lotka-Volterra model to them and concluded that the control and resistant clones compete directly. Unfortunately, due to the low quality of the spatial data, we were not able to use them for parameter inference. Therefore, in Section 6.3, we tried to estimate the parameter values in the CA model using only data from growth curves. We were unable to do this and found that the model was non-identifiable in its current form. Thus we selected four candidate homogeneous *in silico* spheroids (two for each population) that quantitatively matched the homogeneous growth curves data and qualitatively matched the spatial data, and used the CA model to co-culture them *in silico* in Section 6.4. While none of the synthetic heterogeneous spheroids reproduced the PC3 data, we could not reject the null hypothesis because the CA model parameters for the control and resistant cells had not been uniquely identified.

Our secondary aim was to assess the ability of the Lotka-Volterra model to accurately characterise interactions between two synthetic cell lines which do not interact directly. We considered the four heterogeneous *in silico* spheroids generated in Section 6.4. In all cases we found that the Lotka-Volterra model correctly predicted competition between the control and resistant clones. However, the model did not describe the data well in all cases.

The success of our strategy to establish whether the cells interact directly or indirectly depended on our ability to uniquely identify parameter values in the CA model for the control and resistant cell populations. For each population, the task was to estimate the values of the oxygen consumption rate, the rate of lysis and the oxygen concentration threshold values at which the cells become quiescent and necrotic. With better quality images describing the spatial distribution of the PC3 spheroids we

would have been able to extract from them spatial data for use in the inference process. A similar approach was adopted by Jagiella et al. [93] who attempted to infer the growth control mechanisms in tumour spheroids from spatio-temporal image data. Without the spatial information we had to use only growth curves data for which we found that the model was non-identifiable. We found correlations between the values of the oxygen consumption rate and concentration value at which cells become quiescent (Fig. 6.7). In other words, we could select an infinite number of $(\kappa, c_{\mathcal{Q}})$-sets that lead to similar growth curves. We showed that these sets led to different spatial distributions though, suggesting that with the spatial information we would be able to discriminate between them (Fig. 6.9). However, it is unclear whether the other two parameters, p_{lys} and $c_{\mathcal{N}}$ in particular, could be manipulated in a way that would lead to similar observations for different values. In order to address this question, we would have to perform a thorough identifiability analysis. Alternatively, to determine what additional data are required to estimate the parameter values we could perform an experimental design study using synthetic data, similar to that presented in Chapter 4 where we determined when to collect data on the proportions of control and resistant cells in order to reliably estimate parameter values in the Lotka-Volterra model.

Although we could not uniquely estimate parameter values in the CA model for the control and resistant cell populations, we selected four candidate homogeneous *in silico* spheroids (Table 6.2, Figs. 6.11 and 6.12) that fit the data well for further simulations of heterogeneous spheroids in order to demonstrate how our strategy could be used to test the null hypothesis. Of the four considered synthetic heterogeneous spheroids none described the experimental PC3 data well but they exhibited diverse growth dynamics despite simple model assumptions: the co-cultured cell populations did not interact directly and divided only if there was enough space and nutrient available for them to do so (Section 6.4). Our results demonstrate that, in the absence of cross-talk, faster proliferation is not sufficient for one cell population to dominate over the other. Although the resistant cells had faster division rate than the control cells, they were outcompeted by the control population in the *in silico* C_2R_1 and C_1R_1 3:1 spheroids, and the two clones coexisted in the *in silico* C_1R_1 1:1 and 1:3 spheroids, indicating that sensitivity to low nutrient conditions plays a crucial role in determining the outcome of interclonal dynamics.

We also questioned in this chapter the ability of the Lotka-Volterra model to accurately predict the types of interactions between two co-cultured cell populations. We have used the model previously to infer the types of interactions between clones in PC3 and DU145 spheroids (Chapter 4). Although the Lotka-Volterra model did not

capture the growth curves of all our synthetic spheroids particularly well, the model consistently predicted competition between the control and resistant cells. These results increase our confidence in the model.

One unanticipated finding was that we found a correlation between oxygen consumption rate and the strength of the competitive effect in the Lotka-Volterra model. When we pursued this idea further, we discovered that if the oxygen consumption rate is the only difference between co-cultured cell populations then the one with lower consumption rate dominates over time. However, despite competitive advantage, the dominant population with lower consumption rate has lower competitive effect on the other population as predicted by the Lotka-Volterra model.

Chapter 7

Conclusions and future work

Traditionally, cancer has been considered from the gene-centric view. Although it is true that cancer is the result of genetic mutations, cancer cells exist within tissues and there is a constant dialogue between them and other cells and their microenvironment. Consequently, it is not sufficient to study cancer cells in isolation, they must be considered in the context of the environment in which they exist. Taken together, cancer cells, normal cells and the surrounding tissue form an ecosystem [17]. The healthy tissue ecosystem is in a state of homoeostasis—there is a perfect balance between cellular proliferation and apoptosis. Genetic mutations disrupt this homoeostasis and can lead to uncontrolled cellular division. Cancer cells acquire further mutations and these have been the major subject of study of cancer researchers [53, 31]. This genetic diversity leads to the emergence of different phenotypes and it is the latter that are acted upon by Darwinian forces of evolution. The availability of nutrients and space, and interactions between different cell populations are the forces that drive intra-tumour heterogeneity. The interactions between different cell populations and their environment, and their significance for cancer progression and response to treatment, are still poorly understood [188].

Since tumours constantly evolve toward a more aggressive phenotype it can be extremely difficult to predict tumour progression and responses to anti-cancer treatment. Depending on their composition, tumours display different sensitivities to therapeutic interventions. For example, the existence of a small population of resistant cells can have a devastating effect on treatment, promoting the emergence and uncontrolled progression of the resistant phenotype. In the absence of appropriate data, clinicians prescribing radiotherapy treatments routinely assume that tumours are homogeneous. However, rapidly improving imaging techniques [139] mean that it is now possible to obtain global information about the tumour composition. Even

if we know the tumour composition at diagnosis it is not clear how this information can be used to predict prognosis and treatment response more accurately.

The aim of this thesis has been to start to address this issue by developing a methodology that would enable us to characterise interactions between co-cultured cell populations. Our work can be considered in a wider context in which we view cancers from an ecological perspective [17]. Since cancers should be studied in the context of the ecosystem in which they develop, experimental approaches alone may not be sufficient to study them due to the complexity involved. Mathematical models can supplement biological experiments as they provide a relatively fast and cheap tool for hypothesis testing. At the same time, experimental data are necessary to estimate parameter values in mathematical models. Therefore, we used a multidisciplinary approach whereby we conducted *in vitro* experiments guided by mathematical modelling and used statistical inference methods to estimate parameters in our models to study the effect of intratumour heterogeneity on tumour growth and radiation response. We focussed on biological interactions occurring between co-cultured populations of prostate cancer cell lines with different genetic and phenotypic features. Our objectives were to determine if intratumour heterogeneity affects bulk tumour growth and radiation response, if co-cultured cell populations interact, if these interactions are changed by radiation, and if the interactions are direct or indirect.

To fulfil these objectives we first developed a 3D *in vitro* model of avascular tumour growth (Chapter 2). In this assay pairs of clones derived from the same prostate cancer cell lines are co-cultured at different proportions in the presence of basement membrane extract Matrigel to form tumour spheroids. Although derived from the same cell lines, the control and resistant PC3 and DU145 cell populations possess different growth dynamics and different responses to radiation. The spheroids were irradiated with a single dose of 6 Gy and their volumetric growth and proportions measured over time. The resistant spheroids showed more aggressive growth than the control spheroids for both cell lines, though the difference was more pronounced for the PC3 cells which were also more sensitive to radiation. The growth curves of the heterogeneous spheroids did not provide sufficient information to suggest cross-talk between the control and resistant cells for either cell line. Collecting data on the proportions of the control and resistant clones showed that the latter were dominant in PC3 spheroids. Since the resistant cells grow faster and form larger spheroids, it is not surprising that they would outcompete the control cells in the absence of direct communication. However, the proportions data still do not explain the growth curves dynamics. To our surprise, in the DU145 spheroids the control population

was dominant, despite the resistant clone forming larger spheroids, with more rapid proliferation rates. Collectively, the results of the *in vitro* experiments presented in Chapter 2 suggest that the control and resistant may interact but further investigation is necessary.

In Chapter 3 we began to develop our methodology for mathematical modelling of the growth of co-cultured spheroids by focussing on homogeneous spheroids. Our objective was to estimate parameter values in a simple model of avascular tumour growth using the growth curves data. However, it is not sufficient to provide a best point estimate value for a parameter without quantifying its uncertainty. If mathematical models are ever to assist clinicians in planning anti-cancer therapy, then reliable quantitative measurements of uncertainty in the estimated parameter values and model predictions must be provided. We used nonlinear regression and ABC to estimate parameter values in the logistic model, and constructed asymptotic, Monte Carlo and bootstrap confidence intervals and credible intervals to quantify uncertainty around the estimates. By applying these techniques to synthetic data, we found that the asymptotic method provided narrower CIs than the simulation-based techniques (Monte Carlo and bootstrap) and that the rejection sampler algorithm provided similar estimates to nonlinear regression because we used the same deterministic distance function. Our methods were then applied to homogeneous spheroids data.

The growth of heterogeneous spheroids and interactions between co-cultured clones were modelled with a Lotka-Volterra model in Chapter 4. We conducted parameter recovery studies to first show that it is not possible to estimate the parameter values using only growth curves data and then to determine the time points at which the proportions of control and resistant cells should be measured. We also considered three distinct protocols for fitting the Lotka-Volterra model to spheroid data. Following the experimental design studies with synthetic data we measured the proportion of control and resistant cells at the determined time points and applied the three fitting protocols to establish the types of interactions between the clones in the PC3 and DU145 spheroids. Our results showed that the two PC3 clones competed and that the DU145 control cells preyed on the resistant clone. These interactions were not affected by a single dose of radiation.

Having shown competition between the PC3 cell types we aimed to establish whether the competition was indirect (e.g., for resources) or direct (e.g., cell-cell communication. To this end we developed a cellular automaton model. In Chapter 5, we described the model and analysed the relationship between its parameters and

parameters in a simple logistic model of tumour growth. We demonstrated the importance of choosing an appropriate model to fit to CA data and how the growth rate and carrying capacity parameters change in response to variation in CA model parameters.

In Chapter 6, we estimated parameter values in the CA model but were unable to uniquely identify them due to lack of information on spatial distribution of spheroids. We then generated heterogeneous CA spheroids in which the clones do not communicate directly and fit the Lotka-Volterra model to these synthetic data. This work showed that having shorter cell cycle time in the absence of direct competition was not sufficient for the resistant clone to become dominant. This study also revealed that the Lotka-Volterra model was able to accurately predict competition in heterogeneous spheroids with diverse growth kinetics and that a higher oxygen consumption rate in one population was correlated with greater strength of competitive effect that that population had on the other population.

This thesis provides a framework for exploring the effect that intratumour heterogeneity has on tumour growth and radiation response with a particular emphasis on interclonal interactions. Our work emphasises the importance of considering not only the presence of multiple clones within cancers but also their interactions. When radiotherapy is prescribed in the clinic the tumour is assumed to be homogeneous. The work presented here could be extended to compare the predictive powers of the logistic, Lotka-Volterra and CA models. The models could be used to determine how the knowledge of composition and interactions between distinct cell populations can lead to more accurate prognosis and prediction of how the tumour will respond to treatment. To illustrate how our framework can be used to inform clinicians let us consider a couple of examples. In Chapter 4 we found that the PC3 cell populations compete with each other. The data presented in Chapter 2 suggest that the resistant population will outcompete the control cells. However, mathematical modelling revealed that in the long term the control cells would dominate, eliminating the resistant clone for the 3:1 and 1:1 initial compositions (Fig. 4.11, two-step protocols). In such circumstances, it could be more beneficial to postpone treatment until the control population eliminates the treatment-resistant clone via competition. A patient would require lower radiation doses to kill treatment-sensitive control cells sparing normal tissue from exposure to large doses of radiation. Similarly, we found that the DU145 Res cells had a positive effect on the DU145 Ctrl population whilst the latter had a negative effect on the former. In this case, the treatment efficacy could also be improved if the treatment was postponed until the more sensitive population

outcompetes the resistant clone. In Chapter 6 we saw that even indirect competition for resources can lead to diverse dynamics between cell populations with many possible outcomes. If a clinician could predict these dynamics prior to administering treatment they would be better equipped to prescribe the most efficient therapeutic protocol.

The main limitation of this study was the quality of the images describing spatial distribution of spheroids. As a result we were unable to uniquely identify parameter values in the CA model and test the null hypothesis (no cross-talk between cell populations). This study could be repeated once spatial data are available and if direct communication is observed between the clones its impact on growth and radiation response should be investigated. Additionally, it would be beneficial to determine the biological mechanisms of communication and further investigate how these can be exploited to improve therapy outcome. It would very interesting to model the growth of DU145 spheroids with the CA model since they displayed a different type of interactions to the PC3 cells. The CA model can be readily extended to describe direct interactions between control and resistant cells and to simulate radiotherapy treatment. Such study could lead to further insight into how intratumour heterogeneity affects radiation response.

We used a simple Lotka-Volterra model with logistic growth to describe the dynamics and interactions between control and resistant cells. This choice was motivated by the simplicity of the model and our ability to estimate its parameters from available data. However, the model is overly simplistic and does not capture our data well in all cases. For example, the resistant population in heterogeneous DU145 spheroids showed a sign of recovery between days 16 and 25 but the model predicted that it would be eliminated via interactions with the control cells (Chapter 4). The growth and proportions of the spheroids would have to be measured for longer to validate the model predictions. On the other hand, growing the spheroids for longer may not be possible as they lose their compactness and spheroidicity. Another limitation of the Lotka-Volterra model is that it is spatially averaged and does not distinguish between necrotic, hypoxic and proliferating cells. Although in this thesis we did not model response to radiation explicitly, further studies are needed to assess how it is affected by intratumour heterogeneity. The model may need to be extended to track not only a cell type but also the stage of each cell in the cell cycle since sensitivity to radiation is affected by this factor.

This work represents an attempt to bridge the gap between experimentalists and modellers. Despite its limitations, we demonstrated that collaborations are vital

for addressing such complex questions as the impact of intratumour heterogeneity on tumour growth. We hope that this study will motivate further researchers to collaborate. Clinicians and experimentalists are starting to realise the benefits of viewing cancer from an ecological perspective, in which not only genetic mutations are relevant for tumorigenesis, progression and treatment response but also interactions with the existing tissue ecosystem. We believe that in the future this view will lead to interesting conclusions and further breakthroughs in the struggle against cancer.

Appendix A

A.1 Parameter estimates and 95% CIs for synthetic data

Table A.1: Parameter estimates and 95% confidence or credible intervals for $\theta^* = (0.3, 1.0, 0.03)$ and $\sigma = 0.01$

Method	$\hat{r}$	$\hat{K}$	$\hat{V_0}$
Asymptotic	0.2983 (0.2971, 0.2996)	1.0016 (0.9988, 1.0045)	0.0303 (0.0300, 0.0305)
Bootstrap (sd)	0.2978 (0.2923, 0.3040)	1.0012 (0.9927, 1.0097)	0.0305 (0.0289, 0.0320)
Bootstrap (res)	0.2984 (0.2963, 0.3002)	1.0014 (0.9992, 1.0039)	0.0302 (0.0297, 0.0308)
Monte Carlo	0.2983 (0.2952, 0.3012)	1.0009 (0.9942, 1.0075)	0.0303 (0.0297, 0.0310)
ABC	0.2983 (0.2983, 0.2984)	1.0016 (1.0015, 1.0017)	0.0303 (0.0302, 0.0303)

Table A.2: Parameter estimates and 95% confidence or credible intervals for $\theta^* = (0.3, 1.0, 0.03)$ and $\sigma = 0.1$.

Method	$\hat{r}$	$\hat{K}$	$\hat{V_0}$
Asymptotic	0.3013 (0.2867, 0.3159)	0.9891 (0.9591, 1.0192)	0.0303 (0.0279, 0.0328)
Bootstrap (sd)	0.3138 (0.2342, 0.3968)	0.9845 (0.8918, 1.0747)	0.0290 (0.0127, 0.0544)
Bootstrap (res)	0.3011 (0.2767, 0.3238)	0.9881 (0.9591, 1.0174)	0.0304 (0.0247, 0.0376)
Monte Carlo	0.3001 (0.2644, 0.3373)	0.9918 (0.9110, 1.0748)	0.0309 (0.0239, 0.0390)
ABC	0.3013 (0.3010, 0.3016)	0.9891 (0.9884, 0.9899)	0.0303 (0.0303, 0.0304)

Table A.3: Parameter estimates and 95% confidence or credible intervals for $\theta^* = (0.3, 1.0, 0.03)$ and $\sigma = 0.2$.

Method	$\hat{r}$	$\hat{K}$	$\hat{V_0}$
Asymptotic	0.3140 (0.2709, 0.3571)	0.9819 (0.9186, 1.0451)	0.0310 (0.0220, 0.0401)
Bootstrap (sd)	0.3451 (0.2405, 0.4805)	0.9609 (0.8297, 1.0927)	0.0254 (0.0072, 0.0538)
Bootstrap (res)	0.3161 (0.2574, 0.3789)	0.9668 (0.9023, 1.0305)	0.0308 (0.0171, 0.0484)
Monte Carlo	0.3245 (0.2571, 0.3995)	0.9645 (0.8284, 1.1104)	0.0299 (0.0185, 0.0438)
ABC	0.3140 (0.3133, 0.3146)	0.9819 (0.9810, 0.9828)	0.0310 (0.0309, 0.0312)

Table A.4: Parameter estimates and 95% confidence or credible intervals for $\theta^* = (0.1, 1.0, 0.03)$ and $\sigma = 0.01$.

Method	$\hat{r}$	$\hat{K}$	$\hat{V_0}$
Asymptotic	0.1002 (0.0993 ,0.1010)	0.9981 (0.9602, 1.0360)	0.0300 (0.0297, 0.0302)
Bootstrap (sd)	0.1016 (0.0979, 0.1055)	0.9483 (0.8265, 1.0935)	0.0296 (0.0285, 0.0307)
Bootstrap (res)	0.1002 (0.0988, 0.1015)	0.9995 (0.9500, 1.0582)	0.0300 (0.0296, 0.0304)
Monte Carlo	0.1007 (0.0986, 0.1030)	0.9795 (0.8848, 1.0841)	0.0299 (0.0293, 0.0305)
ABC	0.1002 (0.1001, 0.1002)	0.9981 (0.9970, 0.9992)	0.0300 (0.0300, 0.0300)

Table A.5: Parameter estimates and 95% confidence or credible intervals for $\theta^* = (0.1, 1.0, 0.03)$ and $\sigma = 0.1$.

Method	$\hat{r}$	$\hat{K}$	$\hat{V_0}$
Asymptotic	0.1053 (0.0963, 0.1143)	0.7963 (0.5569, 1.0357)	0.0291 (0.0268, 0.0313)
Bootstrap (sd)	0.1144 (0.0901, 0.1472)	0.7623 (0.4475,1.4721)	0.0266 (0.0181, 0.0346)
Bootstrap (res)	0.1057 (0.0961, 0.1189)	0.8176 (0.5738, 1.1161)	0.0290 (0.0255, 0.0320)
Monte Carlo	0.1057 (0.0916, 0.1233)	1.1492 (0.5655, 2.4568)	0.0291 (0.0253, 0.0334)
ABC	0.1053 (0.1053, 0.1053)	0.7963 (0.7960, 0.7966)	0.0291 (0.0291, 0.0291)

Table A.6: Parameter estimates and 95% confidence or credible intervals for $\theta^* = (0.1, 1.0, 0.03)$ and $\sigma = 0.2$.

Method	$\hat{r}$	$\hat{K}$	$\hat{V_0}$
Asymptotic	0.1002 (0.0825, 0.1179)	1.3143 (-0.1111, 2.7396)	0.0291 (0.0245, 0.0336)
Bootstrap (sd)	0.1227 (0.0866, 0.1752)	1.0207 (0.3941, 3.7324)	0.0232 (0.0122, 0.0347)
Bootstrap (res)	0.1043 (0.0866, 0.1289)	1.6358 (0.5978, 5.7582)	0.0277 (0.0211, 0.0337)
Monte Carlo	0.1088 (0.0898, 0.1327)	1.6235 (0.5219, 7.1137)	0.0275 (0.0214, 0.0340)
ABC	0.1001 (0.0985, 0.1019)	1.3274 (1.1952, 1.4707)	0.0291 (0.0286, 0.0295)

A.2 The effect of the number of data points on the parameter estimates

To investigate the effect of the number of data points in the training set (Section 3.3.4) on the parameter estimates and their asymptotic confidence intervals we tabulated the recorded estimates and their uncertainties in Tables A.7 and A.8.

Table A.7: Decreasing the number of data points in the training set for the slow growing spheroids leads to inaccurate parameter estimates and wide 95% confidence intervals. Parameter values: $\theta^* = (0.1, 1.0, 0.03)$, $\sigma = 0.1$.

n	$\hat{r}$	$\hat{K}$	$\hat{V}_0$
15	0.1053 (0.0963, 0.1143)	0.7963 (0.5569, 1.0357)	0.0291 (0.0268, 0.0313)
14	0.1061 (0.0948, 0.1174)	0.7671 (0.4519, 1.0823)	0.0290 (0.0264, 0.0315)
13	0.0978 (0.0873, 0.1083)	1.3764 (0.1009, 2.6519)	0.0302 (0.0280, 0.0323)
12	0.0959 (0.0818, 0.1100)	1.7470 (-1.4291, 4.9231)	0.0304 (0.0278, 0.0330)
11	0.0951 (0.0786, 0.1117)	1.9914 (-3.1211, 7.1039)	0.0305 (0.0276, 0.0335)
10	0.0966 (0.0702, 0.1230)	1.5198 (-4.0630, 7.1026)	0.0304 (0.0265, 0.0342)
9	0.0929 (0.0593, 0.1264)	5.0000 (-85.0530, 95.0530)	0.0307 (0.0262, 0.0352)
8	0.1021 (0.0465, 0.1577)	0.6961 (-2.1634, 3.5557)	0.0300 (0.0240, 0.0360)
7	0.1368 (0.0860, 0.1875)	0.2058 (0.0664, 0.3453)	0.0277 (0.0232, 0.0322)
6	0.1219 (0.0289, 0.2150)	0.2878 (-0.4519, 1.0276)	0.0285 (0.0218, 0.0353)
5	0.1434 (-0.0605, 0.3474)	0.1819 (-0.3200, 0.6838)	0.0275 (0.0149, 0.0400)
4	0.1583 (-1.2864, 1.6030)	0.1494 (-2.0611, 2.3599)	0.0268 (-0.0450, 0.0986)
3	0.1127 (not available)	5.0000 (not available)	0.0277 (not available)

Table A.8: Fast growing spheroids are less sensitive to decreasing number of data points in the training set. Parameter values: $\theta^* = (0.3, 1.0, 0.03)$, $\sigma = 0.1$.

n	$\hat{r}$	$\hat{K}$	$\hat{V}_0$
15	0.3013 (0.2867, 0.3159)	0.9891 (0.9591, 1.0192)	0.0303 (0.0279, 0.0328)
14	0.3000 (0.2862, 0.3139)	0.9949 (0.9651, 1.0246)	0.0305 (0.0281, 0.0328)
13	0.3004 (0.2858, 0.3150)	0.9930 (0.9610, 1.0249)	0.0304 (0.0280, 0.0329)
12	0.3034 (0.2893, 0.3176)	0.9779 (0.9435, 1.0122)	0.0301 (0.0278, 0.0324)
11	0.3037 (0.2884, 0.3191)	0.9763 (0.9375, 1.0150)	0.0301 (0.0276, 0.0325)
10	0.2980 (0.2802, 0.3157)	1.0138 (0.9350, 1.0926)	0.0307 (0.0280, 0.0333)
9	0.2943 (0.2752, 0.3134)	1.0408 (0.9401, 1.1416)	0.0311 (0.0283, 0.0339)
8	0.2916 (0.2717, 0.3116)	1.0640 (0.9464, 1.1815)	0.0313 (0.0285, 0.0342)
7	0.2927 (0.2630, 0.3224)	1.0522 (0.8155, 1.2890)	0.0312 (0.0274, 0.0351)
6	0.3017 (0.2579, 0.3454)	0.9411 (0.5805, 1.3017)	0.0305 (0.0256, 0.0354)
5	0.2903 (0.1953, 0.3854)	1.1401 (-0.6169, 2.8970)	0.0313 (0.0221, 0.0405)
4	0.2977 (-0.3207, 0.9160)	0.9804 (-9.1566, 11.1173)	0.0308 (-0.0191, 0.0807)
3	0.3966 (not available)	0.3522 (not available)	0.0254 (not available)

A.3 Parameter estimates and 95% CIs for homogeneous spheroids data

In this section we include the numerical values resulting from the uncertainty quantification analysis for the homogeneous spheroids data.

Table A.9: Parameter estimates and 95% confidence or credible intervals for the DU145 control spheroids.

Method	$\hat{r}$	$\hat{K}$	$\hat{V}_0$
Asymptotic	0.3150 (0.2919, 0.3381)	0.6256 (0.5856, 0.6656)	0.0117 (0.0095, 0.0139)
Bootstrap (sd)	0.3639 (0.3082, 0.4275)	0.6017 (0.5464, 0.6599)	0.0074 (0.0037, 0.0125)
Bootstrap (res)	0.3180 (0.2774, 0.3643)	0.6199 (0.5907, 0.6520)	0.0114 (0.0072, 0.0167)
Monte Carlo	0.3186 (0.2951, 0.3431)	0.6192 (0.5813, 0.6581)	0.0115 (0.0096, 0.0134)
ABC	0.3150 (0.3149, 0.3151)	0.6256 (0.6254, 0.6258)	0.0117 (0.0117, 0.0117)

Table A.10: Parameter estimates and 95% confidence or credible intervals for the DU145 resistant spheroids.

Method	$\hat{r}$	$\hat{K}$	$\hat{V}_0$
Asymptotic	0.3010 (0.2695, 0.3326)	0.6940 (0.6374, 0.7505)	0.0208 (0.0163, 0.0254)
Bootstrap (sd)	0.2513 (0.1970, 0.3120)	0.7549 (0.6701, 0.8581)	0.0331 (0.0200, 0.0502)
Bootstrap (res)	0.3014 (0.2590, 0.3494)	0.7094 (0.6704, 0.7554)	0.0216 (0.0138, 0.0304)
Monte Carlo	0.3079 (0.2803, 0.3393)	0.7163 (0.6699, 0.7644)	0.0202 (0.0162, 0.0240)
ABC	0.3010 (0.3010, 0.3011)	0.6940 (0.6939, 0.6940)	0.0208 (0.0208, 0.0209)

Table A.11: Parameter estimates and 95% confidence or credible intervals for the PC3 control spheroids.

Method	$\hat{r}$	$\hat{V}_0$
Asymptotic	0.1353 (0.0521, 0.2184)	0.0297 (0.0042, 0.0552)
Bootstrap (sd)	0.1522 (0.1051, 0.1998)	0.0286 (0.0149, 0.0451)
Bootstrap (res)	0.1372 (0.0980, 0.1743)	0.0344 (0.0215, 0.0495)
Monte Carlo	0.1246 (0.0916, 0.1578)	0.0392 (0.0272, 0.0529)
ABC	0.1353 (0.1352, 0.1354)	0.0297 (0.0297, 0.0297)

Table A.12: Parameter estimates and 95% confidence or credible intervals for the PC3 resistant spheroids.

Method	$\hat{r}$	$\hat{K}$	$\hat{V}_0$
Asymptotic	0.3218 (0.2979, 0.3458)	0.7873 (0.7180, 0.8567)	0.0224 (0.0204, 0.0243)
Bootstrap (sd)	0.3562 (0.2478, 0.5059)	0.7789 (0.6095, 1.1168)	0.0195 (0.0065, 0.0359)
Bootstrap (res)	0.3225 (0.2923, 0.3550)	0.7933 (0.7062, 0.8915)	0.0224 (0.0185, 0.0265)
Monte Carlo	0.3291 (0.2793, 0.3869)	0.9263 (0.6902, 1.2755)	0.0220 (0.0162, 0.0280)
ABC	0.3218 (0.3218, 0.3219)	0.7873 (0.7871, 0.7875)	0.0224 (0.0223, 0.0224)

Appendix B

B.1 Analysis of the Lotka-Volterra interactions model

To analyse the linear stability of the system (4.1) we introduce dimensionless variables

$$u_C = \frac{V_C}{K_C}, \quad u_R = \frac{V_R}{K_R}, \quad \tau = r_C t, \quad \rho = \frac{r_R}{r_C}, \quad \gamma_C = \lambda_C \frac{K_C}{K_R}, \quad \gamma_R = \lambda_R \frac{K_R}{K_C} \tag{B.1}$$

and rewrite Eqs. (4.1) in dimensionless form as

$$\begin{aligned} \frac{du_C}{d\tau} &= u_C(1 - u_C - \gamma_R u_R) = f_C(u_C, u_R), \\ \frac{du_R}{d\tau} &= \rho u_R(1 - u_R - \gamma_C u_C) = f_R(u_C, u_R). \end{aligned} \tag{B.2}$$

The steady states u_C^* and u_R^*, which are defined as solution to $f_C(u_C, u_R) = f_R(u_C, u_R) = 0$, and their linear stabilities determined by the community matrix

$$A = \begin{bmatrix} \frac{\partial f_C}{\partial u_C} & \frac{\partial f_C}{\partial u_R} \\ \frac{\partial f_R}{\partial u_C} & \frac{\partial f_R}{\partial u_R} \end{bmatrix}_{u_C^*, u_R^*}$$

are given by:

$$u_C^* = 0, u_R^* = 0 \quad \text{is unstable,}$$

$$u_C^* = 0, u_R^* = 1 \quad \text{is} \quad \begin{cases} \text{unstable (saddle point)} & \text{if } \gamma_R < 1 \\ \text{stable (node)} & \text{if } \gamma_R > 1, \end{cases}$$

$$u_C^* = 1, u_R^* = 0 \quad \text{is} \quad \begin{cases} \text{unstable (saddle point)} & \text{if } \gamma_C < 1 \\ \text{stable (node)} & \text{if } \gamma_C > 1. \end{cases}$$

There is a fourth, non-trivial steady state

$$u_C^* = \frac{1 - \gamma_R}{1 - \gamma_C \gamma_R}, \quad u_R^* = \frac{1 - \gamma_C}{1 - \gamma_C \gamma_R} \tag{B.3}$$

which exists and is biologically relevant if u_C^*, $u_R^* > 0$. Thus its existence and stability depend on the relative values of γ_C and γ_R. We summarise the cases that can arise in Figure B.1.

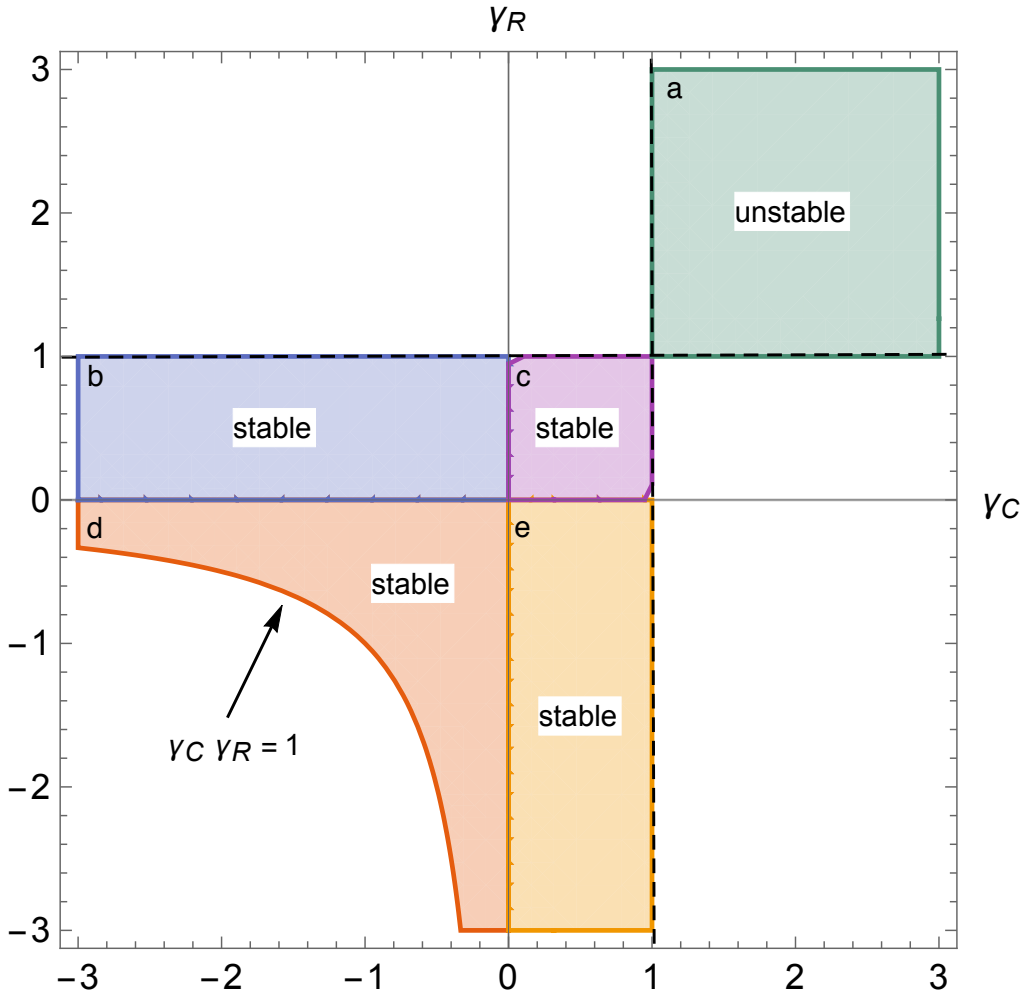

Figure B.1: Diagram representing the regions in the γ_C,γ_R-plane for which the equilibrium point (B.3) exists and is biologically relevant. **a)** (u_C^*, u_R^*) is a saddle point. **b)** and **e)** (u_C^*, u_R^*) is a stable node if $0 < \rho < \frac{-1+\gamma_R+2\gamma_C\gamma_R-2\gamma_C\gamma_R^2}{-1+\gamma_C} - 2\sqrt{\frac{-\gamma_C\gamma_R+2\gamma_C\gamma_R^2+\gamma_C^2\gamma_R^2-\gamma_C\gamma_R^3-2\gamma_C^2\gamma_R^3+\gamma_C^2\gamma_R^4}{(-1+\gamma_C)^2}}$ or $\rho > \frac{-1+\gamma_R+2\gamma_C\gamma_R-2\gamma_C\gamma_R^2}{-1+\gamma_C} + 2\sqrt{\frac{-\gamma_C\gamma_R+2\gamma_C\gamma_R^2+\gamma_C^2\gamma_R^2-\gamma_C\gamma_R^3-2\gamma_C^2\gamma_R^3+\gamma_C^2\gamma_R^4}{(-1+\gamma_C)^2}}$ or a stable focus (spiral point) if $\frac{-1+\gamma_R+2\gamma_C\gamma_R-2\gamma_C\gamma_R^2}{-1+\gamma_C} - 2\sqrt{\frac{-\gamma_C\gamma_R+2\gamma_C\gamma_R^2+\gamma_C^2\gamma_R^2-\gamma_C\gamma_R^3-2\gamma_C^2\gamma_R^3+\gamma_C^2\gamma_R^4}{(-1+\gamma_C)^2}} < \rho < \frac{-1+\gamma_R+2\gamma_C\gamma_R-2\gamma_C\gamma_R^2}{-1+\gamma_C} + 2\sqrt{\frac{-\gamma_C\gamma_R+2\gamma_C\gamma_R^2+\gamma_C^2\gamma_R^2-\gamma_C\gamma_R^3-2\gamma_C^2\gamma_R^3+\gamma_C^2\gamma_R^4}{(-1+\gamma_C)^2}}$. Thus although the stability of the steady state point does not change its dynamics depend on the value of ρ. **c)** and **d)** (u_C^*, u_R^*) is a stable node.

B.2 Fitting protocols: kinetic parameters

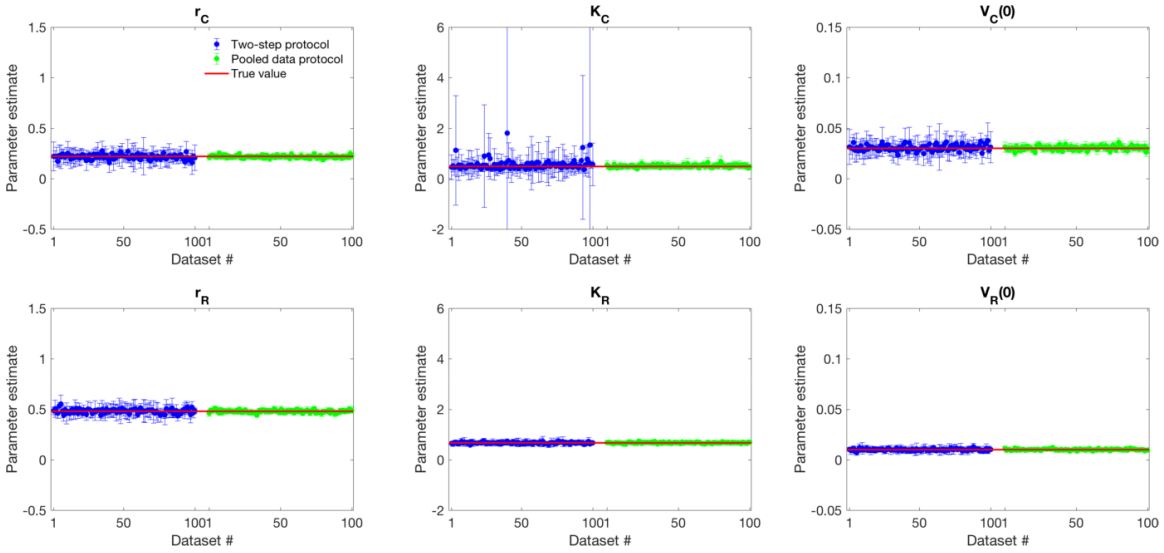

(a) PC3: 5% noise

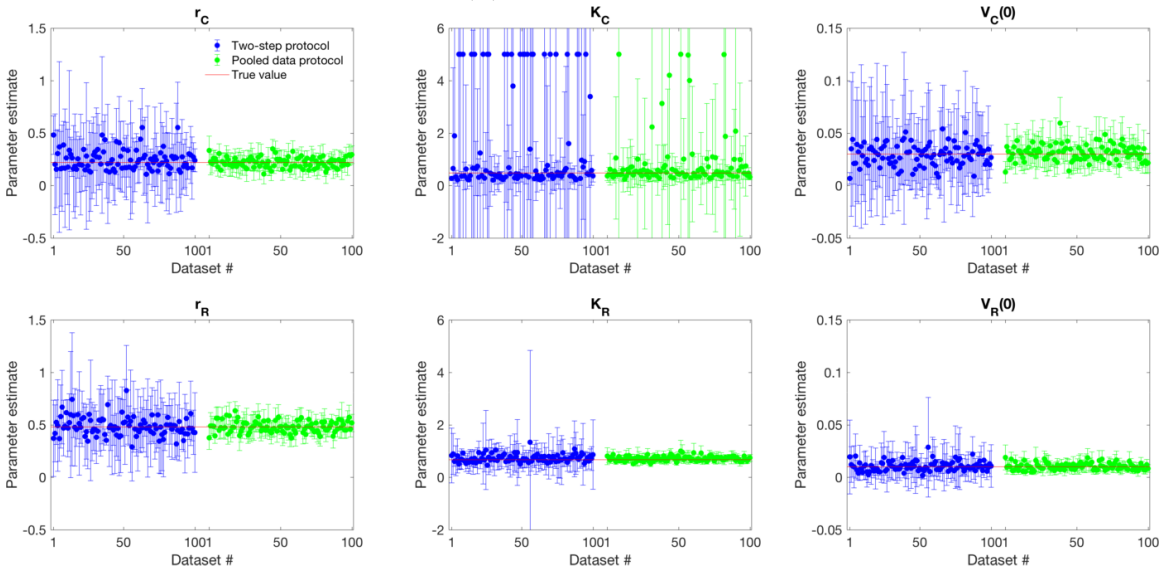

(b) PC3: 20% noise

Figure B.2: Estimated values of the parameters r_C, K_C, $V_C(0)$, r_R, K_R and $V_R(0)$ with 95% CIs for the synthetic PC3 spheroids data with 5% (a) and 20% (b) noise. Blue circles show the values estimated using the two-step protocol. Green circles show the values estimated using the pooled data protocol. Red lines correspond to the "true" values used to generate the data.

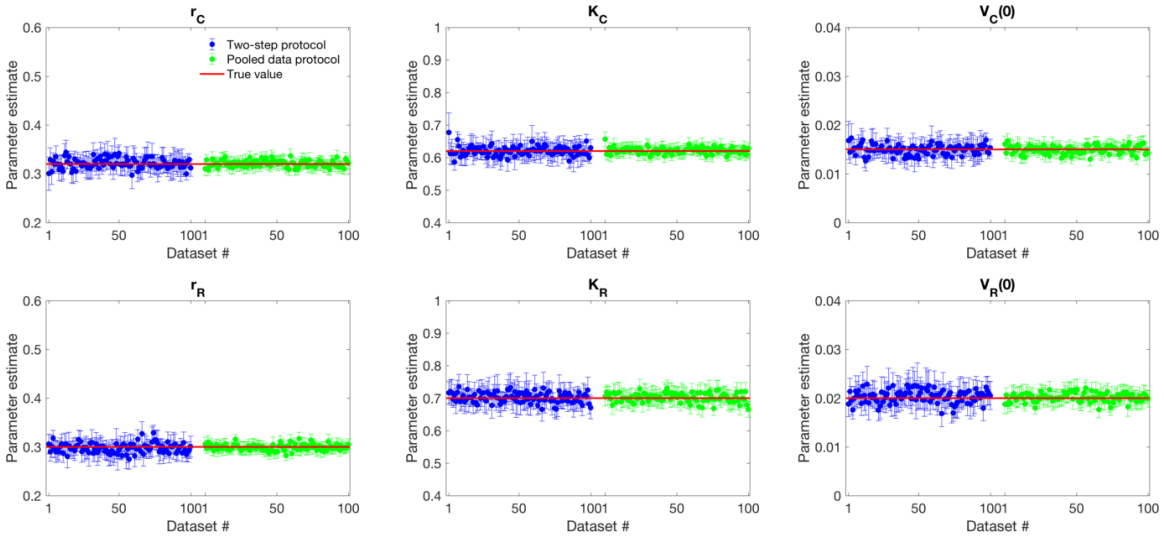

(a) DU145: 5% noise

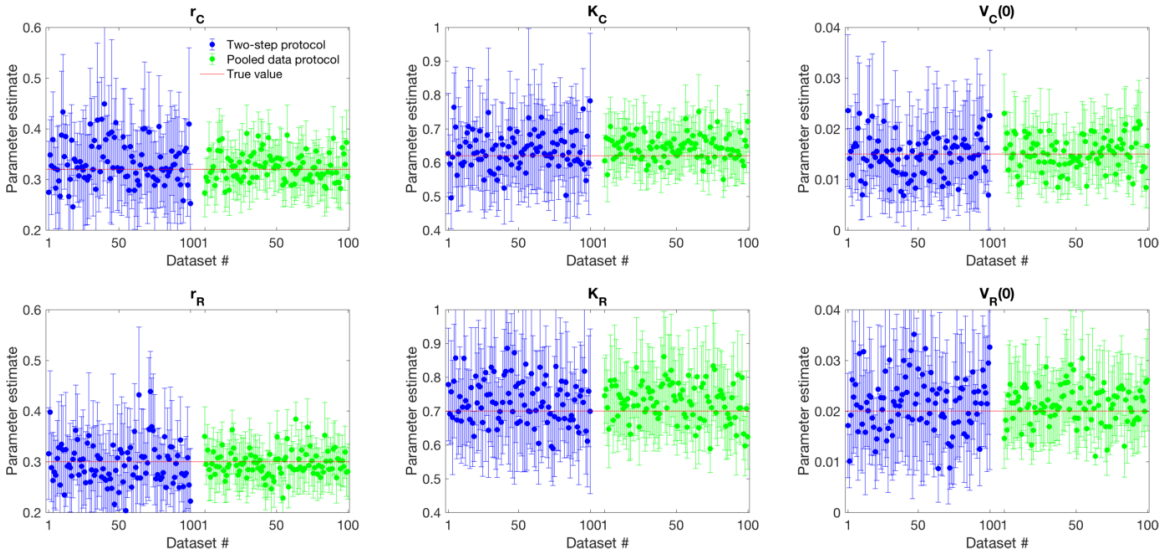

(b) DU145: 20% noise

Figure B.3: Estimated values of the parameters r_C, K_C, $V_C(0)$, r_R, K_R and $V_R(0)$ with 95% CIs for the synthetic DU145 spheroids data with 5% (a) and 20% (b) noise. Blue circles show the values estimated using the two-step protocol. Green circles show the values estimated using the pooled data protocol. Red lines correspond to the "true" values used to generate the data.

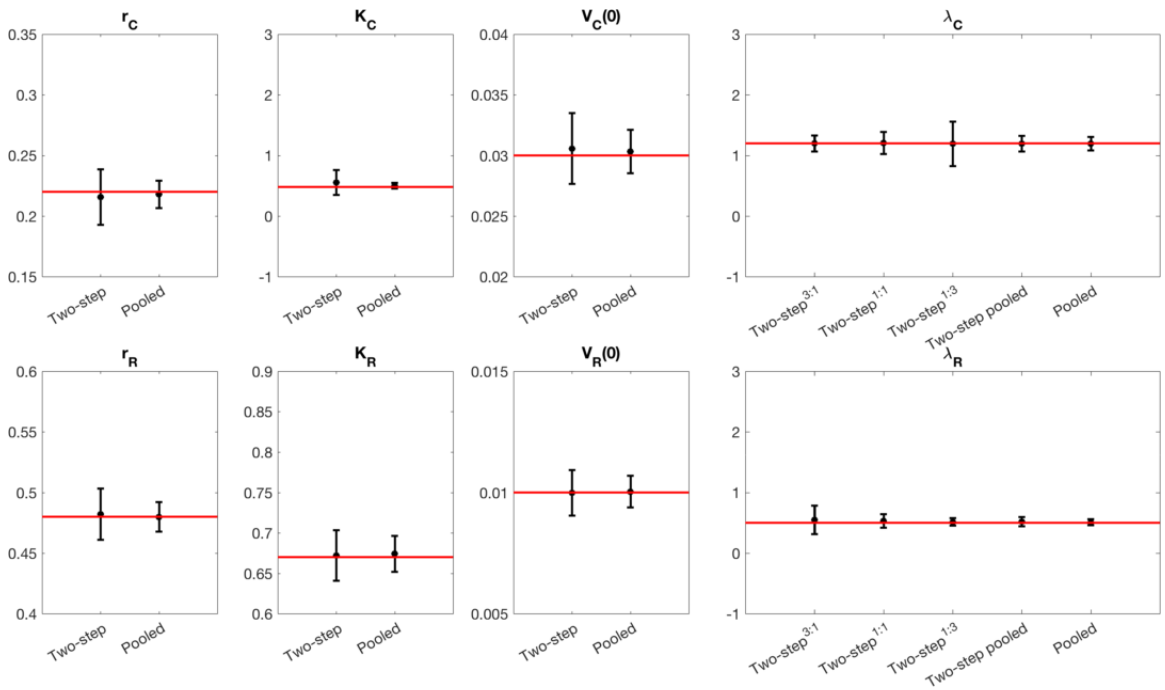

(a) PC3: 5% noise

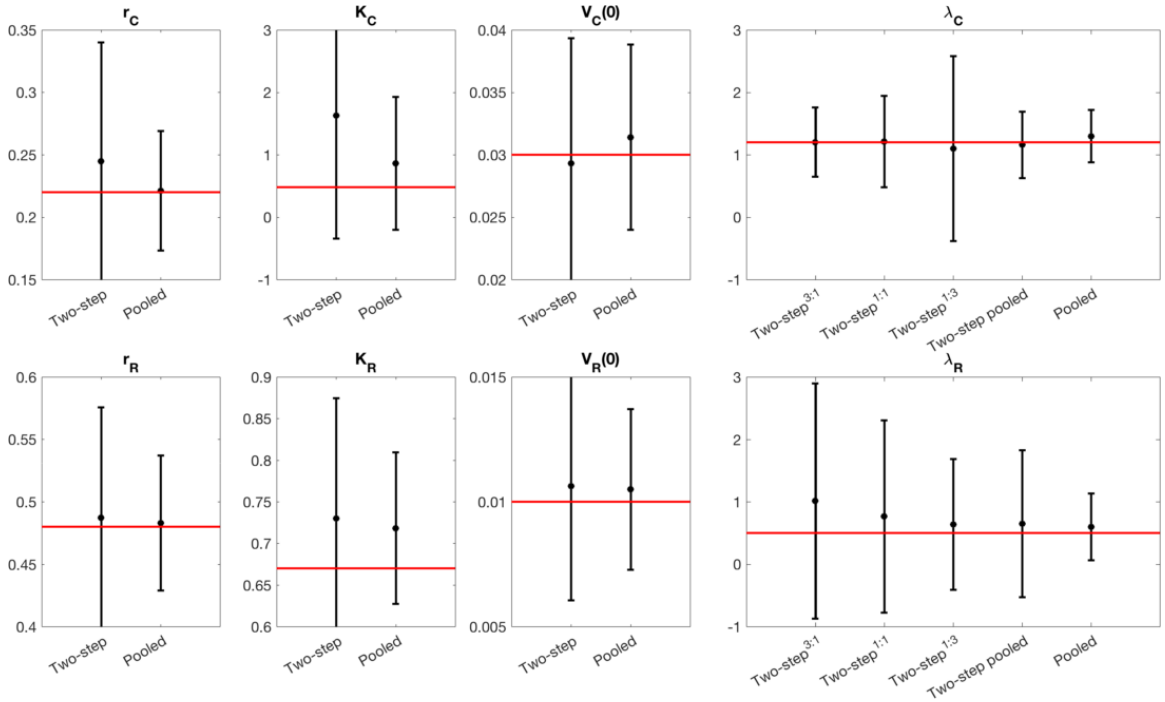

(b) PC3: 20% noise

Figure B.4: Comparison of the parameter values in the Lotka-Volterra model obtained by fitting the model to the synthetic PC3 spheroids data with 5% (a) and 20% (b) noise performed using the three fitting protocols. The values shown represent the mean±1×SD from 100 datasets. True values used to generate the data are represented by red horizontal lines.

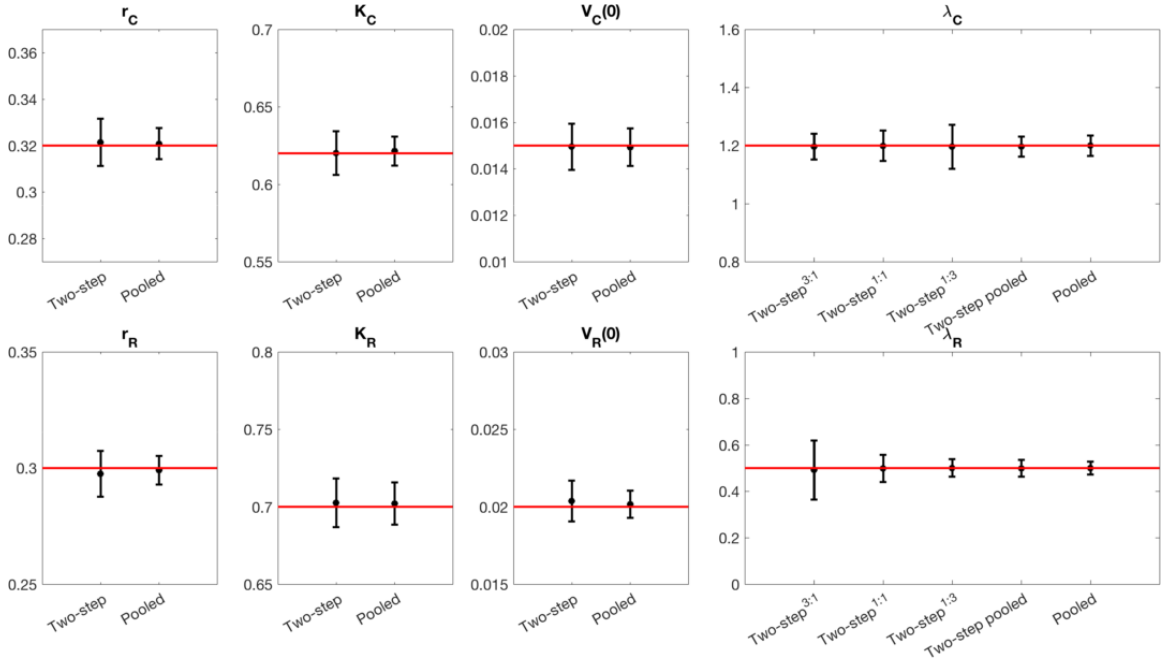

(a) DU145: 5% noise

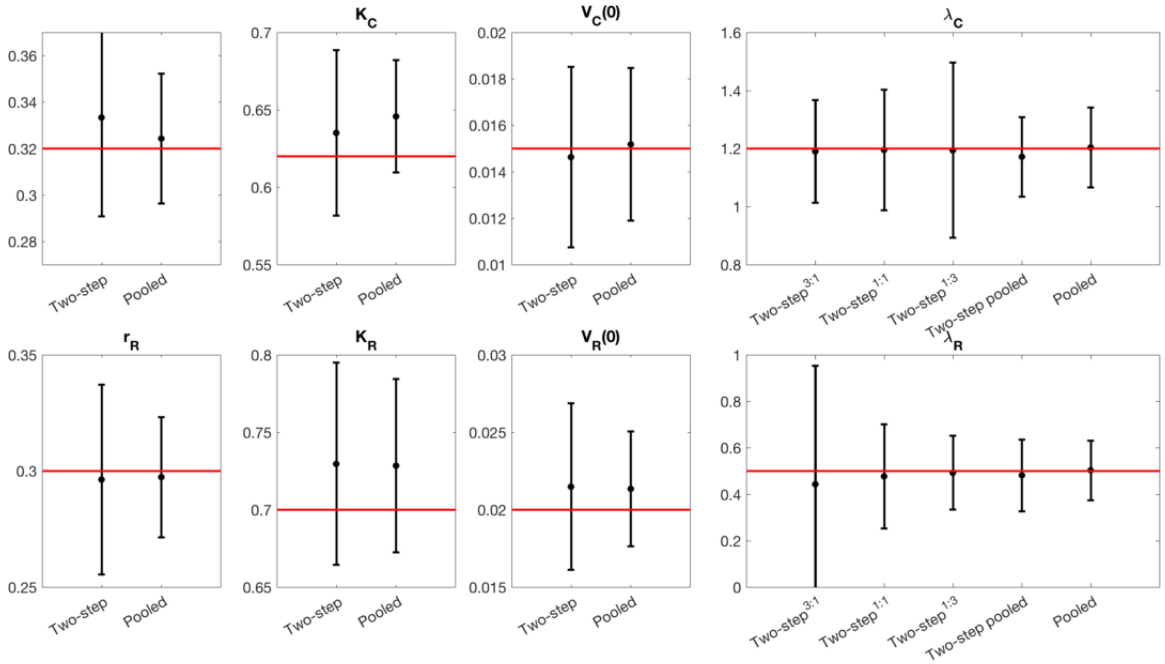

(b) DU145: 20% noise

Figure B.5: Comparison of the parameter values in the Lotka-Volterra model (4.1) obtained by fitting the model to the synthetic DU145 spheroids data with 5% (a) and 20% (b) noise performed using the three fitting protocols. The values shown represent the mean$\pm$1$\times$SD from 100 datasets. True values used to generate the data are represented by red horizontal lines.

B.3 Fitting protocols: interaction parameters

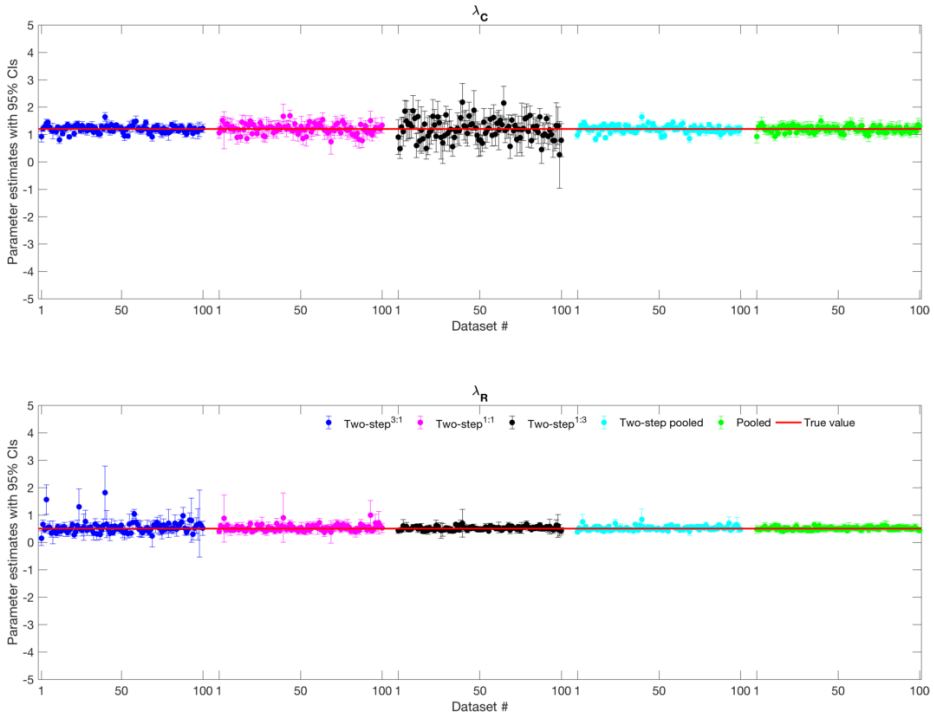

(a) PC3: 5% noise

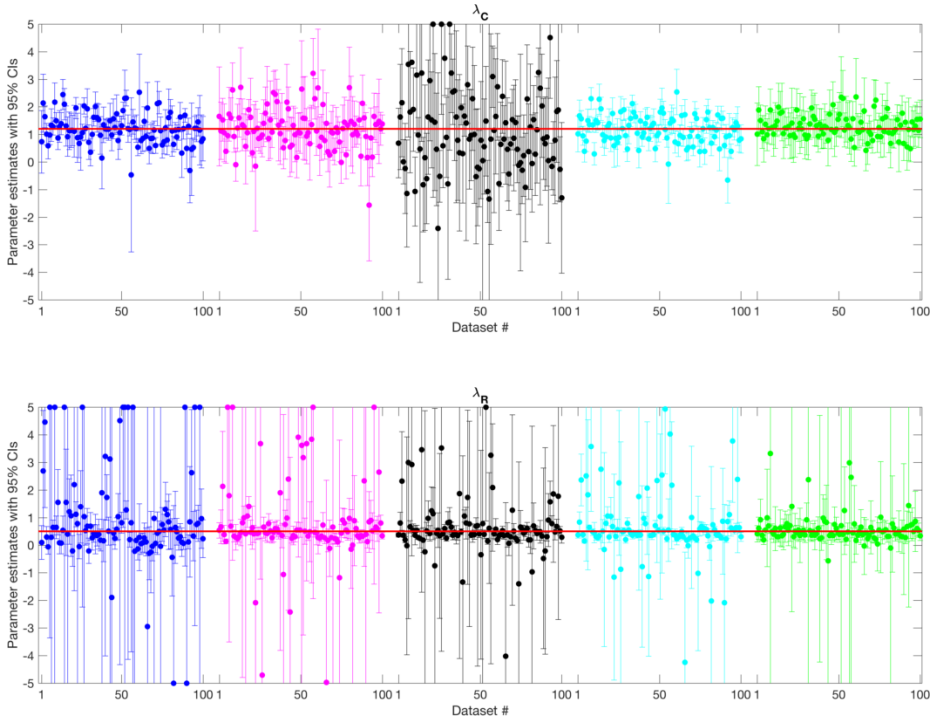

(b) PC3: 20% noise

Figure B.6: Estimated values with 95% CIs of the interaction parameters λ_C and λ_R for the synthetic PC3 spheroids with 5% (a) and 20% (b) noise obtained using the three fitting protocols.

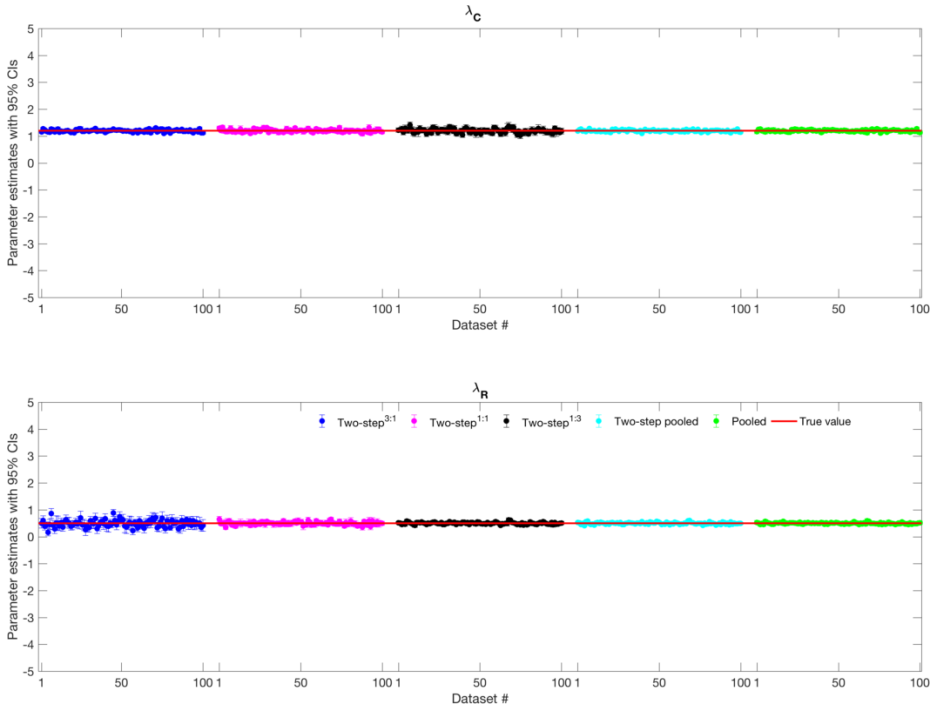

(a) DU145: 5% noise

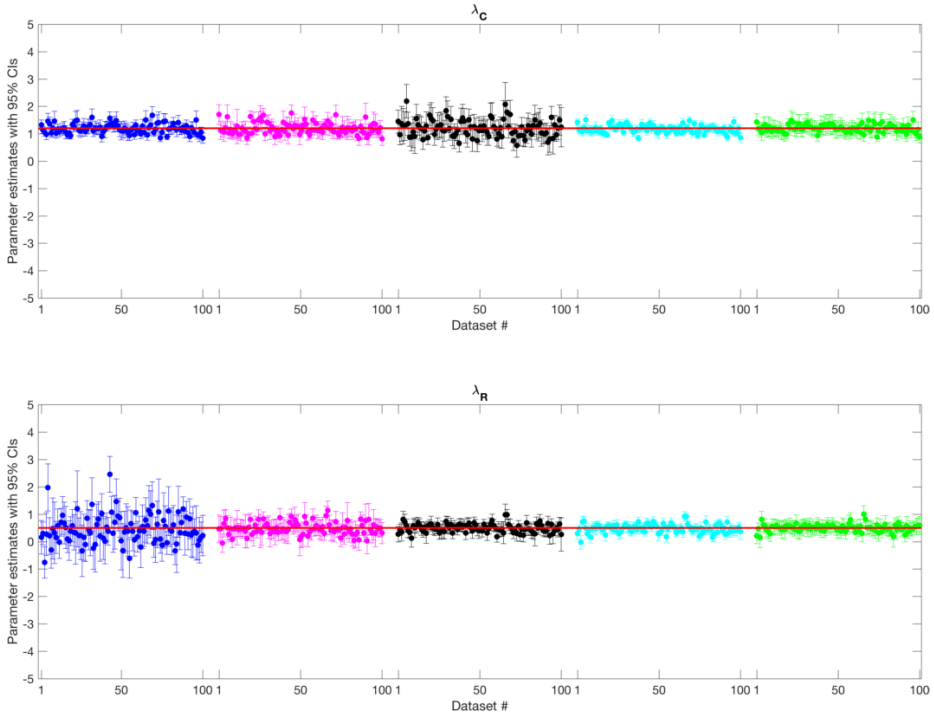

(b) DU145: 20% noise

Figure B.7: Estimated values with 95% CIs of the interaction parameters λ_C and λ_R for the synthetic DU145 spheroids with 5% (a) and 20% (b) noise obtained using the three fitting protocols.

Appendix C

C.1 Analysis of the reaction-diffusion equation numerical solver: spatial grid size

We selected the spatial grid size Δx in our numerical solver of the reaction-diffusion equation (5.4) to correspond to the size of a single cell. Thus both computational grids have a size $N \times N$ where $N = 200$. To demonstrate that our choice leads to a sensible approximation to the solution of the underlying equation we study the impact of decreasing Δx on the solution. We begin by fixing the CA grid containing cells to a representative population and then we solve the oxygen equation (5.4) for a range of spatial grid sizes. We choose two cell populations: one corresponds to a small spheroid consisting of only proliferating cells (Fig.C.1a), and another one to a mature spheroid in which a large necrotic core is surrounded by a layer of quiescent cells and a rim of proliferating cells (Fig.C.1b).

Although we do not know the analytical solution to Eq. (5.4), our numerical approximation should approach this solution as $\Delta x \to 0$ and $\Delta t \to 0$. We investigate the effect of decreasing Δx by systematically doubling the size of the grid on which we solve Eq. (5.4). We consider four different cases: in addition to $N = 200$ we also solve Eq. (5.4) on the grids where $N = 400, 800$ and 1600. Since our numerical scheme is convergent if $\mu \leq 0.25$ where $\mu = \frac{\Delta t}{(\Delta x)^2}$, every time we refine Δx we have to decrease Δt by a factor of 4 to keep $\mu = 0.25$.

Figs. C.1c and C.1d show oxygen profiles within the small and mature spheroids, respectively, for different grid sizes as a function of the distance from the spheroids centre (measured along the spheroid radius from its centre to its surface). Since the spheroids are symmetrical the profiles shown in Figs. C.1c and C.1d are the same in any direction.

As seen in Fig. C.1c oxygen concentration c in the spheroid centre is $c \approx 0.77$ and increases towards the spheroid's surface reaching $c \approx 1$ there. For the mature spheroid

(a) Representative small spheroid

(b) Representative mature spheroid

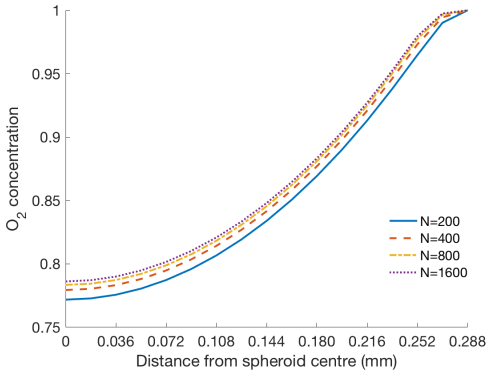

(c) Oxygen profile of small spheroid

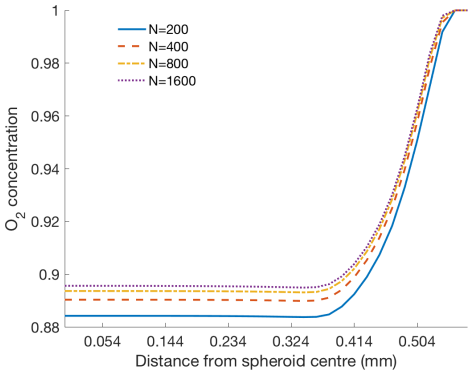

(d) Oxygen profile of mature spheroid

Figure C.1: Representative spheroids (a) and (b) and oxygen profiles along their radii (c) and (d) computed with Eq. (5.4) for different grid sizes ($N = 200, 400, 800, 1600$). Green cells are proliferating, yellow cells are quiescent and grey cells and necrotic. $\kappa = 170$, other parameters as in Table 5.1.

the oxygen concentration is below $c = 0.9$ in the centre and remains constant within the necrotic region (since necrotic cells do not consume oxygen) increasing rapidly at the distance $r \approx 0.35$ mm from the spheroid centre (where quiescent cells appear) reaching $c \approx 1$ at the spheroid's boundary (where $r \approx 0.520$ mm). In both cases, refining Δx results in higher oxygen profiles. However, as N doubles the resulting profiles appear to converge to what we envisage would be the analytical solution to Eq. (5.4). The differences in the oxygen concentration profiles for different grid sizes are more pronounced in the centres of the spheroids, vanishing as we approach the spheroids surfaces.

Although we could use a finer computational grid for our numerical solver in

Table C.1: Values of Δx and Δt for different spatial grid sizes.

N	Δx	Δt
200	5.0×10^{-3}	6.3×10^{-6}
400	2.5×10^{-3}	1.6×10^{-6}
800	1.3×10^{-3}	3.9×10^{-7}
1600	6.3×10^{-4}	9.8×10^{-8}

the CA model simulations, the computational burden associated with amending Δt each time Δx is refined outweighs the potential increase in the solver's accuracy. In Table C.1, we show the values of Δx and Δt for different grid sizes. The computational time for $N = 1600$ is two orders of magnitude higher than for $N = 200$. In practice, solving Eq. (5.4) increased from $\approx$ 20 seconds for $N = 200$ to over 3 hours for $N = 1600$ on a standard computer.

In conclusion, we verified that our numerical solver to Eq. (5.4) on a computational grid of the same size as the CA grid on which cells reside leads to numerically sound answers. Although refining Δx could potentially increase the accuracy of our solver, the associated increase in computation time would prohibit us from simulating the model in reasonable time.

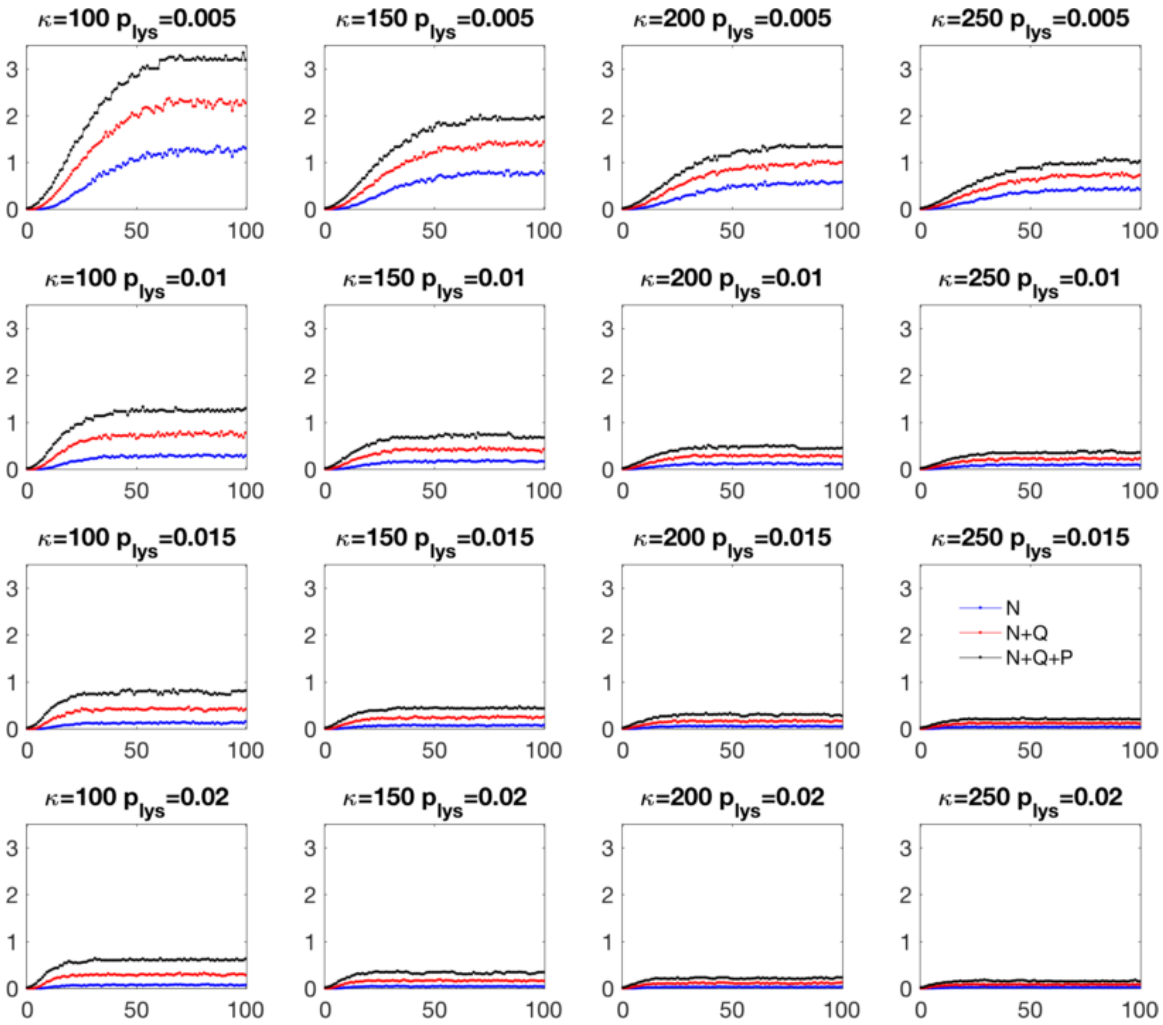

Figure C.2: Spatial distributions of CA homogeneous spheroids generated for a range of κ and p_{lys}. The horizontal axes represent time (days) and the vertical axes spheroid volumes (mm^3).

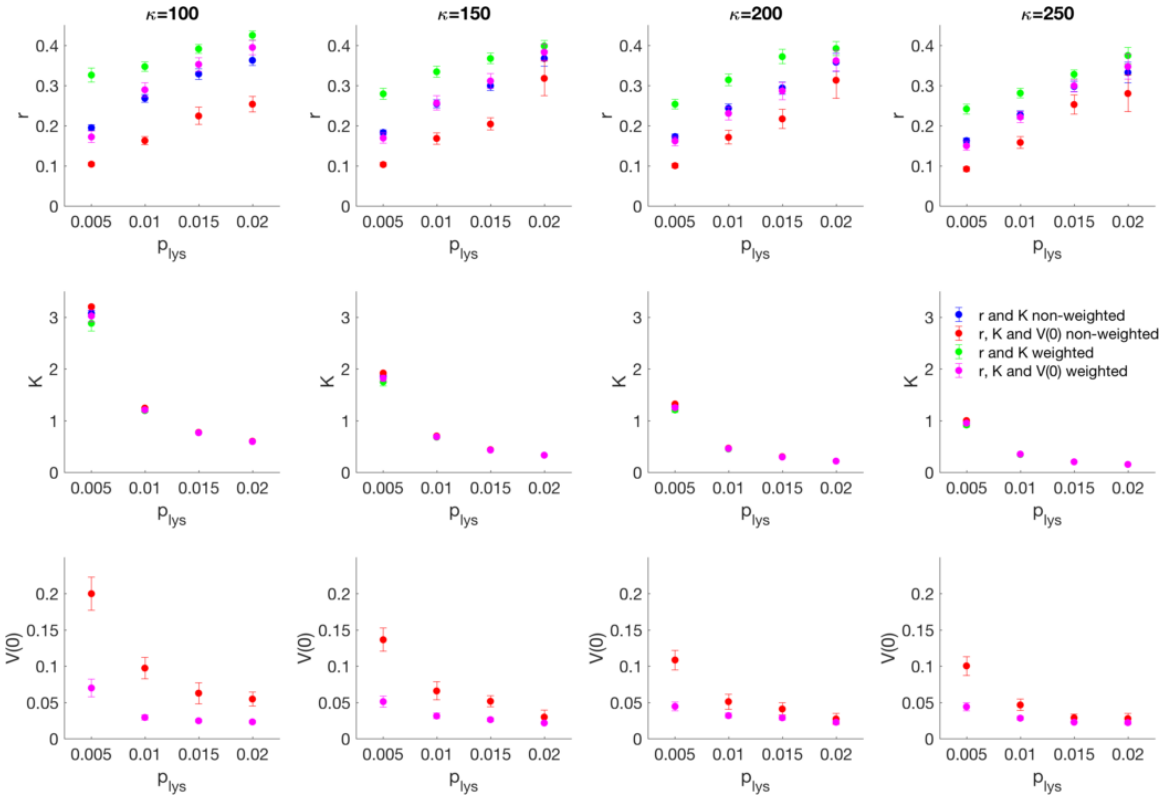

Figure C.3: Estimates of r, K and $V(0)$ obtained with four different regression models for a range of values of κ and p_{lys}. Circles show best point estimates and error bars corresponding 95% CIs.

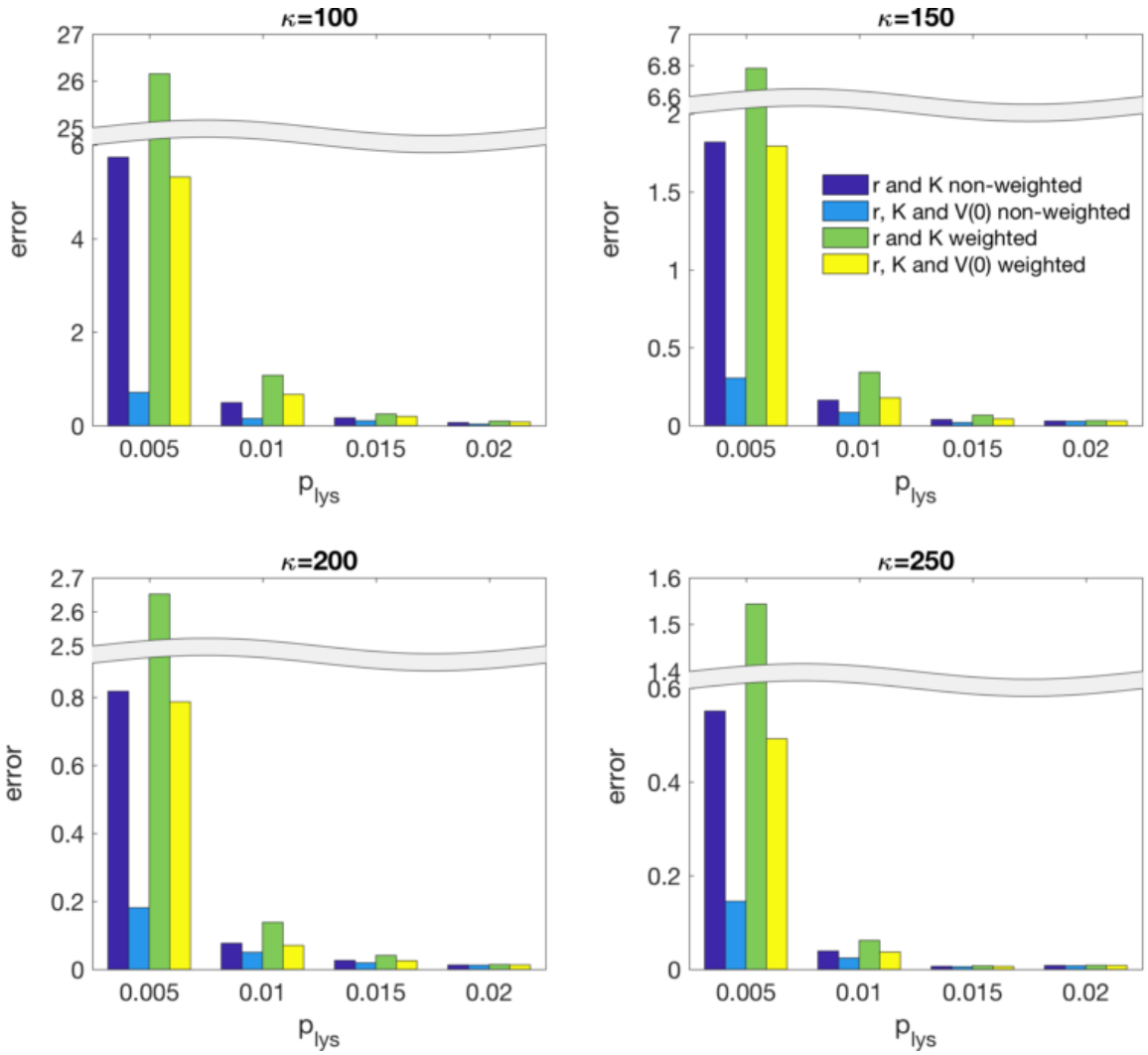

Figure C.4: Errors (sums of squared residuals) obtained for four regression models for a range of values of κ and p_{lys}.

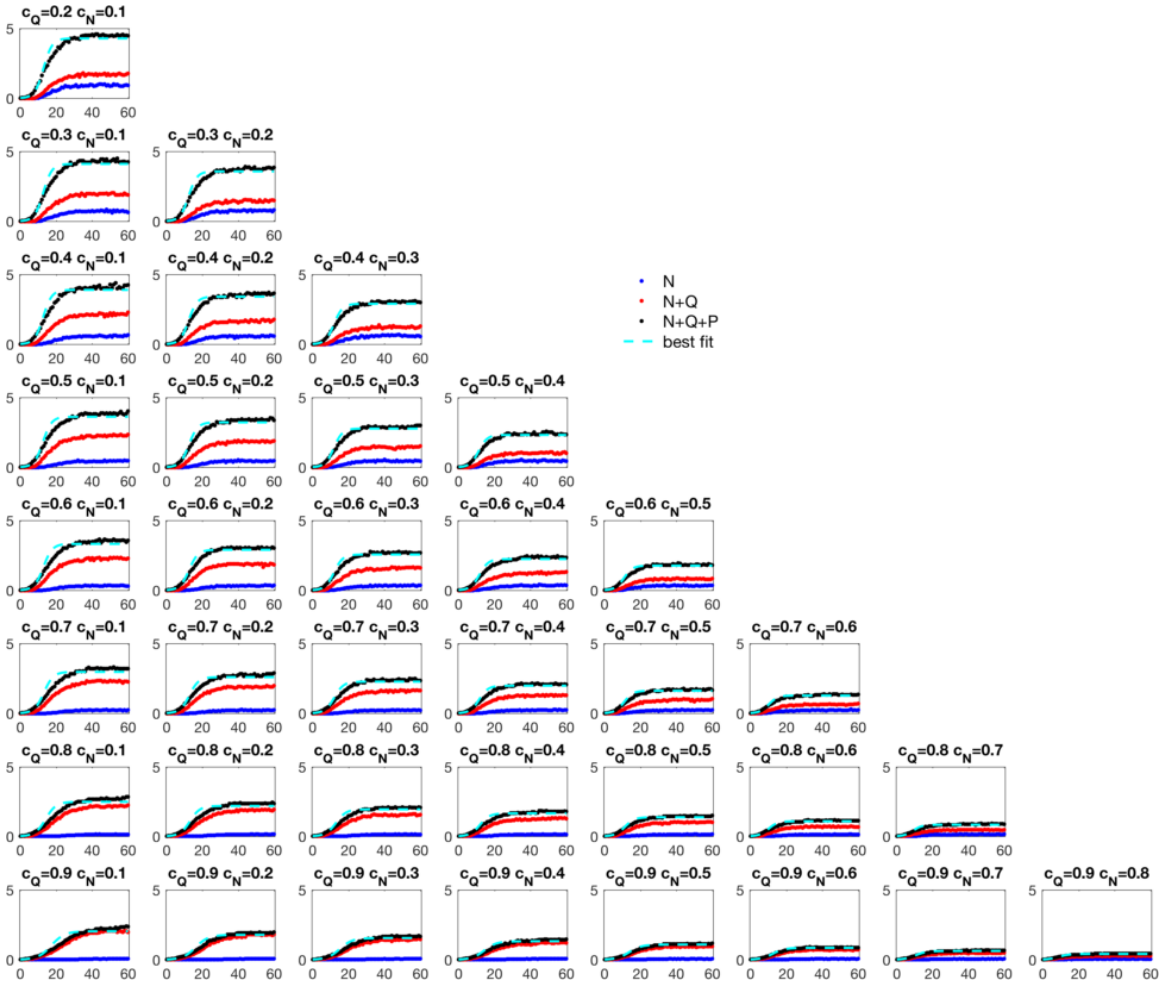

Figure C.5: Spatial distributions of CA homogeneous spheroids generated for a range of $c_{\mathcal{Q}}$ and $c_{\mathcal{N}}$ values and the best fits obtained with weighted-data regression for r and K. The horizontal axes represent time (days) and the vertical axes spheroid volumes (mm^3).

Appendix D

D.1 CA simulations of the growth of heterogeneous spheroids

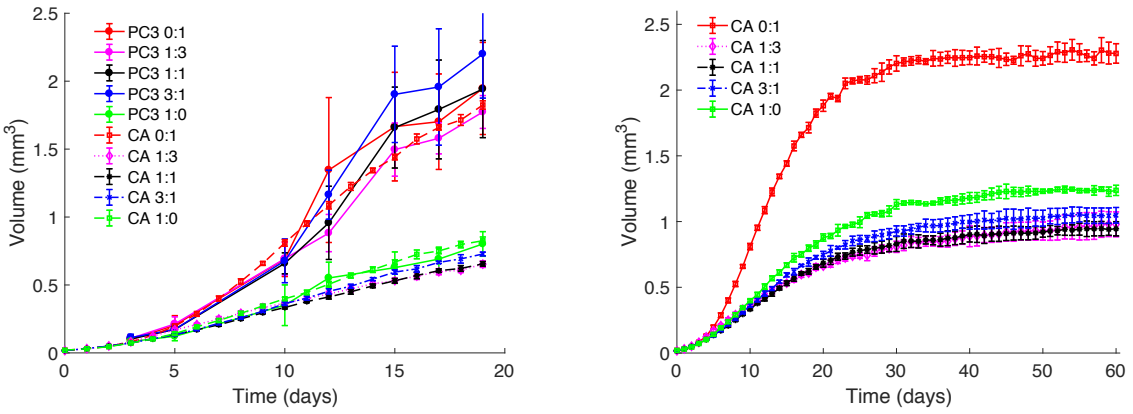

Figure D.1: Growth curves of heterogeneous C_1R_1 spheroids. Comparison of the growth curves of the heterogeneous *in vitro* PC3 and *in silico* C_1R_1 spheroids co-cultured at different ratios of control and resistant cells **(a)**; and long-term behaviour of the C_1R_1 spheroids **(b)**. Data points show the mean±1×SD from 12 independent experiments (PC3 spheroids) or 10 realisations of the CA model. For the parameter values used to generate the C_1R_1 spheroids see Tables 6.2 and 5.1.

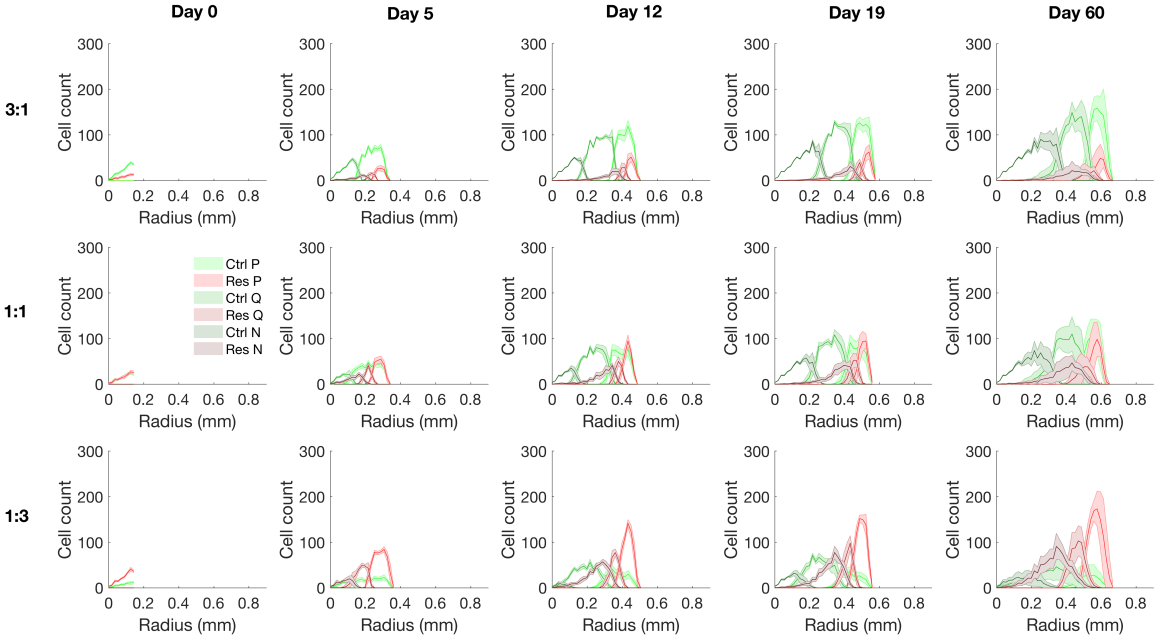

Figure D.2: Series of plots showing how the spatial distribution of heterogeneous C_1R_1 spheroids changes over time. Plots show the number of control and resistant cells in different states (proliferating, quiescent or necrotic) on cross-sections of spheroids as a function of their radius. Solid lines show the mean and the shaded error bars 1×SD based on 10 realisations of the CA model.

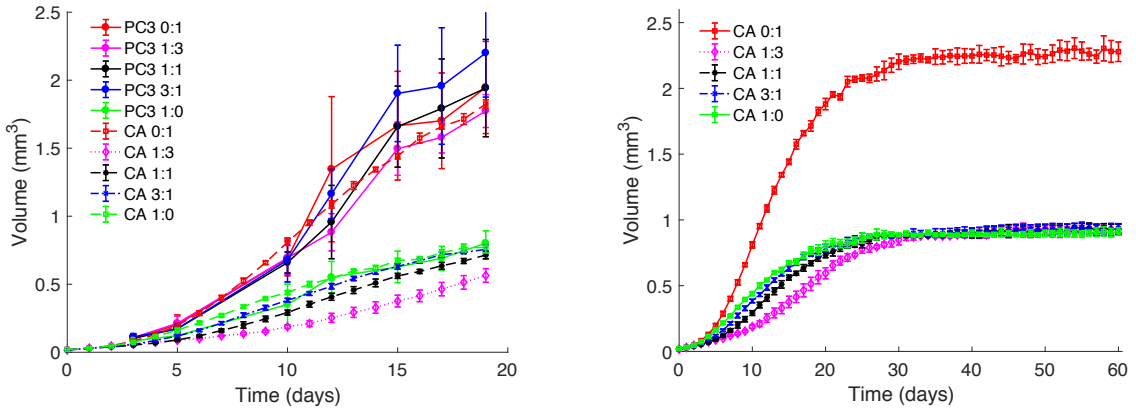

Figure D.3: Growth curves of heterogeneous C_2R_1 spheroids. Comparison of the growth curves of the heterogeneous *in vitro* PC3 and *in silico* C_2R_1 spheroids co-cultured at different ratios of control and resistant cells **(a)**; and long-term behaviour of the C_2R_1 spheroids **(b)**. Data points show the mean±1×SD from 12 independent experiments (PC3 spheroids) or 10 realisations of the CA model. For the parameter values used to generate the C_2R_1 spheroids see Tables 6.2 and 5.1.

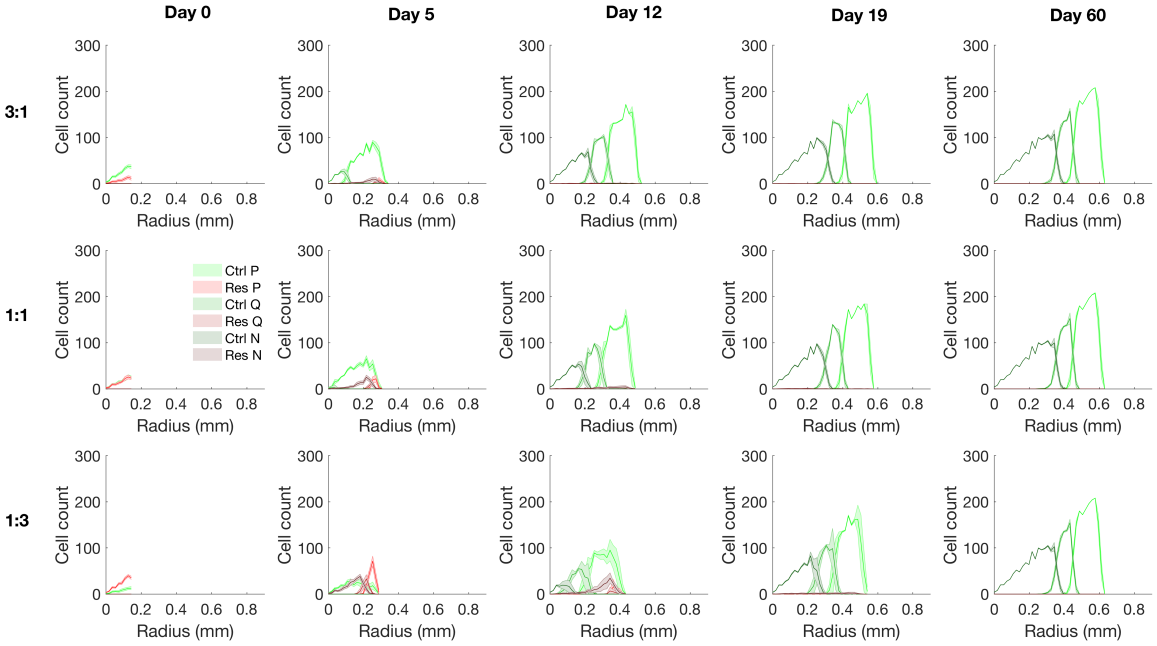

Figure D.4: Series of plots showing how the spatial distribution of heterogeneous C_2R_1 spheroids changes over time. Plots show the number of control and resistant cells in different states (proliferating, quiescent or necrotic) on cross-sections of spheroids as a function of their radius. Solid lines show the mean and the shaded error bars 1×SD based on 10 realisations of the CA model.

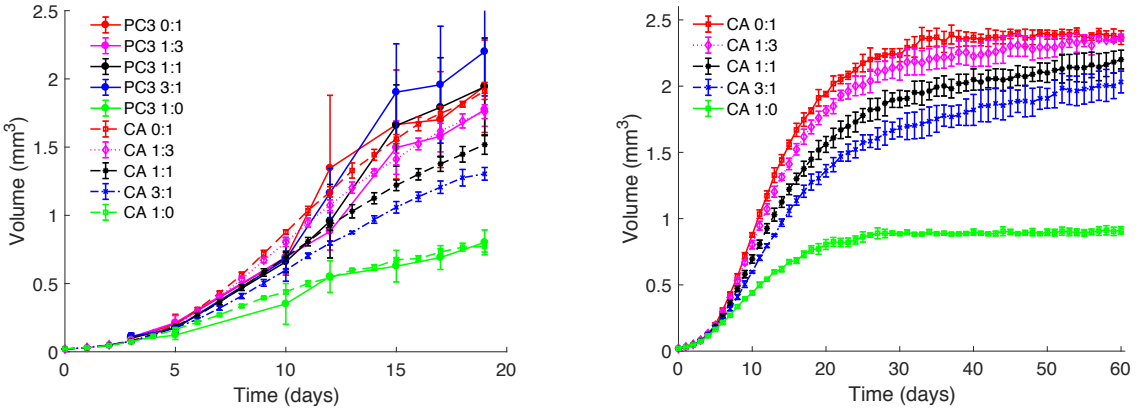

Figure D.5: Growth curves of heterogeneous C_2R_2 spheroids. Comparison of the growth curves of the heterogeneous *in vitro* PC3 and *in silico* C_2R_2 spheroids co-cultured at different ratios of control and resistant cells **(a)**; and long-term behaviour of the C_2R_2 spheroids **(b)**. Data points show the mean±1×SD from 12 independent experiments (PC3 spheroids) or 10 realisations of the CA model. For the parameter values used to generate the C_2R_2 spheroids see Tables 6.2 and 5.1.

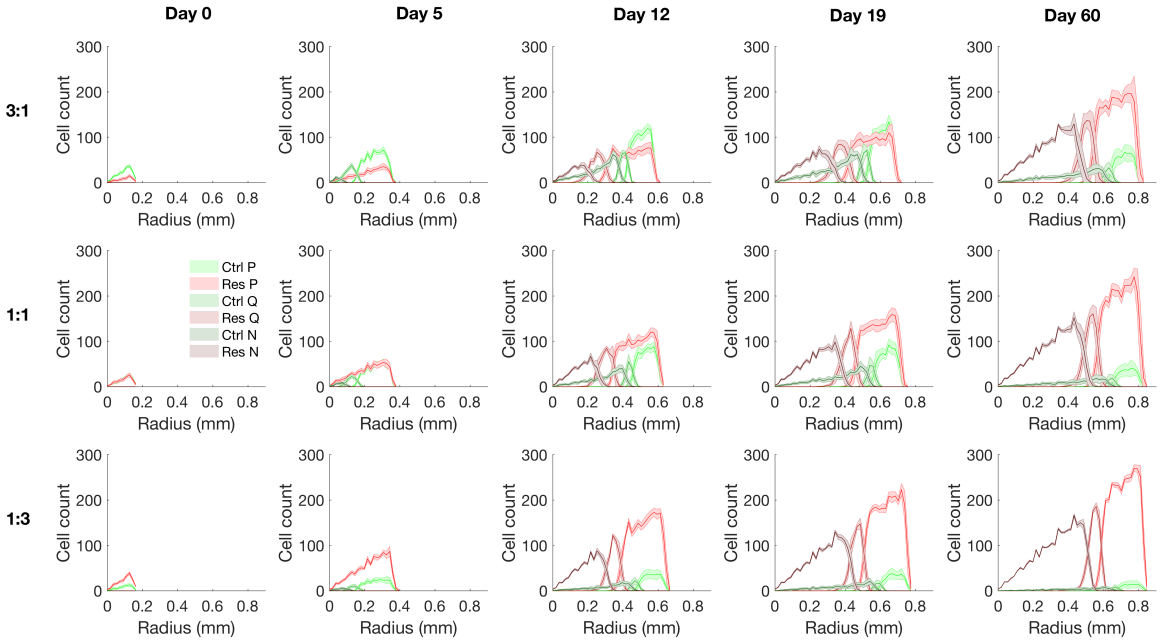

Figure D.6: Series of plots showing how the spatial distribution of heterogeneous C_2R_2 spheroids changes over time. Plots show the number of control and resistant cells in different states (proliferating, quiescent or necrotic) on cross-sections of spheroids as a function of their radius. Solid lines show the mean and the shaded error bars 1×SD based on 10 realisations of the CA model.

D.2 Lotka-Volterra fits to *in silico* heterogeneous CA spheroids

Table D.1: Parameter estimates and 95% CIs resulting from fitting the Lotka-Volterra model (4.3) to the C_1R_2 spheroids data using the two-step, two-step pooled and pooled fitting protocols.

	Two-step protocol	**Two-step pooled protocol**	**Pooled protocol**
r_{C_1}	**0.365** (0.360,0.370)	**0.365** (0.360,0.370)	**0.297** (0.293,0.302)
K_{C_1}	**1.128** (1.113,1.143)	**1.128** (1.113,1.143)	**1.132** (1.128,1.137)
r_{R_2}	**0.447** (0.443,0.450)	**0.447** (0.443,0.450)	**0.487** (0.481,0.493)
K_{R_2}	**2.257** (2.236,2.278)	**2.257** (2.236,2.278)	**2.187** (2.161,2.213)
η_{C_1}	**0.191** (0.178,0.204)$^{3:1}$ **-0.402** (-0.456,-0.348)$^{1:1}$ **-1.253** (-1.490,-1.016)$^{1:3}$	**0.165** (0.153,0.178)	**0.392** (0.368,0.416)
η_{R_2}	**0.242** (0.240,0.244)$^{3:1}$ **0.224** (0.222,0.226)$^{1:1}$ **0.239** (0.235,0.246)$^{1:3}$	**0.240** (0.239,0.241)	**0.212** (0.208,0.215)
σ	0.356	0.383	0.360
WSSR	836.824	966.820	855.474

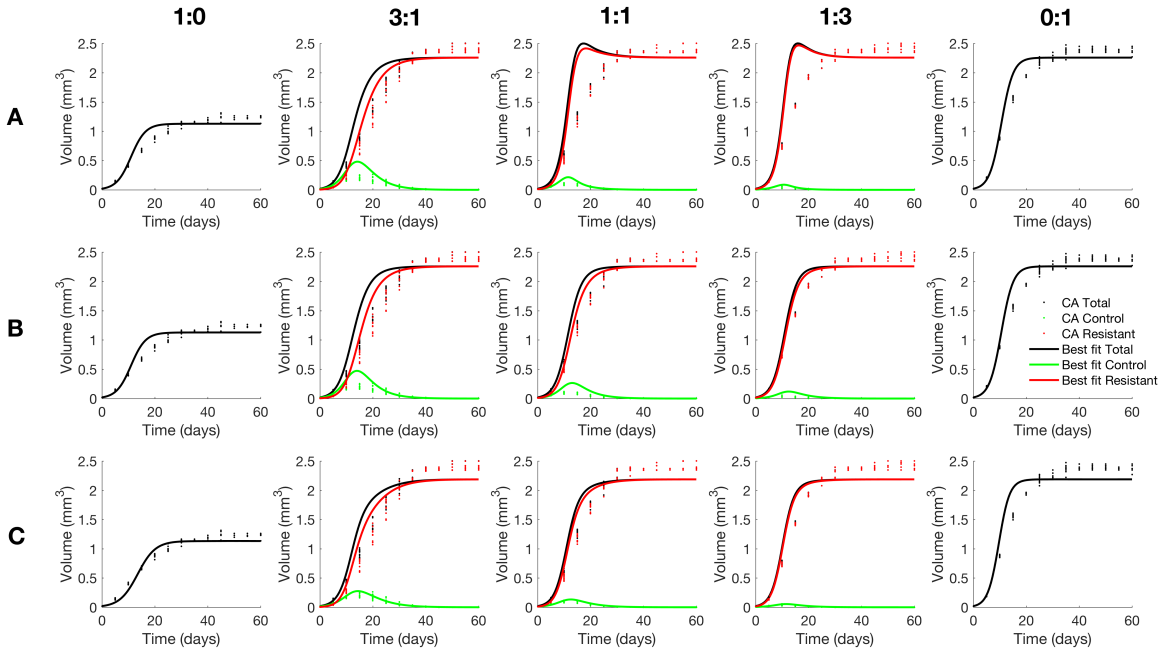

Figure D.7: Best fits of the Lotka-Volterra interactions model to the C_1R_2 spheroids data using the (A) two-step, (B) two-step pooled and (C) pooled fitting protocols.

Table D.2: Parameter estimates and 95% CIs resulting from fitting the Lotka-Volterra model (4.3) to the C_2R_2 spheroids data using the two-step, two-step pooled and pooled fitting protocols.

	Two-step protocol	**Two-step pooled protocol**	**Pooled protocol**
r_{C_2}	**0.417** (0.413,0.422)	**0.417** (0.413,0.422)	**0.396** (0.394,0.399)
K_{C_2}	**0.864** (0.857,0.871)	**0.864** (0.857,0.871)	**0.927** (0.916,0.937)
r_{R_2}	**0.447** (0.443,0.450)	**0.447** (0.443,0.450)	**0.475** (0.473,0.478)
K_{R_2}	**2.257** (2.236,2.278)	**2.257** (2.236,2.278)	**2.397** (2.377,2.418)
η_{C_2}	**0.347** (0.343,0.351)$^{3:1}$ **0.365** (0.358,0.372)$^{1:1}$ **0.311** (0.290,0.332)$^{1:3}$	**0.415** (0.413,0.417)	**0.451** (0.445,0.458)
η_{R_2}	**0.147** (0.145,0.149)$^{3:1}$ **0.171** (0.169,0.173)$^{1:1}$ **0.186** (0.184,0.188)$^{1:3}$	**0.189** (0.188,0.189)	**0.172** (0.170,0.174)
σ	0.161	0.197	0.166
WSSR	170.343	254.677	181.981

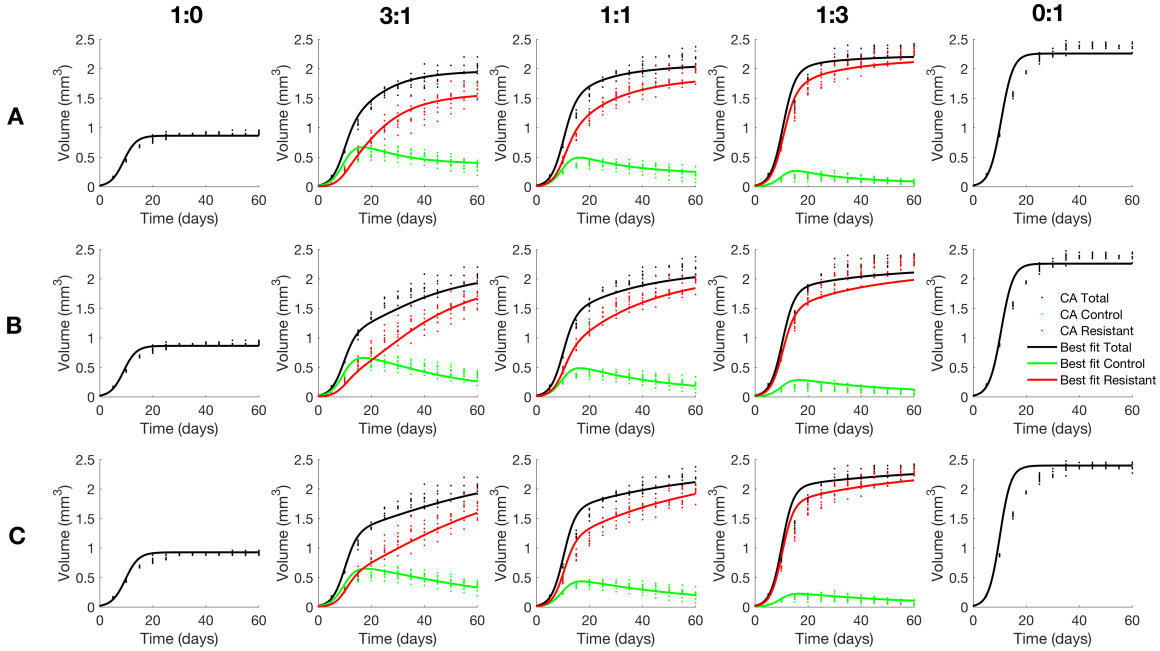

Figure D.8: Best fits of the Lotka-Volterra interactions model to the C_2R_2 spheroids data using the (A) two-step, (B) two-step pooled and (C) pooled fitting protocols.

Table D.3: Parameter estimates and 95% CIs resulting from fitting the Lotka-Volterra model (4.3) to the C_2R_1 spheroids data using the two-step, two-step pooled and pooled fitting protocols.

	Two-step protocol	**Two-step pooled protocol**	**Pooled protocol**
r_{C_2}	**0.417** (0.413,0.422)	**0.417** (0.413,0.422)	**0.416** (0.406,0.425)
K_{C_2}	**0.864** (0.857,0.871)	**0.864** (0.857,0.871)	**0.859** (0.845,0.874)
r_{R_1}	**0.437** (0.433,0.441)	**0.437** (0.433,0.441)	**0.355** (0.346,0.363)
K_{R_1}	**2.153** (2.133,2.174)	**2.153** (2.133,2.174)	**2.229** (2.124,2.333)
η_{C_2}	**1.312** (1.242,1.382)$^{3:1}$ **0.773** (0.752,0.794)$^{1:1}$ **0.785** (0.766,0.802)$^{1:3}$ **0.951** (0.579,1.323)$^{3:1}$	**1.153** (1.134,1.171)	**1.012** (0.984,1.039)
η_{R_1}	**-4.844** (-5.445,-4.242)$^{1:1}$ **-1.465** (-1.628,-1.302)$^{1:3}$	**0.237** (0.217,0.256)	**0.369** (0.318,0.420)
σ	0.496	0.507	0.498
WSSR	1621.214	1694.006	1637.985

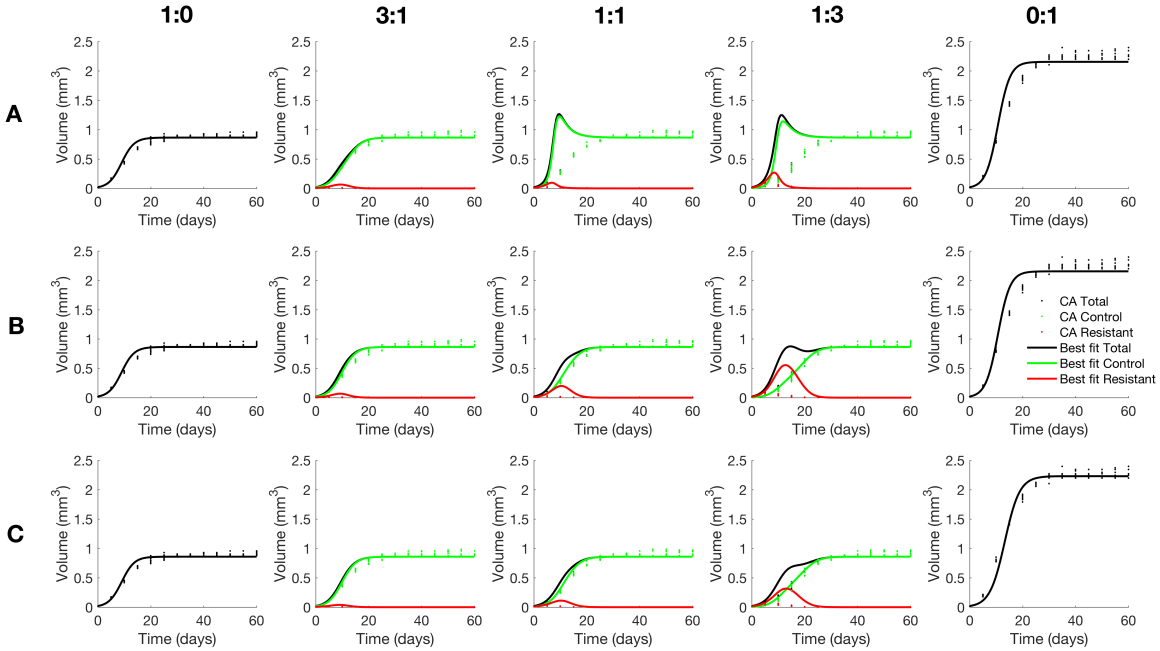

Figure D.9: Best fits of the Lotka-Volterra interactions model to the C_2R_1 spheroids data using the (A) two-step, (B) two-step pooled and (C) pooled fitting protocols.

Table D.4: Parameter estimates and 95% CIs resulting from fitting the Lotka-Volterra model (4.3) to the C_1R_1 spheroids data using the two-step, two-step pooled and pooled fitting protocols.

	Two-step protocol	**Two-step pooled protocol**	**Pooled protocol**
r_{C_1}	**0.365** (0.360,0.370)	**0.365** (0.360,0.370)	**0.439** (0.433,0.445)
K_{C_1}	**1.128** (1.113,1.143)	**1.128** (1.113,1.143)	**0.821** (0.811,0.832)
r_{R_1}	**0.437** (0.433,0.441)	**0.437** (0.433,0.441)	**0.363** (0.359,0.367)
K_{R_1}	**2.153** (2.133,2.174)	**2.153** (2.133,2.174)	**1.805** (1.764,1.846)
η_{C_1}	**0.532** (0.518,0.545)$^{3:1}$ **0.572** (0.553,0.591)$^{1:1}$ **0.839** (0.800,0.878)$^{1:3}$	**0.420** (0.418,0.422)	**0.436** (0.427,0.446)
η_{R_1}	**0.345** (0.326,0.365)$^{3:1}$ **0.241** (0.231,0.251)$^{1:1}$ **0.231** (0.225,0.238)$^{1:3}$	**0.146** (0.144,0.148)	**0.240** (0.232,0.248)
σ	0.380	0.405	0.318
WSSR	951.845	1083.547	666.085

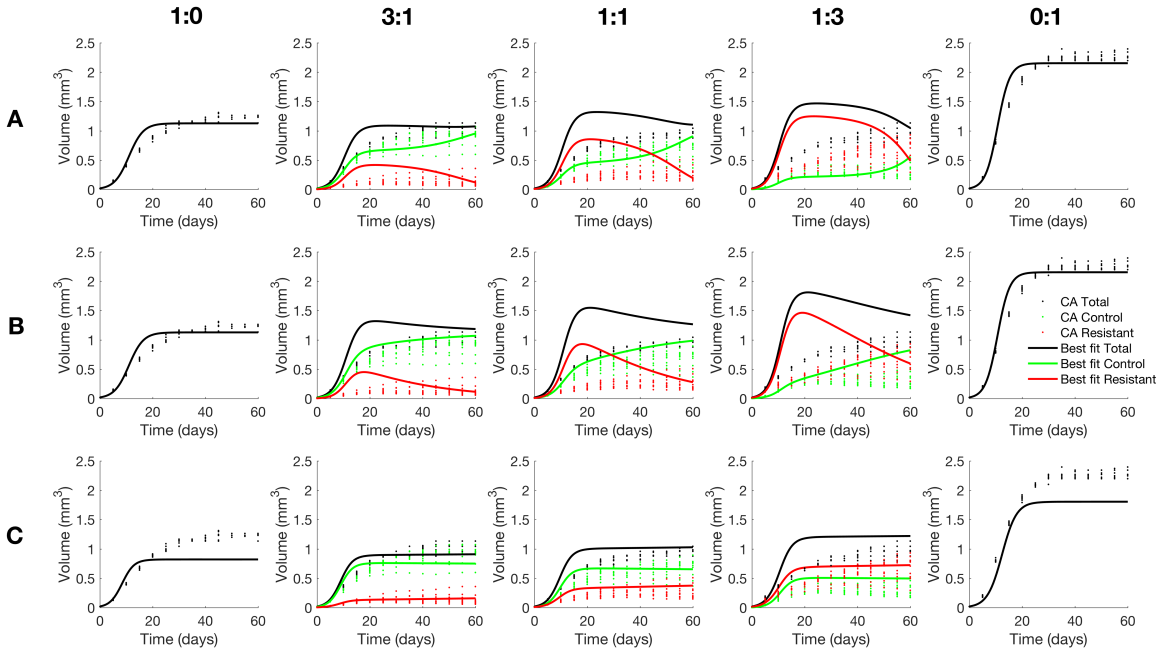

Figure D.10: Best fits of the Lotka-Volterra interactions model to the C_1R_1 spheroids data using the (A) two-step, (B) two-step pooled and (C) pooled fitting protocols.

Bibliography

[1] T. Alarcón, H. M. Byrne, and P. K. Maini. A cellular automaton model for tumour growth in inhomogeneous environment. *J. Theor. Biol.*, 225(2):257–274, 2003.

[2] T. Alarcón, H. M. Byrne, and P. K. Maini. Towards whole-organ modelling of tumour growth. *Prog. Biophys. Mol. Biol.*, 85(2-3):451–472, 2004.

[3] T. Alarcón, H. M. Byrne, and P. K. Maini. A multiple scale model for tumor growth. *Multiscale Model. Simul.*, 3(2):440–475, 2005.

[4] B. Alberts, A. Johnson, J. Lewis, M. Raff, K. Roberts, and P. Walter. *Molecular Biology of the Cell*. Garland Science, New York, 5th edition, 2008.

[5] A. Albini, F. Tosetti, V. W. Li, D. M. Noonan, and W. W. Li. Cancer prevention by targeting angiogenesis. *Nat. Rev. Clin. Oncol.*, 9(9):498–509, 2012.

[6] J. C. L. Alfonso, N. Jagiella, L. Núñez, M. A. Herrero, and D. Drasdo. Estimating dose painting effects in radiotherapy: a mathematical model. *PLoS One*, 9:e89380, 2014.

[7] P. M. Altrock, L. L. Liu, and F. Michor. The mathematics of cancer: integrating quantitative models. *Nat. Rev. Cancer*, 15(12):730–745, 2015.

[8] D. Ambrosi and L. Preziosi. On the closure of mass balance models for tumor growth. *Math. Models Methods Appl. Sci.*, 12(5):737–754, 2002.

[9] A. R. A. Anderson. A hybrid mathematical model of solid tumour invasion: the importance of cell adhesion. *Math. Med. Biol.*, 22(2):163–186, 2005.

[10] A. R. A. Anderson, M. A. J. Chaplain, E. L. Newman, R. J. C. Steele, and A. M. Thompson. Mathematical modelling of tumour invasion and metastasis. *J. Theor. Med.*, 2(2):129–154, 2000.

[11] S. D. Angus and M. J. Piotrowska. A numerical model of EMT6/Ro spheroid dynamics under irradiation: calibration and estimation of the underlying irradiation-induced cell survival probability. *J. Theor. Biol.*, 320:23–32, 2013.

[12] R. P. Araujo and D. L. S. McElwain. A history of the study of solid tumour growth: the contribution of mathematical modelling. *Bull. Math. Biol.*, 66(5):1039–1091, 2004.

[13] C. T. H. Baker, G. A. Bocharov, J. M. Ford, P. M. Lumb, S. J. Norton, C. A. H. Paul, T. Junt, P. Krebs, and B. Ludewig. Computational approaches to parameter estimation and model selection in immunology. *J. Comp. Appl. Math.*, 184(1):50–76, 2005.

[14] D. Balding and D. L. S. McElwain. A mathematical model of tumour-induced capillary growth. *J. Theor. Biol.*, 114(1):53–73, 1985.

[15] H. T. Banks, K. Holm, and D. Robbins. Standard error computations for uncertainty quantification in inverse problems: asymptotic theory vs. bootstrapping. *Math. Comput. Model.*, 52(9-10):1610–1625, 2010.

[16] H. T. Banks, K. J. Holm, and F. Kappel. A Monte Carlo based analysis of optimal design criteria. *J. Inverse Ill-Pose. P.*, 20(1):1–37, 2012.

[17] D. Basanta and A. R. A. Anderson. Exploiting ecological principles to better understand cancer progression and treatment. *Interface Focus*, 3(4):20130020, 2013.

[18] R. Baskar, K. A. Lee, R. Yeo, and K. Yeoh. Cancer and radiation therapy: current advances and future directions. *Int. J. Med. Sci.*, 9(3):193–199, 2012.

[19] A. C. Begg, F. Stewart, and C. Vens. Strategies to improve radiotherapy with targeted drugs. *Nat. Rev. Cancer*, 11(4):239–253, 2011.

[20] S. Benzekry, C. Lamont, A. Beheshti, A. Tracz, J. M. L. Ebos, L. Hlatky, and P. Hahnfeldt. Classical mathematical models for description and prediction of experimental tumor growth. *PLoS Comput. Biol.*, 10(8):e1003800, 2014.

[21] J. Bernier, E. J. Hall, and A. Giaccia. Radiation oncology: a century of achievements. *Nat. Rev. Cancer*, 4(9):737–747, 2004.

[22] A. Bertuzzi, C. Bruni, A. Fasano, A. Gandolfi, F. Papa, and C. Sinisgalli. Response of tumor spheroids to radiation: modeling and parameter estimation. *Bull. Math. Biol.*, 72(5):1069–1091, 2010.

[23] A. Bertuzzi, C. Bruni, F. Papa, and C. Sinisgalli. Optimal solution for a cancer radiotherapy problem. *J. Math. Biol.*, 66(1-2):311–349, 2013.

[24] A. Bertuzzi, A. D'Onofrio, A. Fasano, and A. Gandolfi. Regression and regrowth of tumour cords following single-dose anticancer treatment. *Bull. Math. Biol.*, 65(5):903–931, 2003.

[25] A. Bertuzzi, A. Fasano, A. Gandolfi, and D. Marangi. Cell kinetics in tumour cords studied by a model with variable cell cycle length. *Math. Biosci.*, 177-178:103–125, 2002.

[26] A. Bertuzzi, A. Fasano, A. Gandolfi, and C. Sinisgalli. Cell resensitization after delivery of a cycle-specific anticancer drug and effect of dose splitting: learning from tumour cords. *J. Theor. Biol.*, 244(3):388–399, 2007.

[27] A. Bertuzzi, A. Fasano, A. Gandolfi, and C. Sinisgalli. Reoxygenation and split-dose response to radiation in a tumour model with Krogh-type vascular geometry. *Bull. Math. Biol.*, 70(4):992–1012, 2008.

[28] M. F. Bolontrade, R. R. Zhou, and E. S. Kleinerman. Vasculogenesis plays a role in the growth of Ewing's sarcoma in vivo. *Clin. Cancer Res.*, 8(11):3622–3627, 2002.

[29] C. J. W. Breward, H. M. Byrne, and C. E. Lewis. The role of cell-cell interactions in a two-phase model for avascular tumour growth. *J. Math. Biol.*, 45(2):125–52, 2002.

[30] C. J. W. Breward, H. M. Byrne, and C. E. Lewis. A multiphase model describing vascular tumour growth. *Bull. Math. Biol. Math Biol*, 65(4):609–640, 2003.

[31] R. A. Burrell, N. McGranahan, J. Bartek, and C. Swanton. The causes and consequences of genetic heterogeneity in cancer evolution. *Nature*, 501:338–45, 2013.

[32] A. C. Burton. Rate of growth of solid tumour as a problem of diffusion. *Growth*, 30(2):157–176, 1966.

[33] H. M. Byrne. Dissecting cancer through mathematics: from the cell to the animal model. *Nat. Rev. Cancer*, 10(3):221–230, 2010.

[34] H. M. Byrne, T. Alarcón, M. R. Owen, S. D. Webb, and P. K. Maini. Modelling aspects of cancer dynamics: a review. *Phil. Trans. Roy. Soc. A.*, 364(April):1563–1578, 2006.

[35] H. M. Byrne and M. A. J. Chaplain. Mathematical models for tumour angiogenesis: numerical simulations and nonlinear wave solutions. *Bull. Math. Biol.*, 57(3):461–86, 1995.

[36] H. M. Byrne and M. A. J. Chaplain. Modelling the role of cell-cell adhesion in the growth and development of carcinoma. *Math. Comput. Model.*, 24(12):1–17, 1996.

[37] H. M. Byrne and D. Drasdo. Individual-based and continuum models of growing cell populations: a comparison. *J. Math. Biol.*, 58(4-5):657–687, 2009.

[38] H. M. Byrne, J. R. King, D. L. S. McElwain, and L. Preziosi. A two-phase model of solid tumour growth. *Appl. Math. Lett.*, 16(4):567–573, 2003.

[39] H. M. Byrne and L. Preziosi. Modelling solid tumour growth using the theory of mixtures. *Math. Med. Biol.*, 20(4):341–366, 2003.

[40] L. L. Campbell and K. Polyak. Breast tumor heterogeneity: cancer stem cells or clonal evolution? *Cell Cycle*, 6(19):2332–2338, 2007.

[41] P. Castorina, T. S. Deisboeck, P. Gabriele, and C. Guiot. Growth laws in cancer: implications for radiotherapy. *Radiat. Res.*, 168(3):349–356, 2007.

[42] B. A. Chabner and T. G. Roberts. Timeline: chemotherapy and the war on cancer. *Nat. Rev. Cancer*, 5(1):65–72, 2005.

[43] W. Chen, C. Wong, E. Vosburgh, A. J. Levine, D. J. Foran, and E.Y. Xu. High-throughput image analysis of tumor spheroids: a user-friendly software application to measure the size of spheroids automatically and accurately. *J. Vis. Exp.*, 89:e51639, 2014.

[44] Y. Chen, H. Wang, J. Zhang, K. Chen, and Y. Li. Simulation of avascular tumor growth by agent-based game model involving phenotype-phenotype interactions. *Sci. Rep.*, 5:17992, 2015.

[45] A. S. Cleary, T. L. Leonard, S. A. Gestl, and E. J. Gunther. Tumour cell heterogeneity maintained by cooperating subclones in Wnt-driven mammary cancers. *Nature*, 508:113–117, 2014.

[46] T. F. Coleman and Y. Li. An interior trust region approach for nonlinear minimization subject to bounds. *SIAM J. Optim.*, 6(2):418–445, 1996.

[47] J. Collis, A. J. Connor, M. Paczkowski, P. Kannan, J. Pitt-Francis, H. M. Byrne, and M. E. Hubbard. Bayesian calibration, validation and uncertainty quantification for predictive modelling of tumour growth: a tutorial. *Bull. Math. Biol.*, 79(4):939–974, 2017.

[48] V. Cristini, J. Lowengrub, and Q. Nie. Nonlinear simulation of tumor growth. *J. Math. Biol.*, 46(3):191–224, 2003.

[49] M. E. Davis, Z. G. Chen, and D. M. Shin. Nanoparticle therapeutics: an emerging treatment modality for cancer. *Nat. Rev. Drug Discov.*, 7(9):771–782, 2008.

[50] M. Deininger, E. Buchdunger, and B. J. Druker. The development of imatinib as a therapeutic agent for chronic myeloid leukemia. *Blood*, 105(7):2640–2653, 2005.

[51] G. Delaney, S. Jacob, C. Featherstone, and M. Barton. The role of radiotherapy in cancer treatment: estimating optimal utilization from a review of evidence-based clinical guidelines. *Cancer*, 104(6):1129–1137, 2005.

[52] D. L. Dexter, H. M. Kowalski, B. A. Blazar, Z. Fligiel, R. Vogel, and G. H. Heppner. Heterogeneity of tumor cells from a single mouse mammary tumor. *Cancer Res.*, 38:3174–3181, 1978.

[53] S. J. Diaz-Cano. Tumor heterogeneity: Mechanisms and bases for a reliable application of molecular marker design. *Int. J. Mol. Sci.*, 13(2):1951–2011, 2012.

[54] D. Drasdo. Coarse graining in simulated cell populations. *Adv. Complex Syst.*, 8:319–363, 2005.

[55] W. Düchting and T. Vogelsaenger. Recent progress in modelling and simulation of three-dimensional tumor growth and treatment. *Biosystems*, 18(1):79–91, 1985.

[56] B. Efron. Bootstrap methods: another look at the jackknife. *Ann. Stat.*, 7:1–26, 1979.

[57] H. Enderling, A. R. A. Anderson, M. A. J. Chaplain, A. J. Munro, and J. S. Vaidya. Mathematical modelling of radiotherapy strategies for early breast cancer. *J. Theor. Biol.*, 241(1):158–171, 2006.

[58] H. Enderling and M. A. J. Chaplain. Mathematical modeling of tumor growth and treatment. *Curr. Pharm. Des.*, 20(30):4934–4940, 2014.

[59] H. Enderling, M. A. J. Chaplain, A. R. A. Anderson, and J. S. Vaidya. A mathematical model of breast cancer development, local treatment and recurrence. *J. Theor. Biol.*, 246(2):245–259, 2007.

[60] H. Enderling, M. A. J. Chaplain, and P. Hahnfeldt. Quantitative modeling of tumor dynamics and radiotherapy. *Acta Biotheor.*, 58(4):341–353, 2010.

[61] H. Enderling, D. Park, L. Hlatky, and P. Hahnfeldt. The importance of spatial distribution of stemness and proliferation state in determining tumor radioresponse. *Math. Model. Nat. Phenom.*, 4(3):117–133, 2009.

[62] J. A. Engelberg, G. E. P. Ropella, and C. A. Hunt. Essential operating principles for tumor spheroid growth. *BMC Syst. Biol.*, 2:110, 2008.

[63] A. Ergun, K. Camphausen, and L. M. Wein. Optimal scheduling of radiotherapy and angiogenic inhibitors. *Bull. Math. Biol.*, 65(3):407–424, 2003.

[64] S. Farber, L. K. Diamond, R. D. Mercer, R. F. Sylvester, and J. A. Wolff. Temporary remissions in acute leukemia in children produced by folic acid antagonist, 4-aminopteroyl-glutamic acid (Aminopterin). *N. Engl. J. Med.*, 238(23):787–793, 1948.

[65] S. C. Ferreira, M. L. Martins, and M. J. Vilela. Reaction-diffusion model for the growth of avascular tumor. *Phys. Rev. E*, 65(2):65–73, 2002.

[66] J. Folkman. Role of angiogenesis in tumor growth and metastasis. *Semin. Oncol.*, 29:15–18, 2002.

[67] J. P. Freyer. Role of necrosis in regulating the growth saturation of multicellular spheroids. *Cancer Res.*, 48(9):2432–2439, 1988.

[68] J. P. Freyer, E. Tustanoff, A. J. Franko, and R. M. Sutherland. In situ oxygen consumption rates of cells in V-79 multicellular spheroids during growth. *J. Cell. Physiol.*, 118(1):53–61, 1984.

[69] J. Friedrich, R. Ebner, and L. Kunz-Schughart. Experimental anti-tumor therapy in 3-D: spheroids—old hat or new challenge? *Int. J. Radiat. Biol.*, 83:849–871, 2007.

[70] R. A. Gatenby and E. T. Gawlinski. A reaction-diffusion model of cancer invasion. *Cancer Res.*, 56(24):5745–5753, 1996.

[71] R. A. Gatenby, A. S. Silva, R. J. Gillies, and B. R. Frieden. Adaptive therapy. *Cancer Res.*, 69(11):4894–4903, 2009.

[72] P. Gerlee. The model muddle: In search of tumor growth laws. *Cancer Res.*, 73(8):2407–2411, 2013.

[73] P. Gerlee and A. R. A. Anderson. An evolutionary hybrid cellular automaton model of solid tumour growth. *J. Theor. Biol.*, 246(4):583–603, 2007.

[74] P. Gerlee and A. R. A. Anderson. A hybrid cellular automaton model of clonal evolution in cancer: The emergence of the glycolytic phenotype. *J. Theor. Biol.*, 250(4):705–722, 2008.

[75] P. Gerlee and A. R. A. Anderson. Diffusion-limited tumour growth: simulations and analysis. *Math. Biosci. Eng.*, 7(2):385–400, 2010.

[76] A. Gilman. The initial clinical trial of nitrogen mustard. *Am. J. Surg.*, 105(May):574–578, 1963.

[77] L. H. Gray, A. D. Conger, M. Ebert, S. Hornsey, and O. C. Scott. The concentration of oxygen dissolved in tissues at the time of irradiation as a factor in radiotherapy. *Br. J. Radiol.*, 26(312):638–648, 1953.

[78] H. P. Greenspan. Models for the growth of a solid tumor by diffusion. *Stud. Appl. Math.*, 51(4):317–340, dec 1972.

[79] H. P. Greenspan. On the growth and stability of cell cultures and solid tumors. *J. Theor. Biol.*, 56(1):229–242, 1976.

[80] D. R. Grimes, C. Kelly, K. Bloch, and M. Partridge. A method for estimating the oxygen consumption rate in multicellular tumour spheroids. *J. R. Soc. Interface*, 11:20131124, 2014.

[81] J. Grote, R. Süsskind, and P. Vaupel. Oxygen diffusivity in tumor tissue (DS-Carcinosarcoma) under temperature conditions within the range of 20–40°C. *Eur. J. Phycol.*, 372(1):37–42, 1977.

[82] P. Hahnfeldt, D. Panigrahy, J. Folkman, and L. Hlatky. Tumor development under angiogenic signaling: a dynamical theory of tumor growth, treatment response, and postvascular dormancy. *Cancer Res.*, 59(19):4770–4775, 1999.

[83] D. Hanahan and R. A. Weinberg. The hallmarks of cancer. *Cell*, 100(1):57–70, 2000.

[84] D. Hanahan and R. A. Weinberg. Hallmarks of cancer: the next generation. *Cell*, 144(5):646–674, 2011.

[85] G. Heppner. Tumor heterogeneity. *Cancer Res.*, 44:2259–2265, 1984.

[86] K. E. Hines. A primer on bayesian inference for biophysical systems. *Biophys. J.*, 108(9):2103–2113, 2015.

[87] F. Hirschhaeuser, H. Menne, C. Dittfeld, J. West, W. Mueller-Klieser, and L. A. Kunz-Schughart. Multicellular tumor spheroids: An underestimated tool is catching up again. *J. Biotechnol.*, 148:3–15, 2010.

[88] X. Huang, S. Taeb, S. Jahangiri, U. Emmenegger, E. Tran, J. Bruce, A. Mesci, E. Korpela, D. Vesprini, C. S. Wong, R. G. Bristow, F. F. Liu, and S. K. Liu. miRNA-95 mediates radioresistance in tumors by targeting the sphingolipid phosphatase SGPP1. *Cancer Res.*, 73(23):6972–6986, 2013.

[89] M. E. Hubbard and H. M. Byrne. Multiphase modelling of vascular tumour growth in two spatial dimensions. *J. Theor. Biol.*, 316:70–89, 2013.

[90] A. Ivascu and M. Kubbies. Rapid generation of single-tumor spheroids for high-throughput cell function and toxicity analysis. *J. Biomol. Screen*, 11(8):922–932, 2006.

[91] S. P. Jackson and J. Bartek. The DNA-damage response in human biology and disease. *Nature*, 461:1071–8, 2009.

[92] D. A. Jaffray. Image-guided radiotherapy: from current concept to future perspectives. *Nat. Rev. Clin. Oncol.*, 9(12):688–699, 2012.

[93] N. Jagiella, B. Müller, M. Müller, I. E. Vignon-Clementel, and D. Drasdo. Inferring growth control mechanisms in growing multi-cellular spheroids of NSCLC cells from spatial-temporal image data. *PLoS Comput. Biol.*, 12(2):e1004412, 2016.

[94] Y. Jiao and S. Torquato. Emergent behaviors from a cellular automaton model for invasive tumor growth in heterogeneous microenvironments. *PLoS Comput. Biol.*, 7(12):10–12, 2011.

[95] M. Joiner and A. van der Kogel. *Basic Clinical Radiobiology*. Hodder Arnold, 4th edition, 2009.

[96] M. Joshi, A. Seidel-Morgenstern, and A. Kremling. Exploiting the bootstrap method for quantifying parameter confidence intervals in dynamical systems. *Metab. Eng.*, 8(5):447–55, 2006.

[97] M. R. Junttila and F. J. de Sauvage. Influence of tumour micro-environment heterogeneity on therapeutic response. *Nature*, 501:346–354, 2013.

[98] M. E. Kaighn, K. S. Narayan, Y. Ohnuki, J. F. Lechner, and L. W. Jones. Establishment and characterization of a human prostatic carcinoma cell line (PC-3). *Invest. Urol.*, 17(1):16–23, 1979.

[99] A. R. Kansal, S. Torquato, E. A. Chiocca, and T. S. Deisboeck. Emergence of a subpopulation in a computational model of tumor growth. *J. Theor. Biol.*, 207(3):431–441, 2000.

[100] A. R. Kansal, S. Torquato, G. R. Harsh, E. A. Chiocca, and T. S. Deisboeck. Simulated brain tumor growth dynamics using a three-dimensional cellular automaton. *J. Theor. Biol.*, 203(4):367–382, 2000.

[101] H. Kantarjian, C. Sawyers, A. Hochhaus, F. Guilhot, C. Schiffer, C. Gambacorti-Passerini, D. Niederwieser, D. Resta, R. Capdeville, U. Zoellner, M. Talpaz, and B. Druker. Hematologic and cytogenetic responses to Imatinib mesylate in chronic myelogenous leukemia. *N. Engl. J. Med.*, 346(9):645–652, feb 2002.

[102] H. Kempf, M. Bleicher, and M. Meyer-Hermann. Spatio-temporal cell dynamics in tumour spheroid irradiation. *Eur. Phys. J. D*, 60(1):177–193, 2010.

[103] H. Kempf, H. Hatzikirou, M. Bleicher, and M. Meyer-Hermann. In silico analysis of cell cycle synchronisation effects in radiotherapy of tumour spheroids. *PLoS Comput. Biol.*, 9(11):e1003295, 2013.

[104] K. A. Landman and C. P. Please. Tumour dynamics and necrosis: surface tension and stability. *IMA J. Math. Appl. Med.*, 18:131–158, 2001.

[105] T. Lapidot, C. Sirard, J. Vormoor, B. Murdoch, T. Hoang, J. Caceres-Cortes, M. Minden, B. Paterson, M. A. Caligiuri, and J. E. Dick. A cell initiating human acute myeloid leukaemia after transplantation into SCID mice. *Nature*, 367:645–648, 1994.

[106] K. E. A. LaRue, M. Khalil, and J. P. Freyer. Microenvironmental regulation of proliferation in multicellular spheroids is mediated through differential expression of cyclin-dependent kinase inhibitors. *Cancer Res.*, 64:1621–1631, 2004.

[107] J. T. Leith, D. L. Dexter, J. K. DeWyngaert, E. M. Zeman, M. Y. Chu, P. Calabresi, and A. S. Glicksman. Differential responses to X-irradiation of subpopulations of two heterogeneous human carcinomas *in vitro*. *Cancer Res.*, 42(7):2556–2561, 1982.

[108] J. T. Leith, L. E. Faulkner, S. F. Bliven, and S. Michelson. Tumor bed expression in xenografted artificial heterogeneous colon tumors. *Int. J. Radiat. Biol.*, 15(1):151–158, 1988.

[109] J. T. Leith, S. Michelson, L. E. Faulkner, and S. F. Bliven. Growth properties of artificial heterogeneous human colon tumors. *Cancer Res.*, 47(4):1045–1051, 1987.

[110] J. T. Leith, S. Michelson, and S. Glicksman. Competitive exclusion of clonal subpopulations in heterogeneous tumours after stromal injury. *Brit. J. Cancer*, 59(1):22–7, 1989.

[111] J. Liepe, P. Kirk, S. Filippi, T. Toni, C. P. Barnes, and M. P. H. Stumpf. A framework for parameter estimation and model selection from experimental data in systems biology using approximate Bayesian computation. *Nat. Protoc.*, 9(2):439–56, 2014.

[112] J. S. Lowengrub, H. B. Frieboes, F. Jin, Y. L. Chuang, X. Li, P. Macklin, S. M. Wise, and V. Cristini. Nonlinear modelling of cancer: bridging the gap between cells and tumours. *Nonlinearity*, 23(1):R1–R91, 2010.

[113] K. Mandel, Y. Yang, A. Schambach, S. Glage, A. Otte, and R. Hass. Mesenchymal stem cells directly interact with breast cancer cells and promote tumor cell growth in vitro and in vivo. *Stem Cells Dev.*, 22(23):3114–3127, 2013.

[114] M. Marusic, Z. Bajzer, J. P. Freyer, and S. Vuk-Pavlovic. Analysis of growth of multicellular tumour spheroids by mathematical models. *Cell Prolif.*, 27(2):73–94, 1994.

[115] A. Marusyk and K. Polyak. Tumor heterogeneity: causes and consequences. *Biochim. Biophys. Acta*, 1805(1):105–117, 2010.

[116] MATLAB. *version 1.7.0 (R2015a)*. The MathWorks Inc., Natick, Massachusetts, 2015.

[117] H. McAneney and S. F. O'Rourke. Investigation of various growth mechanisms of solid tumour growth within the linear-quadratic model for radiotherapy. *Phys. Med. Biol.*, 52(4):1039–1054, 2007.

[118] L. M. Merlo, R. E. Kosoff, K. L. Gardiner, and C. C. Maley. An in vitro coculture model of esophageal cells identifies ascorbic acid as a modulator of cell competition. *BMC Cancer*, 11(1):461, 2011.

[119] L. M. F. Merlo, J. W. Pepper, B. J. Reid, and C. C. Maley. Cancer as an evolutionary and ecological process. *Nat. Rev. Cancer*, 6(December):924–935, 2006.

[120] S. Michelson, A. S. Glicksman, and J. T. Leith. Growth in solid heterogeneous human colon adenocarcinomas: comparison of simple logistical models. *Cell Tissue Kinet.*, 20(3):343–355, 1987.

[121] S. Michelson and J. T. Leith. Environmental stress induced by the tumor bed effect leads to subpopulation exclusion within heterogeneous neoplasms: modeling studies. *Radiat. Res.*, 115(3):533–542, 1988.

[122] S. Michelson and J. T. Leith. Effects of differential cell kill on the dynamic composition of heterogeneous tumors. *Computers Math. Applic.*, 20(4):149–159, 1990.

[123] S. Michelson, B. E. Miller, A. S. Glicksman, and J. T. Leith. Tumor microecology and competitive interactions. *J. Theor. Biol.*, 128(2):233–246, 1987.

[124] B. E. Miller, T. Machemer, M. Lehotan, and G. H. Heppner. Tumor subpopulation interactions affecting Melphalan sensitivity in palpable mouse mammary tumors. *Cancer Res.*, 51:4378–4387, 1991.

[125] B. E. Miller, F. R. Miller, and G. H. Heppner. Interactions between tumor subpopulations affecting their sensitivity to the antineoplastic agents cyclophosphamide and methotrexate. *Cancer Res.*, 41(11):4378–4381, 1981.

[126] B. E. Miller, F. R. Miller, and G. H. Heppner. Assessing tumor drug sensitivity by a new in vitro assay which preserves tumor heterogeneity and subpopulation interactions. *J. Cell. Physiol*, 121(S3):105–116, 1984.

[127] B. E. Miller, F. R. Miller, and G. H. Heppner. Factors affecting growth and drug sensitivity of mouse mammary tumor lines in collagen gel cultures. *Cancer Res.*, 45(9):4200–5, 1985.

[128] B. E. Miller, F. R. Miller, and G. H. Heppner. Therapeutic perturbation of the tumor ecosystem in reconstructed heterogeneous mouse mammary tumors. *Cancer Res.*, 49(14):3747–3753, 1989.

[129] B. E. Miller, F. R. Miller, J. T. Leith, and G. H. Heppner. Growth interaction *in vivo* between tumor subpopulations derived from a single mouse mammary tumor. *Cancer Res.*, 40(November):3977–3981, 1980.

[130] B. E. Miller, F. R. Miller, D. Wilburn, and G. H. Heppner. Dominance of a mammary tumor subpopulation in mixed heterogenous tumors. *Cancer Res.*, 48:5747–5753, 1988.

[131] E. J. Moding, M. B. Kastan, and D. G. Kirsch. Strategies for optimizing the response of cancer and normal tissues to radiation. *Nat. Rev. Drug Discov.*, 12(7):526–542, 2013.

[132] C. Mothersill and C. B. Seymour. Radiation-induced bystander effects—implications for cancer. *Nat. Rev. Cancer*, 4(2):158–164, 2004.

[133] A. J. Munro. Bystander effects and their implications for clinical radiotherapy. *J. Radiol. Prot.*, 29(2A):A133–42, 2009.

[134] J. D. Murray. *Mathematical biology.* Springer-Verlag, New York, Berlin, Heidelberg, 3rd edition, 2002.

[135] J. D. Nagy. Competition and natural selection in a mathematical model of cancer. *Bull. Math. Biol.*, 66(4):663–687, 2004.

[136] L. Naumov, A. Hoekstra, and P. Sloot. Cellular automata models of tumour natural shrinkage. *Physica A*, 390(12):2283–2290, 2011.

[137] Nexcelom Bioscience. http://www.nexcelom.com/landing/NCI-60-cell-table.php.

[138] P. C. Nowell. The clonal evolution of tumor cell populations. *Science*, 194(4260):23–28, 1976.

[139] J. P. B. O'Connor, C. J. Rose, J. C. Waterton, R. A. D. Carano, G. J. M. Parker, and A. Jackson. Imaging intratumor heterogeneity: role in therapy response, resistance, and clinical outcome. *Clin. Cancer Res.*, 21(2):249–257, 2015.

[140] T. Oden, R. Moser, and O. Ghattas. Computer predictions with quantified uncertainty, Part I. *SIAM News*, 43(9), 2010.

[141] J. A. O'Donoghue. The response of tumours with Gompertzian growth characteristics to fractionated radiotherapy. *Int. J. Radiat. Biol.*, 72(3):325–339, 1997.

[142] S. F. C. O'Rourke, H. McAneney, and T. Hillen. Linear quadratic and tumour control probability modelling in external beam radiotherapy. *J. Math. Biol.*, 58(4-5):799–817, 2009.

[143] J. C. Panetta. A mathematical model of drug resistance: heterogeneous tumors. *Math. Biosci.*, 147(1):41–61, 1998.

[144] J. C. Panetta and J. Adam. A mathematical model of cycle-specific chemotherapy. *Math. Comput. Model.*, 22(2):67–82, 1995.

[145] R. J. Papac. Origins of cancer therapy. *Yale J. Biol. Med.*, 74(6):391–398, 2001.

[146] M. Partridge. A radiation damage repair model for normal tissues. *Phys. Med. Biol.*, 53(13):3595–3608, 2008.

[147] A. A. Patel, E. T. Gawlinski, S. K. Lemieux, and R. A. Gatenby. A cellular automaton model of early tumor growth and invasion: the effects of native tissue vascularity and increased anaerobic tumor metabolism. *J. Theor. Biol*, 213:315–331, 2001.

[148] B. Pauwels, A. Wouters, M. Peeters, J. B. Vermorken, and F. Lardon. Role of cell cycle perturbations in the combination therapy of chemotherapeutic agents and radiation. *Futur. Oncol.*, 6(9):1485–96, 2010.

[149] T. M. Pawlik and K. Keyomarsi. Role of cell cycle in mediating sensitivity to radiotherapy. *Int. J. Radiat. Oncol. Biol. Phys.*, 59(4):928–942, 2004.

[150] M. J. Piotrowska and S. D. Angus. A quantitative cellular automaton model of in vitro multicellular spheroid tumour growth. *J. Theor. Biol.*, 258:165–178, 2009.

[151] C. P. Please, G. Pettet, and D. L. S. McElwain. A new approach to modelling the formation of necrotic regions in tumours. *Appl. Math. Lett.*, 11(3):89–94, 1998.

[152] G. G. Powathil, D. J. Adamson, and M. A. Chaplain. Towards predicting the response of a solid tumour to chemotherapy and radiotherapy treatments: clinical insights from a computational model. *PLoS Comput Biol*, 9(7):e1003120, 2013.

[153] G. G. Powathil, K. E. Gordon, L. A. Hill, and M .A. J. Chaplain. Modelling the effects of cell-cycle heterogeneity on the response of a solid tumour to chemotherapy: Biological insights from a hybrid multiscale cellular automaton model. *J. Theor. Biol.*, 308:1–19, 2012.

[154] G. G. Powathil, A. J. Munro, M. A. J. Chaplain, and M. Swat. Bystander effects and their implications for clinical radiation therapy: Insights from multiscale in silico experiments. *J. Theor. Biol.*, 401:1–14, 2016.

[155] G. G. Powathil, M. Swat, and M. A. J. Chaplain. Systems oncology: towards patient-specific treatment regimes informed by multiscale mathematical modelling. *Semin. Cancer Biol.*, 30:13–20, 2015.

[156] W. H. Press, S. A. Teukolsky, W. T. Vetterling, and B. P. Flannery. *Numerical recipes: the art of scientific computing*. Cambridge University Press, New York, 3rd edition, 2007.

[157] K. M. Prise and J. M. O'Sullivan. Radiation-induced bystander signalling in cancer therapy. *Nat. Rev. Cancer*, 9(5):351–360, 2009.

[158] J. K. Pritchard, M. T. Seielstad, A. Perez-Lezaun, and M. W. Feldman. Population growth of human Y chromosomes: a study of Y chromosome microsatellites. *Mol. Biol. Evol.*, 16(12):1791–8, 1999.

[159] A. Qi, X. Zheng, C. Du, and B. An. A cellular automaton model of cancerous growth. *J. Theor. Biol.*, 161:1–12, 1993.

[160] V. Quaranta, K. A. Rejniak, P. Gerlee, and A. R. A. Anderson. Invasion emerges from cancer cell adaptation to competitive microenvironments: quantitative predictions from multiscale mathematical models. *Semin. Cancer Biol.*, 18(5):338–348, 2008.

[161] E. A. Reis, L. B. L. Santos, and S. T. R. Pinho. A cellular automata model for avascular solid tumor growth under the effect of therapy. *Physica A*, 388:1303–1314, 2009.

[162] K. A. Rejniak and A. R. A. Anderson. Hybrid models of tumor growth. *Wires. Syst. Biol. Med.*, 3:115–125, 2011.

[163] B. Ribba, T. Colin, and S. Schnell. A multiscale mathematical model of cancer, and its use in analyzing irradiation therapies. *Theor. Biol. Med. Model.*, 3(1):7, 2006.

[164] C. Roche-Lestienne, V. Soenen-Cornu, N. Grardel-Duflos, J. L. Laï, N. Philippe, T. Facon, P. Fenaux, and C. Preudhomme. Several types of mutations of the Abl gene can be found in chronic myeloid leukemia patients resistant to STI571, and they can pre-exist to the onset of treatment. *Blood*, 100(3):1014–1018, 2002.

[165] R. Rockne, E. C. Alvord Jr., J. K. Rockhill, and K. R. Swanson. A mathematical model for brain tumor response to radiation therapy. *J. Math. Biol.*, 58(4-5):561–578, 2009.

[166] S. Rockwell, I. T. Dobrucki, E. Y. Kim, S. T. Marrison, and V. T. Vu. Hypoxia and radiation therapy: past history, ongoing research, and future promise. *Curr. Mol. Med.*, 9(4):442–458, 2009.

[167] T. Roose, S. J. Chapman, and P. K. Maini. Mathematical models of avascular tumor growth. *SIAM Rev.*, 49(2):179–208, 2007.

[168] D. C. Rubinsztein, J. E. Gestwicki, L. O. Murphy, and D. J. Klionsky. Potential therapeutic applications of autophagy. *Nat. Rev. Drug Discov.*, 6(4):304–312, 2007.

[169] R. K. Sachs, L. R. Hlatky, and P. Hahnfeldt. Simple ODE models of tumor growth and anti-angiogenic or radiation treatment. *Math. Comput. Model.*, 33(12-13):1297–1305, 2001.

[170] M. T. Santini, G. Rainaldi, and P. L. Indovina. Multicellular tumour spheroids in radiation biology. *Int. J. Radiat. Biol.*, 75:787–799, 1999.

[171] E. A. Sarapata and L. G. de Pillis. A comparison and catalog of intrinsic tumor growth models. *Bull. Math. Biol.*, 76(8):2010–24, 2014.

[172] D. Schulz-Ertner and H. Tsujii. Particle radiation therapy using proton and heavier ion beams. *J. Clin. Oncol.*, 25(8):953–964, 2007.

[173] G. A. F. Seber and C. J. Wild. *Nonlinear Regression.* John Wiley & Sons, Inc., Hoboken, New Jersey, 2003.

[174] S. M. B. Shrestha, G. R. Joldes, A. Wittek, and K. Miller. Cellular automata coupled with steady-state nutrient solution permit simulation of large-scale growth of tumours. *Int. J. Numer. Meth. Biomed. Engng.*, 29:542–559, 2013.

[175] R. Siegel, C. Desantis, K. Virgo, K. Stein, A. Mariotto, T. Smith, D. Cooper, T. Gansler, C. Lerro, and S. Fedewa. Cancer Treatment and Survivorship Statistics, 2012. *CA Cancer J. Clin.*, pages 1–22, 2013.

[176] W. K. Sinclair and R. A. Morton. Variations in x-ray response during the division cycle of partially synchronized Chinese hamster cells in culture. *Nature*, 199:1158–60, 1963.

[177] W. K. Sinclair and R. A. Morton. X-ray and ultraviolet sensitivity of synchronized Chinese hamster cells at various stages of the cell cycle. *Biophys. J.*, 5(1):1–25, 1965.

[178] I. J. Stamper, H. M. Byrne, M. R. Owen, and P. K. Maini. Modelling the role of angiogenesis and vasculogenesis in solid tumour growth. *Bull. Math. Biol.*, 69(8):2737–2772, 2007.

[179] G. G. Steel, T. J. McMillan, and J. H. Peacock. The 5 Rs of radiobiology. *Int. J. Radiat. Biol. Relat. Stud. Phys. Chem. Med.*, 56(6):1045–1048, 1989.

[180] K. R. Stone, D. D. Mickey, H. Wunderli, G. H. Mickey, and D. F. Paulson. Isolation of a human prostate carcinoma cell line (DU145). *Int. J. Cancer*, 21(3):274–281, 1978.

[181] M. P. H. Stumpf. Approximate Bayesian inference for complex ecosystems. *F1000Prime Rep.*, 6, 2014.

[182] R. M. Sutherland. Cell and environment interactions in tumor microregions: the multicell spheroid model. *Science*, 240(4849):177–184, 1988.

[183] R. M. Sutherland and R. E. Durand. Growth and cellular characteristics of multicell spheroids. *Recent Res. Cancer*, 95:24–49, 1984.

[184] R. M. Sutherland, W. R. Inch, J. A. McCredie, and J. Kruuv. A multi-component radiation survival curve using an in vitro tumour model. *Int. J. Radiat. Biol. Relat. Stud. Phys. Chem. Med.*, 18(5):491–495, 1970.

[185] R. M. Sutherland, J. A. McCredie, and W. R. Inch. Growth of multicell spheroids in tissue culture as a model of nodular carcinomas. *J. Natl. Cancer I.*, 46:113–120, 1971.

[186] K. R. Swanson, E. C. Alvord Jr., and J. D. Murray. A quantitative model for differential motility of gliomas in grey and white matter. *Cell Prolif.*, 33(5):317–329, 2000.

[187] K. R. Swanson, E. C. Alvord Jr., and J. D. Murray. Virtual brain tumours (gliomas) enhance the reality of medical imaging and highlight inadequacies of current therapy. *Br. J. Cancer*, 86(1):14–18, 2002.

[188] D. P. Tabassum and K. Polyak. Tumorigenesis: it takes a village. *Nat. Rev. Cancer*, 15(8):1–11, 2015.

[189] I. Tariq, L. Humbert-Vidan, T. Chen, C. P. South, V. Ezhil, N. F. Kirkby, R. Jena, and A. Nisbet. Mathematical modelling of tumour volume dynamics in response to stereotactic ablative radiotherapy for non-small cell lung cancer. *Phys. Med. Biol.*, 60(9):3695–3713, 2015.

[190] H. D. Thames, H. Rodney W., L. J. Peters, and G. H. Fletcher. Changes in early and late radiation responses with altered dose fractionation: Implications for dose-survival relationships. *Int. J. Radiat. Oncol. Biol. Phys.*, 8(2):219–226, 1982.

[191] R. H. Thomlinson and L. H. Gray. The histological structure of some human lung cancers and the possible implications for radiotherapy. *Br. J. Cancer*, 9:539–549, 1955.

[192] B. Titz and R. Jeraj. An imaging-based tumour growth and treatment response model: investigating the effect of tumour oxygenation on radiation therapy response. *Phys. Med. Biol.*, 53:4471–4488, 2008.

[193] M. M. Tomayko and C. P. L. B. Reynolds. Determination of subcutaneous tumor size in athymic (nude) mice. *Cancer Chemoth. Pharm.*, 24:148–154, 1989.

[194] T. Toni, D. Welch, N. Strelkowa, A. Ipsen, and M. P. Stumpf. Approximate Bayesian computation scheme for parameter inference and model selection in dynamical systems. *J. R. Soc. Interface*, 6(31):187–202, 2009.

[195] B. M. Turner and T. Van Zandt. A tutorial on approximate Bayesian computation. *J. Math. Psychol.*, 56(2):69–85, 2012.

[196] G. Tzedakis, E. Tzamali, K. Marias, and V. Sakkalis. The importance of neighborhood scheme selection in agent-based tumor growth modeling. *Cancer Inform.*, 14(S4):67–81, 2015.

[197] J. P. Ward and J. R. King. Mathematical modelling of avascular-tumour growth. *IMA J. Math. Appl. Med.*, 14(1):39–69, 1997.

[198] T. E. Wheldon, J. Kirk, and J. S. Orr. Optimal radiotherapy of tumour cells following exponential-quadratic survival curves and exponential repopulation kinetics. *Br. J. Radiol.*, 50(597):681–682, 1977.

[199] H. R. Withers. The four R's of radiotherapy. In *Adv. Radiat. Biol.*, volume 5, pages 241–271. Academic Press, 1975.

[200] B. G. Wouters and J. M. Brown. Cells at intermediate oxygen levels can be more important than the "hypoxic fraction" in determining tumor response to fractionated radiotherapy. *Radiat. Res.*, 147(5):541–550, 1997.

[201] C. A. Yates and R. E. Baker. Isotropic model for cluster growth on a regular lattice. *Phys. Rev. E*, 88(2):1–7, 2013.

[202] E. I. Zacharaki, G. S. Stamatakos, K. S. Nikita, and N. K. Uzunoglu. Simulating growth dynamics and radiation response of avascular tumour spheroids - Model validation in the case of an EMT6/Ro multicellular spheroid. *Comput. Meth. Prog. Bio.*, 76:193–206, 2004.

[203] M. Zanoni, F. Piccinini, C. Arienti, A. Zamagni, S. Santi, R. Polico, A. Bevilacqua, and A. Tesei. 3D tumor spheroid models for in vitro therapeutic screening: a systematic approach to enhance the biological relevance of data obtained. *Sci. Rep.*, 6:19103, 2016.